Predicting The Shear Strength of Macro-Synthetic Fiber-Reinforced Concrete

Benedikt F. Farag

A Thesis
submitted in partial fulfillment of the
requirements for the degree of

Master of Science in Civil Engineering

University of Washington

2024

Committee:

Travis E. Thonstad, Chair

Paolo M. Calvi, Chair

Marc O. Eberhard

Program Authorized to Offer Degree:
Civil and Environmental Engineering

©Copyright 2024
Benedikt F. Farag

University of Washington

Abstract

Predicting The Shear Strength of Macro-Synthetic Fiber-Reinforced Concrete

Benedikt F. Farag

Co-Chairs of the Supervisory Committee:
Travis E. Thonstad
Civil and Environmental Engineering

Paolo M. Calvi
Civil and Environmental Engineering

Macro-synthetic fibers are commonly added to concrete mixtures as secondary reinforcement to control temperature and shrinkage cracks in concrete flatwork. The fibers limit the width of cracks that develop in the cast concrete, improving durability and longevity. The fibers also improve the tensile behavior of the material. However, the contribution of macro-synthetic fibers towards the strength of structural elements is generally neglected. A recent experimental program tested twelve macro-synthetic fiber-reinforced concrete (PFRC) panels subjected to pure shear loading and explored the contribution of macro-synthetic fibers to shear strength when used in combination with conventional deformed bar shear reinforcement. The tests indicated that, for typical fiber contents ($\leq$ 0.5% by volume), macro-synthetic fibers did not decrease the shear capacity of the panels but reduced crack widths at various load levels. The experimental program provided some evidence that macro-synthetic fibers are beneficial for shear loading but was limited in scope and in the levels of the experimental variables that could be tested.

To further investigate the influence of macro-synthetic fibers on shear behavior, a parametric study was performed using finite element models to extend the experimental results and explore combinations of parameters that were not tested experimentally. A modeling approach was calibrated using the experimental panel data, where a concrete tension softening model was incorporated to capture the strength contribution of the fibers. The modeling approach was validated against a database of PFRC beams from the literature, which was compiled as part of this research. The modeling approach was then used to conduct a

parametric study, exploring the monotonic pure shear strength of PFRC panels with over 250 combinations of fiber contents, transverse reinforcement ratios, and concrete compressive strengths. The results of the parametric study indicated that macro-synthetic fibers effectively reduced crack widths and enhanced shear strength, depending on the transverse reinforcement ratio and fiber content. Greater benefits were observed for lower transverse reinforcement ratios ($\leq 0.25\%$) and higher fiber contents ($> 1.0\%$), exhibiting slightly different trends for the different concrete compressive strengths.

The ability of existing empirical equations in model codes and in the literature to predict the shear strength of PFRC structural elements was also evaluated. Most current design codes neglect the contribution of macro-synthetic fibers to the shear strength of structural elements, which resulted in significant underestimation of shear strength. Several empirical equations from the literature provided more reasonable estimates of shear strength for both PFRC beams and panels and were used to propose a fiber-reinforcement term that would modify current code-based shear strength prediction equations. Recognizing the structural benefits of macro-synthetic fibers would increase their use and would lead to more durable and resilient reinforced concrete structures.

TABLE OF CONTENTS

Page

LIST OF FIGURES

LIST OF TABLES

ACKNOWLEDGMENTS

First, I would like to thank my advisors Paolo Calvi and Travis Thonstad for providing me this opportunity of working on this project. I highly appreciate their guidance throughout this time that has contributed to my personal growth and the outcomes of this study. The project included multiple challenges that was an invaluable learning experience. I also want to thank Marc Eberhard to be willing to serve on my thesis committee and offering valuable advice for the project.

I also want to thank John Paul Gaston for conducting the comprehensive experimental program that this research is based on. Without his enthusiastic work in the Structures Lab, this project would not have came to light. I appreciated our cooperation throughout the project that helped me to get started.

This project has been one of my greatest challenges throughout my educational career. The nearly two years that I have dedicated to this project did not feel like a long time. From the beginning I was excited about the work and I feel like the time passed way to quickly. I have really enjoyed my time here at UW, where I have felt like home for the past two years.

Chapter 1
INTRODUCTION

Macro-synthetic fibers are often added to concrete mixtures as secondary reinforcement, designed to control shrinkage and temperature cracks. Adding fibers to concrete has also proven to enhance various concrete properties, such as tensile strength, deformation capacity, toughness and overall improved performance (Balaguru and Shah, 1992). In recent years, the use of macro-synthetic fibers for structural applications has gained research interest, whereas the fibers have demonstrated abilities to increase the shear strength of concrete members.

Significant research has been conducted on replacing conventional transverse steel reinforcement bars with distributed fibers, particularly using steel fibers (e.g., Susetyo et al., 2011; You et al., 2010). The impact of this research on steel-fiber reinforced concrete (SFRC) led to a revision of the minimum shear reinforcement requirement in ACI 318-08, permitting the use of steel fibers exceeding 0.75% by volume and meeting various requirements. This change was based on a research by Parra-Montesinos (2006), where a database of 147 SFRC beams was analyzed. The study concluded that all slender SFRC beams with a fiber volume of $V_f \geq 0.75\%$ achieved a shear stress higher than $0.29\sqrt{f'_c}$ ($3.5\sqrt{f'_c}\ psi$).

Despite the extensive research conducted on replacing conventional transverse reinforcement with distributed fibers, the combined use has not been investigated thoroughly. Utilizing a high amount of fiber content can decrease the workability of the concrete, leading to consolidation issues (Zhao et al., 2023). Therefore, significant benefits could arise from the combined use of stirrups and fibers, where fiber content could be reduced compared to using fibers alone. While there is evidence of synergy between them two, it does not always occur (Navas et al., 2018). In current design, conventional steel transverse reinforcement resists most of the shear demand, while the fibers provide enhanced shear strength in addition to providing benefits to the concrete properties.

The majority of fiber-reinforced concrete (FRC) research has focused on steel fibers. However, some drawbacks of steel fibers include high density, susceptibility to corrosion and high production costs (Lambrechts, 2009). As an alternative, synthetic fibers have

proven to provide comparable enhancements for concrete's performance, both in terms of longevity and structural enhancements. Synthetic fibers offer several advantages over steel fibers, including better durability against corrosion (Bentur and Mindess, 1990; Zheng and Feldman, 1995), lower density and reduced cost (Lambrechts, 2009). Synthetic fibers are classified, based on diameter, as either micro- or macro-synthetic fibers. Micro-synthetic fibers are primarily used for plastic shrinkage and crack control (Soroushian et al., 1993) while macro-synthetic fibers are predominantly used to resist cracks caused by external loads (Nana et al., 2021), similarly to steel fibers.

However, since macro-synthetic fibers generally have lower tensile strength than steel fibers, a higher fiber content may be necessary to serve as a minimum transverse reinforcement requirement. To avoid high fiber contents of synthetic fibers, the combined use of conventional steel transverse reinforcement and macro-synthetic fibers is likely to be more practical than relying on macro-synthetic fibers alone. Limited research is available in the literature about the shear performance of structural elements containing transverse reinforcement and macro-synthetic fibers. A handful of experimental programs (e.g., Arslan et al., 2017; Majdzadeh et al., 2006; Navas et al., 2018) have investigated the combined use, identifying significant improvement in shear strength.

Current design code provisions for synthetic fibers are not well defined. The fib Model Code (2010) has provisions for FRC based on its tension-softening or -hardening behavior. The equations require laboratory testing of the material, that can also be estimated with equations. Other design codes such as ACI 318 (2019), Eurocode 2 (2004), AASHTO (2012) and CSA A23.3 (2019) do not consider the contribution of synthetic fibers to shear strength.

To induce the incorporation of design equation for shear strength of macro-synthetic FRC (PFRC), further investigation is necessary to better understand the shear behavior for a combined use of macro-synthetic fibers and conventional steel transverse reinforcement. Additionally, empirical equations for the shear strength of PFRC must be adapted for design code provisions to promote the combined use of macro-synthetic fibers and transverse reinforcement in structural design.

The organization of this thesis is as follows:

- **Chapter 2: Literature Review** provides a review of the available research of fiber-reinforced concrete (FRC), with a focus on macro-synthetic fibers. Several experimental programs are summarized in addition to empirical equations and design code

approaches to estimate shear strength of FRC.

- **Chapter 3: Summary of Experimental Program** describes a recent experimental program conducted by Gaston (2023), investigating the combined use of macro-synthetic fibers and transverse reinforcement to resist pure shear loading conditions.
- **Chapter 4: Finite Element Model Development** describes a calibration of a modeling approach for macro-synthetic fiber-reinforced concrete using the software VecTor2.
- **Chapter 5: Validation of the Modeling Approach** describes a validation of the modeling approach, by modeling both panel and beam specimens sourced from experimental programs in the literature. As part of the validation process, a beam database was compiled, consisting of experimentally tested macro-synthetic FRC beam specimens.
- **Chapter 6: Parametric Study** describes the development of a numerical database of macro-synthetic panel specimens with transverse reinforcement subjected to monotonic pure shear loading. The database was used to evaluate existing empirical and design code approaches for shear strength.
- **Chapter 7: Comparison to Empirical Equations** evaluates the effectiveness of the empirical and design code equations presented in Chapter 2 against the experimental program summarized in Chapter 3, the beam database in Chapter 5 and the numerical database in Chapter 6.
- **Chapter 8: Conclusions and Recommendation for Future Work** summarizes the conclusions drawn from this research, in addition to providing recommendations for future work.

Chapter 2
LITERATURE REVIEW

The aim of this chapter is to provide a summary of the existing literature pertaining to fiber-reinforced concrete (FRC). Experimental evidence concerning the use of steel and synthetic fibers is discussed with emphasis on shear behavior. Some of the empirical equations currently available to estimate shear strength will be presented and subsequently evaluated in Chapter 7. Hence, this chapter provides an overview of the FRC research that has been conducted throughout the years. Furthermore, pertinent critical knowledge gaps will be identified herein, that are addressed in this thesis, thereby providing a motivation for the current study.

2.1 Introduction

The concept of adding fibers to concrete dates back to 1874, when A. Bernard patented the idea of strengthening concrete with the addition of steel splinters (Maidl and Dietrich, 1995). Since then, significant experimental research has been carried out on the mechanical properties of steel fiber-reinforced concrete (SFRC) (e.g., Thomas and Ramaswamy, 2007; Yazıcı et al., 2007, among many others). The addition of steel fibers improves the concrete's tensile strength and contributes to reducing both crack width and crack spacing (Lantsoght, 2019). Research evidence has shown that fibers do not influence the compressive strength significantly (Yehia et al., 2016). Synthetic fibers up to fiber volume of $V_f = 0.25\%$ can result in marginal increase while greater fiber contents tend to decrease the compressive strength (Sani et al., 2022; Yao et al., 2022).

Steel fibers have also been found to improve shear performance of concrete elements due to their ability to effectively bridge cracks and resist crack propagation (Lantsoght, 2019). This bridging action provided by fibers promotes the redistribution of stresses within the concrete matrix and thus enhances the shear strength (Conforti et al., 2016). Studies have shown that the effectiveness of the fibers is predicated on the fiber orientation in addition to the fiber aspect ratio, defined as the ratio between fiber length and fiber diameter (l_f/d_f) (Boulekbache et al., 2012). Although a greater aspect ratio is generally more favorable for

mechanical properties of FRC, an excessive aspect ratio (greater than 100) can result in reduced fluidity, causing construction issues (Zhao et al., 2023).

Substantially less research is available on the mechanical properties of macro-synthetic fiber-reinforced concrete (PFRC) compared to SFRC. However, PFRC gained research interest in recent years because of its ability to inhibit the development of wide cracks in concrete (Wang et al., 2018; Zhao et al., 2023). Therefore, macro-synthetic fibers have emerged as a promising alternative to steel fibers. PFRC presents benefits over steel fibers that include their light weight, low cost, corrosion resistance and production convenience (Karim and Shafei, 2022). Additionally, studies (e.g., Parmentier et al., 2012) have shown that for a given V_f, PFRC elements can perform as well as their SFRC counterparts, exhibiting analogous ultimate shear capacity.

Despite some of the available evidence points to PFRC as a viable alternative to SFRC, the data is too sparse to support definitive conclusions in this sense. For example, Chandrathilaka et al. (2021) identified a lack of analytical models to predict the response of PFRC as one of the aspects that hampers the broad deployment of this material and delays the development of design provisions specific to PFRC.

2.2 Effects of Fiber Content

The addition of fibers to the concrete mix has proven to increase shear strength (e.g., Altoubat et al., 2009; Li et al., 1992; Narayanan and Darwish, 1987). However, there is evidence that increasing the fiber content beyond a certain threshold does not result in significant increase in shear strength. This point (referred to as "saturation point") was estimated to be about $V_f = 1.0\%$ for particular steel fibers tested by Susetyo (2009), who performed experiments on SFRC panels subjected to pure shear loading conditions, as summarized in Chapter 2.4.1. Susetyo (2009) observed that increasing the fiber volume from 1.0% to 1.5% resulted in minor gains in shear strength as demonstrated in Figure 2.1. Note that specimen C1CR was the "control specimen", reinforced by means of steel bars in both the longitudinal and transverse direction (and not containing any fibers), while the FRC specimens contained steel reinforcement in the longitudinal direction, but relied solely on steel fiber-reinforcement in the transverse direction.

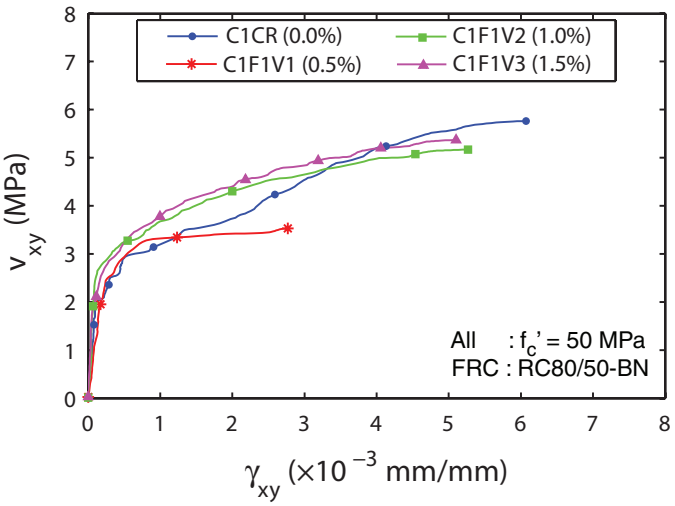

Figure 2.1: Influence of fiber content on shear resistance (Susetyo, 2009)

Fibers have been found to be more effective at low $(0.2 - 0.8\%)$ fiber volume (as e.g., Zhao et al., 2023). For instance, the study by Susetyo (2009) found that increasing the fiber content from 0.5% to 1.0% enhanced the ultimate shear strength of SFRC panels by nearly 50%, as demonstrated in Figure 2.1. It was also observed that panels containing a fiber volume of 1.0%, and no steel reinforcing bars in the transverse direction, exhibited identical ultimate strength to the biaxially reinforced control panel C1CR. Interestingly, a subsequent increase in fiber content to $V_f = 1.5\%$ resulted in a shear strength enhancement less than 4%, indicating the lower relative effectiveness at greater fiber volumes.

A fiber saturation point for any available synthetic fiber is yet to be determined. A systematic research conducted by the research team of Inner Mongolia University of Science and Technology have addressed the mechanical behavior of PFRC closely (Zhao et al., 2023). The research indicated that a dosage of $6 - 9\ kg/m^3$ $(0.7 - 1.0\%$ by volume) of macro-synthetic fibers has demonstrated the most significant improvements for compressive strength, splitting tensile strength, flexural strength and toughness. Considering the mechanical performance and the cost performance ratio, a dosage of $9\,kg/m^3$ and $6\,kg/m^3$ has been suggested for beam and column members respectively (Zhao et al., 2023).

2.3 Combined Use of Macro-Synthetic Fiber-Reinforced Concrete with Stirrups

Synthetic fibers do not possess the same tensile strength as steel fibers and therefore, a supplementary reinforcement component such as conventional steel transverse reinforcement may be necessary. Recent studies (e.g., Ababneh et al., 2017; Arslan, 2014; Majdzadeh et al., 2006) have demonstrated the efficiency of the combined use of macro-synthetic fibers and transverse reinforcement in structural applications. The experiments have shown that macro-synthetic fibers can be used to increase the ultimate shear strength of RC elements with stirrups by margins ranging from 11% to 47% (Navas et al., 2018).

An experimental program by Navas et al. (2018) (summarized in Chapter 2.5) delved into this field by investigating the combined use of macro-synthetic fibers and stirrups. The combined use led to notable enhancement in shear strength as illustrated in Figure 2.2.

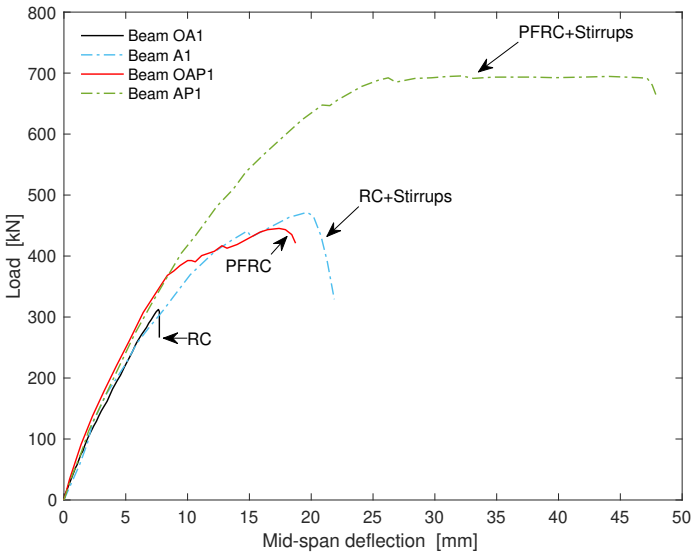

Figure 2.2: Load-deflection responses for RC and PFRC, data from Navas et al. (2018)

The study by Navas et al. (2018) suggests that macro-synthetic fibers provide benefits with respect to both deformation and ultimate strength. Synergistic effects were identified between macro-synthetic fibers and stirrups towards shear strength, where the combined enhancement resulting from their interaction surpassed the added individual enhancements achieved by using either component separately. This synergy was also acknowledged in a study by Majdzadeh et al. (2006), indicating synergistic improvement of 10% for PFRC

beams containing $V_f = 0.5\%$ macro-synthetic fibers and transverse reinforcement ratio of $\rho_y = 0.28\%$. These two studies are among the few experimental programs performed to address the combined use of macro-synthetic fibers and stirrups with respect to shear strength. Additionally, a recent study by Gaston (2023) (see Gaston et al., 2025) tested panels with macro-synthetic fibers with fiber volume $V_f \leq 0.52\%$ and transverse reinforcement $\rho_y \leq 1.14\%$. The experimental program is summarized in Chapter 3.

2.4 Fiber-Reinforced Concrete Panel Tests

Several experimental programs have been performed on FRC panels subjected to pure shear loads. Most of these experiments were conducted at the University of Toronto (e.g., Carnovale, 2013; Chasioti, 2017; Susetyo, 2009). Three of these experimental programs that are most relevant of the present work will be summarized herein. The geometry of a typical panel specimen is shown in Figure 2.3.

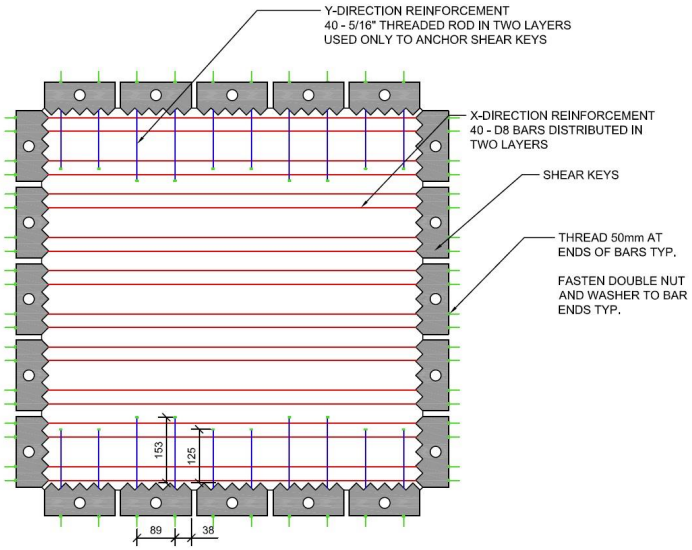

Figure 2.3: Geometry of a typical panel specimen (Carnovale, 2013)

2.4.1 Susetyo et al. (2011)

Susetyo et al. (2011) tested a series of ten, $890 \times 890 \times 70\,mm$, SFRC panel elements under pure shear monotonic loading conditions, using the Panel Element Tester at the University of Toronto (Vecchio, 1979). The horizontal reinforcement ratio was held constant for all specimens at $\rho_x = 3.31\%$ while the transverse reinforcement was $\rho_y = 0.42\%$ for

RC specimens and $\rho_y = 0\%$ for FRC specimens. Table 2.1 summarizes the fundamental properties of the tested specimens.

Table 2.1: Panels tested by Susetyo et al. (2011)

Specimen	f'_c **[MPa]**	**Fiber type**	V_f **[%]**
C1C	65.7	-	-
C1F1V1	51.4	RC80/50-BN	0.5
C1F1V2	53.4	RC80/50-BN	1.0
C1F1V3	49.7	RC80/50-BN	1.5
C1F2V3	59.7	RC80/30-BP	1.5
C1F3V3	45.5	RC80/35-BN	1.5
C2C	90.5	-	-
C2F1V3	78.8	RC80/50-BN	1.5
C2F2V3	76.5	RC80/30-BP	1.5
C2F3V3	62.0	RC80/35-BN	1.5

The objective of the study was to scrutinize the accuracy of the current constitutive models for SFRC under multi-axial stresses. Finite element models of the specimens were implemented using the software VecTor2 (Wong et al., 2013) and tested numerically under the same loading protocol utilized in the experiments. The outcome of the analyses was compared to the experimental results, to assess the accuracy of the constitutive models available in VecTor2 (at the time the study was carried out). The study also investigated the influence of fiber type on ultimate strength and the overall response, by utilizing three different steel fiber types, characterized by different geometry.

The experiments demonstrated that the addition of steel fibers influences the shear strength significantly, as illustrated in Figure 2.1. The shear strength increment was found to depend on the fiber type used. Panel specimens containing shorter fibers exhibited higher shear strength compared to the panels containing longer fibers. A reason for this could be attributed to greater nominal count of shorter fibers compared to longer fibers, for an equal fiber volume. Therefore, the shorter fibers are more uniformly distributed in the concrete, thereby offering improved resistance. Furthermore, fibers with greater aspect ratio enhanced

the behavior of the specimens more markedly compared to fibers with lower aspect ratio.

In addition to improving the shear strength, the steel fibers effectively limited and controlled transverse cracking and tensile straining, mitigating concrete "compression softening" phenomena. As part of the study, a new concrete "tension softening" model was developed, to achieve a more accurate comparison between the results of the experiments and the numerical simulations.

During the experiments, as the loading progressed, the crack spacing was observed to gradually decrease, that resulted in a final crack spacing substantially smaller than the crack spacing recorded at intermediate load stages. Evidently, specifying a constant crack spacing as an input to the numerical simulations could lead to erroneous predicted behavior. Thus, a crack spacing model suitable to represent the crack spacing progression more accurately had to be developed in future research to achieve improved predictions for SFRC panels.

Finally, Susetyo et al. (2011) identified that tension softening governed the tensile behavior. The concrete post-cracking tensile behavior is thought to be influenced by tension stiffening and tension softening. Tension stiffening refers to the concrete's capability to transmit tensile stresses across cracks through the bond between the reinforcement and concrete. In contrast, tension softening describes the post-cracking tensile strength in the concrete (Susetyo et al., 2011).

Because tension softening was not properly addressed in the numerical simulations, both experimental shear strength and deformation capacity were overestimated in the numerical analyses. Further research was necessary to investigate the local crack responses more closely in future studies.

2.4.2 Carnovale and Vecchio (2014)

This experimental program expanded upon the research by Susetyo et al. (2011) and included a total of five panel specimens, with the same specimen geometry and test setup as Susetyo et al. (2011). The study by Carnovale and Vecchio (2014) specifically focused on the shear behavior of macro-synthetic FRC (PFRC) and examined the behavior of both PFRC and SFRC under monotonic and reversed cyclic in-plane shear loading conditions. The fundamental properties and loading protocol of the panels tested by Carnovale and Vecchio (2014) are summarized in Table 2.2.

Table 2.2: Panels tested by Carnovale and Vecchio (2014)

Specimen	f'_c **[MPa]**	**Fiber type**	V_f **[%]**	**Loading type**
DC-P1	71.7	-	-	Reversed cyclic
DC-P2	62.1	RC80/30BP	1.0	Monotonic
DC-P3	50.9	MAC matrix	2.0	Monotonic
DC-P4	64.0	RC80/30BP	1.0	Reversed cyclic
DC-P5	54.3	MAC matrix	2.0	Reversed cyclic

The experimental program revealed that including $V_f = 1.0\%$ of end-hooked steel fibers could effectively replace the transverse reinforcement of $\rho_y = 0.42\%$ used in the control specimen DC-P1. However, panel C1F1V1 tested by Susetyo et al. (2011), that contained $V_f = 0.5\%$ of steel fibers, was not capable of achieving the strength of the control specimen. This aligns with the results by Parra-Montesinos (2006), where a volume fraction of $V_f \geq 0.75\%$ of steel fibers was necessary to replace the minimum transverse reinforcement requirement.

The PFRC specimen DC-P3 did not reach the ultimate shear stress of the control specimen DC-P1, experiencing a strength reduction of 33%. Nonetheless, the strain at failure was substantially higher compared to the other SFRC specimens tested, as shown in Figure 2.4. This suggests that the macro-synthetic fibers illustrated an adequate ability to bridge cracks without significant fiber pullout. The ultimate shear stress achieved by panel specimens DC-P3 ($V_f = 2.0\%$ macro-synthetic fibers) and C1F1V1 ($V_f = 0.5\%$ hooked-end steel fibers) was comparable, demonstrating the effectiveness of macro-synthetic fibers to steel fibers.

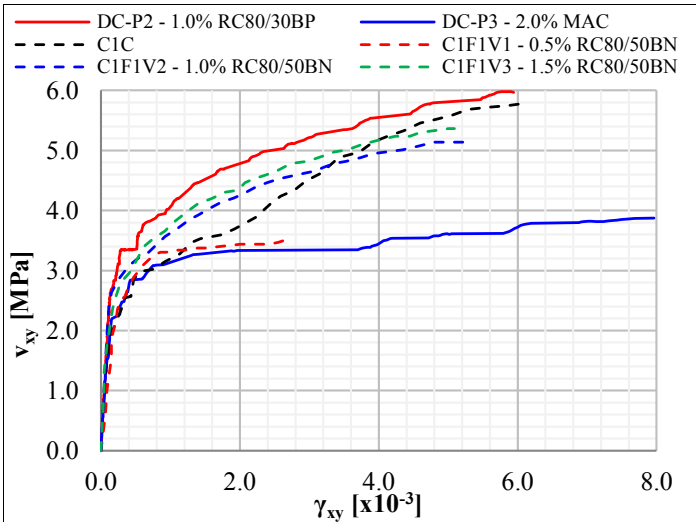

Figure 2.4: Influence of fiber type on shear stress-strain response (Carnovale, 2013)

The PFRC panel DC-P3 exhibited a lower maximum tensile stress compared to the biaxially reinforced control specimen DC-P1 and the SFRC specimen C1F1V3 ($V_f = 1.5\%$). This finding aligns with a previous research indicating that macro-synthetic fibers have a limited engagement at low crack widths due to their low stiffness and lack of anchorage (Buratti et al., 2011). Despite the variation in fiber volume, the ultimate tensile strain achieved by the SFRC panels, tested by Carnovale and Vecchio (2014), was approximately constant. However, the PFRC panel DC-P3 retained a residual stress up to twice as that achieved by the SFRC panels.

Conversely, the PFRC specimen DC-P3 exhibited greater crack widths and crack spacing compared to the SFRC specimens. This demonstrates the abilities of macro-synthetic fibers of sustaining larger cracks without inducing failure, compared to the steel fibers. Despite the mechanical enhancements provided by the macro-synthetic fibers, Carnovale and Vecchio (2014) concluded that the minimum transverse steel could not be replaced with macro-synthetic fibers solely, due to bonding and stiffness drawbacks. Therefore, to harness the benefits of macro-synthetic fibers, a combined use of macro-synthetic fibers and conventional transverse steel reinforcement may be a more viable option.

2.4.3 Chasioti and Vecchio (2017)

The objective of this study was to investigate the influence of fiber hybridization on the shear strength of panel specimens with the same geometry as the specimens tested by Susetyo et al. (2011). The performance of steel hybrid FRC (HyFRC) was examined, consisting of a combination of end-hooked steel macro-fibers and straight short steel micro-fibers. The experimental setup was identical to what Susetyo et al. (2011) employed, whereas the loading protocol consisted of either in-plane monotonic or reversed cyclic loading. The test matrix is reported in Table 2.3.

The micro-fibers proved to be more effective in bridging smaller crack widths but resulted in reduced deformation capacity (i.e. shear strain) due to their short engagement length. However, the HyFRC specimens exhibited reductions in both crack width and crack spacing, demonstrating an overall improved crack control. Overall, fiber hybridization enhanced the shear performance of the specimens, with both shear strength and deformation capacity surpassing the specimens that contain either of the fiber type with the same fiber volume. These synergistic effects of the two fiber types were found to increase with greater fiber volumes.

Table 2.3: Panels tested by Chasioti and Vecchio (2017)

Specimen	**Fiber configuration**	V_f [%]	**Loading**	**Type of loading**
H1.5PSM	Hybrid	1.5	Pure shear	Monotonic
H1.5PSC	Hybrid	1.5	Pure shear	Reversed cyclic
SL1.5PSC	Macrofiber only	1.5	Pure shear	Reversed cyclic
SS1.5PSC	Microfiber only	1.5	Pure shear	Reversed cyclic
H1.0PSM	Hybrid	1.0	Pure shear	Monotonic
H1.0PSC	Hybrid	1.0	Pure shear	Reversed cyclic
SL1.0PSC	Macrofiber only	1.0	Pure shear	Reversed cyclic
SS1.0PSC	Microfiber only	1.0	Pure shear	Reversed cyclic
H1.5PSM-predamaged	Hybrid	1.5	Pure shear	Monotonic
H1.5PSC-predamaged	Hybrid	1.5	Pure shear	Reversed cyclic
H1.0STM	Hybrid	1.0	Shear and biaxial tension	Monotonic
H1.0STC	Hybrid	1.0	Shear and biaxial tension	Reversed cyclic
H0.75PSM	Hybrid	0.75	Pure shear	Monotonic
H2.0PSM	Hybrid	2.0	Pure shear	Monotonic

2.5 Performance of Macro-Synthetic Fiber Reinforced Concrete Beams

This section aims to provide key results from available research that has been conducted on macro-synthetic fiber reinforced concrete (PFRC) beams.

In the past years, numerous experimental programs have been conducted, particularly focused on the use of polypropylene (PP) fibers (which are one type of macro-synthetic fibers) without stirrups (as e.g., Altoubat et al., 2009; Arslan et al., 2017; Conforti et al., 2015). Table 2.4 summarizes the key parameters investigated in selected experimental programs for PFRC beams subjected to bending, along with the main findings observed.

The experimental programs summarized in Table 2.4 indicate that several experimental programs have been conducted on PFRC beams with stirrups. However, experiments on PFRC without stirrups have been more prevalent, for example Almasabha et al. (2023) compiled a database of 102 PFRC specimens without stirrups. Only three studies have particularly addressed the combined use of PFRC and stirrups (Ababneh et al., 2017; Majdzadeh et al., 2006; Navas et al., 2018). Selected papers in Table 2.4 are discussed in more detail below.

Table 2.4: Several PFRC beam experimental programs

Reference	**Fibers** (l_f/d_f)	V_f [%]	ρ_x [%]	ρ_y [%]	**Key conclusions**
Majdzadeh et al. (2006)	Strux 85/50 PP blend (50/0.59)	0 0.5 1.0 1.5	2.62	0 0.28	• Fibers increased the shear strength for all beams. • A fiber saturation point appeared to be $V_f = 1.0\%$ • Fibers and stirrups demonstrated synergistic effects to shear strength
Conforti et al. (2015)	Polypropylene (40/0.75)	0 1.45	1.15 - 1.30	0 0.10	• PP fibers shifted the failure mode from shear to flexure and increased the deformation capacity • Using $V_f = 1.45\%$ of PP fibers can completely substitute minimum shear reinforcement • PP fibers reduced crack width and resulted in a crack spacing reduction of about 40%

Table 2.4 continued

Reference	**Fibers** (l_f/d_f)	V_f [%]	ρ_x [%]	ρ_y [%]	**Key conclusions**
Arslan et al. (2017)	Polymacro PM39 (39/0.77)	0 1.0 2.0 3.0	1.28	0	• PP fibers increased shear strength and deformation capacity • PP fibers were not capable of shifting the failure mode from shear to flexure for $a/d \leq 3.5$ • Maximum normalized shear stress increased with V_f
Navas et al. (2018)	Polypropylene (48/0.84)	0 1.1	1.67 - 2.25	0 0.10 0.15	• PP fibers improve shear strength and deformation capacity • Comparable behavior was observed for PFRC beams and RC beams with transverse reinforcement • Synergistic effects appeared for two of four PFRC beams with transverse steel reinforcement • Macro-synthetic fibers can serve as an effective shear transfer mechanism

Table 2.4 continued

Reference	**Fibers (l_f/d_f)**	**V_f [%]**	**ρ_x [%]**	**ρ_y [%]**	**Key conclusions**
Ababneh et al. (2017)	Polypropylene-polyethylene blend (40/0.44)	0 0.33 0.55 0.77	3.22	0 1.68 3.35	• Stirrups spacing can be increased from $d/4$ to $d/2$ by using $V_f = 0.77\%$ of fibers • Fiber effectiveness decreases with smaller stirrup spacing • Increased V_f resulted in greater shear strength and more ductile failure
Altoubat et al. (2009)	Polypropylene-polyethylene blend (40/0.44)	0 0.50 0.75 1.0	2.15 3.18	0	• Fibers increased shear strength up to 30% for $V_f = 1.0\%$ • Fibers effectively distributed stresses across diagonal cracks • Fibers changed the failure mode from web-shear cracking to flexural shear cracking for short beams

2.5.1 Altoubat et al. (2009)

This experimental program conducted tests on 27 large-scale PFRC beams without stirrups in three point bending, with cross section dimensions of $280 \times 460\,mm$ and $230 \times 390\,mm$. Both short and slender beams were tested with span-to-depth ratio (a/d) of 2.3 and 3.5, respectively.

Including macro-synthetic fibers in the concrete mix led to a significant enhancement in shear strength. For instance, utilizing a fiber volume of $V_f = 0.75\%$ resulted in strength advancements up to 23% and 28% for slender and short beams, respectively. The enhanced shear behavior was contributed by the fibers' ability to decelerate the propagation and widening of diagonal cracks. In contrast, the control specimens (that did not contain macro-synthetic fibers) failed abruptly upon the development of the first diagonal crack.

In addition to enhancing the shear strength, macro-synthetic fibers substantially improved deformation capacity in the range of $62 - 138\%$ for the fiber volumes tested ($0\% - 1.0\%$). Unlike the RC control specimen, which developed a single major diagonal crack, the PFRC beams exhibited multiple flexural and diagonal cracks, that contributed to the enhanced deformation capacity.

Figure 2.5 demonstrates the normalized shear strengths observed in the study by Altoubat et al. (2009). All beam specimens achieved shear strength surpassing the ACI 318-08 limit of $0.17\sqrt{f'_c}$ ($2\sqrt{f'_c}\,psi$), with some of the PFRC beams even exceeding the minimum requirement for SFRC according to ACI 318-08 of $0.3\sqrt{f'_c}$ ($3.5\sqrt{f'_c}\,psi$).

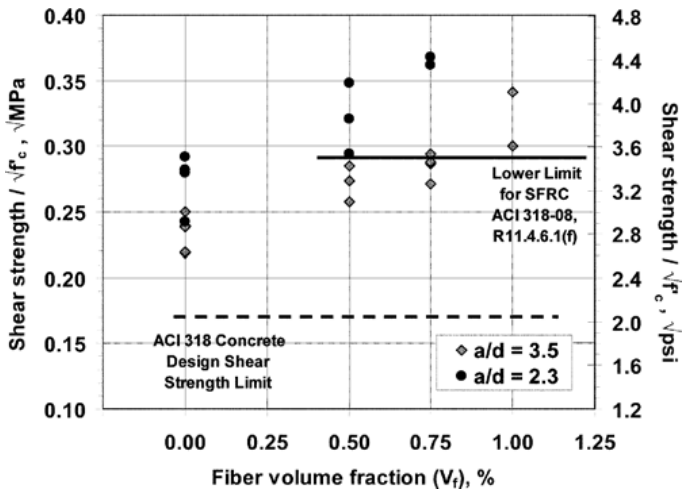

Figure 2.5: Observed normalized shear strengths by Altoubat et al. (2009)

2.5.2 Arslan et al. (2017)

This study investigated the influence of span-to-depth ratio a/d and fiber volume V_f of polypropylene fibers on the shear strength. Nine PFRC beam specimens were tested in flexure, in addition to two RC control specimens (that did not contain fibers). Figure 2.6 shows the geometry of the specimens., where the beam series were distinguished by their a/d ratio (B2.5, B3.5 and B4.5). Each series was tested with a fiber volume of 1.0%, 2.0% and 3.0%. Additionally, two control beams (for series B2.5 and B3.5) were tested.

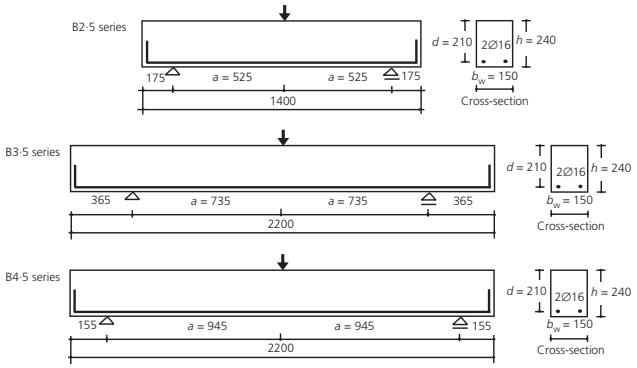

Figure 2.6: Geometry of beams tested by Arslan et al. (2017)

Despite the relatively low compressive strength of the beam specimens, ranging from 13.85 MPa to 27 MPa, the beams exhibited notable performance. The span-to-depth ratio was observed to significantly influence the failure mode. Beam series B2.5 and B3.5 experienced shear failure while beam series B4.5 exhibited flexural failure. The fibers were not capable of shifting the failure mode from shear to flexure. Figure 2.7 illustrates the observed normalized shear strengths for the beam specimens, where the shear strength increased with fiber volume.

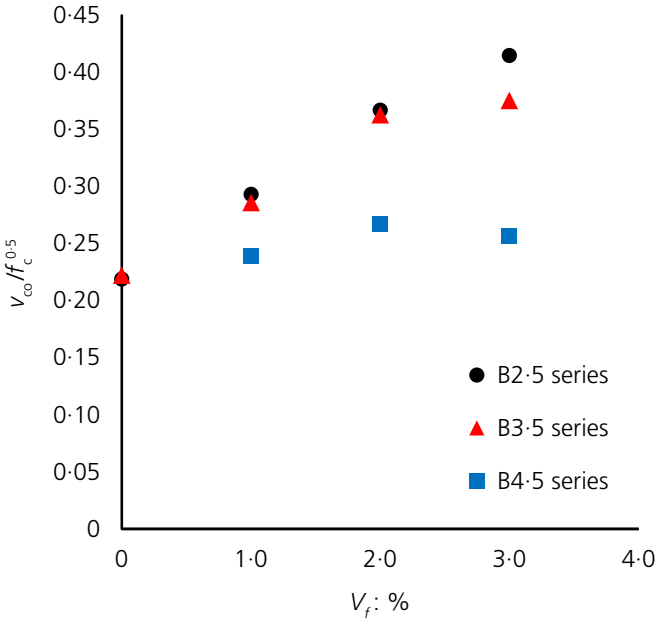

Figure 2.7: Normalized shear strength versus fiber volume (Arslan et al., 2017)

2.5.3 Ababneh et al. (2017)

This experimental program investigated the shear behavior of lightweight PFRC concrete beams with and without transverse reinforcement. Three beam groups were tested in four point bending, where the transverse reinforcement ratio varied between the groups. Table 2.5 summarizes the transverse reinforcement and fiber volume for each group tested.

Table 2.5: Beams tested by Ababneh et al. (2017)

Group no	**Transverse reinforcement**	**Fiber volume [%]**
1	-	0, 0.33, 0.55, 0.77
2	$\rho_y = 3.35\%$	0, 0.33, 0.55, 0.77
3	$\rho_y = 1.68\%$	0, 0.33, 0.55, 0.77

The beam specimens of group 1 failed due to web-shear cracking, whereas the RC beam ($V_f = 0\%$) observed sudden and more brittle failure compared to the PFRC beams. Conversely, the appearance of the diagonal crack did on the other hand not mark the failure for groups 2 and 3, due to the transverse reinforcement. The macro-synthetic fibers increased

the shear strength significantly for group 1, while the strength enhancement for groups 2 and 3 were modest.

Ababneh et al. (2017) concluded that building codes should consider the shear strength contribution of macro-synthetic fibers. The maximum allowed stirrup spacing of $d/2$ (as e.g., ACI 318, 2019) should be revised, when macro-synthetic fibers are used. Furthermore, stirrups could be fully eliminated with the use of macro-synthetic fibers. However, the effectiveness of the fibers diminishes with smaller transverse reinforcement spacing. Figure 2.8 illustrates the load versus midspan deflection for group 2, highlighting fiber effectiveness for all fiber volumes tested ($V_f \leq 0.77\%$).

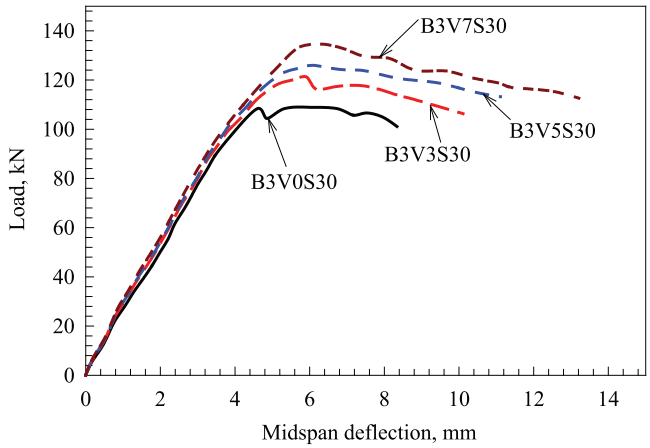

Figure 2.8: Load versus midspan deflection for group 2 ($s = 30\,mm$) (Ababneh et al., 2017)

2.5.4 Navas et al. (2018)

This experimental program explored the use of macro-synthetic fibers as shear reinforcement in slender beams. The study investigated the potential synergy for a combined use of macro-synthetic fibers and stirrups. A total of 16 beams were tested in three point bending, consisting of all following combinations:

- Cross sections A ($305 \times 552\,mm$) and B ($229 \times 552\,mm$)
- Span lengths 1 ($3360\,mm$) and 2 ($4570\,mm$)
- RC ($V_f = 0\%$) and PFRC ($V_f = 1.1\%$)
- Specimens with and without transverse reinforcement

Significant improvement in both shear strength and deformation capacity was observed for the PFRC beams compared to the RC beams. However, deformation capacity improvements were more pronounced in the greater cross section A, attributed to a higher number of fiber crossing the diagonal cracks. Additionally, for cross section A, PFRC beam specimens without stirrups achieved comparable strength and deformation capacity as RC beams with stirrups. This trend was not observed for cross section B.

Synergistic effects between macro-synthetic fibers and stirrups were identified among beams with cross section A (see Figure 2.2), while a negative synergy was observed for beams with cross section B. This discrepancy could be attributed to the narrower width of section B, limiting the number of fibers capable of transferring shear stresses.

2.6 Empirical Shear Predicting Equations

Numerous empirical equations have been proposed in the literature to predict the shear strength of FRC elements. While the majority of these equations were developed for SFRC, some models have been specifically developed for PFRC. This section provides a summary of some of the shear predicting equations developed for SFRC and PFRC. The equations will be evaluated in Chapter 7 to access their accuracy in predicting the shear strength of PFRC members.

Significant research has been carried out to develop and calibrate reliable approaches to estimate the strength of SFRC elements subjected to shear. Some of the equations available in the literature consider the fiber contribution explicitly (e.g., Khuntia et al., 1999; Mansur et al., 1986). The way this term is addressed varies significantly between the different frameworks, as it is challenging to propose a term that accounts for the strength contribution provided solely by the fibers. The interaction between concrete and fibers have been found to be coupled and thus the separation of terms is discouraged (Foster et al., 2018).

A comprehensive overview of some of the shear strength equations currently available for SFRC can be found in Lantsoght (2019). The equations account for fiber contribution in various ways, but mainly empirically. However, a handful of SFRC models based in mechanics have also been formulated (e.g., Hwang et al., 2013; Lantsoght, 2023).

2.6.1 Narayanan and Darwish (1987)

This study investigated the behavior of 49 SFRC beam specimens, including control beams, SFRC beams and beams with conventional stirrups. The strength improvements due to fibers were found to depend on the fiber volume V_f and the fiber geometry. Fibers with greater aspect ratios exhibited higher pullout strengths and were more effective than fibers with a lower aspect ratio. Narayanan and Darwish (1987) presented the fiber factor F as

$$F = \frac{l_f}{d_f} \cdot V_f \cdot b_f \tag{2.1}$$

where b_f is a bond factor taken as 0.5 for round fibers, 0.75 for crimped fibers and 1.0 for indented fibers. The fiber factor F has been utilized in numerous empirical equations as e.g., Arslan et al. (2017); Ashour et al. (1992); Khuntia et al. (1999); Kwak et al. (2002).

Equation (2.2) was developed to predict the shear strength of SFRC members without stirrups. The equation consists of three terms accounting for the fiber-concrete shear contribution, dowel action from the tensile reinforcement and the fiber pullout forces as:

$$v_u = e\left[0.24 f_{spfc} + 80\rho_x \frac{d}{a}\right] + v_b \tag{2.2}$$
$$v_b = 0.41\,\tau\,F$$

Where ρ_x is the longitudinal reinforcement ratio, τ is the interfacial bond stress, e is an arching factor taken as

$$e = 1.0 \quad \text{for } a/d > 2.8$$
$$e = 2.8\frac{d}{a} \quad \text{for } a/d \leq 2.8$$

and

$$f_{spfc} = \frac{f_{cuf}}{20 - \sqrt{F}} + 0.7 + \sqrt{F} \tag{2.3}$$

is the split cylinder strength of fiber-concrete where the cube strength of concrete can be computed as

$$f_{cuf} = \frac{f'_c}{0.85}.$$

The average fiber matrix interfacial bond stress τ was suggested to be $\tau_s = 4.15\,MPa$ for steel fibers (Swamy et al., 1974). However, experimental data for the interfacial bond strength of macro-synthetic fibers is limited in the current literature. However, Prete et al.

(2019) conducted tests on the interfacial bond strength of polypropylene crimped fibers, measuring the strength as $\tau_{pp} = 2.82\,MPa$.

Equation (2.2) has demonstrated accurate predictions for SFRC (as e.g., Zhang et al., 2016). It has also predicted the behavior of PFRC beams with high accuracy (as e.g., Ababneh et al., 2017).

2.6.2 Ashour et al. (1992)

This study proposed two empirical equations based on high-strength SFRC beam specimens. Equation (2.4) was similar to the equation proposed by Zsutty (1971), but included a term accounting for fiber contribution.

$$a/d \geq 2.5: \quad v_u = \left(2.11\sqrt[3]{f'_c} + 7F\right)\left(\rho_x \frac{d}{a}\right)^{0.333} \quad \text{(MPa)} \tag{2.4a}$$

$$a/d < 2.5: \quad v_u = [\text{ Eq. (2.4a) }]\frac{2.5}{a/d} + v_b\left(2.5 - \frac{a}{d}\right) \quad \text{(MPa)}. \tag{2.4b}$$

The other Equation (2.5) proposed was based on the ACI-318 equation, but included a term accounting for fiber contribution.

$$v_u = \left(0.7\sqrt{f'_c} + 7F\right)\frac{d}{a} + 17.2\rho_x \frac{d}{a} \quad \text{(MPa)} \tag{2.5}$$

Both equations (2.4) and (2.5) have been used to evaluate the shear strength of SFRC beams (as e.g., Yazdanbakhsh et al., 2015; Zhang et al., 2016). Equation (2.5) was found to overestimate the shear strength of short beams ($a/d = 2.3$) by Yazdanbakhsh et al. (2015) while Kwak et al. (2002) identified that Equation (2.5) provided a more accurate predictions compared to Equation (2.5) across a database of 139 SFRC beams. Out of the two equations, only Equation 2.5 is evaluated in Chapter 7.

2.6.3 Swamy et al. (1993)

The study examined the influence steel fibers in lightweight concrete beams. The tests were conducted on full-size I-beams with thin webs. A truss model was proposed to predict the shear strength of SFRC beams without stirrups. The proposed model is represented by Equation (2.6).

$$v_u = v_w + v_c = 0.9\sigma_{cu} + v_c \tag{2.6}$$

where

$$\sigma_{cu} = 0.41\tau \cdot \frac{l_f}{d_f} \cdot V_f \quad \text{for } l_f < l_c \tag{2.7a}$$

$$\sigma_{cu} = 0.41 \cdot \left(1 - \frac{\sigma_{fu}}{4\tau}\frac{d_f}{l_f}\cdot\right)\sigma_{fu} \cdot V_f \quad \text{for } l_f \geq l_c \tag{2.7b}$$

where σ_{fu} is the fiber fracture stress and v_c denotes the concrete's shear strength (e.g., according to ACI 318, 2019). The term l_c is the fiber critical length, defined as the embedded length where the fiber will pull out from the concrete matrix before rupturing (see e.g., Juhász and Kis, 2017; Lim, 2006). Then the average fiber matrix interfacial bond stress τ can be taken as $\tau_s = 4.15\,MPa$ for steel fibers (Swamy et al., 1974) or $\tau_{pp} = 2.82\,MPa$ (Prete et al., 2019). However, for the evaluation of Equation (2.6) in Chapter 7, fiber pullout will be assumed and σ_{cu} will be computed by Equation (2.7a).

2.6.4 Kwak et al. (2002)

This research proposed an equation similar to the equation developed by Zsutty (1971), but was modified to account for the fiber contribution. The equation considers the influence of tensile strength on arching action as:

$$v_u = 3.7 \cdot e \cdot f_{spfc}^{2/3}\left(\rho_x \frac{d}{a}\right)^{1/3} + 0.8 \cdot v_b \quad \text{(MPa)} \tag{2.8}$$

where e is taken as

$$e = 1.0 \quad \text{for } a/d > 3.4 \tag{2.9}$$

$$e = 3.4\frac{d}{a} \quad \text{for } a/d \leq 3.4 \tag{2.10}$$

and $v_b = 0.41\tau F$ in accordance to Swamy et al. (1993), where τ is the interfacial bond stress taken as $\tau_{pp} = 2.82\,MPa$ for macro-synthetic fibers Prete et al. (2019).

2.6.5 Arslan et al. (2017)

This work was based on an earlier study by Arslan (2014), where an empirical equation to predict the shear strength of SFRC beams without stirrups was developed. Arslan et al. (2017) adapted the equation to macro-synthetic fibers. The modification was based on fiber pull-out tests for both steel and macro-synthetic fibers, performed by Carnovale (2013). A reasonable range for a polypropylene-to-steel ratio (referred to as PSR) was found to be in

the range of $0.4 - 0.7$ (Carnovale, 2013). Arslan et al. (2017) implemented the PSR ratio to Equation (2.11) to predict the shear strength of PFRC without stirrups.

$$v_{\mathrm{n}} = \left(0.2 f_c'^{2/3} \left(\frac{c}{d}\right) + PSR \cdot \sqrt{\rho_x (1+4F) f_c'}\right) \left(\frac{3}{a/d}\right)^{1/3} \text{(MPa)} \tag{2.11}$$

$$\left(\frac{c}{d}\right)^2 + 600 \left(\frac{\rho_x}{f_c'}\right) \left(\frac{c}{d}\right) - 600 \left(\frac{\rho_x}{f_c'}\right) = 0 \tag{2.12}$$

where F is the fiber factor presented by Narayanan and Darwish (1987). Arslan et al. (2017) assumed $PSR = 0.7$ in Equation (2.11), according to the upper bound of the range suggested by Carnovale (2013). However, this assumption should be updated once further experimental data become available (Arslan et al., 2017).

Equation (2.11) was evaluated for the beam specimens tested by Arslan et al. (2017) (summarized in Chapter 2.5). The average and coefficient of variation (COV) for the experimental-to-predicted strength ratios were 1.09 and 5.0%, respectively. Thus, Equation (2.11) was slightly conservative in predicting the ultimate shear strength of the tested beams.

2.6.6 Ababneh et al. (2017)

This study conducted an experimental program for PFRC beams, summarized in Chapter 2.5. As part of the study, Equation (2.13) was proposed to predict the shear strength of PFRC beams without stirrups.

$$v_u = 1.7(1 + 0.75 V_f) \left(0.16 \lambda \sqrt{f'c} + 17.2 \rho_x \frac{V_u d}{M_u}\right) \text{ (MPa)} \tag{2.13}$$

where V_u and M_u is the design shear force and moment, respectively, and λ accounts for lightweight concrete. The coefficients 1.7 and 0.75 were calibrated on the observed strengths in the experimental program for the RC beam specimens without stirrups.

Several empirical equations for shear strength of FRC without stirrups were evaluated for the experimental results. Among them, the proposed Equation (2.13) and Equation (2.2) by Narayanan and Darwish (1987) provided the most accurate predictions, with an average predicted-to-experimental strength ratio of 0.99 (COV = 2.2%) and 1.00 (COV = 6.1%), respectively.

2.7 Design Code Equations

The modern design codes generally do not consider the contribution of macro-synthetic fibers towards shear strength. However, the fib Model Code (2010) estimates the shear strength of FRC based on residual stresses that can be estimated for PFRC. Other codes, for example ACI 318 (2019), AASHTO (2012) and CSA A23.3 (2019), do not consider any strength contribution of macro-synthetic fibers but allow the minimum shear reinforcement to be replaced for SFRC if performance criteria are met. This section provides overview of shear provisions of four design codes.

2.7.1 fib Model Code (2010)

The fib Model Code (2010) considers the shear strength contribution of fibers by modifying the longitudinal reinforcement ratio by Equation (2.14).

$$v_{Rd,F} = \frac{0.18}{\gamma_c} k \left[100\rho_x \left(1 + 7.5 \frac{f_{Ftuk}}{f_{ctk}} \right) f'_c \right]^{1/3} + 0.15\sigma_{cp} \geq v_{Rd,Fmin} \tag{2.14}$$

where

$$v_{Rd,Fmin} = (v_{min} + 0.15\sigma_{cp})$$
$$v_{min} = 0.035 \cdot k^{3/2} \cdot \sqrt{f'_c}$$
$$k = 1 + \sqrt{\frac{200}{d}} \leq 2.0$$

Then $\gamma_c = 1.0$ is a partial safety factor for concrete without fibers, f_{Ftuk} is the characteristic value of the ultimate residual tensile strength of FRC by Equation (2.15) for $w_u = 1.5\,mm$:

$$f_{Ftuk} = f_{Fts} - \frac{w_u}{CMOD_3}(f_{Fts} - 0.5f_{R3} + 0.2f_{R1}) \geq 0 \tag{2.15}$$

$$f_{Fts} = 0.45 f_{R1}. \tag{2.16}$$

where f_{R1} and f_{R3} are the residual strengths from a bending test at $CMOD_1 = 0.5\,mm$ and $CMOD_3 = 2.5\,mm$, respectively. The residual strengths for PFRC can be estimated by Equation (2.17) by Neto et al. (2013):

$$f_{R1} = 7.5 \cdot \left(V_f \cdot \frac{l_f}{d_f} \right)^{0.8} \tag{2.17a}$$

$$f_{R3} = 6.0 \cdot \left(V_f \cdot \frac{l_f}{d_f} \right)^{0.7} \tag{2.17b}$$

The characteristic tensile strength f_{ctk} is taken as f_{ctm} according to fib Model Code (2010):

$$f_{ctm} = 0.3(f'_c)^{2/3} \quad \text{for } f'_c \leq 50\,MPa \tag{2.18a}$$

$$f_{ctm} = 2.12 \cdot ln\left(1 + 0.1(f'_c + \Delta f)\right) \quad \text{for } f'_c > 50\,MPa \tag{2.18b}$$

where $\Delta f = 8\,MPa$. The term σ_{cp} represents the average axial stress on the cross section due to pretensioning.

The code classifies members with and without transverse reinforcement based on Equation (2.19), where f_{yt} is the yield stress of transverse steel reinforcement.

$$\text{Members with shear reinforcement:} \quad \rho_t \geq 0.08\frac{\sqrt{f'_c}}{f_{yt}} \tag{2.19a}$$

$$\text{Members without shear reinforcement:} \quad \rho_t < 0.08\frac{\sqrt{f'_c}}{f_{yt}}. \tag{2.19b}$$

For FRC members without stirrups the shear resistance v_{Rd} is determined by Equation (2.14). However, for FRC members with shear reinforcement the shear resistance is the sum of the concrete and transverse steel contribution:

$$v_{Rd} = v_{Rd,F} + v_{Rd,s} \leq v_{Rd,max} \tag{2.20}$$

where

$$\begin{aligned}
v_{Rd,s} &= \rho_y \cdot f_{yt}\, cot\,\theta \\
v_{Rd,max} &= k_c \cdot \frac{f'_c}{\gamma_c} \cdot sin\,\theta\; cos\,\theta \\
k_c &= k_\epsilon \cdot \left(\frac{30}{f'_c}\right)^{1/3} \leq k_\epsilon \\
k_\epsilon &= \frac{1}{1.2 + 55\epsilon_1} \leq 0.65 \\
\epsilon_1 &= \epsilon_x + (\epsilon_x + 0.002)\, cot^2\,\theta
\end{aligned}$$

where ρ_y is the transverse reinforcement ratio and $\theta_{min} \leq \theta \leq 45°$ where θ_{min} is determined by Equation (2.21) (level II approximation). Here, the angle will be taken as $\theta = \theta_{min}$

$$\theta_{min} = 20° + 10000\epsilon_x \tag{2.21}$$

where (for the beam and panels specimens analyzed in this study)

$$\epsilon_x = \frac{\frac{M_{Ed}}{z} + V_{Ed}}{E_s \cdot A_s} \leq 0.003$$

where E_s is the modulus of elasticity of the reinforcement, A_s is the cross-sectional area of the flexural reinforcement, V_{Ed} and M_{Ed} is the design shear force and moment, respectively, and z is the effective shear depth.

2.7.2 ACI 318 (2019)

The ACI code does not consider the contribution of synthetic fibers towards shear strength. The shear strength of nonprestressed members is estimated by Equation (2.22) where the concrete contribution is computed by Equation (2.23).

$$v_u = v_c + v_s \tag{2.22}$$

$$v_c = \left[0.66\lambda_s\lambda\left(\rho_w\right)^{1/3}\sqrt{f'_c} + \frac{N_u}{6A_g}\right] \tag{2.23}$$

where λ_s is a size effect factor taken as

$$\lambda_s = \begin{cases} 1.0, & \text{if } A_v \geq A_{v,min} \\ \sqrt{\frac{2}{1+0.004\cdot d}} \leq 1.0, & \text{if } A_v < A_{v,min} \end{cases} \tag{2.24}$$

and λ accounts for lightweight concrete according to ACI 318 (2019, ch. 19.2.4), where $\lambda = 1.0$ for normal-weight concrete. The minimum transverse reinforcement ratio $A_{v,min}$ is determined by Equation (2.25).

$$A_{v,min} = max\left(0.062\sqrt{f'_c}\cdot\frac{b_w\cdot s}{f_{yt}}, \quad 0.35\cdot\frac{b_w\cdot s}{f_{yt}}\right) \tag{2.25}$$

For the web-shear strength of members, v_{cw}, the shear contribution of concrete is computed by Equation (2.26)

$$v_{cw} = 0.29\cdot\lambda\sqrt{f'_c} + 0.3f_{pc} + v_p \tag{2.26}$$

where f_{pc} is compressive stress in concrete after prestress losses and v_p is vertical component of effective prestress force. Equation (2.26) is based on the assumption that web-shear cracking occurs at a principal tensile stress of $0.33\lambda\sqrt{f'_c}$.

For Equations (2.23) and (2.26), the term $\sqrt{f'_c}$ should not be taken greater than $0.7\,MPa$. Moreover, the steel contribution is computed by Equation (2.27), with an upper limit for the contribution of the transverse reinforcement as:

$$v_s = \rho_y\cdot f_{yt} \leq 0.66\sqrt{f'_c}. \tag{2.27}$$

2.7.3 AASHTO (2012)

Similarly to ACI 318 (2019), AASHTO (2012) does not consider the contribution of fibers to shear strength. AASHTO is based on the MCFT and thus employs a different methodology in estimating the shear strength compared to ACI 318 (2019). The nominal shear resistance is determined by Equation (2.28) as a sum of concrete, steel and prestress contribution

$$v_n = min \begin{cases} v_c + v_s + v_p \\ 0.25 f'_c + v_p \end{cases} \tag{2.28}$$

where

$$v_c = 0.083\beta \cdot \sqrt{f'_c} \tag{2.29}$$

$$v_s = \rho_y f_{yt} \cdot (cot\,\theta + cot\,\alpha) sin\,\alpha \tag{2.30}$$

where β accounts for the concrete's ability to transmit tensile stresses by Equation (2.31) and θ is the angle of inclination of compressive stresses by Equation (2.32). Then α is the angle of inclination of transverse reinforcement.

$$\beta = \frac{4.8}{1 + 750\epsilon_s} \qquad \text{for } A_v \geq 0.083\sqrt{f'_c} \cdot \frac{b_v \cdot s}{f_{yt}} \tag{2.31a}$$

$$\beta = \frac{4.8}{1 + 750\epsilon_s} \cdot \frac{1300}{1000 + s_{xe}} \qquad \text{for } A_v < 0.083\sqrt{f'_c} \cdot \frac{b_v \cdot s}{f_{yt}} \tag{2.31b}$$

$$\theta = 29 + 3500\epsilon_s \tag{2.32}$$

Where b_v and s is the member width and stirrup spacing, respectively, and ϵ_s is the longitudinal strain in the tension reinforcement (for the beam and panels specimens analyzed in this study)

$$\epsilon_s = \left| \frac{\frac{M_u}{d_v} + V_u}{E_s \cdot A_s} \right| \leq 0.006 \tag{2.33}$$

where V_u and M_u is the design shear force and moment, respectively, and

$$s_{xe} = s_x \cdot \frac{35}{a_g + 16} \tag{2.34}$$

is the crack spacing parameter,where $300\,mm \leq s_{xe} \leq 2000\,mm$ and s_x is taken as d_v or the maximum distance layers of longitudinal reinforcement, whichever is less.

2.7.4 CSA A23.3 (2019)

The CSA A23.3 is based on the MCFT and is very comparable to AASHTO, with some minor differences. The shear strength is computed by Equation (2.28), but the concrete contribution is computed by Equation (2.35) as:

$$v_c = \lambda \beta \sqrt{f'_c} \tag{2.35}$$

where $\sqrt{f'_c} \leq 8\,MPa$ and $\lambda = 1.0$ for normal-weight concrete. The steel contribution aligns with AASHTO and is computed according to Equation (2.30), but the coefficients β and θ are determined by *the general method* as:

$$\beta = \frac{0.4}{1 + 1500\epsilon_x} \cdot \frac{1300}{1000 + s_{ze}} \geq 0.05 \tag{2.36}$$

$$\theta = 29 + 7000\epsilon_x \tag{2.37}$$

$$\epsilon_x = \frac{\frac{M_f}{d_v} + V_f}{2E_s \cdot A_s} \leq 0.003$$

where V_f and M_f is the design shear and moment, respectively, and d_v is the effective shear depth. Then the equivalent crack spacing parameter is $s_{ze} = 300\,mm$ for sections with minimum transverse reinforcement that satisfy Equation (2.38)

$$A_v \geq 0.06\sqrt{f'_c} \cdot \frac{b_v \cdot s}{f_{yt}} \tag{2.38}$$

but

$$s_{ze} = s_z \cdot \frac{35}{a_g + 15} \tag{2.39}$$

for sections without minimum transverse reinforcement, where s_z is taken as d_v or the maximum distance layers of longitudinal reinforcement, whichever is less. Additionally, for compressive strengths $f'_c \geq 70\,MPa$, $a_g = 0$ should be used in Equation (2.39). As f'_c goes from $60\,MPa$ to $70\,MPa$, a_g shall linearly reduce to zero.

2.8 Summary

In conclusion, macro-synthetic fibers have demonstrated significant benefits for structural members. However, the scarcity of experimental data currently available has hindered the implementation of specific design equations for PFRC into modern design codes. To establish reliable guidelines for the combined use of distributed fibers and deformed steel bars to resist shear loads in structural elements, additional testing and numerical data simulations is needed.

Accounting for the fiber contribution poses a conceptual challenge, as it has been found to be coupled with the contribution of concrete and steel. The development of a design equation specific for PFRC is necessary to promote the widespread use of macro-synthetic FRC, thereby resulting in more ductile and durable concrete structures.

Chapter 3

SUMMARY OF EXPERIMENTAL PROGRAM

This chapter provides a summary of the experimental program conducted by Gaston (2023) (see Gaston et al., 2025). Twelve panels were tested under monotonic shear loading conditions using the Panel Element Tester located at the Structural Engineering Testing Laboratory at University of Washington. The main variables of interest were the transverse reinforcement ratio and the fiber content of macro-synthetic fibers. The transverse reinforcement ratio ρ_y varied from 0% to 1.14% while the fiber volume V_f ranged from 0% to 0.52%. The longitudinal reinforcement ratio ρ_x was maintained constant at 2.28% for all specimens, selected to be two times the maximum transverse reinforcement of $\rho_y = 1.14\%$, to ensure the occurrence of a shear failure mechanism while preventing biaxial yielding failure mode. The experimental program is summarized in Table 3.1, and the reinforcement layout is shown in Figure 3.1.

Table 3.1: Experimental program tested by Gaston (2023)

Panel	**Specimen name**	$\boldsymbol{V_f}$[%]	$\boldsymbol{\rho_y}$[%]
P1	PFRC-000-000	0	0
P2	PFRC-000-029	0	0.29
P3	PFRC-000-058	0	0.58
P4	PFRC-000-114	0	1.14
P5	PFRC-026-000	0.26	0
P6	PFRC-026-029	0.26	0.29
P7	PFRC-026-058	0.26	0.58
P8	PFRC-026-114	0.26	1.14
P9	PFRC-052-000	0.52	0
P10	PFRC-052-029	0.52	0.29
P11	PFRC-052-058	0.52	0.58
P12	PFRC-052-114	0.52	1.14

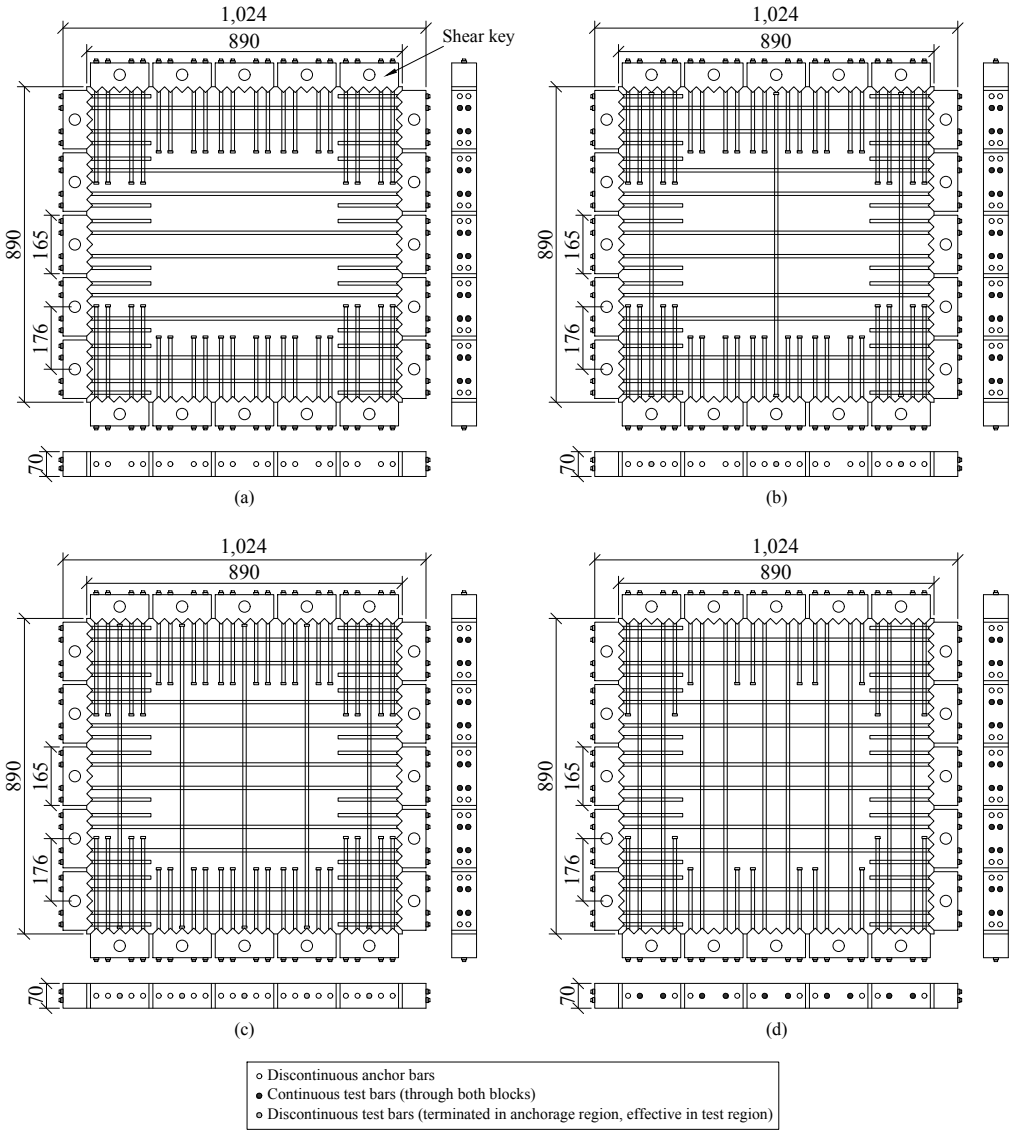

Figure 3.1: Reinforcement layout of the experimental program by Gaston (2023) (a) $\rho_y = 0\%$ (b) $\rho_y = 0.29\%$ (c) $\rho_y = 0.58\%$ (d) $\rho_y = 1.14\%$

3.1 Materials

Table 3.2 summarizes the fiber properties for the polypropylene fibers (GCP Strux 90/40) used in the experimental program. The fiber geometry is shown in Figure 3.2.

Figure 3.3 shows an axial stress-strain response for one sample steel bar used. The reinforcement bars were of type A706 with diameter $d_b = 9.5\ mm$. A total of five steel bars were tested and the average reinforcement properties were computed. Across the five tests,

the average yield and ultimate stress were estimated as $F_y = 512\,MPa$ and $F_u = 698\,MPa$, respectively. Additionally, the elastic modulus was computed as $E_s = 180,000\,MPa$. The reason for a lower elastic modulus than nominal value ($200,000\,MPa$) is attributed to the use of the nominal area in the calculations.

Table 3.2: Fiber properties

Property	**Value**
Length	$40\ mm$
Aspect ratio	90
Elastic modulus	$9,577\ MPa$
Tensile strength	$620\ MPa$
Nominal equivalent diameter	$0.43\ mm$
Nominal fiber count	$187,000$ per kg

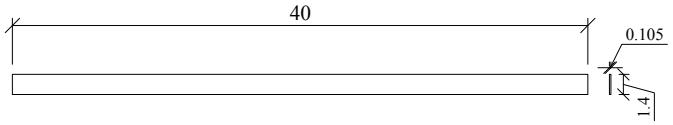

Figure 3.2: Geometry of the fibers (units in mm)

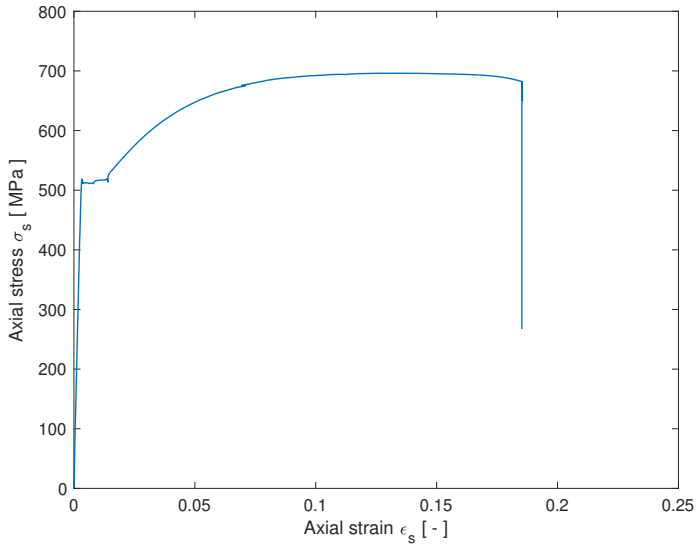

Figure 3.3: Steel bar test performed by Gaston (2023)

In addition to the specimens in Table 3.1, companion specimens were cast to determine material properties including compressive strength f'_c, elastic modulus E_c and flexural strength f_1 (modulus of rupture). Specifically, 100×200 mm cylinders, $100 \times 100 \times 380$ mm beams and $150 \times 150 \times 530$ mm beams were prepared. The beams were tested in four point bending with three equal spans of 100 mm and 150 mm for the 100×100 and 150×150 beams, respectively.

Table 3.3 summarizes the measured compressive strength f'_c and elastic modulus E_c, in addition to the flexural strength f_1 for both beam sizes. The terms f_{150} and f_{600} represent the residual flexural strengths at a midspan deflection of $L/150$ and $L/600$, respectively. The properties were tested on the same day as the corresponding panel specimen. However, flexural strength values are absent for two of the 150×150 mm beams, which were the first two panels tested. The lack of residual strength for beams without fibers is apparent in Table 3.3 (PFRC-000-xxx). Additionally, an experimental value of E_c for specimen PFRC-052-029 was not available due to instrument malfunction during testing.

Table 3.3: Concrete properties and flexural strengths of PFRC beams (all units in MPa) tested by Gaston (2023)

	Concrete properties		**$100 \times 100\,mm$ beams**			**$150 \times 150\,mm$ beams**		
Panel specimen	f'_c	E_c	f_1	f_{150}	f_{600}	f_1	f_{150}	f_{600}
PFRC-000-000	44.5	32,137	5.17			-		
PFRC-000-029	37.7	28,151	5.83			5.44		
PFRC-000-058	31.2	29,917	3.04			-		
PFRC-000-114	42.2	32,281	5.29			4.48		
PFRC-026-000	32.6	26,035	4.93	0.48	0.51	5.92	0.71	0.75
PFRC-026-029	38.3	30,351	5.05	1.05	0.93	4.36	0.99	1.09
PFRC-026-058	34.3	27,014	5.34	0.44	0.68	4.82	0.63	0.65
PFRC-026-114	43.7	31,744	4.89	0.40	0.52	3.83	0.72	0.74
PFRC-052-000	29.4	-	4.05	0.99	1.02	3.67	1.20	1.15
PFRC-052-029	45.0	29,710	5.47	1.21	1.30	4.32	1.40	1.33
PFRC-052-058	35.5	32,723	3.87	0.86	1.09	4.36	0.79	1.00
PFRC-052-114	36.1	28,544	4.56	1.26	1.17	3.44	1.28	1.32

Figure 3.4 shows the load-deflection response for two beam specimens, for reference. The residual strength for PFRC-052-000 is more than double that of PFRC-026-000, which contains half the fiber volume of PFRC-052-000. To mitigate the influence of the different compressive strengths on the response, the load-deflection response was normalized with the peak load, which was 61% higher for the PFRC-026-000 compared to PFRC-052-000.

Figure 3.5 compares the measured values of the elastic modulus reported in Table 3.3 to Equation (3.1) from ACI 318 (2019, Eq. 19.2.2.1b). The measured E_c values (see Table 3.3) followed the same trend as the ACI 318 (2019) equation.

$$E_c = 4700\sqrt{f'_c} \tag{3.1}$$

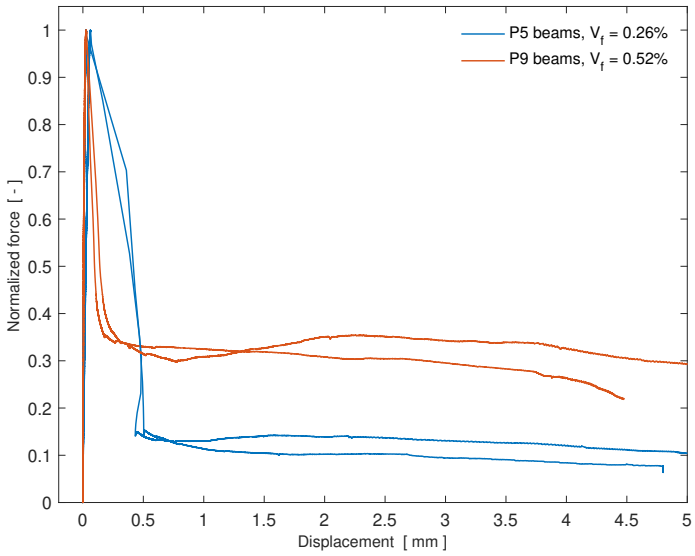

Figure 3.4: Normalized load-deflection response of beams companion to PFRC-026-000 (P5) and PFRC-052-000 (P9)

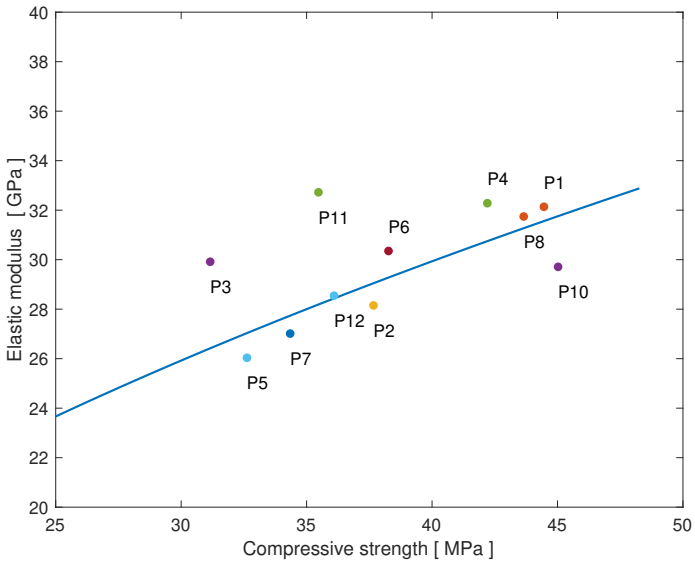

Figure 3.5: Comparison of measured E_c values to ACI 318 (2019)

3.2 Panel Specimen Results

The twelve panels in Table 3.1 were tested in a force-controlled manner. The shear stress v_{xy} was computed based on the applied forces of the Panel Element Tester, while the average strains (ϵ_x, ϵ_y, ϵ_{45} and ϵ_{135}) of the cracked composite material, measured in the

$540 \times 540\,mm$ central test region, were computed using the four corner points (see Gaston, 2023). Therefore, using the Mohr's circle, principal tensile strain ϵ_1, principal compressive strain ϵ_2, shear strain γ_{xy}, reinforcement strains ϵ_{sx} and ϵ_{sy} were computed, in addition to the principal angle of the stress and strain fields θ_σ and θ_ϵ. The analysis procedure followed equations (3.2) - (3.7) below.

The principal tensile and compressive strains were computed by Equation (3.2)

$$\varepsilon_{1,2} = \frac{\varepsilon_x + \varepsilon_y}{2} \pm \sqrt{\left(\frac{\varepsilon_x - \varepsilon_y}{2}\right)^2 + \left(\frac{\gamma_{xy}}{2}\right)^2}. \tag{3.2}$$

The average reinforcement strains were assumed to equal the concrete strains such that (direction i being either x or y)

$$\epsilon_{si} = \epsilon_i \tag{3.3}$$

and the reinforcement stresses were computed using a tri-linear relationship such that

$$f_{si} = \begin{cases} E_s \cdot \epsilon_{si}, & 0 \le \epsilon_{si} \le \epsilon_y \\ F_y, & \epsilon_y \le \epsilon_{si} \le \epsilon_{sh} \\ F_y + \dfrac{F_u - F_y}{\epsilon_u - \epsilon_{sh}} \cdot (\epsilon_{si} - \epsilon_{sh}), & \epsilon_{sh} \le \epsilon_{si} \le \epsilon_u \end{cases} \tag{3.4}$$

where $\epsilon_y = F_y/E_s$ is the yield strain, ϵ_{sh} is where strain hardening occurs and ϵ_u is the ultimate strain of the reinforcement bars. For the specimens without transverse reinforcement, the reinforcement stress in the y direction was taken as $f_{sy} = 0$.

As there was no applied normal stress on the panel, the concrete stresses were computed by Equation (3.5)

$$f_{ci} = -\rho_i \cdot f_{si} \tag{3.5}$$

Thus, the orientation of the principal strain and stress fields was computed by equations (3.6) and (3.7) respectively.

$$\theta_\epsilon = \frac{1}{2}\tan^{-1}\left(\frac{\gamma_{xy}}{\epsilon_x - \epsilon_y}\right) \tag{3.6}$$

$$\theta_\sigma = \frac{1}{2}\tan^{-1}\left(\frac{2v_{xy}}{f_{cx} - f_{xy}}\right) \tag{3.7}$$

Table 3.4 provides a summary for the key components at the cracking and ultimate load stage for each panel specimen.

Table 3.4: Panel cracking and ultimate load stage properties

Panel specimen	v_{cr} [MPa]	γ_{cr} [10^{-3}]	f_{c1}^{max} [MPa]	v_u [MPa]	γ_{xy} [10^{-3}]	ϵ_x [10^{-3}]	ϵ_y [10^{-3}]	f_{c1} [MPa]	f_{c2} [MPa]	ϵ_1 [10^{-3}]	ϵ_2 [10^{-3}]	f_{sx} [MPa]	f_{sy} [MPa]	w_m [mm]	s_m [mm]
PFRC-000-000	1.99	0.12	2.18	2.12	0.71	0.11	0.42	1.92	-2.35	0.65	-0.13	19.0	0	-	-
PFRC-000-029	1.39	0.09	1.45	4.27	13.31	2.04	13.74	0.34	-10.47	16.75	-0.97	367.4	512.8	0.522	109
PFRC-000-058	1.59	0.09	1.60	5.41	12.21	2.76	9.72	0.00	-13.95	13.27	-0.79	495.9	512.0	0.500	69
PFRC-000-114	1.92	0.22	1.93	7.82	13.73	4.21	8.35	0.00	-17.10	13.45	-0.89	512.0	512.0	0.326	64
PFRC-026-000	1.20	0.13	1.17	1.43	1.37	0.96	0.37	0.46	-4.40	1.41	-0.08	172.6	0	-	-
PFRC-026-029	1.78	0.08	1.71	4.31	13.80	1.60	11.05	0.77	-9.10	14.68	-2.03	288.6	512.0	0.314	69
PFRC-026-058	1.61	0.38	1.29	4.24	5.49	1.44	4.45	0.08	-8.93	6.08	-0.18	260.1	512.0	0.250	69
PFRC-026-114	1.81	0.37	1.76	7.43	11.95	2.26	7.92	0.08	-15.18	11.71	-1.52	406.6	512.0	0.410	69
PFRC-052-000	1.38	0.24	1.53	1.50	0.36	0.07	0.18	1.36	-1.66	0.31	-0.06	12.9	0	-	-
PFRC-052-029	1.79	0.31	2.02	5.00	20.75	2.38	19.75	0.63	-12.18	24.60	-2.46	429.0	519.5	0.470	64
PFRC-052-058	1.81	0.37	1.54	4.94	8.09	2.02	7.04	0.03	-11.22	9.29	-0.23	363.0	512.0	0.297	69
PFRC-052-114	1.84	0.47	2.50	7.47	13.03	2.54	8.52	0.00	-15.95	12.70	-1.63	457.8	512.0	0.426	64

Figure 3.6 shows the normalized shear stress-strain response for all twelve specimens. When comparing the ultimate shear stress of the specimens, the different compressive strengths (see Table 3.3) has to be taken into account, as it directly impacts the shear strength. Thus, to ensure an equitable comparison, the shear stresses in Figure 3.6 were normalized by $\sqrt{f'c}$. It should be noted that the panels PFRC-026-058 and PFRC-052-058 had consolidation issues during construction and thus had lower strengths than anticipated. These panels contained the intermediate transverse reinforcement that affected the trend identification for the fiber ratios (Gaston, 2023).

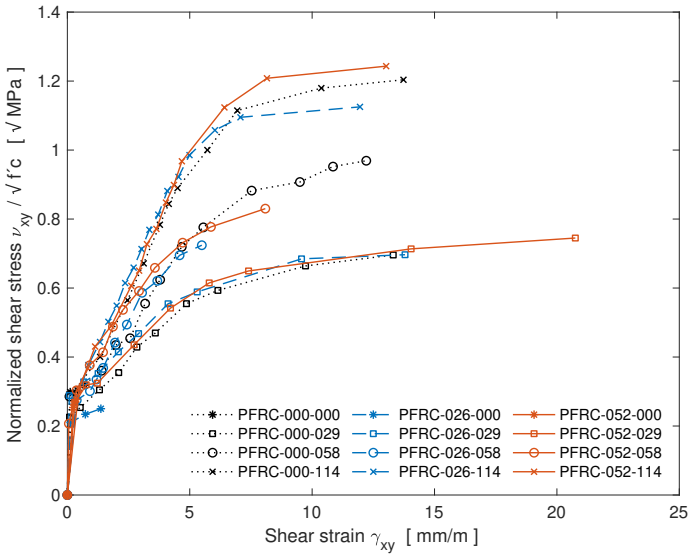

Figure 3.6: Normalized shear stress-strain response for the tested panels

Figure 3.7 shows the normalized shear strength versus fiber volume for the tested specimens. The normalized shear strength was not observed to be significantly reduced or enhanced with fiber volume and remained approximately constant with increasing fiber volume. As mentioned, the panels with fibers and a transverse reinforcement ratio of $\rho_y = 0.58\%$ had consolidation issues during construction and therefore exhibited lower shear strength compared to the panels with $\rho_y = 0.58\%$ and $V_f = 0\%$.

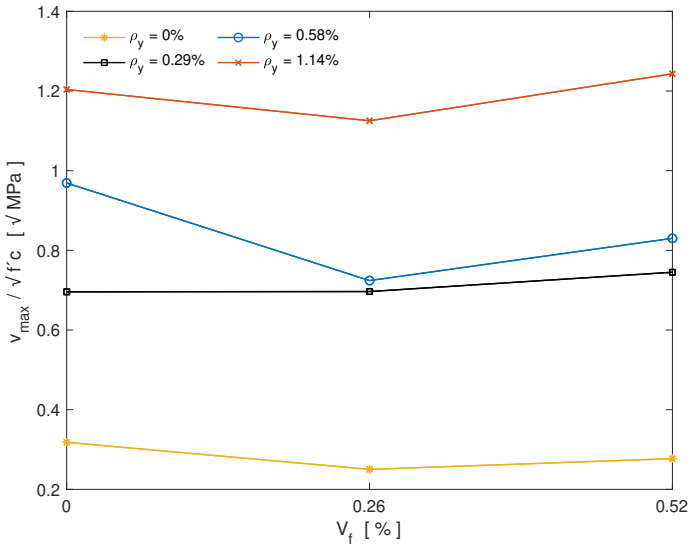

Figure 3.7: Normalized maximum shear stress versus fiber volume

Figure 3.8 shows the shear strain at failure, γ_u, versus fiber volume. For specimens with transverse reinforcement ratio of $\rho_y = 0.29\%$, γ_u increased directly with fiber content. As said, both FRC panels with $\rho_y = 0.58\%$ had consolidation issues and therefore did not reach the ultimate load stage, resulting in a reduction in the shear strain at failure for the FRC panels with $\rho_y = 0.58\%$. However, for panels with the highest transverse reinforcement of $\rho_y = 1.14\%$, the ultimate shear strain remained relatively consistent, demonstrating that the fiber content had a minimal influence on the deformation capacity. Consequently, the fibers were most effective in enhancing the deformation capacity of the panels with a low transverse reinforcement ratio ($\rho_y = 0.29\%$).

Panels without transverse reinforcement exhibited the highest shear strain at failure γ_u at $V_f = 0.26\%$, while γ_u was the lowest at $V_f = 0.52\%$. A similar trend occurred in a research on end-hooked steel fibers, where the lowest value of γ_u was recorded for the highest fiber content tested, $V_f = 1.5\%$ (Luo and Vecchio, 2016). A reason for this could be that higher fiber volume can result in consolidation issues leading to lower deformation capacity.

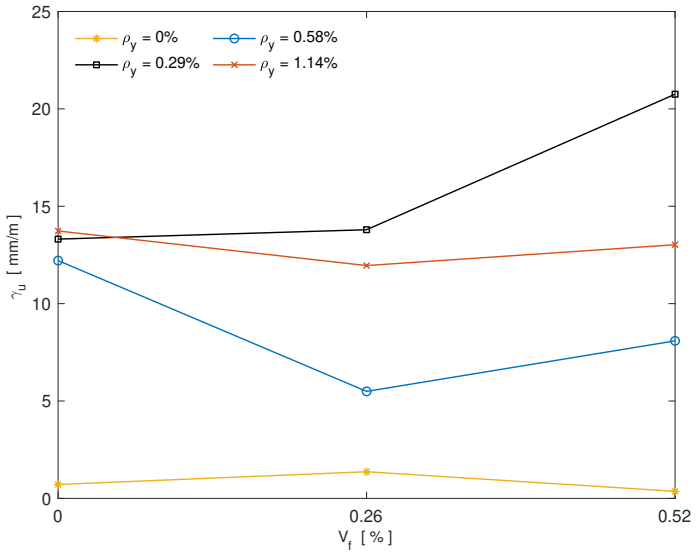

Figure 3.8: Shear strain at failure γ_u versus fiber content

Figure 3.9 illustrates the relation between the crack width and V_f at a fixed shear stress of $0.33\sqrt{f'c}$. The panels without transverse reinforcement did not reach this shear stress level and are therefore not shown. The fibers significantly influenced the crack width of the specimens, whereas both the maximum and the average crack width reduced with fiber content. A higher fiber volume caused a reduction in maximum crack width, and these effects were more pronounced at lower ρ_y values, especially for $\rho_y = 0.29\%$. Therefore, the fibers were effective in enhancing both the deformation capacity and reducing crack widths for a transverse reinforcement ratio of $\rho_y = 0.29\%$.

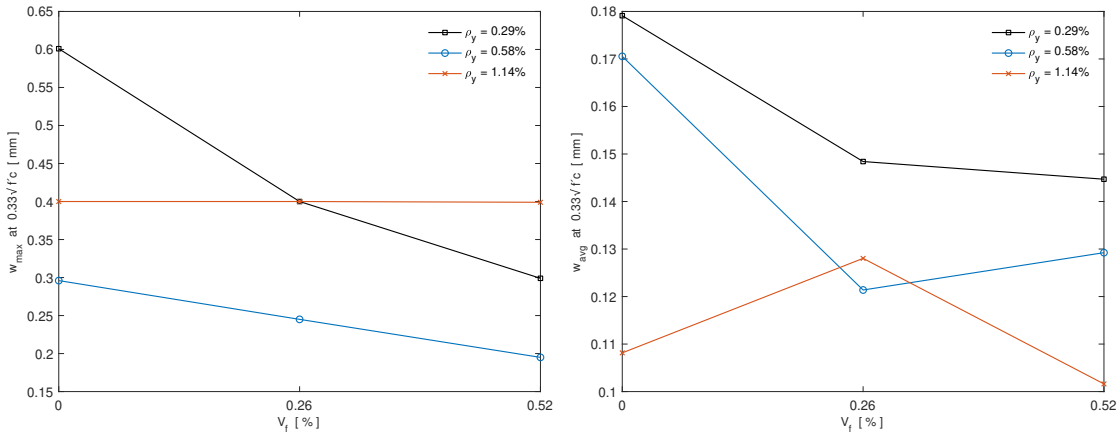

(a) (b)

Figure 3.9: Crack widths at $v_{xy} = 0.33\sqrt{f'c}$ versus fiber content (a) Maximum crack width (b) Average crack width

3.3 Conclusions

From this experimental study, the addition of macro-synthetic fibers did not result in any decrease in shear strength and did not result in the same increase in shear strength observed by other experimental programs on synthetic fibers. For example, Li et al. (1992) measured addition of $V_f = 1.0\%$ micro-synthetic fibers in a normalized shear strength increase up to 65% with a mean of 38% and COV of 18.7%. This increase was more pronounced for greater span-to-depth (a/d) ratios (Li et al., 1992).

Table 3.5 compares study by Li et al. (1992) and the experimental program by Gaston (2023). The different results are attributed to several factors including the span-to-depth a/d ratio, fiber volume V_f and the loading protocol.

Table 3.5: Experimental programs by Gaston (2023) and Li et al. (1992)

Parameter	**Gaston (2023)**	**Li et al. (1992)**
a/d ratio	1.0	$1.0 - 3.0$
V_f	$0 - 0.52\%$	1.0%
Loading	Pure shear	Bending (shear and flexure)
Testing	Force-controlled	Displacement-controlled

The observed benefits of fiber addition appeared to depend on ρ_y (Gaston, 2023). Greater advantages were observed for lower ρ_y ratios ($\rho_y = 0.29\%$) compared to the heavily reinforced panels ($\rho_y = 1.14\%$). This is consistent with the results by Navas et al. (2018), where macro-synthetic appeared to be more effective for $\rho_y = 0.10\%$ compared to $\rho_y = 0.15\%$.

The experimental panels represented typical fiber addition rates used in practice and a concrete mixture that was not optimized for large fiber volumes. The values of the experimental parameters were therefore necessarily limited.

To explore a larger parameter space, numerical models were calibrated to the experimental results to explore fiber volumes and transverse reinforcement ratios that could not be tested experimentally. This demonstrates the necessary addition rates of macro-synthetic fibers to achieve shear strength improvements for panel specimens. Using this expanded dataset is crucial to propose a design equation for macro-synthetic fiber-reinforced concrete.

Chapter 4
FINITE ELEMENT MODEL DEVELOPMENT

This chapter presents a modeling approach for macro-synthetic FRC (PFRC) elements subjected to pure shear loading conditions. The calibration of the numerical models presented was based on the results of the panel experimental program summarized in Chapter 3 (Gaston, 2023). The modeling of the panel specimens was performed using the software VecTor2 (Wong et al., 2013), which is a finite element software specifically designed to perform the two dimensional nonlinear analysis of reinforced concrete elements.

4.1 Overview of MCFT and VecTor2

This section provides a brief overview of the development of the Modified Compression Field Theory (MCFT) (Vecchio and Collins, 1986), which forms the basis of the finite element program VecTor2. Related theories are also discussed and compared to the MCFT. Additionally, specific constitutive models implemented in VecTor2 are introduced.

4.1.1 Development of the MCFT

When the MCFT was introduced, it filled a significant gap in the literature. There was no accepted theory to predict the full load-deformation response of concrete panels subjected to in-plane biaxial loads, as demonstrated by the poor results of an international blind competition with 43 engineers from different countries (Collins et al., 1985). Many of the models submitted assumed that cracked concrete could resist a compressive capacity equal to, or close to, f'_c. This assumption was unconservative and the most accurate models were the ones that accounted for a reduction in the compressive capacity as the tensile strain transverse to the compression increased.

The MCFT is a refined version of the compression-field theory (CFT) that was introduced in 1974 (see Collins, 1978; Mitchell and Collins, 1974) for RC elements subjected to torsion and shear loading. The CFT posits that cracked concrete does not resist any tension forces and the shear force is primarily countered by diagonal compression fields (Sadeghian

and Vecchio, 2018). These assumptions made the CFT conservative in estimating the ultimate shear strength of RC elements.

The MCFT enhanced the CFT by incorporating compressive strength reduction based on experimental findings by Vecchio (1982). The study conducted tests on 30 panels subjected to biaxial stresses, demonstrating that concrete resists some tension forces between cracks. This additional resistance, combined with the shear stresses on the crack faces, augmented the shear strength of the panel elements, reducing the conservatism of the CFT.

Similarly to the CFT, the MCFT treats cracked concrete as a new material, with its own constitutive relationships. However, the MCFT is based on a smeared rotating crack model that considers stresses and strains in average sense. The crack direction is gradually reoriented with respect to the material response and loading conditions (Sadeghian and Vecchio, 2018). One of the main assumptions of the theory is that the orientation of the principal strain and principal stress fields align. The equations of the MCFT consist of equilibrium-, compatibility- and constitutive relationships. These three sets of relationships are explained in detail by Vecchio and Collins (1986) and are summarized in Figure 4.1.

The compatibility relationships assume prefect bond between steel reinforcement and concrete. Therefore, the average strains in the reinforcement, ϵ_s, and concrete, ϵ_c, are equal for the x and y direction such that

$$\epsilon_x = \epsilon_{cx} = \epsilon_{sx}$$

$$\epsilon_y = \epsilon_{cy} = \epsilon_{sy}.$$

where ϵ_x and ϵ_y are the element total strains. The principal strains can be computed from the Mohr's circle:

$$\begin{aligned} \epsilon_{\mathrm{c1}}, \epsilon_{\mathrm{c2}} &= \frac{(\epsilon_{\mathrm{cx}} + \epsilon_{\mathrm{cy}})}{2} \pm \frac{1}{2}\sqrt{(\epsilon_{\mathrm{cx}} - \epsilon_{\mathrm{cy}})^2 + \gamma_{\mathrm{cxy}}^2} \\ \theta_{\mathrm{c}} &= \frac{1}{2}\tan^{-1}\left(\frac{\gamma_{\mathrm{cxy}}}{\epsilon_{\mathrm{cy}} - \epsilon_{\mathrm{cx}}}\right) \end{aligned} \tag{4.1}$$

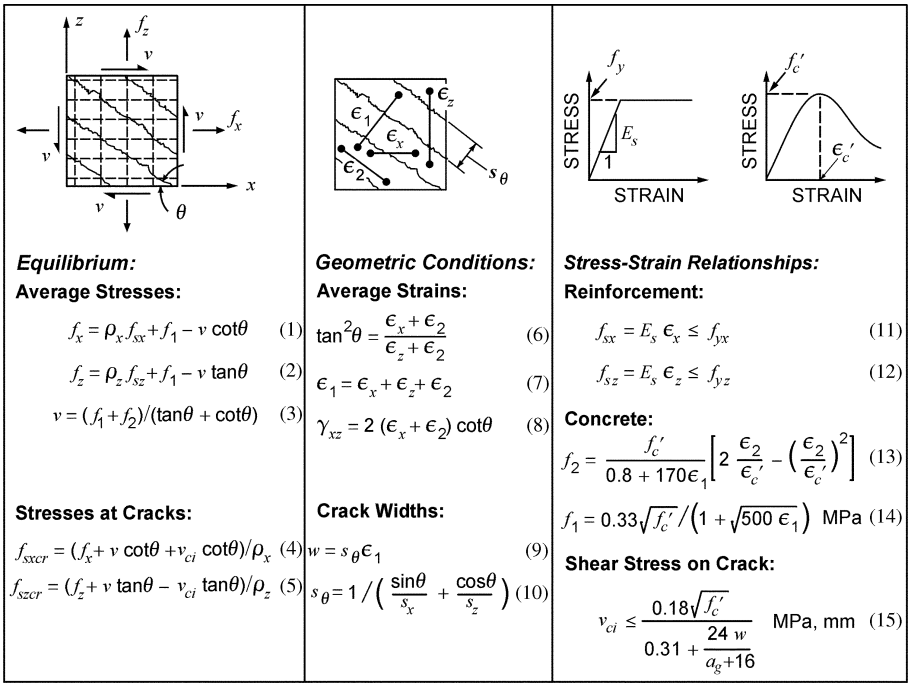

Figure 4.1: Equations of the modified compression field theory (Bentz et al., 2006)

Over the years, the MCFT has gained widespread acceptance for analysis of reinforced concrete structures. A simplified version of the MCFT, the simplified MCFT (SMCFT) was introduced in 2006 to predict the shear strength of RC elements with almost the same accuracy as the MCFT (Bentz et al., 2006). The SMCFT estimates the shear strength as the sum of contributions from concrete, v_c, and transverse reinforcement, v_s, by Equation (4.2)

$$v = v_c + v_s = \beta\sqrt{f_c'} + \rho_y f_{yt} \cdot cot\,\theta \tag{4.2}$$

The SMCFT forms the basis for both the Canadian concrete design code (CSA A23.3, 2019) and the AASHTO LRFD Bidge Design Specifications (AASHTO, 2012). Both codes estimate the shear strength as a function of two parameters β and θ, which depended on the longitudinal strain ϵ_x, measured at the mid-depth of the cross section.

Prior to the development of the SMCFT, AASHTO provided tabulated values for β and θ for members with and without transverse reinforcement based on the MCFT (Bentz et al., 2006). The idea of the SMCFT was to offer a simpler methodology that engineers would easily understand instead of using tabulated values. Following the introduction of the SMCFT, AASHTO adopted direct equations for β and θ based on the SMCFT, replacing

the tabulated values.

4.1.2 MCFT for Fiber-Reinforced Concrete

The MCFT was originally developed for RC concrete elements. However, it has been adapted to FRC in recent years by introducing constitutive models that specifically account for the influence of fibers on the tensile stress.

One of these models is the Variable Engagement Model (VEM), developed to describe the behavior of FRC subjected to uniaxial tension (Voo and Foster, 2003). The model relates the tensile stress to crack opening displacement by Equation (4.3).

$$f_{c1} = K_f K_d \cdot \frac{l_f}{d_f} \cdot V_f \cdot \tau_b \tag{4.3}$$

where

$$K_f = \frac{\tan^{-1}(w_{COD}/\alpha)}{\pi}\left(1 - \frac{2 \cdot w_{COD}}{l_f}\right)^2$$

$\alpha = d_f/3.5$ (fiber engagement parameter),

$K_d =$ fiber efficiency factor, decreases with increasing V_f but generally taken as 1.0,

$V_f =$ fiber volume,

$l_f =$ fiber length,

$d_f =$ fiber diameter,

$\tau_b =$ mean shear stress between the fibers and the concrete matrix,

$\mathrm{w}_{COD} =$ crack opening displacement

A study conducted by Susetyo et al. (2011) demonstrated that the VEM was sensitive to parameters such as the fiber engagement parameter α, average crack spacing s_m and the tensile strength f_{cr}. These parameters significantly influenced the results of the numerical simulations and required calibration to achieve accurate predictions of the available experimental results. Additionally, the VEM resulted in underestimation of the experimentally observed principal tensile stress, highlighting the need for a more appropriate tension softening model (Susetyo et al., 2011).

The growing research on FRC led to the development of the Diverse Embedment Model (DEM) (Lee et al., 2011) and the Simplified Diverse Embedment Model (SDEM) (Lee et al.,

2013). The SDEM eliminates the double integration present in the DEM, significantly improving computational efficiency. A verification study on the accuracy of the SDEM indicated that both the tensile and flexural behavior of SFRC members can be predicted accurately using the SDEM (Lee et al., 2013). The model is currently the default model for *FRC tension* in VecTor2, accounting for the contribution of distributed fibers to the concrete's tensile strength. The previous models (i.e., such as VEM and DEM) have also been implemented into the software (Wong et al., 2013).

4.1.3 Comparison of MCFT and DSFM

Several studies have demonstrated that the MCFT is capable of achieving high accuracy when used to predict the response of a wide range of structural members subjected to a variety of loading conditions (Vecchio, 2000). However, looking at the results of more than 150 experiments, Vecchio (2000) pointed out that the MCFT can exhibit limitations or weaknesses in specific situations. For example:

- Shear strength and stiffness are generally underestimated for:
  - Panels with high reinforcement ratios in both directions
  - Panels subjected to high biaxial compression in addition to shear loading
  - Panels with reinforcement and loading conditions such that there is no rotation of the principal stress strain conditions (e.g. $\rho_x = \rho_y$ and proportional loading)
- Shear strength and stiffness are commonly overestimated for uniaxially reinforced panels or panels with a low transverse reinforcement ratio

To address these issues, Vecchio extended the MCFT and formulated the Disturbed Stress Field Model (DSFM) (Vecchio, 2000). While the MCFT is a fully rotating smeared crack model that treats the concrete as an orthotropic material, aligning the angle of inclination of principal stress and strain (Vecchio, 2001), the DSFM accounts for crack slip. This affects the compatibility relations within the model. The slip model in Equation (4.4) by Walraven (1981) was adopted into the DSFM (Vecchio, 2000).

$$\delta_s{}^a = \frac{v_{ci}}{1.8w_m^{-0.8} + \left(0.234w_m^{-0.707} - 0.20\right) \cdot f_{cc}} \tag{4.4}$$

where w_m is the average crack width, f_{cc} is the concrete cube strength and v_{ci} is the local shear stress at crack. The shear slip strain is then computed as

$$\gamma_s{}^a = \frac{\delta_s{}^a}{s_m} \tag{4.5}$$

where s_m is the average crack spacing. However, a complementary approach to the model by Walraven (1981) is to relate the principal stress direction to the principal strains. The principal stress direction tends to lag behind the principal strain direction. Based on the initial crack direction θ_{ic} the rotation in the principal strain field $\Delta\theta_\epsilon$ is determined as

$$\Delta\theta_\epsilon = \theta_\epsilon - \theta_{ic} \tag{4.6}$$

at each load stage. The change in the principal stress field direction is thus

$$\begin{aligned} \Delta\theta_\sigma &= \Delta\theta_\epsilon \quad \text{for} \quad |\Delta\theta_\epsilon| > \theta^\ell \\ \Delta\theta_\sigma &= \Delta\theta_\epsilon - \theta^\ell \quad \text{for} \quad |\Delta\theta_\epsilon| \leq \theta^\ell \end{aligned} \tag{4.7}$$

and the direction of the principal stress field is thus

$$\theta_\sigma = \theta_{ic} + \Delta\theta_\sigma \tag{4.8}$$

where the lag θ^ℓ is taken as 5° for biaxially reinforced elements, 7.5° for uniaxially reinforced elements and 10° for unreinforced elements (Vecchio, 2000).

A validation study was conducted in which a total of 54 shear-critical beam specimens, with or without minimum shear reinforcement, were analyzed usign both the DSFM and the MCFT. The MCFT resulted in a mean predicted-to-observed strength ratio of 1.07 (COV = 16.9%) while the DSFM resulted in a mean predicted-to-experimental strength ratio of 1.00 (COV = 20.3%) (Vecchio et al., 2001). Thus, although the DSFM may provide a more realistic representation of the behavior of RC elements subjected to multiaxial loads than the MCFT, both theories provide comparable strength estimates across most conditions. This suggests that the assumption of coaxiality of principal stress and strain field embedded in the MCFT, has a minor effect on the predicted strength in most cases.

4.1.4 The VecTor2 Software

Both MCFT and DSFM provide a theoretical foundation for the software VecTor2 (Wong et al., 2013). VecTor2 is a two-dimensional nonlinear finite element program that adopts

a smeared rotating crack model, specifically designed for analysis of reinforced concrete elements. The finite element implementation is described in detail in the VecTor2 User Manual Wong et al. (2013). Figure 4.2 provides an overview of the constitutive models for the MCFT and the DSFM, in addition to the CFT.

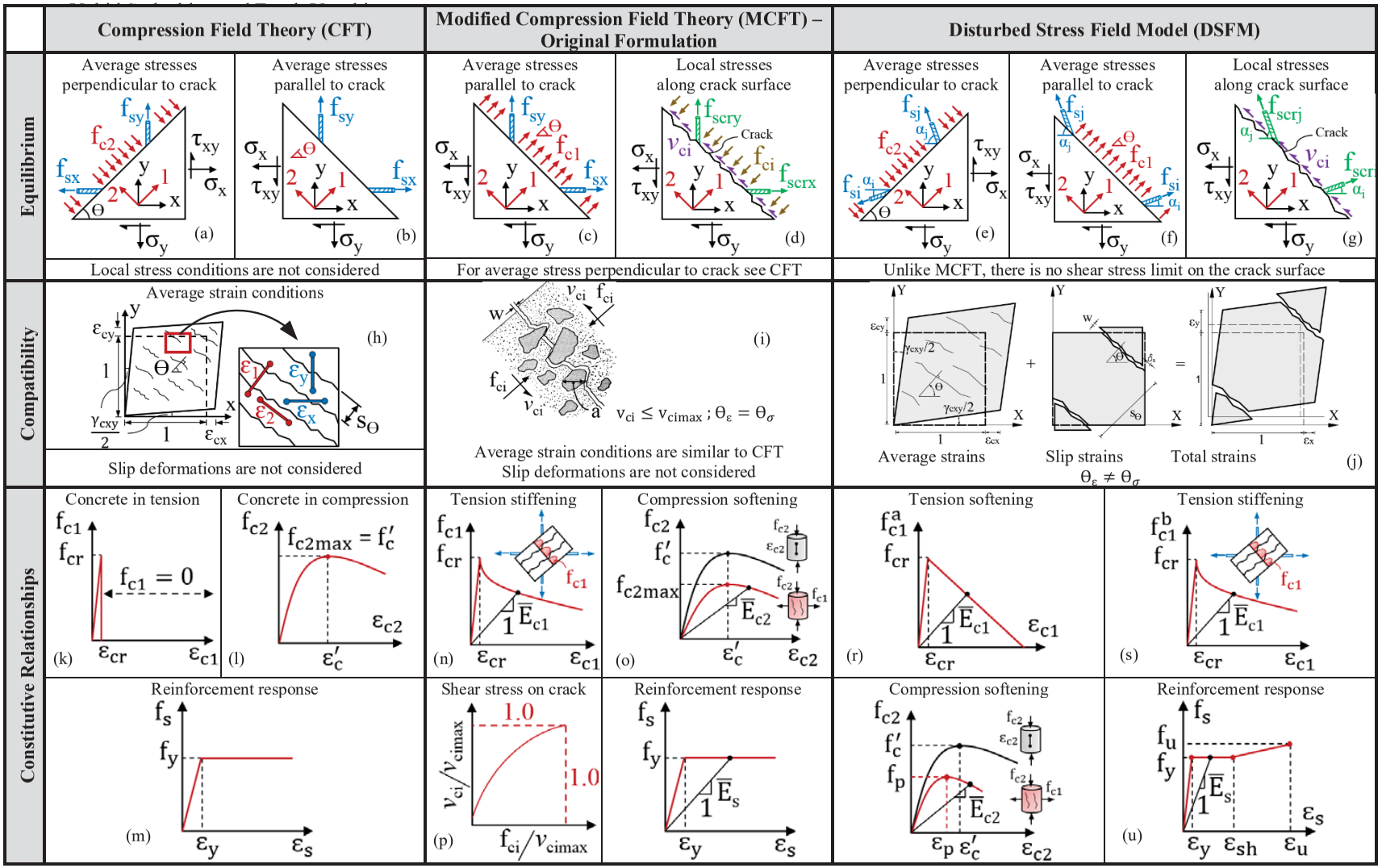

Figure 4.2: Constitutive models for the CFT, the MCFT and the DSFM (Sadeghian and Vecchio, 2018)

4.2 Panel Model Development

The numerical models of the specimens tested by Gaston (2023) were implemented in the software VecTor2. The modeling was conducted using FormWorks, a graphics-based pre-processor for VecTor2 (Wong et al., 2013). The specimens were modeled as a single quadrilateral concrete element with smeared steel reinforcement. This is in agreement with modeling approaches developed by others (Carnovale, 2013; Chasioti, 2017; Susetyo, 2009). The single element model is shown in Figure 4.3. The desired shear loading conditions were generated with nodal forces arranged as shown in Figure 4.3. The specimens were subjected to monotonically increased loading, starting from 0 kN and incremented by 0.5 kN at every load stage.

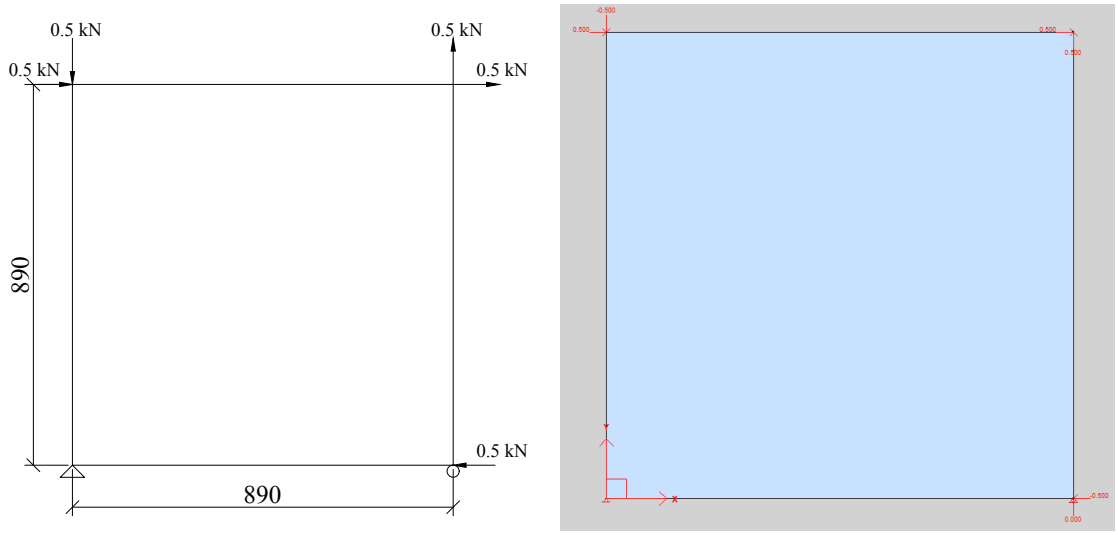

(a) (b)

Figure 4.3: VecTor2 model (a) Panel sketch (b) FormWorks model

The reinforcement properties were obtained from the five experimentally tested steel bars conducted by Gaston (2023); the stress-strain curve obtained from one of these tests are shown in Figure 3.3. Hence, the reinforcement properties used in the VT2 models were those summarized in Table 4.1. The horizontal reinforcement ratio was set at $\rho_x = 2.28\%$ for all specimens and ρ_y was specified according to Table 3.1.

Table 4.1: Reinforcement properties used in VecTor2

Parameter	**Value**
Reinforcement diameter d_b	9.5 mm
Yield strength F_y	512 MPa
Ultimate strength F_u	698 MPa
Elastic modulus E_s	180 GPa
Strain hardening Strain ϵ_{sh}	$13 \cdot 10^{-3}$
Ultimate strain ϵ_u	$180 \cdot 10^{-3}$

All models were assigned a thickness of $t = 70\ mm$, and the concrete was assigned the compressive strength and elastic modulus values summarized in Table 3.3. However, in the absence of an experimental E_c value for specimen PFRC-052-000, the default VT2 value for E_c was used, computed as:

$$E_c = 3320\sqrt{f'c} + 6900 = 24,902\,MPa.$$

A $70\,mm$ maximum crack spacing was specified for both x- and y-direction, for all panel specimens. This modeling decision was supported by the experimental results, indicating that the maximum crack spacing is a parameter that remained essentially constant and was not remarkably affected by the fiber content (see Table 3.4).

4.3 Calibration of Panel Models

This section provides an overview of the calibration of the panel models presented in Chapter 4.2. The calibration procedure was conducted as follows:

(1) First, all panel specimens were modeled as RC elements. To evaluate the fiber models embedded in VecTor2, the PFRC panels (P5-P12) were also modeled as PFRC, with polypropylene (PP) fibers assigned to the concrete material. All the default constitutive models in VT2 were selected. The tensile strength was set equal to the maximum observed principal tension stress from Table 3.4, i.e., $f'_t = f^{max}_{c1}$.

(2) The default constitutive models selected in (1) utilized the DSFM formulation. The panels were then modeled with the MCFT formulation, by neglecting crack slip. Other constitutive models and f'_t were unchanged from (1).

(3) The specified tensile strength f'_t was found to significantly influence the predicted response of the specimens. Four different methodologies for f'_t were evaluated for the MCFT model from (2).

(4) A "tension-softening" model based on the experimental data was calibrated to account for the strength provided by the macro-synthetic fibers used in the experimental program.

The calibration of the panel models is discussed in more detail in the following subsections. Note that panel specimens that observed consolidation issues (PFRC-026-058 and PFRC-052-058) were not included in average or standard deviation calculations (marked with *).

4.3.1 Panels Modeled as RC and PFRC

VecTor2 provides various options to model FRC elements by allowing users to choose from four types of fiber reinforcement:

Steel - Hooked	Polypropylene - Deformed
Steel - Straight	Polypropylene - Straight

The required inputs for defining the fiber reinforcement include fiber volume V_f, fiber length l_f, fiber diameter d_f and fiber tensile strength F_{fu}. The fibers are incorporated into the concrete material and the tensile strength of the fiber-reinforced concrete is computed using the selected FRC-tension constitutive model (i.e., VEM or SDEM).

Initially, all constitutive models were set to the default option. All specimens were modeled as plain reinforced concrete (RC). However, to explore the effects of the fiber models embedded in VecTor2, the PFRC panels (P5-P12) were also modeled with fibers. The PFRC panels were thus assigned a FRC material, defined as concrete material with polypropylne straight fibers (PP), with the fiber properties summarized in Table 3.2. For both the RC models and the PFRC models, the tensile strength was specified as the maximum observed principal tensile strength of the panels, f_{c1}^{max}, measured experimentally and reported in Table 3.4.

The RC models and the PP models displayed analogous peak shear stress with average predicted-to-experimental strength ratios of 0.98 and 0.97 and standard deviation (Std) of 0.12 and 0.14 for RC and PP, respectively. Note that average and Std for the PP models only

included the PFRC panels tested (P5-P12) while the average and Std for the RC models included all twelve specimens.

The two models exhibited comparable accuracy with respect to the shear strain at failure γ_u as well, with an average of 1.06 and 1.02 with Std of 0.26 and 0.16 for RC and PP, respectively. Figure 4.4 illustrates a comparison of the full shear stress-strain response for two representative specimens, obtained from the RC and PP models. The RC models generally achieved better predictions of the experimental response.

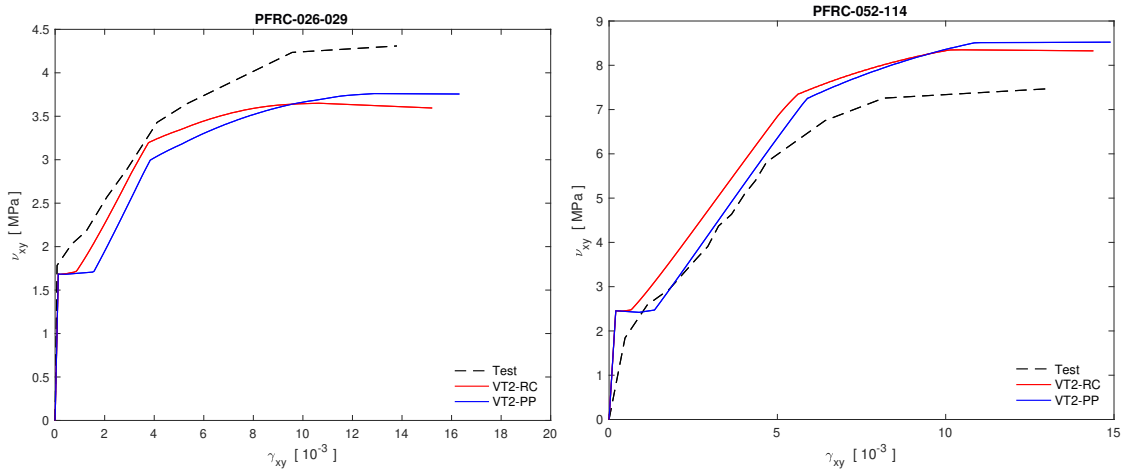

(a) (b)

Figure 4.4: Shear stress-strain response for the RC and PP models (a) PFRC-026-029 (b) PFRC-052-114

The PFRC models developed in VT2 resulted in a decrease in post-cracking shear stress compared to the corresponding RC models. This is in contrast with what was observed by Susetyo (2009), where fiber addition augmented the post-cracking shear stress. Consequently, utilizing PP fibers to model the response of FRC specimens did not seem reasonable modeling approach, since the predicted post-cracking response did not align with experimental findings. The jump in shear strain at cracking (see Figure 4.4) may be attributed to fiber engagement, but this behavior was not observed in the experimental program by Gaston (2023). Therefore, the use the PP fiber model in VT2 was discontinued for the modeling calibration.

4.3.2 Using the MCFT and the DSFM

The model development outlined above utilized all the default constitutive models in VT2. The default model for crack slip is the Walraven model by Equation (4.4), and therefore the analysis was carried out based on the DSFM. An evaluation was performed on the accuracy of the two theories.

The DSFM correspond to the "RC" model shown in Figure 4.4. To evaluate the MCFT, crack slip was neglected while other constitutive models were not modified. The comparison of the two theories is shown for two representative specimens in Figure 4.5. It is evident that the MCFT provides more accurate strength estimates than the DSFM for both specimens illustrated, in addition to PFRC-000-029 (not shown). The theories provided comparable responses for other specimens of the experimental program. However both theories are somewhat inaccurate for specimen PFRC-052-029 in Figure 4.5(b). In terms of ultimate shear strain γ_u, the DSFM appeared to be more accurate in predicting γ_u compared to the MCFT.

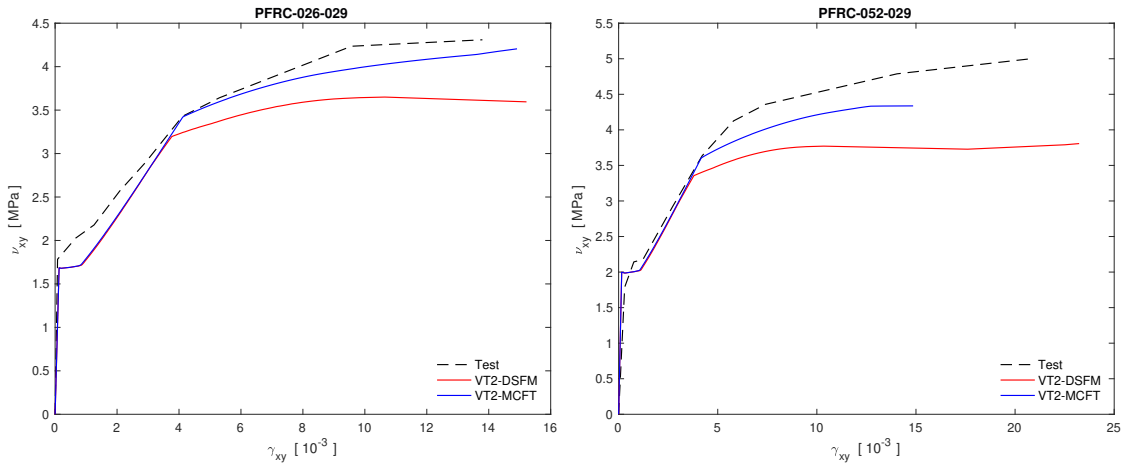

(a) (b)

Figure 4.5: Shear stress-strain response for the DSFM and the MCFT (a) PFRC-026-029 (b) PFRC-052-029

Overall, both theories provided accurate strength predictions with average predicted-to-experimental strength ratio of 0.98 and 1.00 (and standard deviation of 0.12 and 0.09) for the DSFM and the MCFT, respectively. By comparing the predictions for each panel

specimen, the MCFT appeared somewhat more accurate than the DSFM, although both theories provided comparable results in most cases.

4.3.3 Effects of the Specified Tensile Strength in VecTor2

Various relationships have been employed to estimate the direct tensile strength of RC and FRC as a function of modulus of rupture. Petersen (2009) utilized the relationship by AS3600-2001 (Standards Australia, 2001) based on Equation (4.9).

$$f'_t = \frac{f_1}{1.5} \tag{4.9}$$

Other relationships have also been developed that relate modulus of rupture to the compressive strength, for example Equation (4.10) by Ahmed et al. (2016):

$$f_1 = \lambda_1 \cdot \lambda_2 \cdot 0.45 \cdot {f'_c}^{2/3} \tag{4.10}$$

where λ_1 and λ_2 are both taken as 1.0 for 28-day unconfined concrete. Using the fib Model Code (2010) relationship for tensile strength, $f'_t = 0.3 f_c^{2/3}$, Equation (4.10) can be rearranged as:

$$f_1 = \frac{0.45 f'_t}{0.3} = 1.5 f'_t.$$

This yields the same relationship expressed by Equation (4.9). It is important to note that both equations were developed for plain concrete. However, one study that investigated FRC found that for SFRC with $V_f = 1.0\%$, the ratio of f_1/f'_t averaged 2.12 with an upper bound of 3.0 (Maalej and Li, 1994).

Gaston (2023) measured modulus of rupture values, f_1, experimentally for the beam specimens (companion to the panels). The measured values, reported in Table 3.3, were compared to the observed maximum principal tensile strength of the panel specimens, f_{c1}^{max} in Figure 4.6, illustrating the ratio of f_{c1}^{max}/f_1 for both beam sizes tested by Gaston (2023).

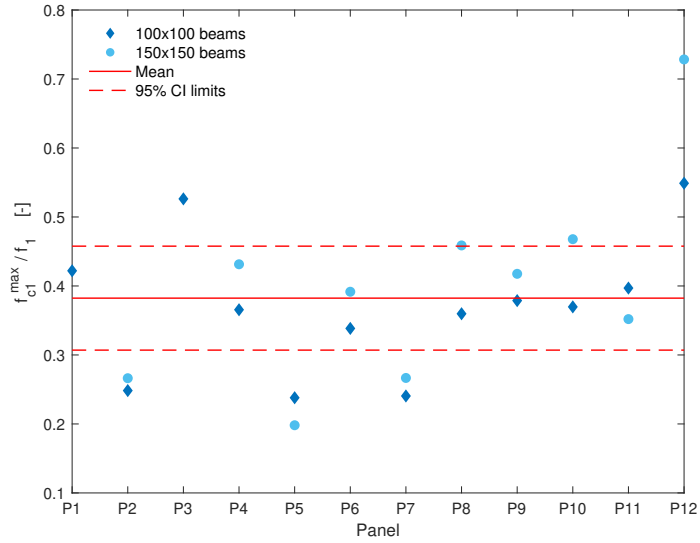

Figure 4.6: Ratio of principal tensile strength to modulus of rupture

The average f_{c1}^{max}/f_1 ratio for all tested beams in Figure 4.6 is

$$\frac{f_{c1}^{max}}{f_1} = 0.38$$

which yields

$$f_1 = 2.64 f_t'.$$

This approximately aligns with the findings of the FRC study on SFRC (Maalej and Li, 1994) but is notably higher than the values predicted by equations (4.9) and (4.10). However, no clear trends were observed with respect to the fiber volume V_f in Figure 4.6 and due to the scattering of the datapoints, the 95% confidence intervals were relatively broad at 0.15.

Consequently, the impact of the specified tensile strength on the behavior of an FRC element subjected to shear was examined in VT2. Four relationships for the tensile strength were scrutinized :

(i) Average from Figure 4.6 of $f_t' = 0.38 f_1$

(ii) Average for $V_f = 1.0\%$ steel fibers: $f_t' = 0.5 f_1$ (Maalej and Li, 1994)

(iii) Equation (4.9): $f_t' = 0.67 f_1$ (Petersen, 2009)

(iv) VT2 default tensile strength: $f_t' = 0.33\sqrt{f_c}$.

Relationships (i), (ii) and (iii) above relate the tensile strength directly to the modulus of rupture f_1. For each of these relationships, the experimentally measured f_1 value was

used to estimate the tensile strength. The f_1 values for the 150×150 beams in Table 3.3 were used for each panel specimen. However, f_1 values for two 150×150 beams were absent. For those two cases, experimental values for the 100×100 beams were used for f_1. The predicted-to-experimental strength ratios are presented in Table 4.2. Additionally, a comparison is shown for two representative panel specimens in Figure 4.7.

Table 4.2: Predicted-to-experimental strength ratios for the tensile strength, f'_t, inputs from cases (i), (ii), (iii) and (iv), in addition to $f'_t = f_{c1}^{max}$

Panel	**Specimen name**	$\mathbf{0.38}f_1$	$\mathbf{0.5}f_1$	$\mathbf{0.67}f_1$	**VT2 default**	f_{c1}^{max}
P1	PFRC-000-000	0.92	1.21	1.62	1.04	1.03
P2	PFRC-000-029	0.98	0.99	1.02	0.98	0.96
P3	PFRC-000-058	0.99	1.01	1.04	1.03	1.01
P4	PFRC-000-114	1.06	1.07	1.08	1.07	1.06
P5	PFRC-026-000	1.57	2.07	2.76	1.31	0.84
P6	PFRC-026-029	0.97	0.98	0.99	0.97	0.98
P7	PFRC-026-058*	1.37	1.41	1.38	1.38	1.34
P8	PFRC-026-114	1.12	1.12	1.13	1.12	1.12
P9	PFRC-052-000	0.94	1.22	1.63	1.19	1.02
P10	PFRC-052-029	0.85	0.87	0.88	0.87	0.87
P11	PFRC-052-058*	1.16	1.19	1.20	1.18	1.16
P12	PFRC-052-114	1.09	1.09	1.10	1.10	1.11
	Average:	1.05	1.16	1.32	1.07	1.00
	Std:	0.19	0.32	0.54	0.12	0.09

According to Table 4.2, it is evident that utilizing a fraction of the modulus of rupture did generally not provide as accurate results as employing the default tensile strength in VT2. Using the average f_{c1}^{max}/f_1 ratio from case (i) and the default tensile strength resulted in a comparable average predicted-to-experimental strength ratio, while the standard deviation was significantly lower for the latter. Therefore, using a fraction of the modulus of rupture for the tensile strength did not seem a viable approach for the calibration of the model.

The predicted-to-experimental strength ratios for the VT2 default tensile strength were

not as accurate as using $f'_t = f^{max}_{c1}$, both in terms of the average of 1.05 and 1.00 and standard deviation of 0.19 and 0.09, respectively. However, the VT2 default tensile strength provided a reasonable estimate of the tensile strength f'_t, to accurately predict the shear strength of the panel specimens.

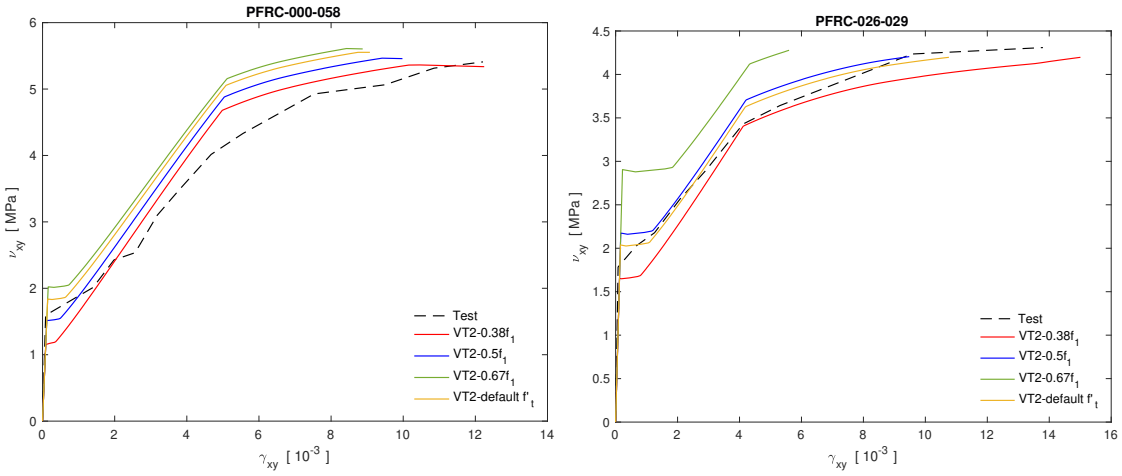

(a) (b)

Figure 4.7: Influence of specifyed tensile strength on the shear stress-strain response (a) PFRC-000-058 (b) PFRC-026-029

4.3.4 Transverse Reinforcement Ratio ρ_y

As a result from Table 4.2 ($f'_t = f^{max}_{c1}$), specimens containing the maximum transverse reinforcement ($\rho_y = 1.14\%$) were significantly overpredicted. The specified reinforcement ratio in VT2 appeared to cause this disparity. With respect to the reinforcement layout in Figure 3.1(d), the outermost transverse reinforcement bars were only 60 mm from the edge of the panel specimens. These edge steel bars might have been ineffective in contributing to the shear strength. To address this, an effective transverse reinforcement ratio for these panels was computed by discounting the outermost transverse steel bars such that

$$\rho_{y4,\text{eff}} = \frac{A_s}{A_g} = \frac{8 \cdot A_b}{A_g} = \frac{8 \cdot 71\ mm^2}{70 \cdot 890\ mm^2} = 0.91\ \%. \tag{4.11}$$

The $\rho_{y4,\text{eff}}$ computed by Equation (4.11) is 20% lower than the reported $\rho_{y4} = 1.14\%$ in Table 3.1. The panel specimens, experimentally tested by Gaston (2023), identified with $\rho_y = 1.14\%$ were modeled with $\rho_{y4} = 1.14\%$ and $\rho_{y4,\text{eff}} = 0.91\%$. The constitutive models

were selected as the default models, except for neglecting *crack slip*. The tensile strength was specified as $f'_t = f^{max}_{c1}$, as it provided the most accurate estimates in Table 4.2 in terms of strength.

Table 4.3 shows the predicted-to-experimental strength ratios for $\rho_{y4} = 1.14\%$ and $\rho_{y4,\text{eff}} = 0.91\%$. The effective transverse reinforcement ratio $\rho_{y4,\text{eff}} = 0.91\%$ improved the predicted-to-experimental strength ratios for all three panels that resulted in overall average ratio of 0.97 (Std = 0.06), compared to 1.00 (Std = 0.09) in Table 4.2 (for all twelve panels). Despite the average ratio was not as accurate by using $\rho_{y4,\text{eff}} = 0.91\%$ instead of $\rho_{y4} = 1.14\%$, the standard deviation was reduced by 30%.

Table 4.3: Predicted-to-experimental strength ratios for $\rho_{y4} = 1.14\%$ and $\rho_{y4,\text{eff}} = 0.91\%$

Panel	**Specimen name**	$\boldsymbol{\rho_{y4}}$	$\boldsymbol{\rho_{y4,\text{eff}}}$
P4	PFRC-000-114	1.06	0.95
P8	PFRC-026-114	1.12	1.00
P12	PFRC-052-114	1.11	1.00

Figure 4.8 shows the shear stress-strain response for specimens PFRC-026-114 and PFRC-052-114. The predicted response using the effective ratio of 0.91% is significantly more accurate than the reported ratio of 1.14%. Therefore, the outermost reinforcement steel bars in Figure 3.1(d) appeared not to contribute to the shear strength, due to the short distance to the edge of the panel specimen.

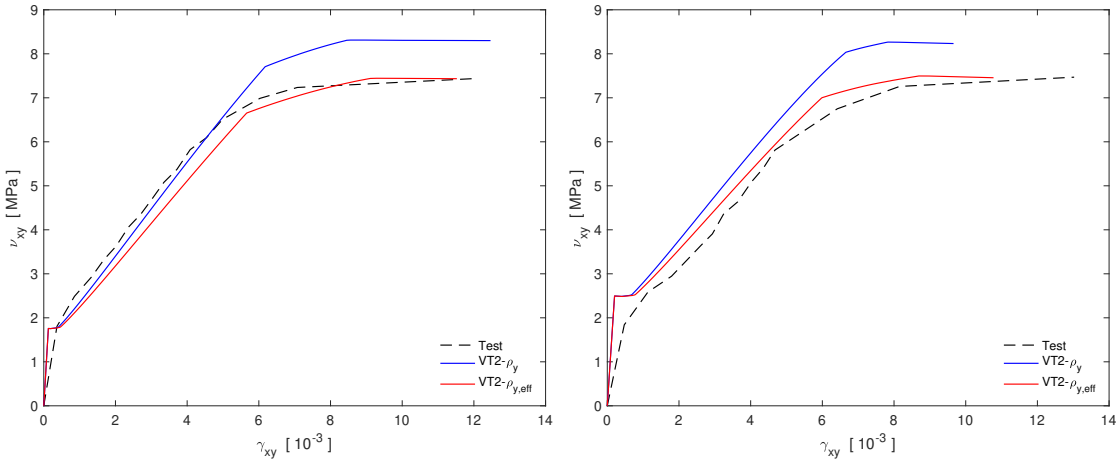

Figure 4.8: Shear stress-strain response using $\rho_y = 1.14\%$ versus $\rho_{y,\text{eff}} = 0.91\%$ (a) PFRC-026-114 (b) PFRC-052-114

4.3.5 Calibrated Tension Softening Model

The predicted strengths in Tables 4.2 and 4.3 rely on constitutive models for reinforced concrete without accounting for any fibers. However, earlier studies have demonstrated that macro-synthetic fibers contribute to the shear strength of PFRC (e.g., Altoubat et al., 2009; Carnovale and Vecchio, 2014; Navas et al., 2018).

Hence, to provide a reliable means of incorporating the effects of macro-synthetic fibers for the concrete material in VecTor2, a tension softening model was calibrated based on the experimental results obtained by Gaston (2023). A customized tension softening model can be integrated to VecTor2 using a piecewise linear model defined by four input points on the Auxiliary Input page in FormWorks. This can be achieved either in a strain-based or crack-based manner. For strain-based tension softening, the input entails four datapoints representing $f_{c1} - \epsilon_{c1}$, as illustrated in Figure 4.9. For the crack-based tension softening, the same four point input approach applies. However, VecTor2 converts the datapoints to $f_{c1} - w$ data according to Equation (4.12).

$$w = \frac{\epsilon_{c1}}{s_{cr}} \tag{4.12}$$

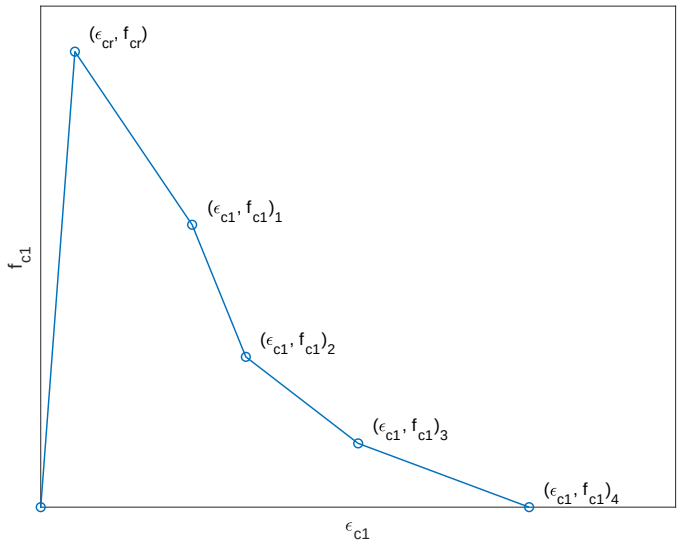

Figure 4.9: Custom tension softening in FormWorks

To develop a tension softening model for macro-synthetic fibers, the tension softening response observed in the experimental program conducted by Gaston (2023) was analyzed. The $f_{c1} - \epsilon_{c1}$ responses for the four panels containing equal fiber volume were normalized. Based on simple spreadsheet calculations, an exponential tension softening was fitted through the datapoints of the form

$$\frac{f_{c1}}{f_{cr}} = (1 - b) \cdot e^{-a \cdot \epsilon_{c1}} + b \tag{4.13}$$

where ϵ_{c1} is the concrete principal tensile stress (unitless), f_{c1} is the concrete principal tensile stress and f_{cr} is the cracking stress, taken as the tensile stress f'_t specified in VT2. The parameters a and b are thus dimensionless constants, adjusted upon fitting the model to the normalized tension softening experimental data. The constants a and b that provided a satisfactory match with the experimental data are summarized in Table 4.4.

Table 4.4: Calibrated coefficients a and b for Equation (4.13)

V_f [%]	a	b
0	450	0
0.26	400	0.15
0.52	350	0.22

The coefficients in Table 4.4 were analyzed to establish a relationship expressed in terms of the fiber volume V_f. Thus, the relationships in Equation (4.14) for a and b were developed. Therefore, the proposed tension softening model is:

$$\begin{aligned} \frac{f_{c1}}{f_{cr}} &= (1-b)\cdot e^{-a\cdot\epsilon_{c1}} + b \\ a &= 450 - 20000\cdot V_f \geq 50 \\ b &= 3\sqrt{V_f} \end{aligned} \tag{4.14}$$

where V_f is a fiber volume fraction, specifically 0, 0.0026 and 0.0052 for the experimental program by Gaston (2023). The derived relationships closely approximates the coefficients in Table 4.4. Notably, this tension softening model is tailored to the experimental program, utilizing macro-synthetic fibers. However, the relationships in Equation (4.14) could also depend on fiber properties, such as fiber length or fiber aspect ratio. Further research is necessary to generalize this model, and validate these relationships across a broader range of fiber volumes and different macro-synthetic fiber types. To prevent the occurrence of "numerical" tension hardening, which occurs if $a < 0$, a constraint of $a \geq 50$ was imposed. This value was selected somewhat arbitrarily and warrants further experimental validation.

A comparison between the tension softening model by Equation (4.13) and the experimental data used for calibration is shown in Figure 4.10.

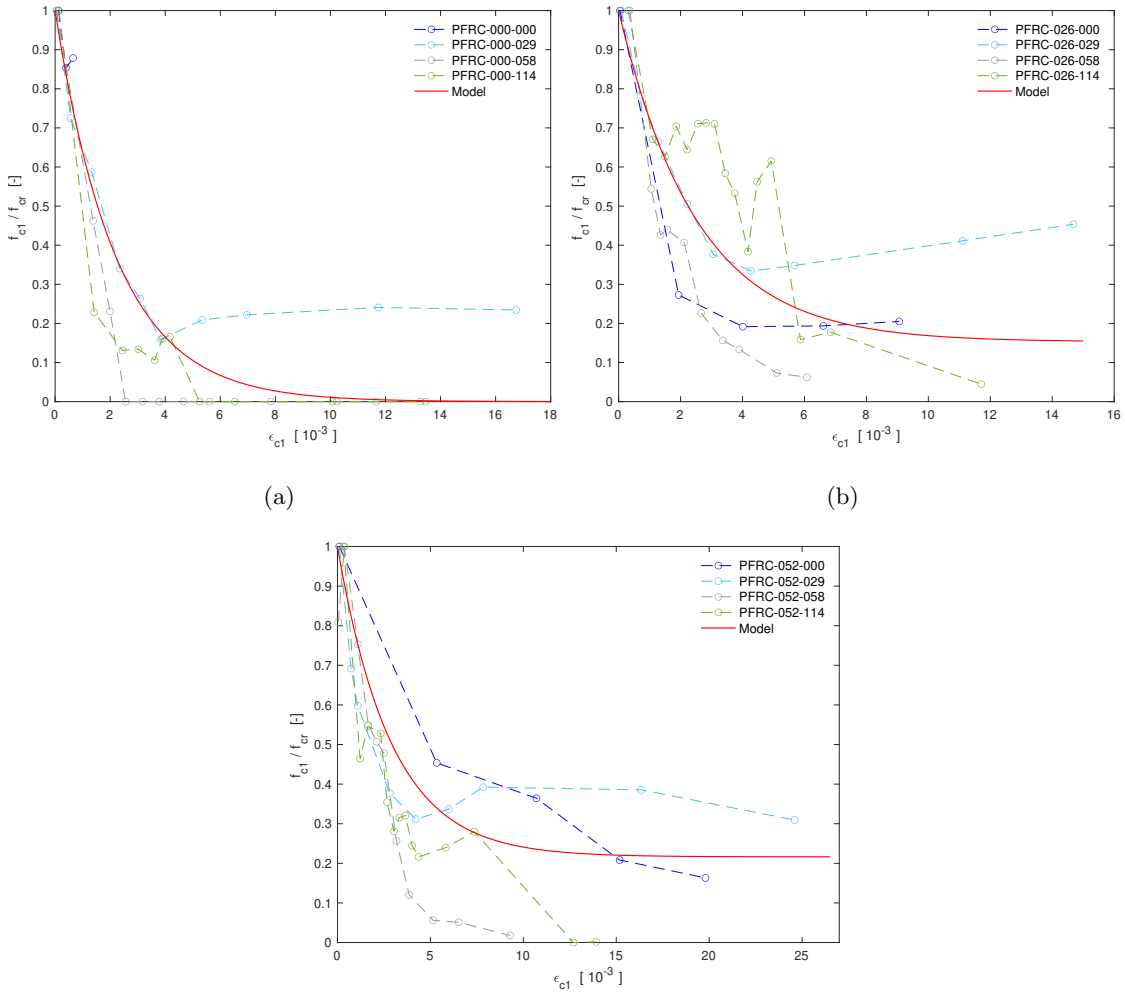

Figure 4.10: Calibrated tension softening model to the experimental data (a) $V_f = 0\%$ (b) $V_f = 0.26\%$ (c) $V_f = 0.52\%$

This calibrated tension softening was used as one of the input parameters to the VecTor2 models for the panel specimens. This required a discretization of the predicted tension softening response in Figure 4.10 into four points as shown in Appendix A. This modeling scheme accounts for the influence of the fibers by implementing the tension softening model by Equation (4.14). Until this point, the calibration has been conducted using the default Hordijk tension softening model (Cornelissen et al., 1986). A comparison of the predicted-to-experimental strength ratios by using the Hordijk model and the proposed tension softening model by Equation (4.14) is reported in Table 4.5.

Table 4.5: Predicted-to-experimental strength ratios using the tension softening (TS) model (Eq. 4.14) and the Hordijk model

Panel	**Specimen**	**TS model**	**Hordijk**
P1	PFRC-000-000	1.06	1.03
P2	PFRC-000-029	0.96	0.96
P3	PFRC-000-058	1.01	1.01
P4	PFRC-000-114	0.95	0.95
P5	PFRC-026-000	0.93	0.84
P6	PFRC-026-029	0.98	0.98
P7	PFRC-026-058*	1.34	1.34
P8	PFRC-026-114	1.04	1.00
P9	PFRC-052-000	1.14	1.02
P10	PFRC-052-029	1.00	0.87
P11	PFRC-052-058*	1.18	1.16
P12	PFRC-052-114	1.04	1.00
	Average:	1.01	0.97
	Std:	0.06	0.06

According to Table 4.5, the tension softening model by Equation (4.14) yields an accurate average predicted-to-experimental ratio of 1.01 compared to 0.97 for the Hordijk model. The standard deviations equal 0.06 for both models. The proposed tension softening model in Equation (4.14) improves the predictions for specimens PFRC-026-000 and PFRC-052-029 significantly, which were underpredicted by the Hordijk model, as demonstrated in Figure 4.11. Other specimens exhibited comparable results, as indicated in Table 4.5.

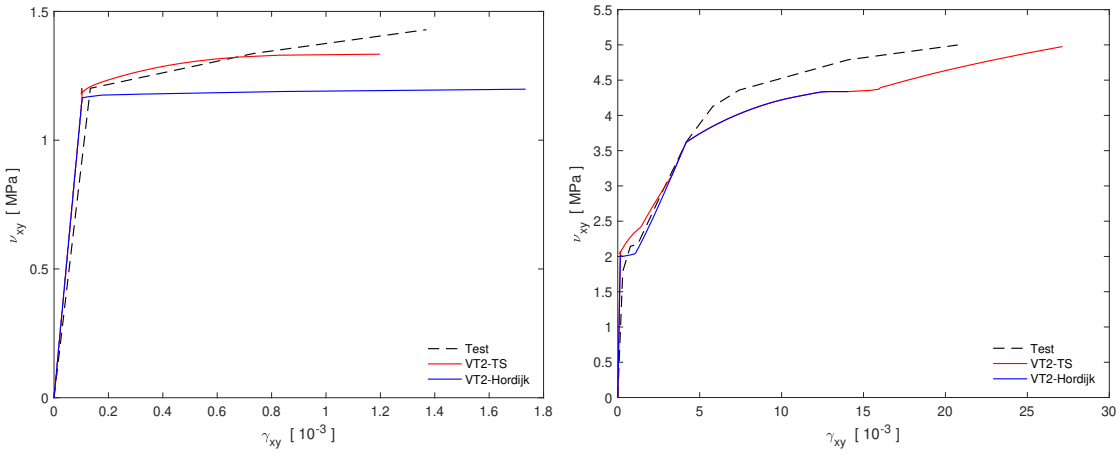

(a) (b)

Figure 4.11: Shear stress-strain response for the tension softening model (4.14) versus the Hordijk model (a) PFRC-026-000 (b) PFRC-052-029

Table 4.6 summarizes the final calibrated modeling results. The transverse reinforcement ratio ρ_y reported in Table 3.1 was used for all specimens, except the heavily reinforced panels. For those panels, the effective reinforcement ratio $\rho_{y,\text{eff}} = 0.91\%$ was employed by neglecting the outermost steel bars that appeared to contribute insignificantly to the shear strength.

The constitutive models were selected as the default models, except for the neglecting *crack slip* and *FRC tension*. The tension softening model (4.14) was used as an input parameter, by entering the discretized datapoints of the predicted response in Figure 4.5 (see Appendix A).

Table 4.6: Final modeling results

Panel	**Specimen name**	v_{exp} **[MPa]**	v_{vt2} **[MPa]**	**pred/exp**
P1	PFRC-000-000	2.12	2.25	1.06
P2	PFRC-000-029	4.27	4.09	0.96
P3	PFRC-000-058	5.41	5.49	1.01
P4	PFRC-000-114	7.82	7.46	0.95
P5	PFRC-026-000	1.43	1.34	0.93
P6	PFRC-026-029	4.31	4.21	0.98
P7	PFRC-026-058*	4.24	5.69	1.34
P8	PFRC-026-114	7.43	7.70	1.04
P9	PFRC-052-000	1.50	1.72	1.14
P10	PFRC-052-029	5.00	4.98	1.00
P11	PFRC-052-058*	4.94	5.85	1.18
P12	PFRC-052-114	7.47	7.78	1.04
			Average:	1.01
			Std:	0.06

4.3.6 Modeling Approach

The constitutive models selected to model the response of PFRC elements are summarized in Tables 4.7, 4.8, 4.9 and 4.10. The recommended tension softening is the proposed Equation (4.14), that requires custom input to the model.

Table 4.7: Concrete constitutive models used

Compression Pre-Peak:	Hognestad (Parabola)
Compression Post-Peak:	Modified Park-Kent
Compression Softening:	Vecchio 1992-A (e1/e2-Form)
Tensions stiffening:	Modified Bentz 2005
Tensions softening:	Custom Input (Strain Based)
FRC tension:	Not Considered
Confined Strength:	Kupfer / Richart
Dilation:	Variable - Isotropic
Cracking Criterion:	Mohr-Coulomb (Stress)
Crack Stress Calc:	Basic (DSFM / MCFT)
Crack Width Check:	Agg/2.5 Max Crack Width
Crack Slip Calc:	Not considered
Creep and Relaxation:	Not Considered
Hysteretic Response:	Nonlinear w/ Plastic Offsets

Table 4.8: Reinforcement and bond constitutive models used

Hysteretic Response:	Bauschinger Effect (Seckin)	**Buckling:**	Akkaya 2012
Dowel Action:	Tassios (Crack Slip)	**Conrete Bond:**	Eligehausen

Table 4.9: Analysis parameters used

Maximum Number of Iterations:	60
Averaging Factor:	0.6
Convergence Limit:	0.00001
Convergence Criteria:	Displacements - Weighted Average
Analysis Mode:	Static Nonlinear - Load Step
Modeling Format:	Stand Alone

Table 4.10: Analysis models used

Strain History:	Previous Loading Considered
Strain Rate Effects:	Not Considered
Structural Damping:	Not Considered
Geometric Nonlinearity:	Considered
Cracking Spacing:	CEB-FIP 1978 - Deformed
Modeling Format:	Stand Alone

4.4 Panel Modeling Results

The predicted response was compared to the experimental behavior of the panel specimens tested by Gaston (2023). The modeling approach outlined in Chapter 4.3.6 was utilized for the panels. The comparison was evaluated in terms of the following outcomes:

(i) $v_{xy} - \gamma_{xy}$: Shear stress to shear strain
(ii) $f_{c1} - \epsilon_{c1}$: Principal tension stress to principal tension strain
(iii) $f_{c2} - \epsilon_{c2}$: Principal compression stress to principal compression strain
(iv) $\theta_\sigma - v_{xy}$: Orientation of principal stress field to shear stress
(v) $\theta_\epsilon - v_{xy}$: Orientation of principal strain field to shear stress
(vi) $\theta_\sigma - \theta_\epsilon$: Orientation of principal stress field to orientation of principal strain field

The comparison of $\theta_\sigma - \theta_\epsilon$ illustrates how the coaxial assumption of the MCFT compares to the experimental response. The full comparison between the experimental panel behavior and the predicted response from the numerical models are outlined in Appendix A.

For most of the specimens, the predicted response provided accurate predictions compared to the experimental response. Figure 4.12 demonstrates that the shear response was accurately predicted. It was more challenging for the model to accurately predict the behavior of the panels without transverse reinforcement that experienced failure soon after cracking. For those specimens, the principal stress and strain fields predictions did not align with the experimental results. However, the principal stress and strain fields were accurately predicted for specimens containing transverse reinforcement.

The relationship between the orientation of the principal stress and strain fields generally aligned with the MCFT assumption of coaxiality of θ_σ and θ_ϵ, as illustrated in Figure 4.13.

This is consistent with the validation study by Vecchio et al. (2001) that the assumption of coaxiality of the stress and strain fields of the MCFT provides accurate results.

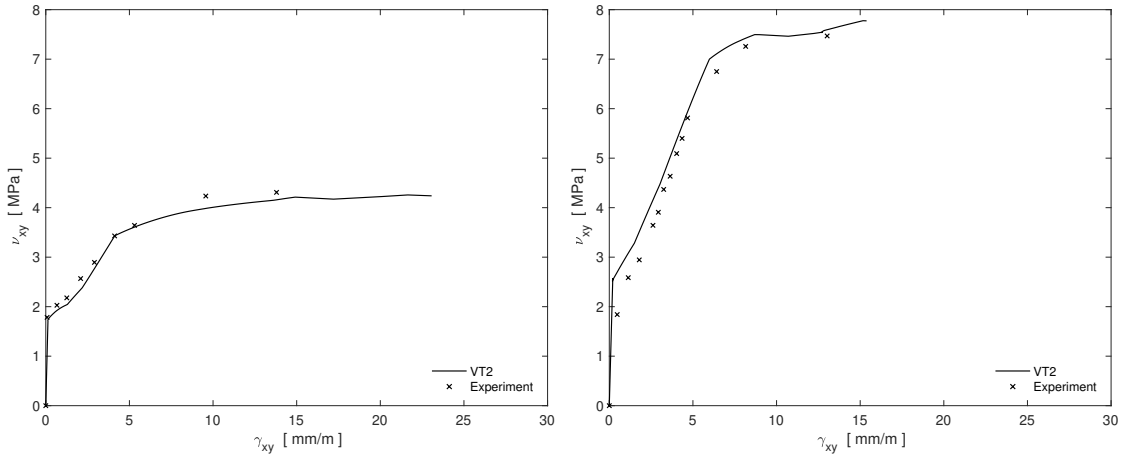

(a) (b)

Figure 4.12: Predicted versus experimental response for shear stress-strain (a) PFRC-026-029 (b) PFRC-052-114

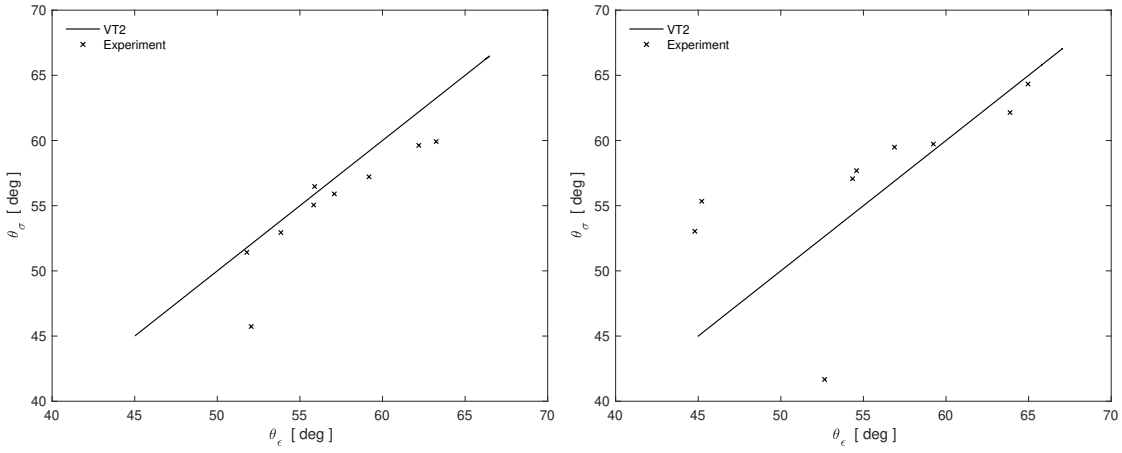

(a) (b)

Figure 4.13: Orientation of the principal stress field to the principal strain field (a) PFRC-026-029 (b) PFRC-052-029

Chapter 5
VALIDATION OF THE MODELING APPROACH

This chapter uses panel and beam tests from the literature to validate the modeling approach outlined in Chapter 4.3.6. The discussion focuses primarily on strength assessment, hence comparing the predicted ultimate shear capacity to the experimental ultimate shear strength. The validation included three parts:

- Panel specimens from previous experimental programs, including biaxially reinforced concrete panels and PFRC panels without transverse reinforcement, subjected to monotonic and reversed cyclic pure shear loading.
- PFRC companion beams tested by Gaston (2023) (companion to panel specimens P1-P12).
- Structural PFRC beam specimens (with longitudinal reinforcement steel bars, and some with stirrups) from the literature. To this end, a comprehensive database was compiled, consisting of tested PFRC beams with and without stirrups and corresponding control specimens.

5.1 Modeling of Panel Specimens

The experimental program by Gaston (2023) was the first study dedicated to the shear response of PFRC panels containing steel reinforcement in both the x- and y-directions, under pure shear loading conditions. Previously, only two PFRC panel tests had been conducted. Carnovale (2013) tested specimens DC-P3 and DC-P5 (see Table 2.2) to investigate if macro-synthetic fibers could replace traditional transverse steel reinforcement (stirrups).

The two specimens tested by Carnovale (2013) incorporated a fiber volume of $V_f = 2.0\%$ and were subjected to monotonic and reverse cyclic loading, respectively. These two PFRC panel specimens were modeled herein following the modeling approach outlined in Chapter 4.3.6. Additionally, two control RC specimens were modeled, namely C1C and DC-P1, tested by Susetyo (2009) and Carnovale (2013), respectively. The reinforcement layout of the panel specimens used for validation is represented in Figure 5.1, with the key properties summarized in Table 5.1.

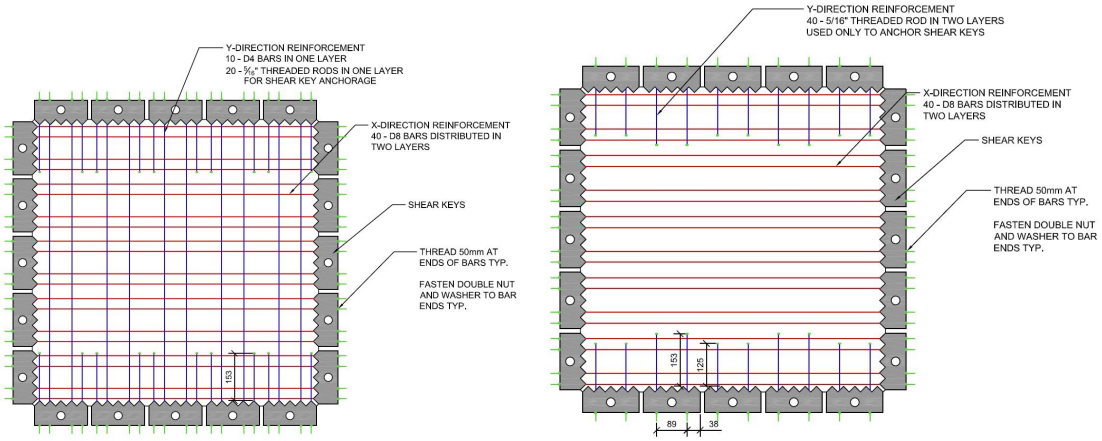

(a) (b)

Figure 5.1: Specimen design (Carnovale, 2013) for (a) C1C and DC-P1 (b) DC-P3 and DC-P5

Table 5.1: Panel specimens used for validation

Series	**Tested By**	f'_c **[MPa]**	**Fiber type**	V_f **[%]**	**Loading type**
C1C	Susetyo (2009)	65.7	-	-	Monotonic
DC-P1	Carnovale (2013)	71.7	-	-	Reversed cyclic
DC-P3	Carnovale (2013)	50.9	MAC matrix	2.0	Monotonic
DC-P5	Carnovale (2013)	54.3	MAC matrix	2.0	Reversed cyclic

Figure 5.2 compares the shear stress-strain response from the numerical analysis to the experimental response. Since the tensile strength was found to influence the predicted strength significantly, it was specified in the numerical models both as the VT2 default tensile strength and the maximum observed principal tensile stress f_{c1}^{max} in the panel tests conducted by Susetyo (2009) and Carnovale (2013). The tension softening model by Equation (4.14) was implemented to the numerical models according to the input parameters summarized in Appendix B.

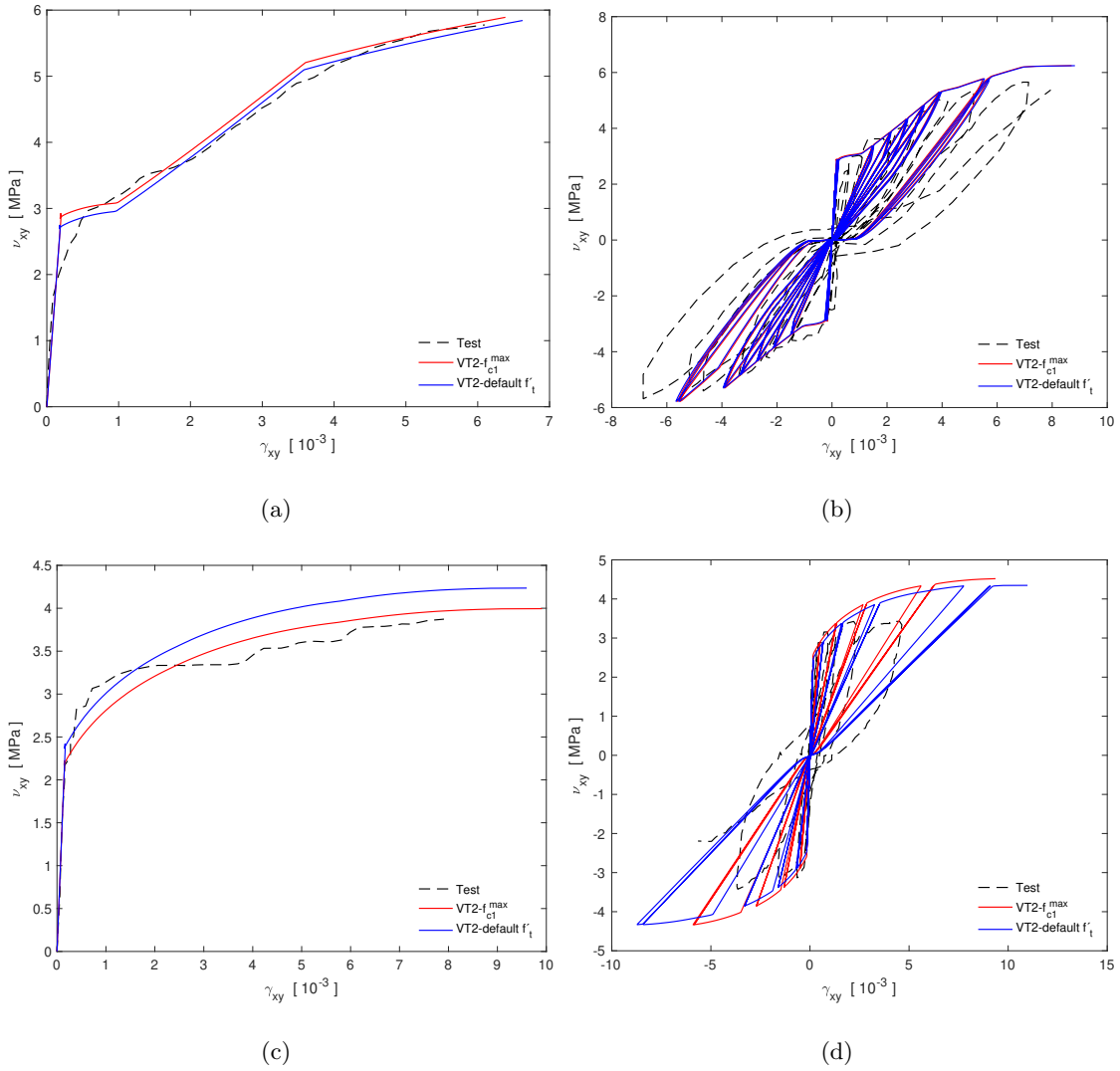

Figure 5.2: Predicted versus experimental shear stress-strain response for panels used for validation (a) C1C (b) DC-P1 (c) DC-P3 (d) DC-P5

Figure 5.2 highlights the high level of accuracy of the modeling strategy adopted for the RC panels. The modeling approach demonstrates abilities to simulate both monotonic and reverse cyclic loading for RC panels, with predicted-to-experimental strength ratio of 1.01 and 1.10 for C1C (monotonic) and DC-P1 (reverse cyclic), respectively, using the default VT2 tensile strength.

For the PFRC specimens, the model appears to capture the post-cracking response of panel DC-P3 under monotonic loading, particularly when the tensile strength is specified as the maximum observed principal tensile strength from the experiment, f_{c1}^{max}, resulting in

a predicted-to-experimental strength ratio of 1.03. However, using the default VT2 tensile strength yields a slight decrease in accuracy with a predicted-to-experimental strength ratio of 1.09. Panel DC-P5 subjected to reverse cyclic loading was over-predicted by approximately 30%, attributed to the lack of cyclic deterioration in the tension softening model (4.14) that was calibrated for monotonic loading.

It should also be noted that specimens DC-P3 and DC-P5 contained significantly higher fiber volume of $V_f = 2.0\%$ compared to the experimental program by Gaston (2023), which had a maximum of $V_f = 0.52\%$. The predicted response for DC-P3 in Figure 5.2(c) demonstrates that the parameters calibrated for the tension softening model (4.14) extrapolate reasonably well for greater fiber volumes than used for the calibration.

5.2 Modeling of Companion PFRC Beams

The companion $150 \times 150 \times 530$ mm PFRC beam specimens tested by Gaston (2023) (companion to the panel specimens) were also modeled. The beams contained the same fiber volume as the corresponding panel specimens, summarized in Table 3.1.

Figure 5.3 shows the numercal model developed for the beam specimens in VecTor2. Since the beams were symmetric about the midspan, only half of each specimen was modeled, assigning appropriate boundary conditions of a horizontal roller support at the base and vertical rollers at the midspan across the beam depth.

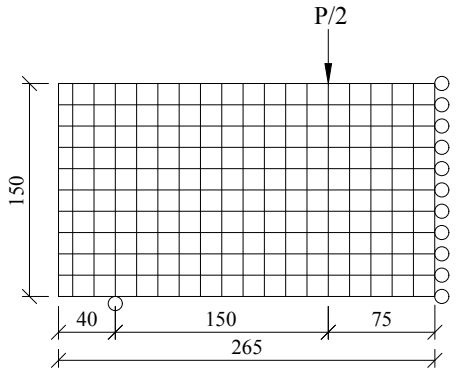

Figure 5.3: Sketch of a beam model in VecTor2

The beam specimens were casted with the same concrete as the corresponding panel specimens. Therefore, the beams were assigned the same material properties as the companion panel models developed in Chapter 4. Since the specified tensile strength significantly influ-

enced the predicted shear strength, three different relationships for f'_t were used. The tensile strength was specified as the maximum principal tensile stress observed in the experiments (f_{c1}^{max}), 50% of the modulus of rupture value observed from the beam tests (in accordance to the findings by Maalej and Li, 1994) and the VT2 default tensile strength ($0.33\sqrt{f'_c}$). Table 5.2 compares the predicted response to the experimental behavior, both in terms of shear strength and residual strength.

Table 5.2: Predicted-to-experimental strength ratios for companion PFRC beams

	Corresponding	**Peak**			**Residual**[2]		
Beam	**panel specimen**	$\boldsymbol{f_{c1}^{max}}$	$\boldsymbol{0.5f_1}$	**VT2 def**	$\boldsymbol{f_{c1}^{max}}$	$\boldsymbol{0.5f_1}$	**VT2 def**
B1	PFRC-000-000	0.82	0.95	0.84	-	-	-
B2	PFRC-000-029	0.52	0.89	0.71	-	-	-
B3	PFRC-000-058	1.08	1.07	1.27	-	-	-
B4	PFRC-000-114	0.84	0.96	0.91	-	-	-
B5	PFRC-026-000	0.42	0.88	0.62	1.05	2.33	1.55
B6	PFRC-026-029	0.79	0.97	0.92	1.01	1.26	1.19
B7	PFRC-026-058	0.57	0.93	0.78	1.27	2.14	1.76
B8	PFRC-026-114	0.93	1.00	1.10	1.41	1.52	1.70
B9	PFRC-052-000	0.84	0.99	0.96	0.97	1.16	1.13
B10	PFRC-052-029	0.93	0.98	1.01	1.11	1.19	1.22
B11	PFRC-052-058	0.75	1.00	0.92	1.62	2.20	2.03
B12	PFRC-052-114	1.36	1.02	1.14	1.45	1.05	1.20
	Average:	0.82	0.97	0.93	1.24	1.61	1.47
	Std:	0.25	0.05	0.18	0.24	0.53	0.33

The specified tensile strength significantly influenced the predicted-to-experimental ratios in Table 5.2. Using the maximum principal tensile stress f_{c1}^{max} did not accurately predict the peak load of the beams resulting in average predicted-to-experimental strength ratio of 0.82 (Std = 0.25). Utilizing half the modulus of rupture $0.5f_1$ provided the most accurate results, resulting in average ratio of 0.97 (Std = 0.05). This aligns with experimental results

[2]Residual predicted-to-experimental ratio is computed for a mid-span deflection of $\delta = 3\ mm$.

by Maalej and Li (1994), who concluded that the flexural strength of FRC is about twice the direct tension strength, as discussed earlier.

However, using $0.5f_1$ for the tensile strength was not accurate for predicting the residual strength of the beams, resulting in average of 1.61 (Std = 0.53). Using $f'_t = f^{max}_{c1}$ provided the most accurate results, with average of 1.24 (Std = 0.24).

It is worth noting that the tension softening model proposed in Equation (4.14) was calibrated for the response of the PFRC panels in pure shear loading, while the beams were subjected to flexure. The tension softening model (4.14) might have overestimated the tension softening behavior of the PFRC companion beams. However, the model generally provided accurate predictions of the load-deflection response as demonstrated in Figure 5.4.

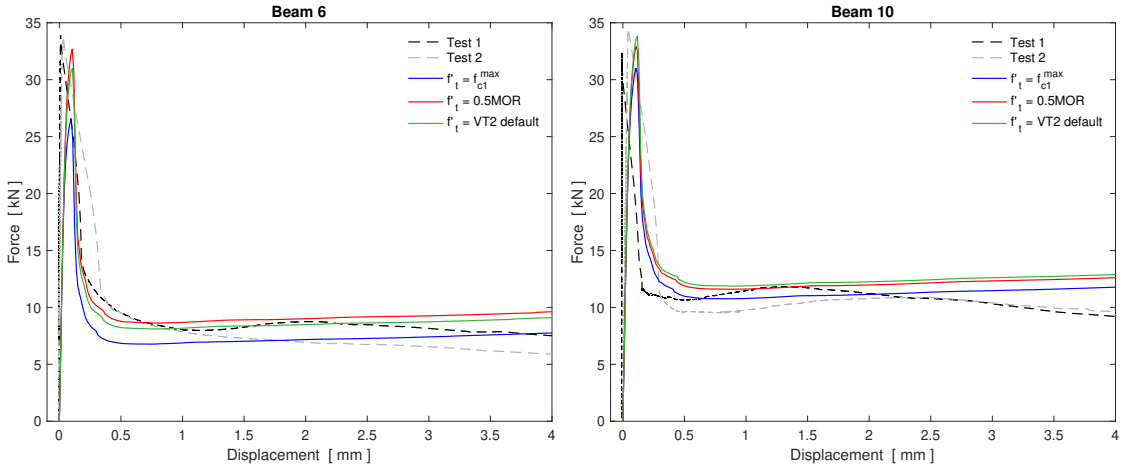

(a) (b)

Figure 5.4: Predicted versus experimental load-deflection response for companion PFRC beams (a) PFRC-026-029 (b) PFRC-052-029

5.3 Modeling of Structural PFRC Beams

This section validates the modeling approach against structural PFRC beam members (with longitudinal reinforcement) from the literature, with and without transverse reinforcement. The beams were modeled in VecTor2 and compared to the reported experimental behavior in terms of peak strength. A beam database was compiled from the available literature,

where beams containing steel fibers or prestressed PFRC beams were not included. The beams were separated into four subgroups:

(i) RC beams (without stirrups)
(ii) PFRC beams (without stirrups)
(iii) RC beams with stirrups
(iv) PFRC beams with stirrups

Significant research has been performed on PFRC beams subjected to flexure in the literature. Various fiber types have been investigated, differing in geometry and mechanical properties. The compiled database of beam specimens was focused on macro-synthetic fibers. The classification between micro- and macro-synthetic fibers was based on the criteria outlined by ACI Committee 544 (2018) in terms of the fiber diameter d_f such that:

$$\begin{aligned} &\text{Micro-fibers: } d_f < 0.3\,mm \\ &\text{Macro-fibers: } d_f \geq 0.3\,mm. \end{aligned} \tag{5.1}$$

The primary focus was to identify experimental programs that included beam specimens with macro-synthetic fibers, with or without stirrups. An extensive literature review revealed that there is a very limited amount of experimental data available for PFRC beam specimens with stirrups. Significantly more experimental data exists for PFRC beams without stirrups, but is still very limited in comparison with SFRC beams.

A total of nine experimental programs were identified that tested PFRC beam specimens in flexure. The beam database consisted of 72 beams, including 37 macro-synthetic FRC beams without stirrups, 11 macro-synthetic FRC beams with stirrups, 15 corresponding control RC beams and 9 corresponding RC beams with stirrups. An overview of the beam specimens from each experimental program is summarized in Table 5.3, while a summary of key parameters of the database is provided in Table 5.4. The beam database is presented in Table 5.5.

Table 5.3: Experimental programs used for the beam database

Experimental Program	**RC**	**PFRC**	**RC & Stirrups**	**PFRC & Stirrups**
Majdzadeh et al. (2006)	1	3	1	1
Greenough and Nehdi (2008)	1	3	0	0
Altoubat et al. (2009)	3	7	0	0
Sahoo et al. (2015)	0	1	1	0
Conforti et al. (2015)	2	4	1	0
Arslan et al. (2017)	2	9	0	0
Ababneh et al. (2017)	1	3	2	6
Navas et al. (2018)	4	4	4	4
Murad and Abdel-Jabbar (2022)	1	3	0	0

Table 5.4: Overview of key parameters of the beam database

Parameter	**Average**	**Max**	**Min**
d [mm]	273	481	120
b_w [mm]	236	890	100
L_{span} [mm]	2091	4570	800
a/d [-]	3.2	5.2	1.7
ρ_ℓ [%]	2.2	3.2	1.2
f'_c [MPa]	37.6	47.1	13.9
V_f [%]	1.1	3.0	0.3

The numerical models of the beams were implemented considering only half of each beam, similarly to the modeling procedure for the companion PFRC beams in Chapter 5.2. Hence, the half-beam specimens were modeled with a horizontal roller at the support and vertical rollers across the section depth at the mid-span. The concrete material was modeled using four-node quadrilateral elements while the steel reinforcement was modeled as a two-node truss-bar elements where a perfect bonding was assumed between steel bars and concrete. The transverse reinforcement, if present, was modeled as smeared reinforcement.

Figure 5.5 shows the VT2 model developed for specimen W430PC (Conforti et al., 2015) for reference. To ensure adequate analysis, the element size was chosen such that the number of elements across the beam depth was at least 10 elements.

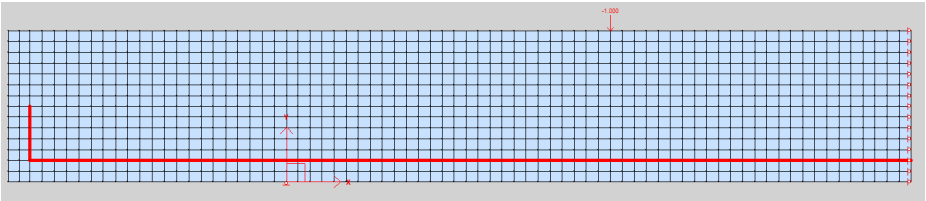

Figure 5.5: VecTor2 model for W430PC, tested by Conforti et al. (2015)

The concrete properties were assigned the thickness and compressive strength reported in Table 3.3. Additionally, measured values of elastic modulus and aggregate size were assigned when available. The default VT2 values (Wong et al., 2013) were used for all other concrete properties, except for crack spacing.

The crack spacing assigned for the models was determined according to the guidelines in AASHTO (2012) and CSA A23.3 (2019) using Equations (2.34) and (2.39), respectively. However, the crack spacing was not taken greater than the member height h, in accordance with Zhang (2020). The crack spacing in the x- and y-direction was thus determined by Equation (5.2) as:

$$\textbf{Beams without stirrups:} \quad s_x = s_y = min(h, s_{csa}, s_{aashto}) \tag{5.2a}$$

$$\textbf{Beams with stirrups:} \quad s_y = min(s, s_x) \tag{5.2b}$$

where s is stirrup spacing.

For the steel reinforcement, the elastic modulus E_s was specified as $E_s = 200,000\,MPa$ for all steel bars. The yield and ultimate stress were assigned experimentally measured values, whenever it was reported. In the absence of experimental data, the yield and ultimate stress were assigned values of $F_y = 420\,MPa$ and $F_u = 620\,MPa$, respectively, corresponding to grade 60 steel reinforcement.

Table 5.5 presents the compiled beam database, in addition to the experimental and predicted shear strength, computed from the ultimate load F_u as:

$$v_u = \frac{F_u}{2 \cdot b_w \cdot d}. \tag{5.3}$$

The predicted strength of the beams appeared to be somewhat overpredicted by the numerical models. The average predicted-to-experimental strength ratio considering all beams in the database (i.e., all beams in Table 5.5) was 1.112 (COV = 21.8%).

Table 5.5: Beam database for PFRC beams

Reference	ID	d [mm]	a/d [-]	ρ_l [%]	ρ_t [%]	f'_c [MPa]	V_f [%]	l_f [mm]	AR_f [-]	$v_{u,exp}$ [MPa]	$v_{u,p}$ [MPa]	$v_{u,p}/v_{u,exp}$ [-]
Majdzadeh et al. (2006)	B1	120	3.0	2.62	0.28	45.3	-	-	-	3.11	3.38	1.09
	B2	120	3.0	2.62	-	47.1	-	-	-	2.11	2.50	1.18
	B3	120	3.0	2.62	0.28	37.8	0.50	50	85	3.78	3.34	0.88
	B6	120	3.0	2.62	-	43.9	0.50	50	85	2.39	3.05	1.28
	B7	120	3.0	2.62	-	44.2	1.00	50	85	3.14	3.26	1.04
	B8	120	3.0	2.62	-	43.1	1.50	50	85	2.89	3.39	1.17
Greenough and Nehdi (2008)	Reference	265	3.0	1.78	-	39.2	-	-	-	1.25	1.31	1.05
	P-WV-50-0.5	265	3.0	1.78	-	41.9	0.50	50	63	1.47	2.15	1.47
	P-WV-50-0.75	265	3.0	1.78	-	39.0	0.75	50	63	1.79	2.21	1.24
	P-WV-50-1.0	265	3.0	1.78	-	37.9	1.00	50	63	1.68	2.27	1.35
Altoubat et al. (2009)	L1-0.0	400	3.5	2.15	-	40.9	-	-	-	1.53	1.29	0.85
	L1-0.50	400	3.5	2.15	-	41.9	0.50	40	90	1.72	1.89	1.10
	L1-0.75	400	3.5	2.15	-	41.9	0.75	40	90	1.93	2.02	1.04
	L2-0.0	330	3.5	3.18	-	40.9	-	-	-	1.53	1.65	1.07
	L2-0.50	330	3.5	3.18	-	41.9	0.50	40	90	1.75	2.26	1.30
	L2-0.75	330	3.5	3.18	-	41.9	0.75	40	90	1.84	2.37	1.29
	L2-1.0	330	3.5	3.18	-	35.6	1.00	40	90	2.00	2.23	1.12
	Sh2-0.0	330	2.3	3.18	-	40.9	-	-	-	1.78	2.98	1.68
	Sh2-0.50	330	2.3	3.18	-	41.9	0.50	40	90	2.09	3.38	1.61
	Sh2-0.75	330	2.3	3.18	-	41.9	0.75	40	90	2.23	3.46	1.55
Sahoo et al. (2015)	RC	172	5.2	2.34	0.22	36.2	-	-	-	2.09	2.05	0.98
	PFRC	172	5.2	2.34	-	37.6	1.00	12.5	25	1.49	1.93	1.30
Conforti et al. (2015)	W430PC	215	2.5	1.30	-	31.2	-	-	-	1.80	1.62	0.90
	W510PFRC	255	2.5	1.24	-	26.0	1.45	40	53	2.24	2.13	0.95
	W650PFRC	215	3.0	1.15	-	26.0	1.45	40	53	2.17	2.22	1.02
	W770PC	255	2.5	1.23	-	31.2	-	-	-	1.66	1.39	0.83
	W770MSR	255	2.5	1.23	0.10	31.2	-	-	-	2.32	2.28	0.98
	W770PFRC	255	2.5	1.23	-	26.0	1.45	40	53	2.29	2.11	0.92
	W890PFRC	295	2.2	1.23	-	26.0	1.45	40	53	2.23	2.02	0.91
Arslan et al. (2017)	B2.5R	210	2.5	1.28	-	26.5	-	-	-	1.13	1.29	1.15
	B2.5P1.0	210	2.5	1.28	-	27.0	1.00	39	51	1.52	1.62	1.06
	B2.5P2.0	210	2.5	1.28	-	13.9	2.00	39	51	1.36	0.90	0.66
	B2.5P3.0	210	2.5	1.28	-	18.5	3.00	39	51	1.78	1.17	0.66
	B3.5R	210	3.5	1.28	-	26.5	-	-	-	1.14	0.95	0.83
	B3.5P1.0	210	3.5	1.28	-	27.0	1.00	39	51	1.48	1.42	0.95
	B3.5P2.0	210	3.5	1.28	-	13.9	2.00	39	51	1.35	0.82	0.60
	B3.5P3.0	210	3.5	1.28	-	18.5	3.00	39	51	1.61	1.06	0.66
	B4.5P1.0	210	4.5	1.28	-	27.0	1.00	39	51	1.24	1.27	1.02
	B4.5P2.0	210	4.5	1.28	-	13.9	2.00	39	51	0.99	0.76	0.76
	B4.5P3.0	210	4.5	1.28	-	18.5	3.00	39	51	1.10	1.01	0.92

Table 5.5 continued

	B1V0S0	125	2.4	3.22	-	43.1	-	-	-	1.96	2.47	1.26
	B1V3S0	125	2.4	3.22	-	44.4	0.33	40	90	2.56	2.69	1.05
	B1V5S0	125	2.4	3.22	-	45.1	0.55	40	90	2.80	2.82	1.01
	B1V7S0	125	2.4	3.22	-	45.9	0.77	40	90	3.08	2.98	0.97
	B2V0S30	125	2.4	3.22	3.35	43.1	-	-	-	4.36	5.47	1.26
Ababneh	B2V3S30	125	2.4	3.22	3.35	44.4	0.33	40	90	4.84	5.56	1.15
et al. (2017)	B2V5S30	125	2.4	3.22	3.35	45.1	0.55	40	90	5.04	5.58	1.11
	B2V7S30	125	2.4	3.22	3.35	45.9	0.77	40	90	5.40	5.60	1.04
	B3V0S60	125	2.4	3.22	1.68	43.1	-	-	-	3.12	5.21	1.67
	B3V3S60	125	2.4	3.22	1.68	44.4	0.33	40	90	3.80	5.33	1.40
	B3V5S60	125	2.4	3.22	1.68	45.1	0.55	40	90	4.12	5.43	1.32
	B3V7S60	125	2.4	3.22	1.68	45.9	0.77	40	90	4.28	5.62	1.31
	OA1	473	3.9	1.68	-	41.8	-	-	-	1.08	1.14	1.05
	OA2	474	4.8	2.23	-	42.2	-	-	-	1.17	1.17	1.00
	OB1	473	3.9	2.23	-	38.3	-	-	-	1.27	1.25	0.99
	OB2	471	4.8	2.24	-	39.8	-	-	-	1.05	1.16	1.11
	A1	473	3.9	1.68	0.10	39.8	-	-	-	1.64	1.84	1.12
	A2	473	4.8	2.23	0.10	40.8	-	-	-	1.66	1.70	1.03
	B1	474	3.9	2.22	0.15	40.1	-	-	-	2.15	2.05	0.95
Navas et al.	B2	474	4.8	2.22	0.15	41.0	-	-	-	2.02	2.02	1.00
(2018)	OAP1	473	3.9	1.67	-	43.1	1.10	48	56	1.55	1.93	1.25
	OAP2	473	4.8	2.23	-	44.9	1.10	48	56	1.69	1.98	1.18
	OBP1	471	3.9	2.24	-	42.7	1.10	48	56	1.68	2.03	1.21
	OBP2	469	4.9	2.25	-	42.0	1.10	48	56	1.38	1.84	1.34
	AP1	475	3.9	1.67	0.10	44.0	1.10	48	56	2.40	2.30	0.96
	AP2	474	4.8	2.23	0.10	44.6	1.10	48	56	2.34	2.14	0.91
	BP1	481	3.8	2.19	0.15	45.0	1.10	48	56	2.52	2.61	1.04
	BP2	475	4.8	2.22	0.15	44.2	1.10	48	56	2.24	2.21	0.98
Murad and	Control	225	1.7	1.19	-	41.7	-	-	-	1.90	2.72	1.43
Abdel-	P2	225	1.7	1.19	-	45.3	0.22	54	68	2.19	2.95	1.35
Jabbar	P4	225	1.7	1.19	-	40.8	0.44	54	68	1.71	3.00	1.75
(2022)	P8	225	1.7	1.19	-	37.7	0.88	54	68	2.07	3.04	1.47

Figure 5.6 compares the experimental and numerical load-deformation response for two representative beam specimens. Given the wide range of aspect ratios, reinforcement ratios, fiber volumes, and concrete compressive strengths contained in the database, it was concluded that satisfactory prediction of the peak strength was achieved (see Table 5.5), while other aspects of the force-deformation response were not.

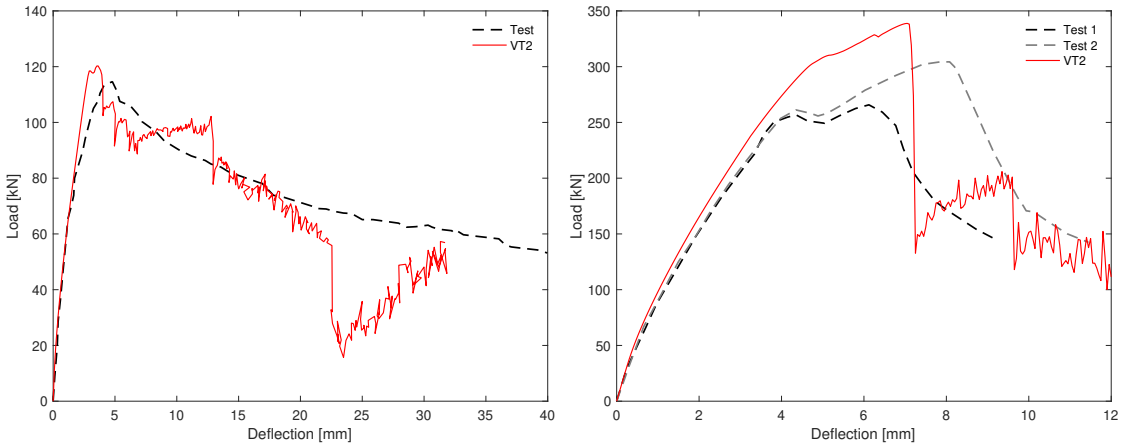

(a) (b)

Figure 5.6: Predicted versus experimental load-deformation response (a) B3 (Majdzadeh et al., 2006) (b) L2-1.0 (Altoubat et al., 2009)

Table 5.6 shows the average predicted-to-experimental strength ratio and COV for each experimental program. The numerical models tend to provide unconservative estimates of the experimental strength for all experimental programs except for the studies by Conforti et al. (2015) and Arslan et al. (2017). A reason for this could be that the experimental program by Conforti et al. (2015) tested wide-shallow beams that experienced enhanced shear behavior ($30-40\%$) compared to deeper beams. The experimental program by Arslan et al. (2017) included few specimens with a reported compressive strength of only $14\,MPa$.

The coefficient of variation (COV) in Table 5.6, computed for the average predicted-to-experimental strength ratio, varied significantly between the different experimental programs (the values ranged from 6.5% to 22.4%). The lowest COV was computed for the experimental program conducted by Conforti et al. (2015). However, given the broad range of specimens in Table 5.5, comprising 72 beams from 9 experimental programs, and considering that the numerical modeling approach adopted was calibrated from panel experiments, the accuracy of the numerical models in predicting the peak strength of the PFRC beams was remarkable.

Table 5.6: Summary of predicted-to-experimental strength ratios for the experimental programs

Reference	**Avg [-]**	**Std [-]**	**COV [%]**	**Min [-]**	**Max [-]**
Majdzadeh et al. (2006)	1.11	0.14	12.4	0.88	1.28
Greenough and Nehdi (2008)	1.28	0.18	13.8	1.05	1.47
Altoubat et al. (2009)	1.26	0.28	21.9	0.85	1.68
Sahoo et al. (2015)	1.14	0.22	19.5	0.98	1.30
Conforti et al. (2015)	0.93	0.06	6.5	0.83	1.02
Arslan et al. (2017)	0.84	0.19	22.4	0.60	1.15
Ababneh et al. (2017)	1.21	0.20	16.6	0.97	1.67
Navas et al. (2018)	1.07	0.12	11.3	0.91	1.34
Murad and Abdel-Jabbar (2022)	1.50	0.17	11.5	1.35	1.75

Table 5.7 shows the average predicted-to-experimental strength ratio and COV for the different beam types in Table 5.5. All beam types resulted in a comparable average ratio of about 1.1. The results were impressive since only material strengths and crack spacing were used as input parameters for the modeled beams. However, higher accuracy may be achieved through a more robust calibration of the tension softening model (4.14) implemented in the numerical models.

To this end, it should be recalled that the tension softening model implemented in the numerical models was calibrated for elements containing a maximum fiber volume of $V_f = 0.52\%$, based on the experimental program by Gaston (2023). It is possible that extrapolating beyond this fiber volume introduces some inaccuracy in the response. This aspect should be investigated and addressed as part of future work.

Table 5.7: Summary of predicted-to-experimental strength ratios for the beam types

Beam type	**Count**	**Avg [-]**	**Std [-]**	**COV [%]**	**Min [-]**	**Max [-]**
All Beams	72	1.11	0.24	21.8	0.60	1.75
RC	15	1.09	0.23	21.2	0.83	1.68
PFRC	37	1.12	0.27	24.3	0.60	1.75
RC with Stirrups	9	1.12	0.23	20.3	0.95	1.67
PFRC with Stirrups	11	1.10	0.18	16.0	0.88	1.40

Figure 5.7 provides a graphic representation of the predicted strengths against the experimental strengths for the beams in Table 5.5. Figure 5.7(a) illustrates that most of the beams tested in the literature possessed a peak strength of less than $200\,kN$. Only three experimental programs conducted beam tests with higher strength. The experimental program conducted by Conforti et al. (2015) included beams with load capacity up to nearly $1200\,kN$. It can be seen that the predicted load capacity appeared to be predicted with higher accuracy as the experimental load capacity increases. However, to conclusively validate this observation, additional beam experiments with capacities greater than $500\,kN$ are required.

Figure 5.7(b) compares the predicted-to-experimental strength in terms of peak shear stress; the experimental shear capacity of the beams in Table 5.5 ranges from 1 to $5.5\,MPa$. The model demonstrated an ability to predict the full range with high accuracy, despite some tendency to underpredict the lower shear strengths and overpredict the higher strengths. The beams tested by Murad and Abdel-Jabbar (2022) and Altoubat et al. (2009), that contained a low span-to-depth ratio ($a/d \leq 2.3$), are notably overpredicted. Additionally, the specimens tested by Ababneh et al. (2017) that contained transverse reinforcement are significantly overpredicted (with predicted shear strength above $5\,MPa$). It should be noted that those specimens contained a very high transverse reinforcement ratio ($\rho_y > 1.5\%$) that exceeded the ACI 318 (2019) maximum transverse reinforcement limits for beams.

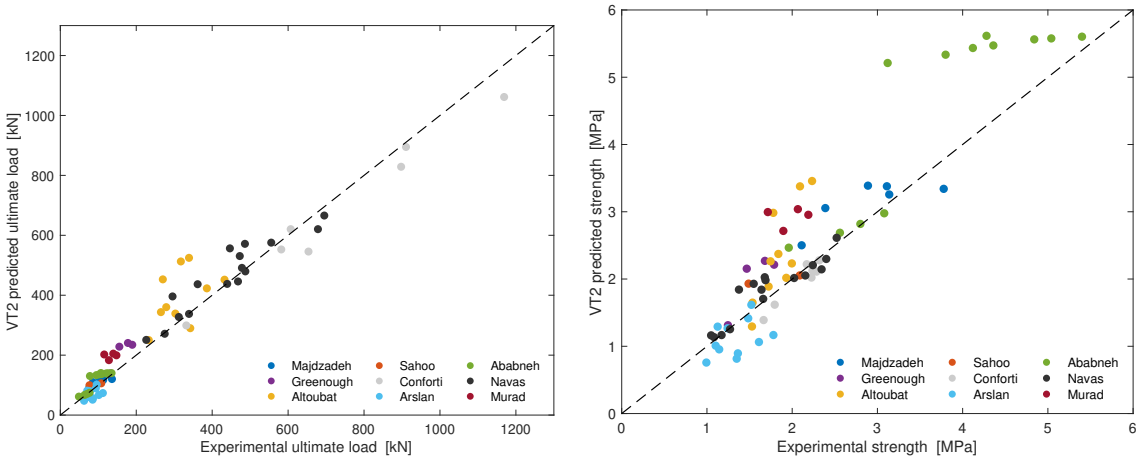

(a) (b)

Figure 5.7: Predicted against experimental strength for the beam database (a) Ultimate load (b) Ultimate shear stress

Figure 5.8 shows the predicted-to-experimental strength ratio as a function of fiber volume V_f and span-to-depth ratio a/d. With respect to the fiber volume, the strength prediction accuracy appeared to improve with greater fiber volume. Notably, the fiber volume was the only fiber parameter considered in the VT2 modeling. Parameters such as the fiber material type, fiber length, fiber aspect ratio and fiber tensile strength were not considered for the VT2 analysis. Despite this, the modeling approach demonstrated a capability to provide adequate results for the PFRC beams summarized in Table 5.5, with predicted-to-experimental ratio ranging between 0.6 (due to a low $f'_c = 14\,MPa$) and 1.75 (due to a low $a/d = 1.7$).

With respect to the span-to-depth ratio, the modeling approach tended to provide higher average predicted-to-experimental strength ratio for lower span-to-depth ratios ($a/d \leq 3.0$) than for greater span-to-depth ratios ($a/d > 3.0$) with computed average ratios of 1.17 (COV = 23.5%) and 1.06 (COV = 18.0%), respectively. At lower span-to-depth ratios the failure mechanism is more complex, involving bond and compression struts.

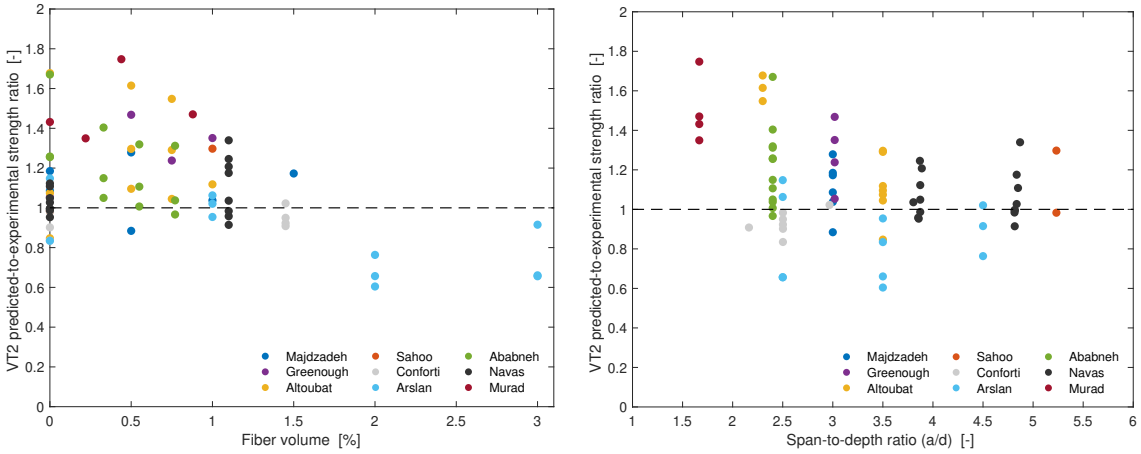

(a) (b)

Figure 5.8: Predicted-to-experimental strength ratio versus (a) Fiber volume V_f (b) Span-to-depth ratio (a/d)

Overall, the modeling approach was able to capture the strength of PFRC beams from the literature, which were not part of the calibrated dataset. The approach was not as accurate for beams with low span-to-depth ratio ($a/d < 2.5$) compared to beams with greater span-to-depth ratio ($a/d \geq 2.5$). The fiber volume was not observed to influence the predictions significantly.

The validation of the approach in this way gave confidence that numerical results could be used to further explore the parameter space.

Chapter 6
PARAMETRIC STUDY

In this chapter, a parametric study was conducted on PFRC panel specimens subjected to pure shear. The VecTor2 modeling approach outlined in Chapter 4.3.6 was utilized to predict the panel responses. Apparent from the literature review in Chapter 2, there is limited experimental data available for PFRC members with stirrups. The parametric study conducted herein simulates the behavior of PFRC panels and produced a numerical database that could be used to evaluate the current empirical and design code models, that is discussed in Chapter 7.

The study specifically involved varying three parameters to explore their influence on the mechanical behavior of PFRC panels under pure shear loading. The parameters investigated were the concrete compressive strength, f'_c, transverse reinforcement ratio, ρ_y, and fiber volume, V_f. Other important parameters that were not addressed included span-to-depth ratio a/d, effective depth d and loading type.

6.1 Outline of the Parametric Study

Table 6.1 summarizes the values of the investigated parameters (the compressive strength f'_c, transverse reinforcement ratio ρ_y, and fiber volume V_f). Exploring a range of combinations of ρ_y and V_f provides a better understanding about the interaction between them. Furthermore, the compressive strength of the concrete could potentially influence the interaction, since it impacts the tensile and crushing strength of the panels.

The parametric study will thus encompass a three-dimensional space defined by the values in Table 6.1. The values covered a reasonable range for the parameters, that can be used in practice. For instance, a transverse reinforcement ratio $\rho_y > 1.5\%$ is not common and a fiber volume $V_f > 2.0\%$ can result in consolidation problems (see Sahoo et al., 2015). The range for the compressive strength was chosen to cover the lowest strength used in practice of $20\,MPa$ (Tomosawa and Noguchi, 1993) up to a high strength of $95\,MPa$ (Vidya et al., 2017).

Table 6.1: Parameters of interest in the parametric study

Parameter	**Values**
f'_c [MPa]	20, 45, 70, 95
ρ_y [%]	0, 0.1, 0.25, 0.5, 0.75, 1.0, 1.25, 1.5
V_f [%]	0, 0.25, 0.5, 0.75, 1.0, 1.25, 1.5, 1.75, 2.0

The parameters of interest outlined in Table 6.1 generated a total number of 288 unique combinations. Each of these combinations was modeled in VecTor2 as a single element panel model, corresponding to Figure 4.3. For each model, the shear stress and shear strain were extracted to be analyzed and compared to the other parametric models.

The reinforcement was modeled as smeared reinforcement in the x and y directions with the properties in Table 6.2. The concrete material was defined with a thickness of $70\,mm$, while all other parameters were assigned the default VT2 value, estimated based on f'_c.

However, the crack spacing required a user defined input, but was not found to influence the shear stress-strain response (see Appendix C). This was evident by varying the transverse reinforcement ratio and the fiber volume from 0% to 2.0% for concrete compressive strengths of $45\,MPa$ and $70\,MPa$. The ultimate shear resistance remained unaffected and the overall shear stress-strain response was not significantly influenced. In order to stay consistent with the modeling of the panels tested by Gaston (2023) (see Chapter 4), a fixed maximum crack spacing of $70\,mm$ was specified (in x and y direction) for the models of the parametric study.

Table 6.2: Reinforcement properties for parametric study

Parameter	**Value**
ρ_x	2.5%
d_b	10 mm
F_y	420 MPa
F_u	520 MPa
E_s	200,000 MPa
ϵ_{sh}	$10 \cdot 10^{-3}$
ϵ_u	$150 \cdot 10^{-3}$

6.2 Parametric Study Results

The shear stress-strain responses from all models in the parametric study and corresponding analysis are shown in Appendix C. The analyses focused on strength and deformation capacity and only a representative subset of the data is shown here.

Figure 6.1 shows the shear stress-strain response for panels with $f'_c = 45\,MPa$ and two different transverse reinforcement ratios of $\rho_y = 0.1\%$ and $\rho_y = 1.0\%$. The macro-synthetic fibers demonstrate abilities to enhance the ultimate shear strength for both transverse reinforcement ratios showed in Figure 6.1. A fiber volume of $V_f = 2.0\%$ results in 69% increase in shear strength compared to $V_f = 0\%$ for a transverse reinforcement of $\rho_y = 0.1\%$. However, a 27% enhancement in shear strength was observed for a transverse reinforcement of $\rho_y = 1.0\%$, for the same fiber volumes. Therefore, the fibers appear to demonstrate greater effectiveness at lower transverse reinforcement values.

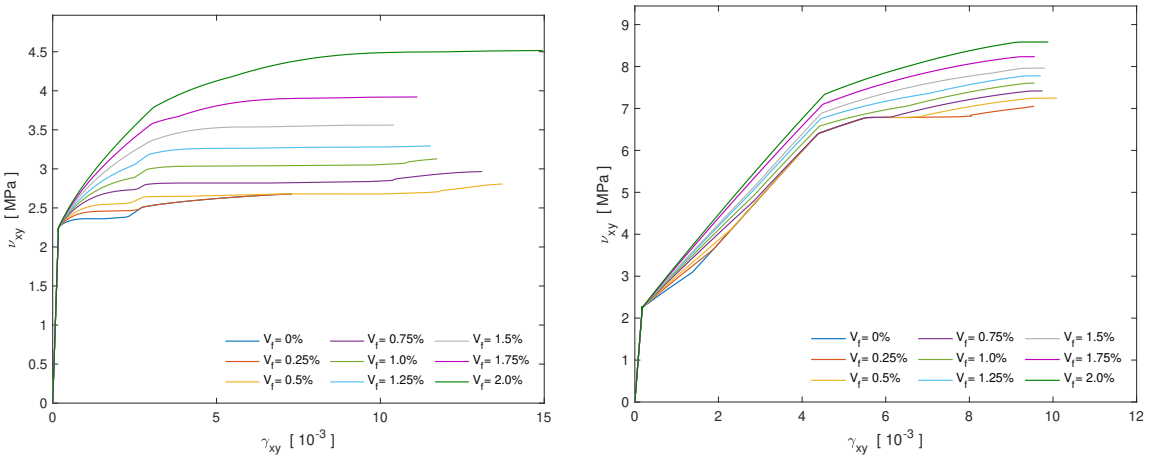

(a) (b)

Figure 6.1: Shear stress-strain response for $f'_c = 45\,MPa$ and (a) $\rho_y = 0.1\%$ (b) $\rho_y = 1.0\%$

Figure 6.2 shows the shear strength v_{max} and ultimate shear strain γ_u against transverse reinforcement ratio ρ_y for the panels with $f'_c = 45\,MPa$. The shear strength increased with transverse reinforcement ratio ρ_y. Conversely, the shear strain at failure, γ_u, initially increased with transverse reinforcement ratio, reaching a peak at a reinforcement ratio of 0.1% or 0.25%. The ultimate shear strain was not sensitive to fiber volume for panels with reinforcement ratios $\rho_y \geq 0.75\%$ and converged to a value of $\gamma_u = 8 \cdot 10^{-3}$ at a transverse

reinforcement ratio of $\rho_y = 1.5\%$, except for the RC panel ($V_f = 0\%$). This trend was observed for all concrete strengths investigated.

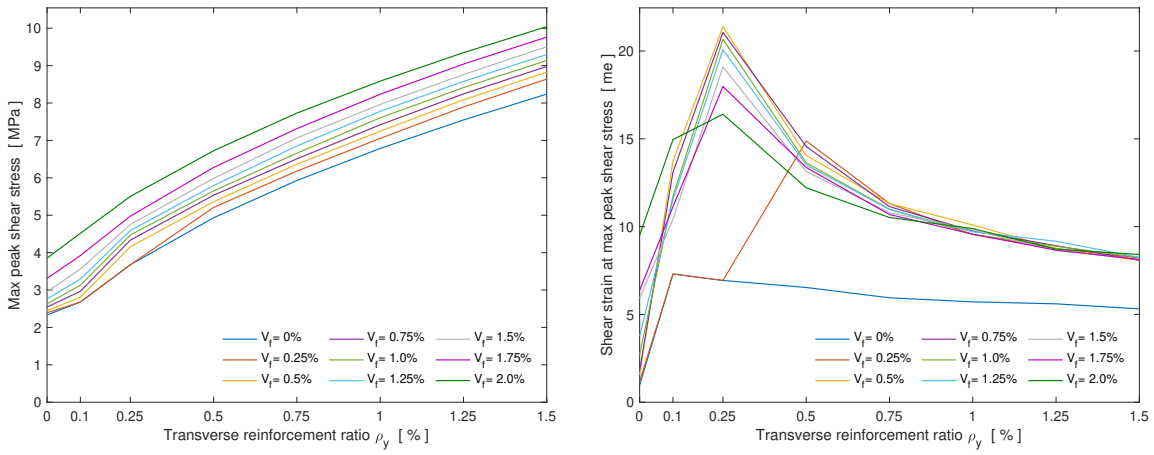

(a) (b)

Figure 6.2: Effects of ρ_y (for $f'_c = 45\,MPa$) on (a) Shear strength v_{max} (b) Ultimate shear strain γ_u

Figure 6.3 shows the shear strength enhancement due to macro-synthetic fibers versus fiber volume (up to $V_f = 2.0\%$) for the transverse reinforcement ratios and concrete strength investigated. The strength improvement was found to be more effective for panels with higher concrete strength of $f'_c \geq 70\,MPa$ compared to the lower concrete strengths of $f'_c \leq 45\,MPa$. The effectiveness generally decreased with a greater amount of transverse reinforcement, regardless of concrete strength.

In the $20\,MPa$ series, the most significant strength enhancement was observed for panels without transverse reinforcement (resulting in strength enhancement up to 60% compared to the RC panels). Conversely, the strength advancement was less pronounced for highly reinforced panels ($\rho_y > 1.0\%$), where a strength improvement of less than 10% was observed with the inclusion of fibers. Additionally, the deformation capacity of these panels remained largely unaffected.

For panels with a concrete strength of $f'_c \geq 70\,MPa$, the fibers were found to be the least effective for panels without transverse reinforcement and low fiber contents up to $V_f = 1.0\%$. The strength enhancement provided by the fibers was less than 10% for those

panels. Notably, the fibers (at $V_f = 2.0\%$) were able to provide a strength improvement of about 70% and 80% for concrete strengths of $f'_c \leq 45\,MPa$ and $f'_c \geq 70\,MPa$, respectively. This strength improvement was dependent on the transverse reinforcement ratio.

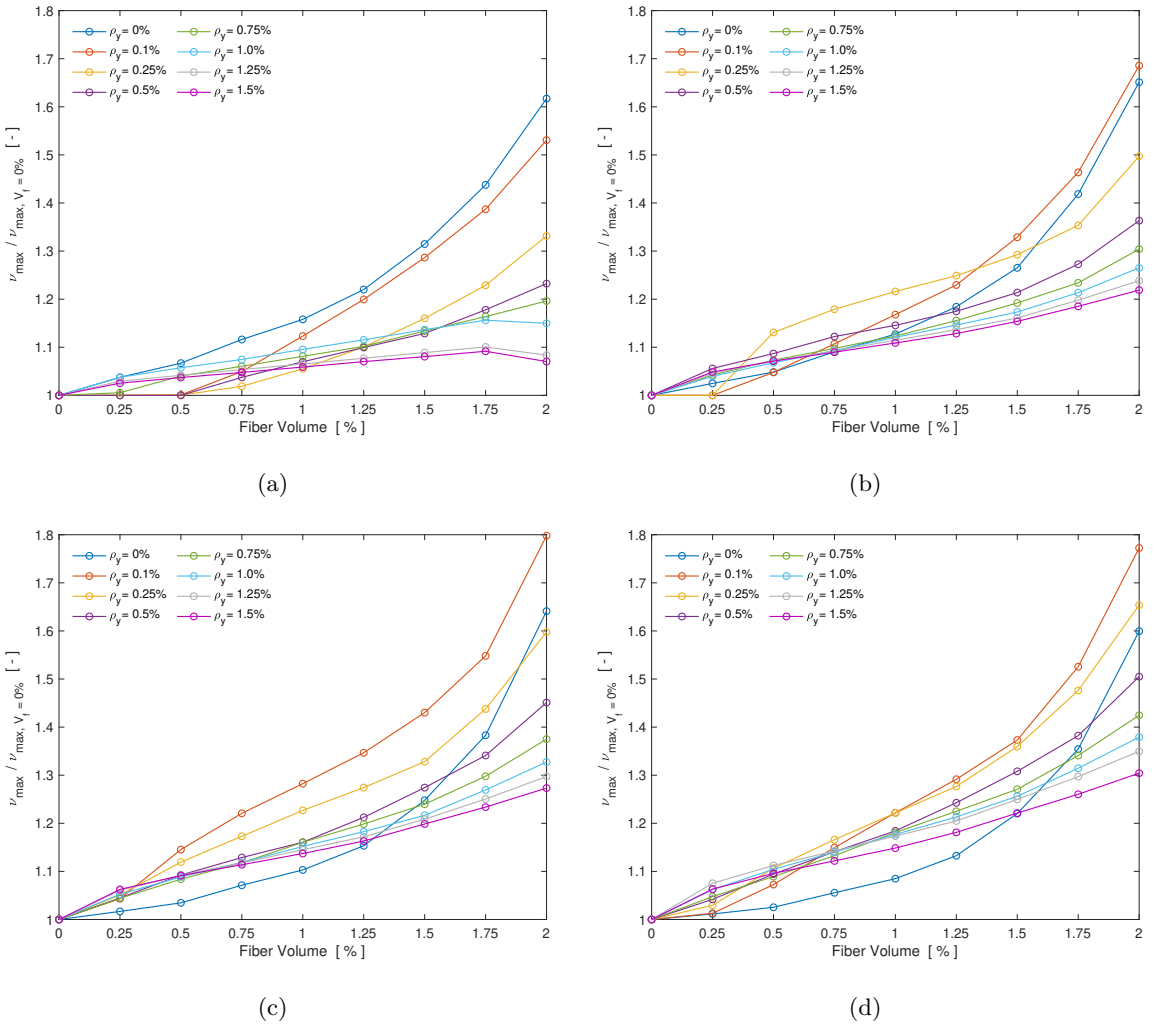

Figure 6.3: Fiber strength enhancement (a) $f'_c = 20\,MPa$ (b) $f'_c = 45\,MPa$ (c) $f'_c = 70\,MPa$ (d) $f'_c = 95\,MPa$

Figure 6.4 shows the ultimate shear stress as contours as a function of both the transverse reinforcement ratio ρ_y and the fiber volume V_f for each of the four concrete compressive strengths. The contour lines represent the ultimate shear strength of the panels, demonstrating the various combinations of ρ_y and V_f that could be used to achieve a specific shear strength. For example, given a concrete strength of $f'_c = 70\,MPa$, a shear strength of

6 MPa could be achieved with $\rho_y = 0.75\%$ and $V_f = 0\%$ or with $\rho_y = 0.25\%$ and $V_f = 2.0\%$. This can result in a significant reduction of transverse steel reinforcement in design.

The lines are considerably steeper for concrete compressive strengths of $f'_c \geq 70\,MPa$ compared to $f'_c \leq 45\,MPa$, demonstrating that the synergistic effects of the transverse reinforcement and fiber volume appear to be more pronounced for higher concrete strengths.

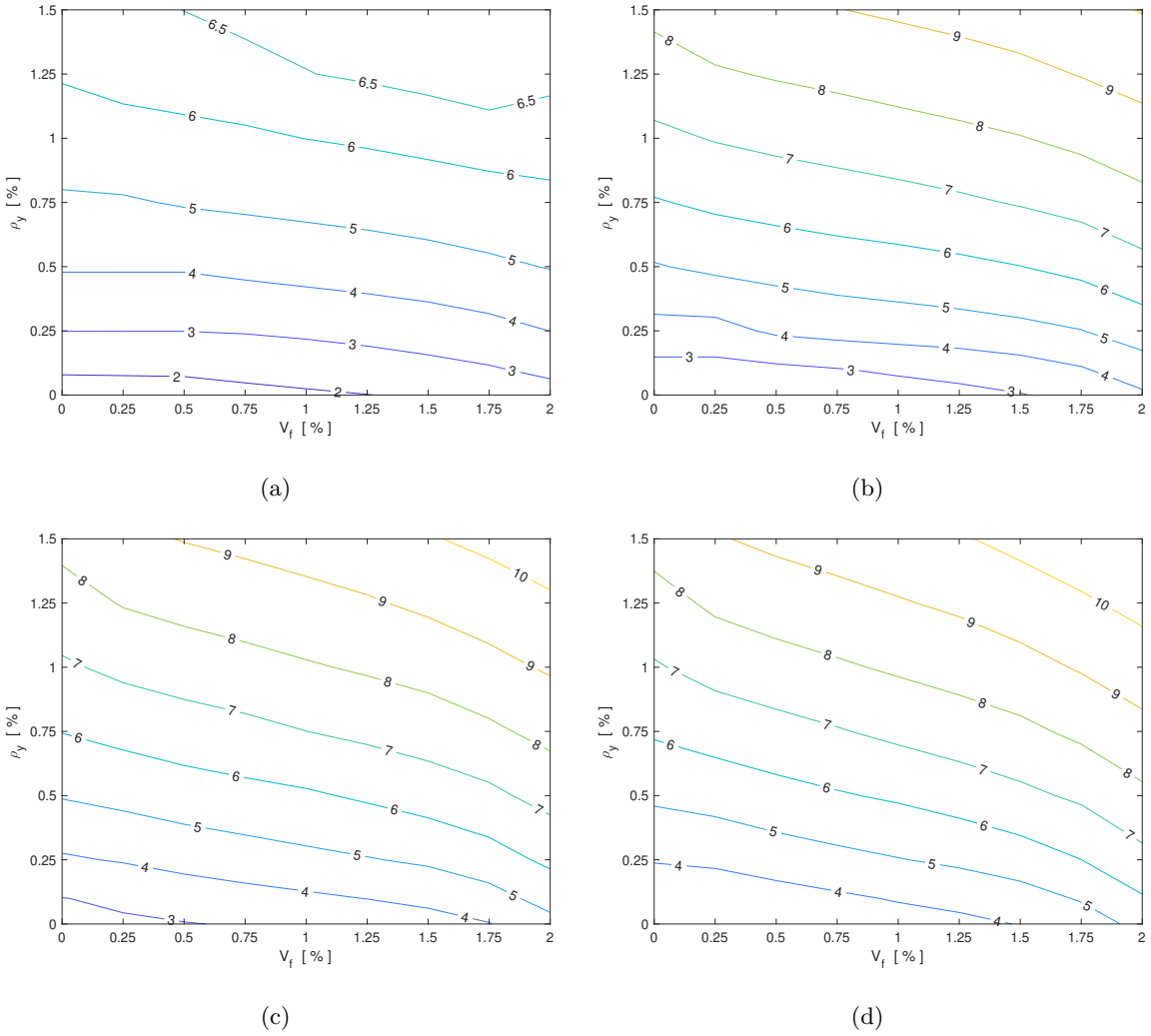

Figure 6.4: Ultimate shear strengths of the parametric panels (a) $f'_c = 20\,MPa$ (b) $f'_c = 45\,MPa$ (c) $f'_c = 70\,MPa$ (d) $f'_c = 95\,MPa$

Figure 6.5 shows the observed failure mode of the parametric study. The addition of fibers did not significantly effect the deformation capacity of the panels, however the addition of fibers demonstrated an ability to shift the failure mode. The mode of failure

was determined to be first failure mode that occurred for the panels, according to the following four failure modes (i) - (iv):

(i) **Crushing failure with transverse yielding**, satisfying:

$$\frac{f_{c2}}{f_{c2,\,max}} > 1.0 \quad \text{and} \quad \epsilon_y \geq \epsilon_{yield} = \frac{F_y}{E_s}$$

where (by the Vecchio 1992-A model):

$$\frac{f_{c2,\,max}}{f'_c} = \frac{1}{1 + 0.35(r - 0.28)^{0.80}} \quad \text{and} \quad r = \frac{-\epsilon_{c1}}{\epsilon_{c2}} \leq 400.$$

(ii) **Crushing failure without transverse yielding**, satisfying:

$$\frac{f_{c2}}{f_{c2,\,max}} > 1.0 \quad \text{and} \quad \epsilon_y < \epsilon_{yield}.$$

(iii) **Biaxial yielding failure**, satisfying:

$$\epsilon_x \geq \epsilon_{yield} \quad \text{and} \quad \epsilon_y \geq \epsilon_{yield}.$$

(iv) **Aggregate interlock**, in instances where the first three failure modes listed above did not appear, the failure mode was determined to be aggregate interlock.

where ϵ_x is the strain in the longitudinal reinforcement and ϵ_y is the strain in the transverse (shear) reinforcement.

The observed failure modes were found to be influenced by the concrete compressive strength, as illustrated in Figure 6.5. For panels with a concrete strength of $20\,MPa$, the fibers were able to shift the failure mode from aggregate interlock to crushing failure for the panels without transverse reinforcement, by providing a fiber volume of $V_f \geq 1.0\%$. Furthermore, for a transverse reinforcement of $\rho_y = 0.75\%$, the fibers induced yielding of transverse reinforcement with a fiber volume $V_f \geq 1.25\%$. Panels employing a transverse reinforcement $\rho_y \geq 1.0\%$ exhibited consistent crushing failure with yielding of the transverse reinforcement.

For panels with a concrete compressive strength of $f'_c = 45\,MPa$ and transverse reinforcement $\rho_y \geq 1.25\%$, biaxial yielding failure was observed. Unlike for the crushing failure modes for the $f'_c = 20\,MPa$ panels, the fibers were not capable of shifting the failure mode from crushing to biaxial yielding at $\rho_y = 1.0\%$. However, the fibers were able to shift

the failure mode from aggregate interlock to crushing for the panels without transverse reinforcement, with a fiber volume of $V_f \geq 1.0\%$.

The observed failure mode for panels with $f'_c = 70\,MPa$ and $f'_c = 95\,MPa$ was biaxial yielding for $\rho_y \geq 0.1\%$. However, the fibers were able to shift the failure mode from aggregate interlock to $x-$reinforcement yielding for the panels without transverse reinforcement with a fiber volume of $V_f \geq 1.0\%$.

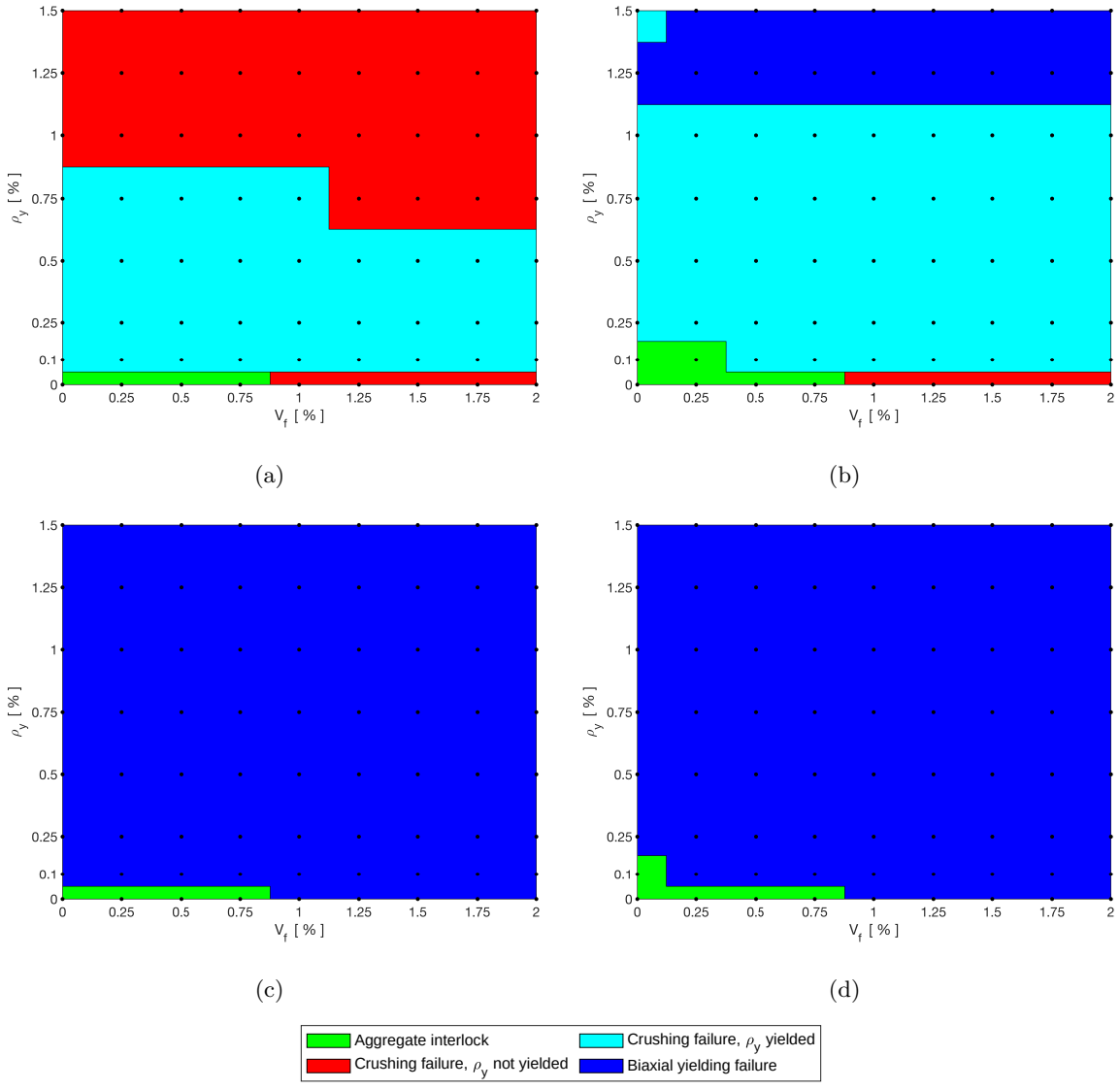

Figure 6.5: Failure modes of the parametric panels (a) $f'_c = 20\,MPa$ (b) $f'_c = 45\,MPa$ (c) $f'_c = 70\,MPa$ (d) $f'_c = 95\,MPa$

Figure 6.6 shows the crack widths at a shear stress of $0.4\sqrt{f'_c}$. The panels that did not reach this shear stress are not included, explaining the absence of few data points in Figure 6.6 (those panels had transverse reinforcement ratio $\rho_y \leq 0.25\%$ and fiber volumes $V_f \leq 1.0\%$). Since the model consisted of a single element, a single crack width was reported at every load stage in VecTor2.

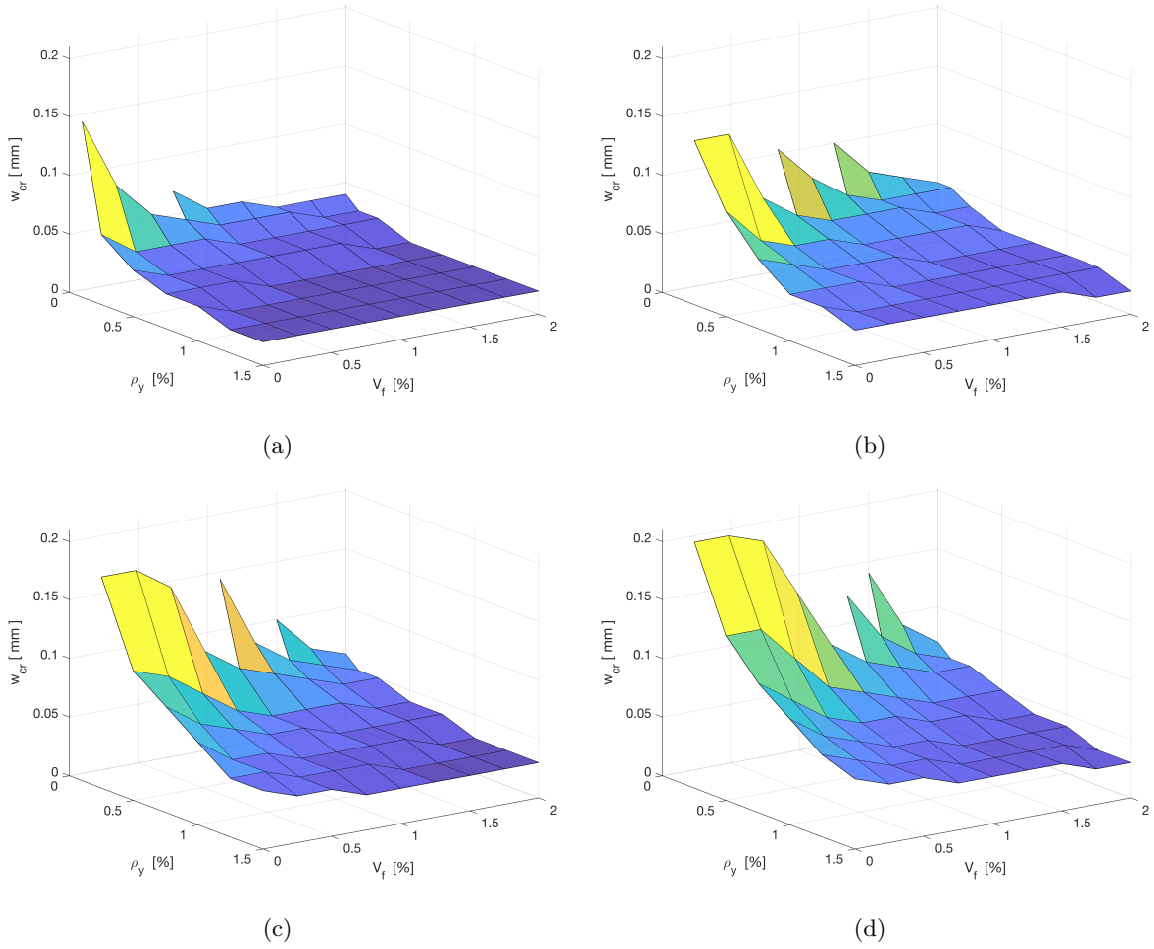

Figure 6.6: Crack widths of the parametric panels at $v_{xy} = 0.4\sqrt{f'_c}$ (a) $f'_c = 20\,MPa$ (b) $f'_c = 45\,MPa$ (c) $f'_c = 70\,MPa$ (d) $f'_c = 95\,MPa$

Figure 6.6 illustrates that both transverse reinforcement and fibers were effective in reducing the crack width. However, the effectiveness of the fibers in limiting the crack width was less pronounced at a high transverse reinforcement of $\rho_y > 0.75\%$, where the transverse reinforcement appeared to control the crack width. For panels with $f'_c \geq 70\,MPa$, the fibers

demonstrated greater effectiveness compared to panels with $f'_c \leq 45\,MPa$ in reducing the crack width. For panels with $f'_c = 45\,MPa$ and $\rho_y = 0.25\%$, the fibers reduced the crack width of the RC panel of $0.21\,mm$ to $0.06\,mm$ for a PFRC panel with $V_f = 2.0\%$, resulting in 70% crack width reduction.

6.3 Summary of the Parametric Study

The parametric study conducted in this chapter investigated the combined use of macro-synthetic fibers and transverse steel reinforcement, with four concrete strengths. The results demonstrated the interaction between macro-synthetic fibers and transverse reinforcement, where different trends were identified for the concrete strengths investigated.

- The enhancements of fibers were more pronounced at lower ρ_y ratios, in terms of strength, deformation capacity and crack widths. However, the strength improvements for the panels with a concrete strength of $f'_c = 20\,MPa$ were significantly less compared to the other concrete strengths (in terms of %-improvement from panels without fibers and equal transverse reinforcement ratios).

- For panels with concrete strengths of $f'_c \geq 45\,MPa$ and a transverse reinforcement ratio of $\rho_y = 0.25\%$, adding a fiber volume of $V_f \geq 1.0\%$ resulted in at least 20% shear strength improvement, achieving up to 65% shear strength improvement for $V_f = 2.0\%$. This is consistent with studies by Arslan et al. (2017); Navas et al. (2018).

- The fibers were effective in decreasing the crack width at a fixed shear stress of $0.4\sqrt{f'_c}$ for all of the concrete compressive strengths investigated. The ability of the fibers to reduce the crack widths were significantly more pronounced at lower transverse reinforcement ratios. Given a reinforcement ratio greater than 0.5%, the fibers did not show any significant benefits in crack width reduction for panels with $f'_c \leq 45\,MPa$. These benefits were more prominent for panels with $f'_c \geq 70\,MPa$.

Chapter 7

COMPARISON TO EMPIRICAL EQUATIONS

This chapter evaluates the effectiveness of the empirical strength predicting equations and design code provisions presented in Chapter 2 against the experimental PFRC panel results presented in Chapter 3, the experimental PFRC beam tests summarized in Chapter 5 and the results of the numerical parametric study for PFRC panels presented in Chapter 6. The strength predicting equations presented in Chapter 2 are summarized in Tables 7.1 and 7.2.

It should be noted that some of the strength models presented in Chapter 2 were developed for structural members without transverse reinforcement. For those models, the shear strength contribution from the transverse steel reinforcement (in terms of stress) was computed as

$$v_s = \rho_y \cdot F_y.$$

It should also be noted that many of the expressions were developed for beams and included a span-to-depth (a/d) ratio term. For the panel elements evaluated, this term was taken as 1.0.

Table 7.1: Empirical shear strength equations for FRC

Author	**FRC shear strength [MPa]**
Narayanan and Darwish (1987)	$v_u = e\left[0.24 f_{spfc} + 80\rho_x \frac{d}{a}\right] + 0.41\,\tau\,F$ $F = \frac{l_f}{d_f} \cdot V_f \cdot b_f$
Ashour et al. (1992)	$v_u = \left(0.7\sqrt{f'_c} + 7F\right)\frac{d}{a} + 17.2\rho_x \frac{d}{a}$
Swamy et al. (1993)	$v_u = 0.9\sigma_{cu} + v_c = 0.9 \cdot 0.41\tau \cdot \frac{l_f}{d_f} \cdot V_f + v_c$
Kwak et al. (2002)	$v_u = 3.7 \cdot e \cdot f_{spfc}^{2/3}\left(\rho_x \frac{d}{a}\right)^{1/3} + 0.8 \cdot v_b$
Arslan et al. (2017)	$v_u = \left(0.2 f_c'^{2/3}\left(\frac{c}{d}\right) + PSR \cdot \sqrt{\rho(1+4F) f'_c}\right)\left(\frac{3}{a/d}\right)^{1/3}$
Ababneh et al. (2017)	$v_u = 1.7(1 + 0.75V_f)\left(0.16\lambda\sqrt{f'c} + 17.2\rho\frac{V_u d}{M_u}\right)$

Table 7.2: Model code equations for the shear strength of FRC

Model Code	**FRC shear strength [MPa]**
fib Model Code (2010)	$v_u = \frac{0.18}{\gamma_c} k \left[100\rho_x \left(1 + 7.5\frac{f_{Ftuk}}{f_{ctk}}\right) f'_c\right]^{1/3}$
ACI 318 (2019)	$v_u = 0.66\lambda_s\lambda\left(\rho_w\right)^{1/3}\sqrt{f'_c}$
AASHTO (2012)	$v_u = 0.083\beta \cdot \sqrt{f'_c}$
CSA A23.3 (2019)	$v_u = \beta\sqrt{f'_c}$

7.1 Comparison to Panel Element Experimental Program

This section compares the empirical strength equations and design code provisions from Chapter 2, summarized in Tables 7.1 and 7.2, to the results of the experimental program conducted by Gaston (2023), summarized in Chapter 3. The panel specimens affected by consolidation issues (marked with *) were not included in the analysis herein, since those specimens did not reach their ultimate strength.

The panel modeling in Chapter 4 revealed that transverse reinforcement bars adjacent to the anchor blocks around the perimeter of the panel for the heavily reinforced panels ($\rho_y = 1.14\%$) appeared to not contribute to the shear strength of the panels because of how close they were to the highly disturbed edge region (see Figure 3.1d). Therefore, an effective transverse reinforcement $\rho_{y,eff} = 0.91\%$ was employed for the heavily reinforced panels in the equations (instead of $\rho_y = 1.14\%$ reported in the experimental program).

Table 7.3 reports the predicted-to-experimental strength ratios for all specimens tested in the experimental program. Table 7.4 provides statistical analysis of the results in Table 7.3, reporting the average, standard deviation and coefficient of variation, in addition to maximum and minimum ratios for each of empirical and design code equations.

Table 7.3: Predicted-to-experimental strength ratios for empirical and design code equations

Specimen	**Narayanan**	**Ashour**	**Swamy**	**Kwak**	**Arslan**	**Ababneh**	**fib**	**ACI**	**AASHTO**	**CSA**
PFRC-000-000	1.24	2.39	0.39	1.10	0.98	1.17	0.58	0.39	0.60	0.52
PFRC-000-029	0.94	1.45	0.62	0.85	0.80	0.89	0.89	0.62	0.89	0.77
PFRC-000-058	1.00	1.34	0.74	0.91	0.88	0.95	1.02	0.74	1.03	0.88
PFRC-000-114	0.93	1.23	0.75	0.89	0.86	0.91	0.93	0.75	0.97	0.81
PFRC-026-000	1.92	3.74	0.68	1.64	1.45	1.60	1.15	0.51	0.80	0.70
PFRC-026-029	0.99	1.63	0.67	0.91	0.84	0.89	0.99	0.61	0.88	0.76
PFRC-026-058*	1.34	1.95	1.02	1.25	1.19	1.23	1.43	0.96	1.32	1.13
PFRC-026-114	1.01	1.41	0.83	0.98	0.93	0.96	1.04	0.79	1.03	0.86
PFRC-052-000	1.87	3.88	0.77	1.58	1.38	1.43	1.18	0.45	0.71	0.62
PFRC-052-029	0.90	1.64	0.65	0.86	0.79	0.80	0.91	0.55	0.78	0.67
PFRC-052-058*	1.19	1.85	0.92	1.12	1.06	1.07	1.27	0.83	1.13	0.97
PFRC-052-114	1.01	1.46	0.84	0.97	0.93	0.93	1.05	0.77	1.01	0.85

Table 7.4: Summary of the predicted-to-experimental strength ratios in Table 7.3

Model	**Average [-]**	**StD [-]**	**COV [%]**	**Max [-]**	**Min [-]**
Narayanan	1.18	0.39	32.9	1.92	0.90
Ashour	2.02	1.00	49.4	3.88	1.23
Swamy	0.69	0.13	18.7	0.84	0.39
Kwak	1.07	0.30	27.7	1.64	0.85
Arslan	0.99	0.23	23.8	1.45	0.79
Ababneh	1.05	0.26	25.0	1.60	0.80
fib	0.97	0.17	17.1	1.18	0.58
ACI	0.62	0.14	23.3	0.79	0.39
AASHTO	0.87	0.15	16.7	1.03	0.60
CSA	0.74	0.12	15.5	0.88	0.52

Table 7.3 shows that, among the empirical models considered, Equation (2.11) by Arslan et al. (2017) provided the most accurate strength predictions, with average of 0.99 and COV of 23.8%. Equations (2.13) by Ababneh et al. (2017) and (2.8) by Kwak et al. (2002) also provided reasonably accurate average strength predictions, although somewhat on the

unconservative side. The COV for those equations was 26% and 30%, respectively. Other empirical strength equations did not exhibit a high degree of accuracy with mean predicted-to-experimental ratios above 1.1 or below 0.7.

Table 7.3 also shows that the design codes considered provided, on average, conservative strength estimates. Among those, the fib Model Code (2010) provided the most accurate shear strength predictions with overall predicted-to-experimental strength ratio of 0.97 and COV = 17.1%.

Figure 7.1 shows the predicted shear strengths against the experimental strengths for the empirical models (left) and the design codes (right). The design code predictions tend to provide more conservative predictions than the empirical equations from the literature. However, both the empirical equations and the design code models appear to provide reasonable estimates overall for the ultimate shear strength of the panel specimens examined, where the equations by fib Model Code (2010) and Arslan et al. (2017) provided the most accurate predictions. Note that the predictions by Ashour et al. (1992) were not included in Figure 7.1 and other figures below, because of the low dependability displayed.

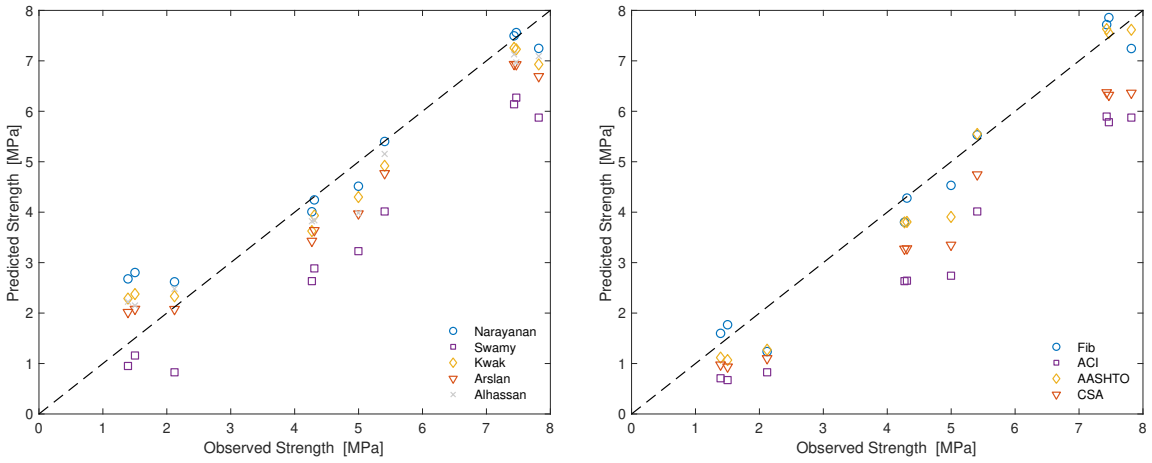

(a) (b)

Figure 7.1: Predicted versus experimental strength for the experimental program (a) Empirical equations (b) Design code equations

Figure 7.2 shows the predicted-to-experimental strength ratio against fiber volume and transverse reinforcement ratio. Both the empirical equations and the design codes provided

conservative results for the RC panels. However, except for Equation (2.6) by Swamy et al. (1993), the empirical equations significantly overestimated the strength of two of the FRC panels (PFRC-026-000 and PFRC-052-000). This was attributed to a significant overestimation of the fiber contribution to the shear strength, which was reasonable, given that most of the empirical strength equations were developed for steel fibers (as e.g., Kwak et al. 2002; Narayanan and Darwish 1987). However, the design codes provided conservative strength predictions at all fiber volume levels.

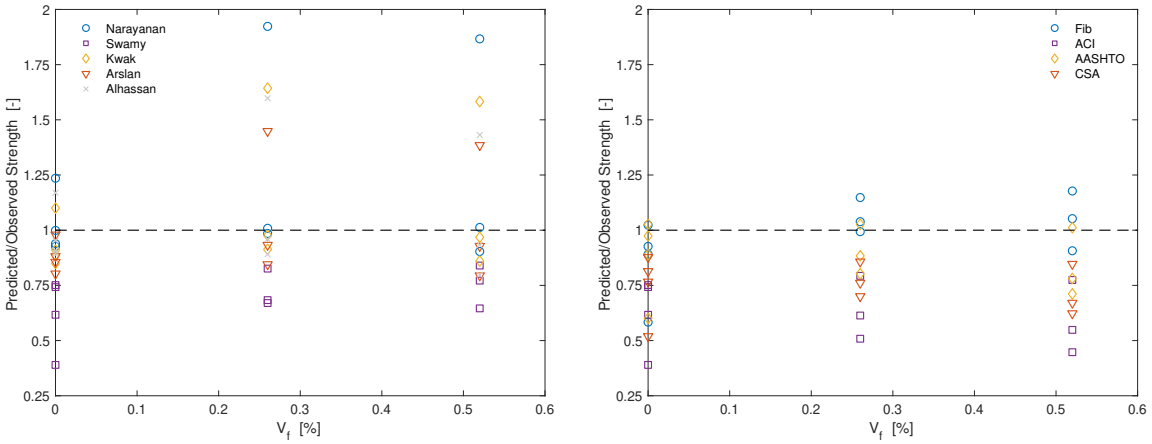

(a) (b)

Figure 7.2: Predicted-to-experimental strength ratio versus fiber volume for the experimental program (a) Empirical equations (b) Design code equations

Figure 7.3 shows the predicted-to-experimental ratio as a function of transverse reinforcement ratio. Panel specimens without transverse reinforcement ratio ($\rho_y = 0\%$) and the highly reinforced panels ($\rho_y = 0.91\%$) were accurately predicted, in terms of strength, by the empirical equations. The predictions were more scattered for specimens containing intermediate reinforcement ratios (ρ_y of 0.29% and 0.58%). The overpredicted specimens in Figures 7.2 and 7.3 indicate that specimens that contained $V_f \geq 0.26\%$ and ρ_y between $0.29 - 0.58\%$ are significantly overpredicted by the empirical models. However, the design code models provided conservative estimates of the shear strength, where the fiber volume V_f nor the transverse reinforcement ratio ρ_y affected the results significantly.

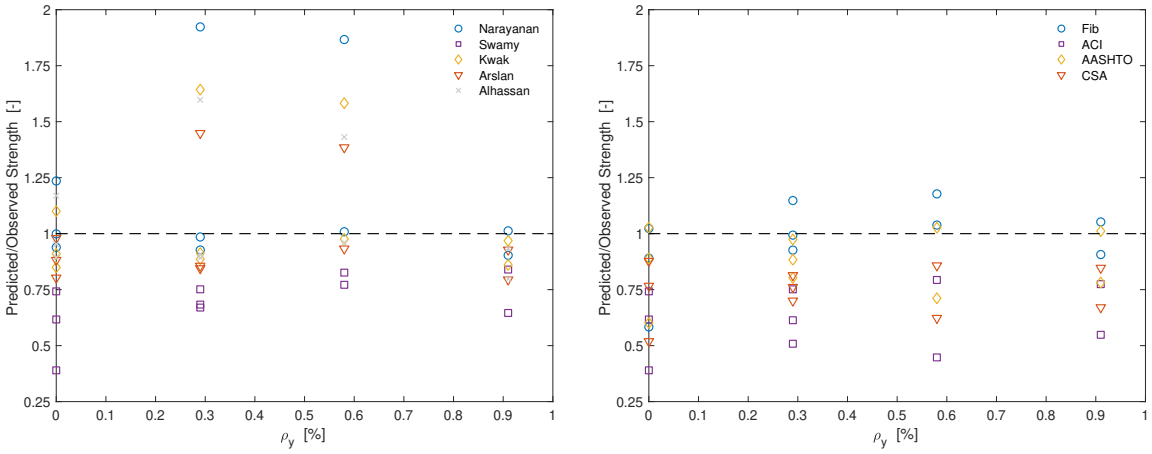

(a) (b)

Figure 7.3: Predicted-to-experimental strength ratio versus transverse reinforcement ratio for the experimental program (a) Empirical equations (b) Design code equations

7.2 Comparison to Beam Experiments from the Literature

The predicted shear strengths by the empirical equations and the model code equations were compared to the experimental beam strengths summarized in Chapter 5.

The models provided a reasonable estimate for most of the beam specimens. However, all empirical equations and design code models significantly overpredicted the beams tested by Ababneh et al. (2017) that contained transverse reinforcement. The predicted-to-experimental ratio was in the range of $2-4$ for those beam specimens. This unconservative predicted strength was attributed to the high transverse reinforcement ratio utilized in for those beams of $\rho_y > 1.7\%$. This ratio exceeds the maximum transverse reinforcement ratio permitted by ACI 318 (2019) for a non-prestressed beam with $f'_c = 45\,MPa$ and $F_y = 420\,MPa$ (corresponding to the beams) of

$$\rho_{y,\,max} \leq \frac{0.66\sqrt{f'_c}}{F_y} = \frac{0.66\sqrt{45}}{420} = 1.06\%.$$

Those beam specimens by Ababneh et al. (2017) that contained transverse reinforcement influenced the overall results significantly, since the steel contribution was computed without an upper limit as $v_s = \rho_y F_y$. Including those specimens resulted in overall COV of 60% for the average predicted-to-experimental strength ratio. In order to obtain a reasonable

comparison of the overall results, the experimental program by Ababneh et al. (2017) was not included in the analysis herein.

Table 7.5 provides a summary of the predicted-to-experimental strength ratios for the empirical equations and the design code models. Equation (2.2) by Narayanan and Darwish (1987) provides the most accurate strength estimates with average predicted-to-experimental strength ratio of 1.01 (COV = 20.4%). Equation (2.11) by Arslan et al. (2017) also provided accurate predictions with average of 1.02 (COV = 21.5%). Except for Equation (2.6) by Swamy et al. (1993), all empirical equations provided unconservative estimates of the shear strength in terms of average predicted-to-experimental strength ratio.

Table 7.5: Summary of the predicted-to-experimental strength ratios for the beam database (excluding beams by Ababneh et al. (2017))

Model	**Average [-]**	**StD [-]**	**COV [%]**	**Max [-]**	**Min [-]**
Narayanan	1.01	0.21	20.4	1.70	0.60
Ashour	1.16	0.30	25.4	2.00	0.72
Swamy	0.91	0.26	28.9	2.04	0.48
Kwak	1.17	0.26	22.3	2.11	0.81
Arslan	1.02	0.22	21.5	1.50	0.61
Alhassan	1.11	0.26	23.1	1.77	0.66
fib	1.25	0.29	23.2	2.11	0.68
ACI	0.64	0.18	28.2	1.08	0.33
AASHTO	1.07	0.26	24.5	1.66	0.62
CSA	0.92	0.23	24.8	1.42	0.52

The fib Model Code (2010) provided unconservative shear strength estimates with average predicted-to-experimental strength ratio of 1.25 (COV = 23.2%), which is recorded the highest average among the models. The AASHTO (2012) and CSA A23.3 (2019) approaches provided the most accurate results for the code provisions with predicted-to-experimental strength ratio of 1.07 (COV = 24.5%) and 0.92 (COV = 24.8%), respectively. However, the ACI 318 (2019) approach resulted in the most conservative predictions, with overall predicted-to-experimental strength ratio of 0.64 (COV = 28.2%).

Figure 7.4 shows the predicted strength by Narayanan (Narayanan and Darwish, 1987) and AASHTO (AASHTO, 2012) against the experimental beam strengths.Those two models are shown for reference and the other approaches can be found in Appendix D.

Overall, the experimental programs exhibit accurate predictions for these two approaches in Figure 7.4. The experimental program by Conforti et al. (2015) is conservative of about 30% by the Narayanan approach. One possible explanation is that the beam specimens tested by Conforti et al. (2015) were wide-shallow beams (with b/d of 2.0 and 3.0 and exhibited enhanced shear behavior compared to deeper beams), different to the database used to calibrate the approach by Narayanan and Darwish (1987). The AASHTO (2012) approach overpredicted the experimental program by Navas et al. (2018) by 30% on average, where specimens without fibers were significantly overpredicted (50% on average) while beams that contained fibers resulted in more accurate predictions.

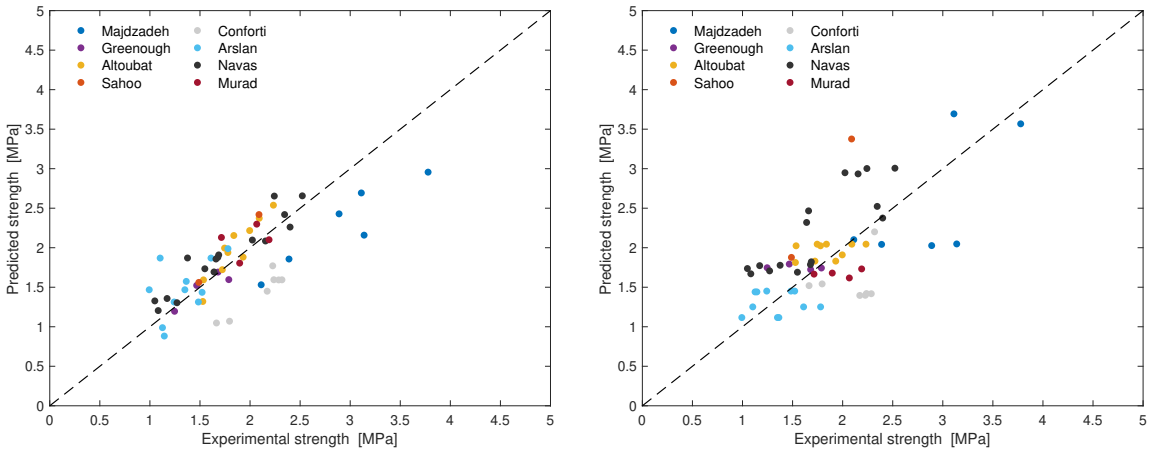

(a) (b)

Figure 7.4: Predicted versus experimental strength for (a) Narayanan and Darwish (1987) (b) AASHTO (2012)

Figure 7.5 shows the same data as Figure 7.4 (predicted against experimental strength), but categorized by beam type. All beam types were accurately predicted by the approach by Narayanan and Darwish (1987), while the AASHTO (2012) approach resulted in unconservative predictions of 35% for beams with stirrups.

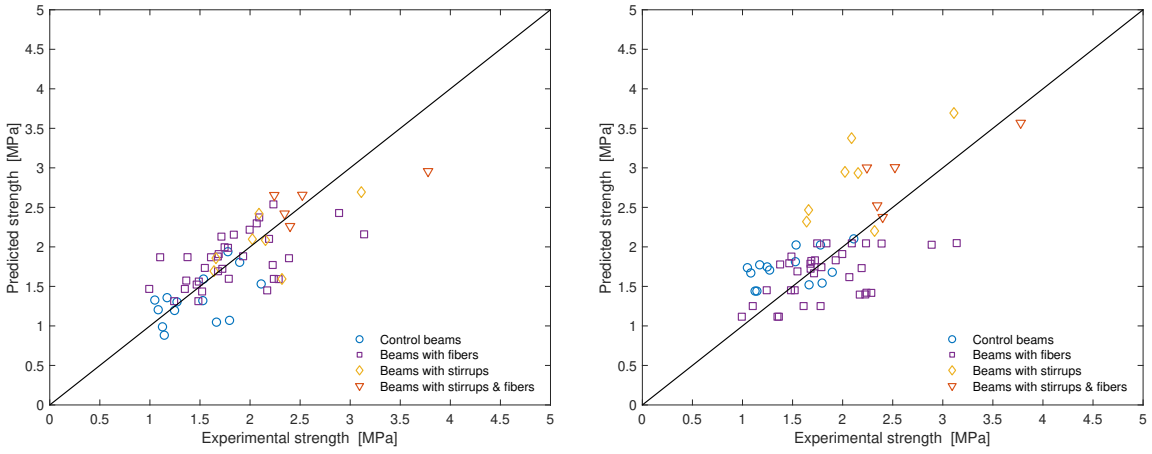

(a) (b)

Figure 7.5: Predicted versus experimental strength (by beam type) for (a) Narayanan and Darwish (1987) (b) AASHTO (2012)

7.3 Comparison to Parametric Study Results

The accuracy of the empirical equations and the design code models is evaluated by considering the predicted-to-numerical strength ratios for the parametric study conducted in Chapter 6.

Table 7.6 summarizes the average predicted-to-numerical strength ratios for the models. The approaches by Arslan et al. (2017) and Kwak et al. (2002) exhibited the most accurate results, despite slightly unconservative with an average ratio of 1.09 (COV = 8.6%) and 1.07 (COV = 9.5%), respectively. The empirical equation by Ababneh et al. (2017) also provided reasonable estimates of the shear strengths, resulting in a conservative average of 0.9 (COV = 12.9%).

The fib Model Code (2010) provided reasonable accurate shear strength estimates, with an average strength ratio of 0.94 (COV = 15.2%). Other design code procedures resulted in more conservative estimates in terms of average strength ratio and exhibited greater scattering with COV up to 26.8%.

Table 7.6: Predicted-to-numerical strength ratios for the parametric study

Model	**Average [-]**	**StD [-]**	**COV [%]**	**Max [-]**	**Min [-]**
Narayanan	1.13	0.16	13.8	1.68	0.88
Ashour	2.10	0.52	24.9	3.94	1.37
Swamy	0.78	0.12	15.4	1.00	0.35
Kwak	1.07	0.10	9.5	1.39	0.88
Arslan	1.09	0.09	8.6	1.35	0.93
Ababneh	0.90	0.12	12.9	1.20	0.65
Fib.	0.94	0.14	15.2	1.25	0.50
ACI	0.60	0.16	26.5	0.97	0.22
AASHTO	0.84	0.20	24.3	1.21	0.34
CSA	0.72	0.19	26.8	1.02	0.20

Equation (2.11) by Arslan et al. (2017), assumed a polypropylene-to-steel (PSR) ratio of $PSR = 0.7$, however they concluded that additional testing was needed to determine a value for PSR. Carnovale (2013) determined that PSR could range from $0.4 - 0.7$. The best fit of the model by Arslan et al. (2017) to the numerical database was found when $PSR = 0.5$, that resulted in average predicted-to-numerical strength ratio of 0.99 (COV = 9.0%).

Figure 7.6 shows the predicted strengths by the approach by Arslan et al. (2017) (PSR = 0.7) against numerical strengths from the parametric study. The predicted strengths align overall with the numerical strengths. However, some of the panels associated a compressive strength of $20\,MPa$ were overpredicted. Those panels contained a high transverse reinforcement ($\rho_y \geq 1.0\%$).

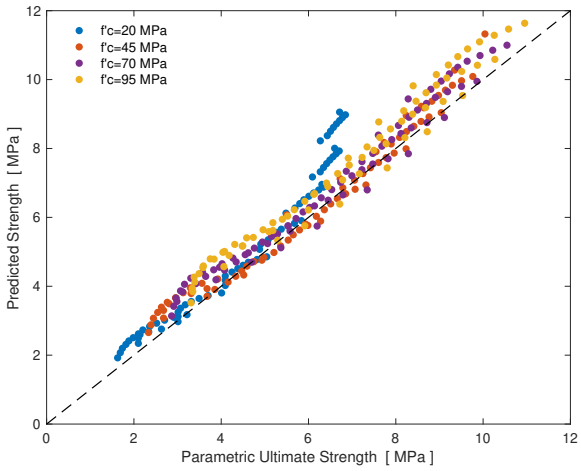

Figure 7.6: Predicted strength by Arslan et al. (2017) versus numerical strength

Figure 7.7 shows the predicted-to-numerical strength ratio against transverse reinforcement ratio ρ_y (left) and fiber volume V_f (right). The solid lines represent the average ratio at each transverse reinforcement ratio or fiber volume for panels with each of the four concrete compressive strengths. A transverse reinforcement ratio between 0.25% and 1.0% provided accurate results in terms of average predicted-to-numerical strength ratio in Figure 7.7(a), while other transverse reinforcement ratios resulted in overprediction of the strength. However, the fiber volume did not influence the prediction on average as the solid lines in Figure 7.7(b) demonstrate.

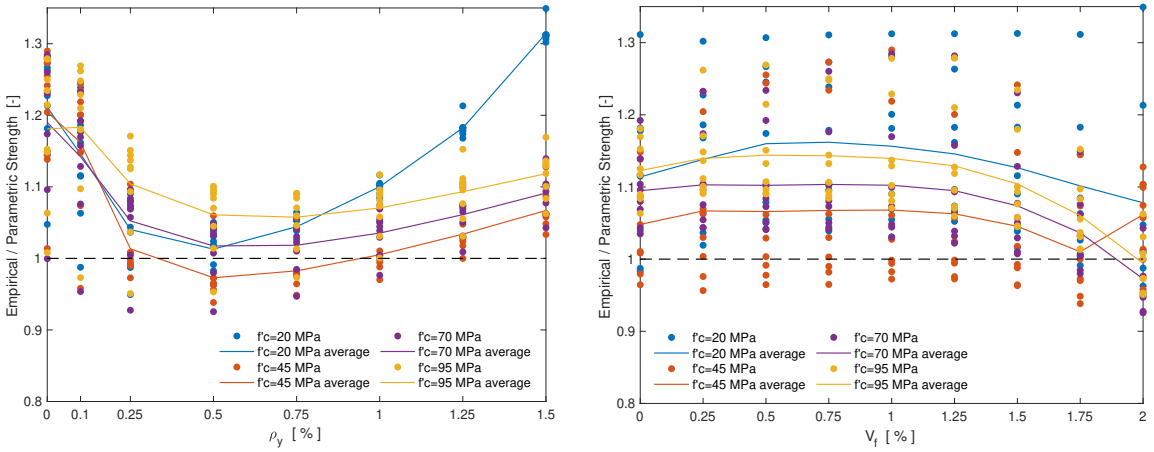

(a) (b)

Figure 7.7: Predicted-to-numerical strength ratio by Arslan et al. (2017) versus (a) Transverse reinforcement ratio ρ_y (b) Fiber volume V_f

Figure 7.8 shows the predicted strengths by the fib Model Code (2010) against the numerical strengths from the parametric study. The panels with a compressive strength of $20\,MPa$ hit the $v_{Rd,max}$ cap (by the fib Model Code, 2010) for $\rho_y \geq 0.5\%$. This cap influenced the overall predictions by some extent. However, other concrete strengths remained unaffected by the $v_{Rd,max}$ limit and resulted in accurate predictions across the range of the parameters investigated.

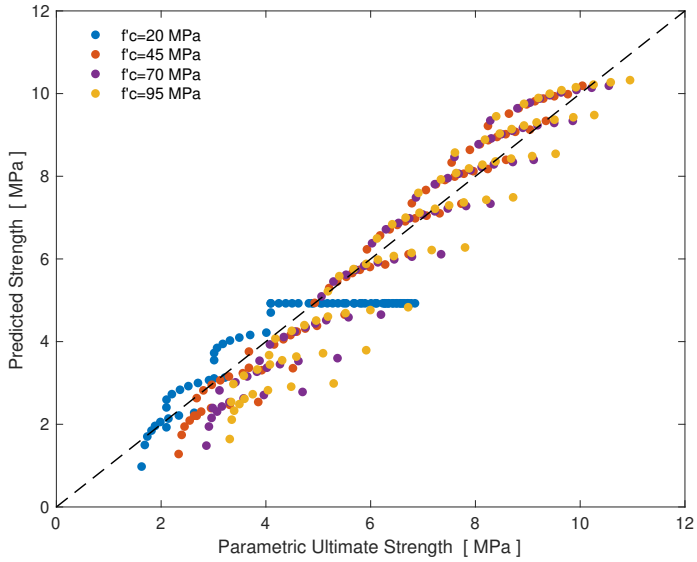

Figure 7.8: Predicted strength by the fib Model Code (2010) versus numerical strength

Figure 7.9 shows the predicted-to-numerical strength by the fib Model Code (2010) against the transverse reinforcement ρ_y and fiber volume V_f. The $v_{Rd,max}$ cap influenced the predictions for the $f'_c = 20\,MPa$ panels in Figure 7.9(a).

Panels associated a compressive strength $f'_c \geq 45\,MPa$ were significantly underpredicted for low transverse reinforcement ratios of $\rho_y \leq 0.25\%$. The average predicted-to-numerical strength ratio was in the range of $0.65 - 0.75$ for panels without transverse reinforcement. A transverse reinforcement $\rho_y \geq 0.5\%$ provided accurate results on average.

The fiber volume did not influence the average predicted-to-numerical strength ratio significantly. The average ratio was conservative for all fiber volumes ($V_f \leq 2.0\%$), where higher fiber volume provided more conservative results as demonstrated in Figure 7.9(b).

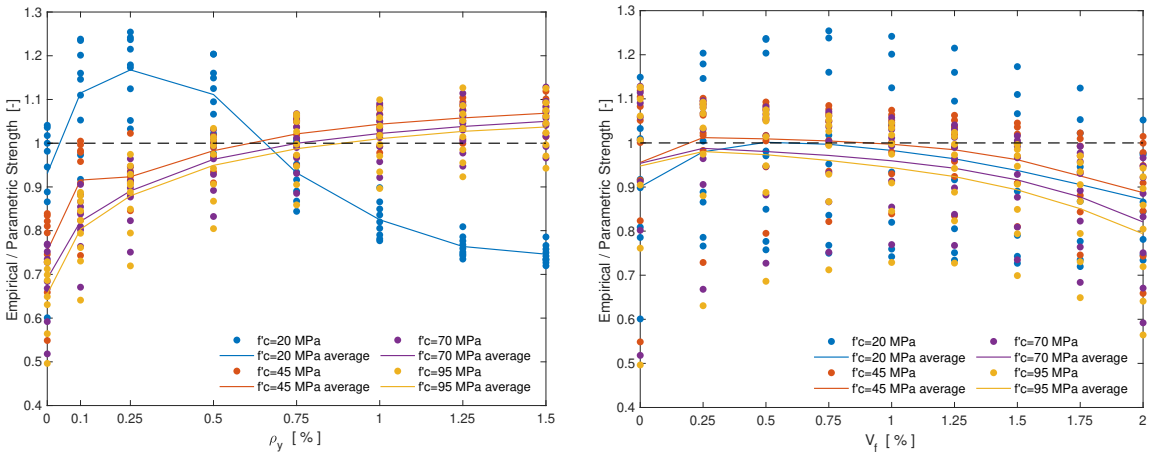

(a) (b)

Figure 7.9: Predicted-to-numerical strength by the fib Model Code (2010) versus (a) Transverse reinforcement ratio ρ_y (b) Fiber volume V_f

7.4 Proposed Shear Predicting Equation

The evaluation of the empirical equations and the design code models demonstrated that some of the existing shear predicting equations were able to predict the shear strength of PFRC members accurately for the three validation datasets, for example Ababneh et al. (2017); Arslan et al. (2017); Kwak et al. (2002). The design codes generally resulted in consistent conservative predictions, where the fib Model Code (2010) provided the most accurate strength estimates. To improve the prediction of the shear strength of PFRC elements, an empirical equation is proposed, building on these existing equations.

The proposed equation for the shear strength of PFRC elements consists of contribution from concrete, transverse steel reinforcement and macro-synthetic fibers as:

$$v_u = v_c + v_s + v_f \tag{7.1}$$

where v_u is the ultimate shear strength and v_c, v_s and v_f are the concrete, transverse steel reinforcement and macro-synthetic fiber contributions, respectively.

The concrete contribution v_c is computed based on the loading protocol by Equation (7.2), depending on the member type. The PFRC panel specimens were subjected to pure shear loading while the PFRC beams were subjected to bending. The expression for beams is based on Equation 22.5.5.1(b) of ACI 318 (2019), while the panel expression is based on

the web-shear strength by Equation 22.5.6.3.2 of ACI 318 (2019).

$$v_c = \begin{cases} 0.66\lambda_s\lambda\left(\rho_x\right)^{1/3}\sqrt{f'_c} & \text{for beams} \\ 0.29\lambda\sqrt{f'_c} & \text{for panels} \end{cases} \tag{7.2}$$

where λ_s is computed by Equation (2.24) and the term $\sqrt{f'_c}$ should not be taken greater than $8.3\,MPa$, corresponding to the $100\,psi$ limit in ACI 318 (2019).

The steel contribution v_s is computed directly from the transverse reinforcement ratio as $\rho_y \cdot F_y$, with an upper limit of $0.66\sqrt{f'_c}$, in accordance to Equation 22.5.1.2 of ACI 318 (2019). The fiber contribution term v_f is similar to the one proposed by Arslan et al. (2017), but with $PSR = 0.5$ and a parameter α that was calibrated for the data. Based on the results for beams and panels, it seemed like that the fibers contributed more to beams compared to panels. The parameter α was calibrated for beams and panels separately and was found to be 8.0 and 4.0 for beams and panels, respectively. The steel and fiber contributions are thus computed as:

$$v_s = \rho_y \cdot F_y \leq 0.66\sqrt{f'_c} \tag{7.3}$$

$$v_f = PSR \cdot \sqrt{\rho_x \cdot (1 + \alpha \cdot F)} \cdot \left(\frac{3}{a/d}\right)^{1/3} \tag{7.4}$$

where the span-to-depth ratio is taken as $a/d = 1.0$ for panel specimens.

The predicted-to-observed strength ratios for the proposed Equation (7.1) is summarized in Table 7.7. The proposed Equation provides accurate predictions in terms of average predicted-to-observed strength ratio, resulting in average ratio between 0.99 and 1.01 for all three datasets with a reasonable COV, never exceeding 19.9%.

Table 7.7: Predicted-to-observed strength ratios for the proposed Equation (7.1)

Dataset	**Average**	**StD**	**COV [%]**	**Max**	**Min**
Experimental Program	1.00	0.15	14.9	1.33	0.88
Beam Database	0.99	0.20	19.9	1.32	0.60
Parametric Study	1.01	0.12	11.5	1.28	0.76

Figure 7.10 shows the predicted strength against the observed strength for the three datasets. The proposed Equation (7.1) results in accurate predictions for all three datasets, despite some scattering for the beam database.

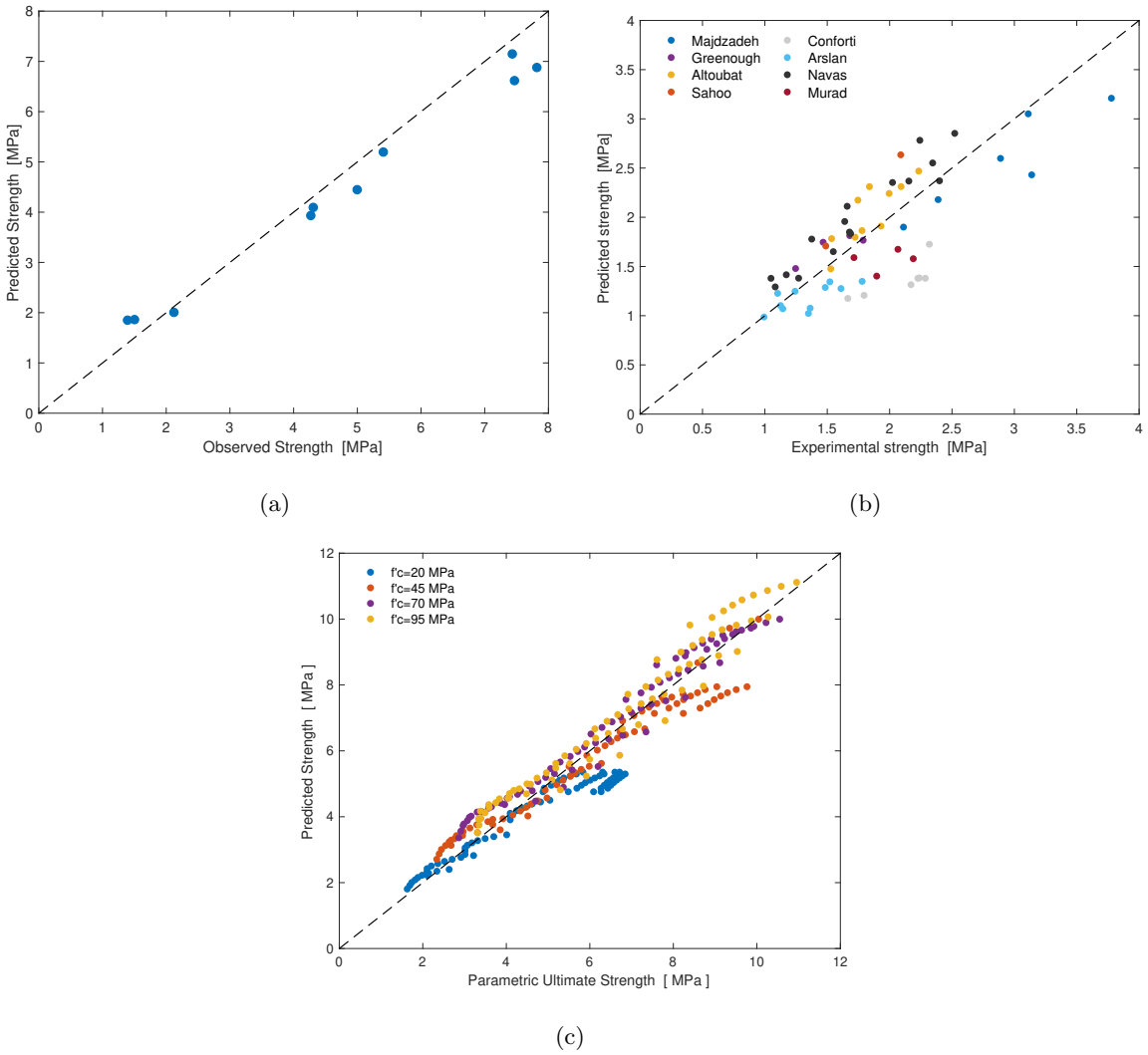

Figure 7.10: Predicted versus observed strengths by the proposed Equation (7.1) (a) Experimental program (b) Beam database (c) Parametric study

Table 7.8 compares the accuracy of the proposed Equation (7.1) to existing approaches by Arslan et al. (2017) and fib Model Code (2010), since they were found to provide the most accurate strength estimates for the datasets analyzed. The predictions of the modeling approach in VecTor2 (presented in Chapter 4.3.6) is also shown in Table 7.8 for the experimental program summarized in Chapter 3 and the beam database summarized in Chapter 5.

The numerical database of the parametric study was developed using the VecTor2 modeling approach. Therefore it is not reasonable to compare the parametric study to the VecTor2 modeling approach in Table 7.8 (as the average would be 1.00 and COV = 0.0%).

The proposed Equation (7.1) provides the most accurate predictions in Table 7.8 for the three datasets. However, it has to be noted that the VecTor2 modeling approach was calibrated for the experimental program.

The approach by Arslan et al. (2017) also shows a good agreement with the observed strengths, providing significantly more accurate results than the VecTor2 modeling approach for the beam database with average predicted-to-observed strength ratio of 1.02 (COV = 21.5%) and 1.11 (COV = 21.8%), respectively. However, the fib Model Code (2010) appears to provide accurate results for panel specimens with average ratios of 0.97 and 0.94 for the experimental program and the parametric study, respectively, while providing unconservative results for the beam database with an average ratio of 1.24.

Table 7.8: Comparison of predicted-to-observed strength ratios for the proposed equation to two existing approaches and the VecTor2 modeling approach

Dataset	**Approach**	**Avg**	**Std**	**COV [%]**	**Max**	**Min**
Experimental program	Proposed equation	1.00	0.16	15.7	1.33	0.88
	Arslan et al. (2017)	0.99	0.23	23.8	1.45	0.79
	fib Model Code (2010)	0.97	0.17	17.1	1.18	0.58
	VecTor2	1.01	0.06	5.9	1.14	0.93
Beam database	Proposed equation	0.99	0.20	19.9	1.32	0.60
	Arslan et al. (2017)	1.02	0.22	21.5	1.50	0.61
	fib Model Code (2010)	1.24	0.30	23.8	2.11	0.68
	VecTor2	1.11	0.24	21.8	1.75	0.60
Parametric study	Proposed equation	1.01	0.12	11.5	1.28	0.76
	Arslan et al. (2017)	1.09	0.09	8.6	1.35	0.93
	fib Model Code (2010)	0.94	0.14	15.2	1.25	0.50

Chapter 8

CONCLUSIONS AND RECOMMENDATION FOR FUTURE WORK

8.1 Summary

A non-linear numerical modeling approach, using the finite-element software VecTor2, was developed to examine the combined use of macro-synthetic fibers and conventional steel transverse reinforcement to resist shear loads. The model was calibrated using PFRC experimental panel data, validated using PFRC experimental data from the literature and used to perform a parametric study. The ability of shear strength predictive equations was evaluated using the data.

Calibration of the modeling approach was performed using data from the experimental program conducted by Gaston (2023), which investigated the shear behavior of twelve PFRC panels with various levels of transverse reinforcement. The fiber volumes for the experimental specimens ranged between 0% and 0.52%, while the transverse reinforcement ratio varied from 0% to 1.14%.

The finite element modeling was conducted in VecTor2, that has been commonly used for comparable panel specimens. The main challenge of the modeling was to account for the strength provided by the macro-synthetic fibers. A tension softening model was calibrated on the tested panels and demonstrated accurate predictions for the experimental program.

The modeling approach was validated using data from PFRC panel and beam tests available in the literature, forming a database of PFRC beam specimens. Although there is limited data for PFRC elements with conventional transverse reinforcement available in the literature, the results of the analysis indicated an ability of the approach to accurately estimate the ultimate strength for various structural elements.

The performance of elements with both macro-synthetic fibers and deformed steel bar transverse reinforcement was further investigated. An extensive parametric study was conducted in VecTor2, examining the shear strength for 288 PFRC panels with transverse reinforcement subjected to pure shear. The parameters of interest included the concrete's compressive strength f'_c, transverse reinforcement ratio ρ_y and fiber volume V_f. The database

generated was analyzed, considering ultimate shear strength, to examine the interaction of ρ_y and V_f, and the potential effects of f'_c.

The experimental data from Gaston (2023) and the beam database, in addition to the numerical database from the parametric study, was compared to empirical shear strength equations by Narayanan and Darwish (1987), Ashour et al. (1992), Swamy et al. (1993), Kwak et al. (2002), Arslan et al. (2017) and Ababneh et al. (2017). Additionally, a handful of design code approaches were evaluated to predict the shear strength, including the fib Model Code (2010), ACI 318 (2019), AASHTO (2012) and CSA A23.3 (2019).

8.2 Conclusions

From these analyses, the following conclusions can be revealed:

- Macro-synthetic fibers provided significant enhancement in shear strength, up to 80% increase in shear strength was observed for panels with transverse reinforcement of $\rho_y = 0.1\%$ and a fiber volume of $V_f = 2.0\%$ compared to panel models without fibers ($V_f = 0\%$). This enhancement was most pronounced for low transverse reinforcement ratios ($\rho_y \leq 0.25\%$). For panels with $\rho_y \geq 1.0\%$ the improvements were up to 30% in shear strength. This aligns with the trends Watanabe et al. (2010) identified for SFRC.
- Benefits provided by macro-syntetic fibers are influenced by the concrete's compressive strength to some extent. Panels with $f'_c = 70\,MPa$ and $f'_c = 95\,MPa$ without transverse reinforcement exhibited minor shear strength enhancement (less than 10%) provided by the fibers for fiber volumes up to 1.0%. However, strength advancements were overall greater for concrete strengths of $f'_c = 70\,MPa$ and $f'_c = 95\,MPa$ (up to 30%) compared to $f'_c = 20\,MPa$ and $f'_c = 45\,MPa$ (up to 20%) for panels containing transverse reinforcement for any fiber volume investigated.
- Macro-synthetic fibers were found to shift the failure mode of PFRC panels without transverse reinforcement from aggregate interlock to crushing failure or $x-$yielding failure by utilizing a fiber volume of $V_f \geq 1.0\%$. However, his observation is in contrast what was observed by Carnovale and Vecchio (2014) experimentally, where a PFRC panel subjected to pure shear with $V_f = 2.0\%$ of macro-synthetic fibers failed due to aggregate interlock.

- Macro-synthetic fibers reduced crack widths and the effects were more pronounced for panels with $f'_c = 70\,MPa$ and $f'_c = 95\,MPa$. However, negligible reductions in crack width were observed for transverse reinforcement $\rho_y \geq 0.75\%$, independent of concrete strength.
- Several existing empirical equations in the literature and model code approaches and demonstrated the ability to predict the shear strength of PFRC structural elements accurately. The approach by Arslan et al. (2017) indicated reliable estimates of the shear strength with a predicted-to-numerical strength average ratio of 1.09 and COV of 8.6%. However a slight modification of the approach resulted in an average of 0.99 and COV of 9.0% (where a lower PSR value was employed).
- Most current design codes neglect the contribution of macro-synthetic fibers to the shear strength of structural elements, which results in underestimation of shear strength. The fib Model Code (2010), which includes the contribution of fibers, exhibited superior performance across series of design code approaches evaluated, with mean predicted-to-numerical strength ratio of 0.94 and COV of 15%.
- The proposed empirical equation to predict the shear strength of PFRC elements demonstrated accurate predictions to the experimental and numerical data used in this study. The equation resulted in a predicted-to-observed average of 1.00 with a COV not exceeding 19.9%. The equation utilizes the fiber term presented by Arslan et al. (2017) with minor modification. However, the equation considers the shear loading protocol for PFRC members, employing different equations for PFRC beams and panels.

8.3 Future Work

Although these are promising results, there are limitations on the presented study including experimental validation data and the proposed tension softening model for PFRC. With respect to future research work, the following recommendations are made:

- Continued experimental work on PFRC members with transverse reinforcement is necessary to expand the currently available database. Presently, only 17 PFRC structural elements with transverse reinforcement exist in the literature, 6 panels tested by Gaston (2023) and 11 beams.
- The observed trends in shear strength enhancement due to macro-synthetic fibers need

to be confirmed with experimental testing. This requires testing of comprehensive experimental programs, exploring various combinations of transverse reinforcement ratios, fiber volume and compressive strength.

- Development of a general PFRC tension softening model is necessary. The model used in this study only considered fiber volume V_f and the concrete cracking strength f'_t to influence the tension softening response of PFRC. However, many other fiber and concrete parameters influence the response (e.g., fiber length l_f, fiber aspect ratio AR_f and bond stress between fibers and concrete matrix). Additionally, a general PFRC tension softening model should be validated for other loading conditions than pure shear as well.
- Constitutive models accounting for macro-synthetic fibers should be implemented into VecTor2.
- Current model code procedures should consider the strength contribution of macro-synthetic fibers. This would increase the combined use of macro-synthetic fibers and transverse reinforcement in design, resulting more durable structures with higher deformation capacities in addition to savings in steel reinforcement.

REFERENCES

AASHTO (2012). *AASHTO LRFD Bridge Design Specifications*. Section 5: Concrete Structures. American Association of State Highway and Transportation Officials.

Ababneh, A., Al-Rousan, R., Alhassan, M., and Alqadami, M. (2017). Influence of synthetic fibers on the shear behavior of lightweight concrete beams. *Advances in Structural Engineering*, 20(11):1671–1683.

ACI 318 (2019). Building code requirements for structural concrete. American Concrete Institute.

ACI Committee 544 (2018). Aci prc-544.4-18: Guide to design with fiber-reinforced concrete. American Concrete Institute.

Ahmed, M., Mallick, J., and Hasan, M. A. (2016). A study of factors affecting the flexural tensile strength of concrete. *Journal of King Saud University-Engineering Sciences*, 28(2):147–156.

Almasabha, G., Al-Shboul, K. F., Shehadeh, A., and Alshboul, O. (2023). Machine learning-based models for predicting the shear strength of synthetic fiber reinforced concrete beams without stirrups. 52:299–311.

Altoubat, S., Yazdanbakhsh, A., and Rieder, K.-A. (2009). Shear behavior of macro-synthetic fiber-reinforced concrete beams without stirrups. *ACI Materials Journal*, 106(4):381.

Arslan, G. (2014). Shear strength of steel fiber reinforced concrete (sfrc) slender beams. *KSCE Journal of Civil Engineering*, 18(2):587–594.

Arslan, G., Keskin, R. S. O., and Ozturk, M. (2017). Shear behaviour of polypropylene fibre-reinforced-concrete beams without stirrups. *Proceedings of the Institution of Civil Engineers-Structures and Buildings*, 170(3):190–198.

Ashour, S. A., Hasanain, G. S., and Wafa, F. F. (1992). Shear behavior of high-strength fiber reinforced concrete beams. *Structural Journal*, 89(2):176–184.

Balaguru, P. N. and Shah, S. P. (1992). *Fiber-reinforced cement composites*. McGraw-Hill, New York.

Bentur, A. and Mindess, S. (1990). *Fibre Reinforced Cementitious Composites*. Crc Press.

Bentz, E. C., Vecchio, F. J., and Collins, M. P. (2006). Simplified modified compression field theory for calculating shear strength of reinforced concrete elements. *ACI structural journal*, 103(4):614.

Boulekbache, B., Hamrat, M., Chemrouk, M., and Amziane, S. (2012). Influence of yield stress and compressive strength on direct shear behaviour of steel fibre-reinforced concrete. *Construction and Building Materials*, 27(1):6–14.

Buratti, N., Mazzotti, C., and Savoia, M. (2011). Post-cracking behaviour of steel and macro-synthetic fibre-reinforced concretes. *Construction and building materials*, 25(5):2713–2722.

Carnovale, D. and Vecchio, F. J. (2014). Effect of fiber material and loading history on shear behavior of fiber-reinforced concrete. *ACI Structural Journal*, 111(5).

Carnovale, D. J. (2013). *Behaviour and analysis of steel and macro-synthetic fibre reinforced concrete subjected to reversed cyclic loading: a pilot investigation*. PhD thesis, University of Toronto Toronto, ON, Canada.

Chandrathilaka, E., Baduge, S. K., Mendis, P., and Thilakarathna, P. (2021). Structural applications of synthetic fibre reinforced cementitious composites: A review on material properties, fire behaviour, durability and structural performance. 34:550–574.

Chasioti, S. (2017). *Hybrid steel fibre reinforced concrete in shear: from the material to the structural level*. University of Toronto (Canada).

Chasioti, S. G. and Vecchio, F. J. (2017). Shear behavior and crack control characteristics of hybrid steel fiber-reinforced concrete panels. *ACI Structural Journal*, 114(1):209.

Collins, M. P. (1978). Towards a rational theory for rc members in shear. *Journal of the Structural Division*, 104(4):649–666.

Collins, M. P., Vecchio, F. J., and Mehlhorn, G. (1985). An international competition to predict the response of reinforced concrete panels. *Canadian Journal of Civil Engineering*, 12(3):624–644.

Conforti, A., Minelli, F., Tinini, A., and Plizzari, G. A. (2015). Influence of polypropylene fibre reinforcement and width-to-effective depth ratio in wide-shallow beams. *Engineering Structures*, 88:12–21.

Conforti, A., Tiberti, G., and Plizzari, G. A. (2016). Splitting and crushing failure in frc elements subjected to a high concentrated load. *Composites Part B: Engineering*, 105:82–92.

Cornelissen, H., Hordijk, D., and Reinhardt, H. (1986). Experimental determination of crack softening characteristics of normalweight and lightweight. *Heron*, 31(2):45–46.

CSA A23.3 (2019). Design of concrete structures. Standard CSA A23.3:19, Canadian Standards Association, Toronto, Ontario.

Eurocode 2 (2004). *Eurocode 2: Design of Concrete Structures*.

fib Model Code (2010). CEB-FIP model code 2010. CEB, Lausanne, Switzerland.

Foster, S. J., Agarwal, A., and Amin, A. (2018). Design of steel fiber reinforced concrete beams for shear using inverse analysis for determination of residual tensile strength. *Structural Concrete*, 19(1):129–140.

Gaston, J. P., Farag, B., Calvi, P. M., and Thonstad, T. (2025). Shear behavior of marco-synthetic fiber-reinforced concrete. *Submitted to ACI Structural journal in May 2024*.

Gaston, J. P. B. (2023). Shear behavior of macro-synthetic fiber-reinforced concrete panels.

Greenough, T. and Nehdi, M. (2008). Shear behavior of fiber-reinforced self-consolidating concrete slender beams. *ACI materials Journal*, 105(5):468.

Hwang, J.-H., Lee, D. H., Kim, K. S., Ju, H., and Seo, S.-Y. (2013). Evaluation of shear performance of steel fibre reinforced concrete beams using a modified smeared-truss model. *Magazine of Concrete Research*, 65(5):283–296.

Juhász, K. and Kis, V. (2017). The effect of the length of macro synthetic fibres on their performance in concrete. In *IOP Conference Series: Materials Science and Engineering*, volume 246, page 012027. IOP Publishing.

Karim, R. and Shafei, B. (2022). Investigation of five synthetic fibers as potential replacements of steel fibers in ultrahigh-performance concrete. *Journal of Materials in Civil Engineering*, 34(7):04022126.

Khuntia, M., Stojadinovic, B., and Goel, S. C. (1999). Shear strength of normal and high-strength fiber reinforced concrete beams without stirrups. *Structural Journal*, 96(2):282–289.

Kwak, Y.-K., Eberhard, M. O., Kim, W.-S., and Kim, J. (2002). Shear strength of steel fiber-reinforced concrete beams without stirrups. *ACI Structural journal*, 99(4):530–538.

Lambrechts, A. (2009). Steel–and synthetic fibre reinforced concrete. which fibre to use for which application and why.

Lantsoght, E. O. (2019). How do steel fibers improve the shear capacity of reinforced concrete beams without stirrups? *Composites Part B: Engineering*, 175:107079.

Lantsoght, E. O. (2023). Theoretical model of shear capacity of steel fiber reinforced concrete beams. *Engineering Structures*, 280:115722.

Lee, S.-C., Cho, J.-Y., and Vecchio, F. J. (2011). Diverse embedment model for steel fiber-reinforced concrete in tension: Model development. *ACI materials Journal*, 108(5):516.

Lee, S.-C., Cho, J.-Y., and Vecchio, F. J. (2013). Simplified diverse embedment model for steel fiber-reinforced concrete elements in tension. *Materials Journal*, 110(4):403–412.

Li, V. C., Ward, R. J., and Hamza, A. M. (1992). Steel and synthetic fibers as shear reinforcement.

Lim, C. N. (2006). *Flexural Behavior of Steel Fiber Reinforced Concrete (SFRC)*. PhD thesis, Universiti Teknologi Malaysia.

Luo, J. W. and Vecchio, F. J. (2016). Behavior of steel fiber-reinforced concrete under reversed cyclic shear. *ACI Structural Journal*, 113(1):75.

Maalej, M. and Li, V. C. (1994). Flexural/tensile-strength ratio in engineered cementitious composites. *Journal of Materials in Civil Engineering*, 6(4):513–528.

Maidl, B. and Dietrich, J. (1995). *Steel fibre reinforced concrete*. Ernst, Verlag für Architektur und technische Wissenschaften.

Majdzadeh, F., Soleimani, S. M., and Banthia, N. (2006). Shear strength of reinforced concrete beams with a fiber concrete matrix. *Canadian Journal of Civil Engineering*, 33(6):726–734.

Mansur, M., Ong, K., and Paramasivam, P. (1986). Shear strength of fibrous concrete beams without stirrups. *Journal of structural engineering*, 112(9):2066–2079.

Mitchell, D. and Collins, M. P. (1974). Diagonal compression field theory-a rational model for structural concrete in pure torsion. 71(8):396–408.

Murad, Y. and Abdel-Jabbar, H. (2022). Shear behavior of rc beams prepared with basalt and polypropylene fibers. *Case Studies in Construction Materials*, 16:e00835.

Nana, W., Tran, H., Goubin, T., Kubisztal, G., Bennani, A., Bui, T., Cardia, G., and Limam, A. (2021). Behaviour of macro-synthetic fibers reinforced concrete: Experimental, numerical and design code investigations. In *Structures*, volume 32, pages 1271–1286. Elsevier.

Narayanan, R. and Darwish, I. (1987). Use of steel fibers as shear reinforcement. *Structural Journal*, 84(3):216–227.

Navas, F. O., Navarro-Gregori, J., Herdocia, G. L., Serna, P., and Cuenca, E. (2018). An experimental study on the shear behaviour of reinforced concrete beams with macro-synthetic fibres. *Construction and Building Materials*, 169:888–899.

Neto, B. N. M., Barros, J. A., and Melo, G. S. (2013). A model for the prediction of the punching resistance of steel fibre reinforced concrete slabs centrically loaded. *Construction and Building Materials*, 46:211–223.

Parmentier, B., Cauberg, N., and Vandewalle, L. (2012). Shear resistance of macro-synthetic and steel fibre reinforced concrete beams without stirrups. In *Proceedings of the 8th*

RILEM International Symposium on Fibre Reinforced Concrete: Challenges and Opportunities, Guimaraes, Portugal, pages 19–21.

Parra-Montesinos, G. J. (2006). Shear strength of beams with deformed steel fibers. *Concrete international*, 28(11):57–66.

Petersen, R. B. (2009). *In-plane shear behaviour of unreinforced masonry panels strengthened with fibre reinforced polymer strips*. PhD thesis, University of Newcastle.

Prete, C. D., Buratti, N., Manzi, S., and Mazzotti, C. (2019). Macro synthetic fibre reinforced concrete: Influence of the matrix mix design on interfacial bond behavior. *IOP Conference Series. Materials Science and Engineering*, 596(1).

Sadeghian, V. and Vecchio, F. (2018). The modified compression field theory: then and now. *ACI Struct J, Special Publication (SP-328: Shear in Structural Concrete)*, pages 3–1.

Sahoo, D. R., Maran, K., and Kumar, A. (2015). Effect of steel and synthetic fibers on shear strength of rc beams without shear stirrups. *Construction and Building Materials*, 83:150–158.

Sani, M., Muftah, F., Muda, M. F., and Ho, L. S. (2022). Comparative study on compressive— strength of fibre-reinforced concrete made with industrial hybrid fibre and natural waste fibre. *Journal of Engineering Science and Technology*, 17(6):3815–3833.

Soroushian, P., Mirza, F., and Alhozajiny, A. (1993). Plastic shrinkage cracking of polypropylene fiber reinforced concrete. *Materials Journal*, 92(5):553–560.

Standards Australia (2001). *AS 3600-2001 Concrete Structures*. ASI, Sydney, Australia.

Susetyo, J. (2009). *Fibre reinforcement for shrinkage crack control in prestressed, precast segmental bridges*. PhD thesis, University of Toronto.

Susetyo, J., Gauvreau, P., and Vecchio, F. J. (2011). Effectiveness of steel fiber as minimum shear reinforcement. *ACI Structural Journal*, 108(4).

Swamy, R., Mangat, P., and Rao, C. K. (1974). The mechanics of fiber reinforcement of cement matrices. *Special Publication*, 44:1–28.

Swamy, R. N., Jones, R., and Chiam, A. T. (1993). Influence of steel fibers on the shear resistance of lightweight concrete i-beams. *Structural Journal*, 90(1):103–114.

Thomas, J. and Ramaswamy, A. (2007). Mechanical properties of steel fiber-reinforced concrete. *Journal of materials in civil engineering*, 19(5):385–392.

Tomosawa, F. and Noguchi, T. (1993). Relationship between compressive strength and modulus of elasticity of high-strength concrete. In *Proceedings of the Third International symposium on utilization of high-strength concrete*, volume 2, pages 1247–1254. Norwegian Concrete Assn Lillehammer, Norway.

Vecchio, F. (1982). The response of reinforced concrete to in-plane shear and normal stresses. *Publication*, (82).

Vecchio, F., Lai, D., Shim, W., and Ng, J. (2001). Disturbed stress field model for reinforced concrete: validation. *Journal of Structural Engineering*, 127(4):350–358.

Vecchio, F. J. (1979). *Shear rig design*. PhD thesis, University of Toronto.

Vecchio, F. J. (2000). Disturbed stress field model for reinforced concrete: formulation. *Journal of structural engineering*, 126(9):1070–1077.

Vecchio, F. J. (2001). Disturbed stress field model for reinforced concrete: implementation. *Journal of Structural Engineering*, 127(1):12–20.

Vecchio, F. J. and Collins, M. P. (1986). The modified compression-field theory for reinforced concrete elements subjected to shear. *ACI J.*, 83(2):219–231.

Vidya, B., Blessyzion, G., et al. (2017). A study on development of high strength concrete (95 mpa). *IUP Journal of Structural Engineering*, 10(3).

Voo, J. Y. L. and Foster, S. J. (2003). Variable engagement model for the design of fibre reinforced concrete structures.

Walraven, J. C. (1981). Fundamental analysis of aggregate interlock. *Journal of the Structural Division*, 107(11):2245–2270.

Wang, J., Dai, Q., Si, R., and Guo, S. (2018). Investigation of properties and performances of polyvinyl alcohol (pva) fiber-reinforced rubber concrete. *Construction and Building Materials*, 193:631–642.

Watanabe, K., Kimura, T., and Niwa, J. (2010). Synergetic effect of steel fibers and shear-reinforcing bars on the shear-resistance mechanisms of rc linear members. *Construction and Building Materials*, 24(12):2369–2375.

Wong, P., Vecchio, F., and Trommels, H. (2013). Vector2 & formworks user's manual second edition. *University of Toronto, Canada*.

Yao, X., Pei, Z., Zheng, H., Guan, Q., Wang, F., Wang, S., and Ji, Y. (2022). Review of mechanical and temperature properties of fiber reinforced recycled aggregate concrete. *Buildings*, 12(8):1224.

Yazdanbakhsh, A., Altoubat, S., and Rieder, K.-A. (2015). Analytical study on shear strength of macro synthetic fiber reinforced concrete beams. *Engineering Structures*, 100:622–632.

Yazıcı, Ş., İnan, G., and Tabak, V. (2007). Effect of aspect ratio and volume fraction of steel fiber on the mechanical properties of sfrc. *Construction and Building Materials*, 21(6):1250–1253.

Yehia, S., Douba, A., Abdullahi, O., and Farrag, S. (2016). Mechanical and durability evaluation of fiber-reinforced self-compacting concrete. *Construction and Building Materials*, 121:120–133.

You, Z., Ding, Y., and Niederegger, C. (2010). Replacing stirrups of self-compacting concrete beams with steel fibers. *Transactions of Tianjin University*, 16:411–416.

Zhang, F., Ding, Y., Xu, J., Zhang, Y., Zhu, W., and Shi, Y. (2016). Shear strength prediction for steel fiber reinforced concrete beams without stirrups. *Engineering Structures*, 127:101–116.

Zhang, Z. (2020). *Finite Element Modelling of Ultra-High Performance Fibre Reinforced Concrete*. University of Toronto (Canada).

Zhao, C., Wang, Z., Zhu, Z., Guo, Q., Wu, X., and Zhao, R. (2023). Research on different types of fiber reinforced concrete in recent years: An overview. *Construction and Building Materials*, 365:130075.

Zheng, Z. and Feldman, D. (1995). Synthetic fibre-reinforced concrete. *Progress in Polymer Science*, 20(2):185–210.

Zsutty, T. (1971). Shear strength prediction for separate catagories of simple beam tests. 68(2):138–143.

Appendix A

EXPERIMENTAL PROGRAM MODELING RESULTS

Panels with consolidation issues (marked with *) are not included in the average and standard deviation calculation calculations for v_{max} and γ_u. Moreover, panels with $\rho_y = 0\%$ were not included in the average and standard deviation calculations for γ_u.

Table A.1: Modeling results with and without PP fibers: v_{max}

Panel	**Specimen name**	v_{exp} [MPa]	v_{vt2rc} [MPa]	v_{vt2pp} [MPa]	**pred/exp-RC**	**pred/exp-PP**
P1	PFRC-000-000	2.12	2.11	-	0.99	-
P2	PFRC-000-029	4.27	3.59	-	0.84	-
P3	PFRC-000-058	5.41	5.47	-	1.01	-
P4	PFRC-000-114	7.82	8.32	-	1.06	-
P5	PFRC-026-000	1.43	1.21	1.21	0.85	0.85
P6	PFRC-026-029	4.31	4.60	3.76	1.07	0.87
P7	PFRC-026-058*	4.24	5.55	5.83	1.31	1.37
P8	PFRC-026-114	7.43	8.32	8.43	1.12	1.13
P9	PFRC-052-000	1.50	1.52	1.52	1.01	1.01
P10	PFRC-052-029	5.00	3.81	4.01	0.76	0.80
P11	PFRC-052-058*	4.94	5.58	6.01	1.13	1.22
P12	PFRC-052-114	7.47	8.35	8.52	1.12	1.14
				Average:	0.98	0.97
				Std:	0.12	0.14

Table A.2: Modeling results with and without PP fibers: γ_u in Table A.1

Panel	**Specimen name**	γ_{exp} [MPa]	γ_{vt2rc} [MPa]	γ_{vt2pp} [MPa]	**pred/exp-RC**	**pred/exp-PP**
PP1	PFRC-000-000	0.71	1.72	-	2.41	-
P2	PFRC-000-029	13.31	19.24	-	1.45	-
P3	PFRC-000-058	12.21	14.49	-	1.19	-
P4	PFRC-000-114	13.73	10.16	-	0.74	-
P5	PFRC-026-000	1.37	2.20	2.41	1.61	1.76
P6	PFRC-026-029	13.80	20.87	31.01	1.51	2.25
P7	PFRC-026-058*	5.49	25.19	24.60	4.59	4.48
P8	PFRC-026-114	11.95	14.65	14.32	1.23	1.20
P9	PFRC-052-000	0.36	0.85	0.41	2.33	1.12
P10	PFRC-052-029	20.75	47.29	47.34	2.28	2.28
P11	PFRC-052-058*	8.09	23.43	22.21	2.90	2.75
P12	PFRC-052-114	13.03	10.48	14.90	0.80	1.14
				Average:	1.06	1.02
				Std:	0.26	0.16

Table A.3: Modeling results comparing DSFM and MCFT: v_{max}

Panel	**Specimen name**	v_{exp} [MPa]	v_{dsfm} [MPa]	v_{mcft} [MPa]	**pred/exp-DSFM**	**pred/exp-MCFT**
P1	PFRC-000-000	2.12	2.11	2.18	0.99	1.03
P2	PFRC-000-029	4.27	3.59	4.09	0.84	0.96
P3	PFRC-000-058	5.41	5.47	5.49	1.01	1.01
P4	PFRC-000-114	7.82	8.32	8.32	1.06	1.06
P5	PFRC-026-000	1.43	1.21	1.20	0.85	0.84
P6	PFRC-026-029	4.31	4.60	4.21	1.07	0.98
P7	PFRC-026-058*	4.24	5.55	5.67	1.31	1.34
P8	PFRC-026-114	7.43	8.32	8.31	1.12	1.12
P9	PFRC-052-000	1.50	1.52	1.53	1.01	1.02
P10	PFRC-052-029	5.00	3.81	4.34	0.76	0.87
P11	PFRC-052-058*	4.94	5.58	5.71	1.13	1.16
P12	PFRC-052-114	7.47	8.35	8.27	1.12	1.11
				Average:	0.98	1.00
				Std:	0.12	0.09

Table A.4: Modeling results comparing DSFM and MCFT: γ_u in Table A.3

Panel	**Specimen name**	γ_{exp} [MPa]	γ_{dsfm} [MPa]	γ_{mcft} [MPa]	**pred/exp-DSFM**	**pred/exp-MCFT**
P1	PFRC-000-000	0.71	1.72	0.16	2.41	0.22
P2	PFRC-000-029	13.31	10.86	14.89	0.82	1.12
P3	PFRC-000-058	12.21	14.49	9.38	1.19	0.77
P4	PFRC-000-114	13.73	10.16	8.61	0.74	0.63
P5	PFRC-026-000	1.37	2.20	1.73	1.61	1.27
P6	PFRC-026-029	13.80	20.87	14.91	1.51	1.08
P7	PFRC-026-058*	5.49	18.67	12.60	3.40	2.29
P8	PFRC-026-114	11.95	14.65	8.56	1.23	0.72
P9	PFRC-052-000	0.36	0.85	0.80	2.33	2.21
P10	PFRC-052-029	20.75	23.23	12.89	1.12	0.62
P11	PFRC-052-058*	8.09	18.60	10.94	2.30	1.35
P12	PFRC-052-114	13.03	10.48	7.83	0.80	0.60
				Average:	1.06	0.79
				Std:	0.26	0.20

Table A.5: Tensile strength (f'_t) inputs [MPa] for Table 4.2

Panel	f_1	$0.38f_1$	$0.5f_1$	$0.67f_1$	**VT2 default**
P1	5.17	1.96	2.58	3.45	2.20
P2	5.44	2.07	2.72	3.63	2.03
P3	3.04	1.15	1.52	2.03	1.84
P4	4.48	1.70	2.24	2.99	2.14
P5	5.92	2.25	2.96	3.95	1.88
P6	4.36	1.66	2.18	2.91	2.04
P7	4.82	1.83	2.41	3.21	1.93
P8	3.83	1.46	1.92	2.56	2.18
P9	3.67	1.40	1.84	2.45	1.79
P10	4.32	1.64	2.16	2.88	2.21
P11	4.36	1.66	2.18	2.91	1.97
P12	3.44	1.31	1.72	2.29	1.98

Table A.6: Tension softening inputs for the proposed model by Equation (4.14)

PFRC-000-000		PFRC-000-029		PFRC-000-058		PFRC-000-114	
ϵ_{c1} [mm/m]	f_{c1} [MPa]	ϵ_{c1} [mm/m]	f_{c1} [MPa]	ϵ_{c1} [mm/m]	f_{c1} [MPa]	ϵ_{c1} [mm/m]	f_{c1} [MPa]
1.0	1.390	1.0	0.924	1.0	1.019	1.0	1.232
3.2	0.517	3.2	0.343	3.2	0.379	3.2	0.458
6.2	0.134	6.2	0.089	6.2	0.098	6.2	0.119
12.0	0.010	12.0	0.007	12.0	0.007	12.0	0.009
PFRC-026-000		PFRC-026-029		PFRC-026-058		PFRC-026-114	
ϵ_{c1} [mm/m]	f_{c1} [MPa]	ϵ_{c1} [mm/m]	f_{c1} [MPa]	ϵ_{c1} [mm/m]	f_{c1} [MPa]	ϵ_{c1} [mm/m]	f_{c1} [MPa]
1.2	0.795	1.2	1.159	1.2	0.872	1.2	1.193
3.2	0.457	3.2	0.666	3.2	0.501	3.2	0.686
6.5	0.254	6.5	0.370	6.5	0.279	6.5	0.381
14.0	0.183	14.0	0.267	14.0	0.201	14.0	0.275
PFRC-052-000		PFRC-052-029		PFRC-052-058		PFRC-052-114	
ϵ_{c1} [mm/m]	f_{c1} [MPa]	ϵ_{c1} [mm/m]	f_{c1} [MPa]	ϵ_{c1} [mm/m]	f_{c1} [MPa]	ϵ_{c1} [mm/m]	f_{c1} [MPa]
1.3	1.098	1.3	1.448	1.3	1.100	1.3	1.793
3.8	0.654	3.8	0.863	3.8	0.656	3.8	1.069
7.8	0.413	7.8	0.544	7.8	0.413	7.8	0.674
16.0	0.336	16.0	0.444	16.0	0.337	16.0	0.549

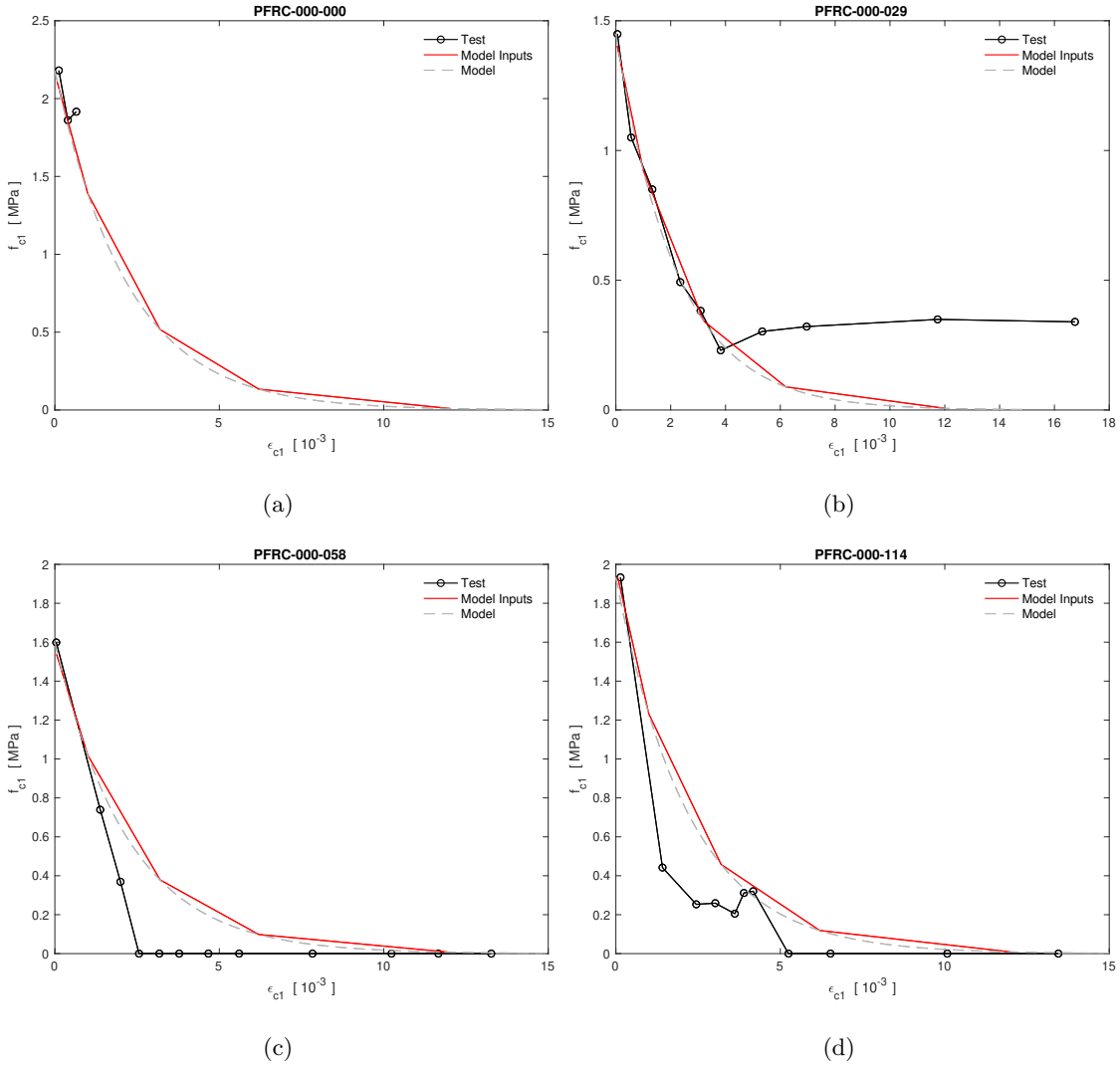

Figure A.1: Discretization of the tension softening model for inputs to the FormWorks model by Table A.6 (a) PFRC-000-000 (b) PFRC-000-029 (c) PFRC-000-058 (d) PFRC-000-114

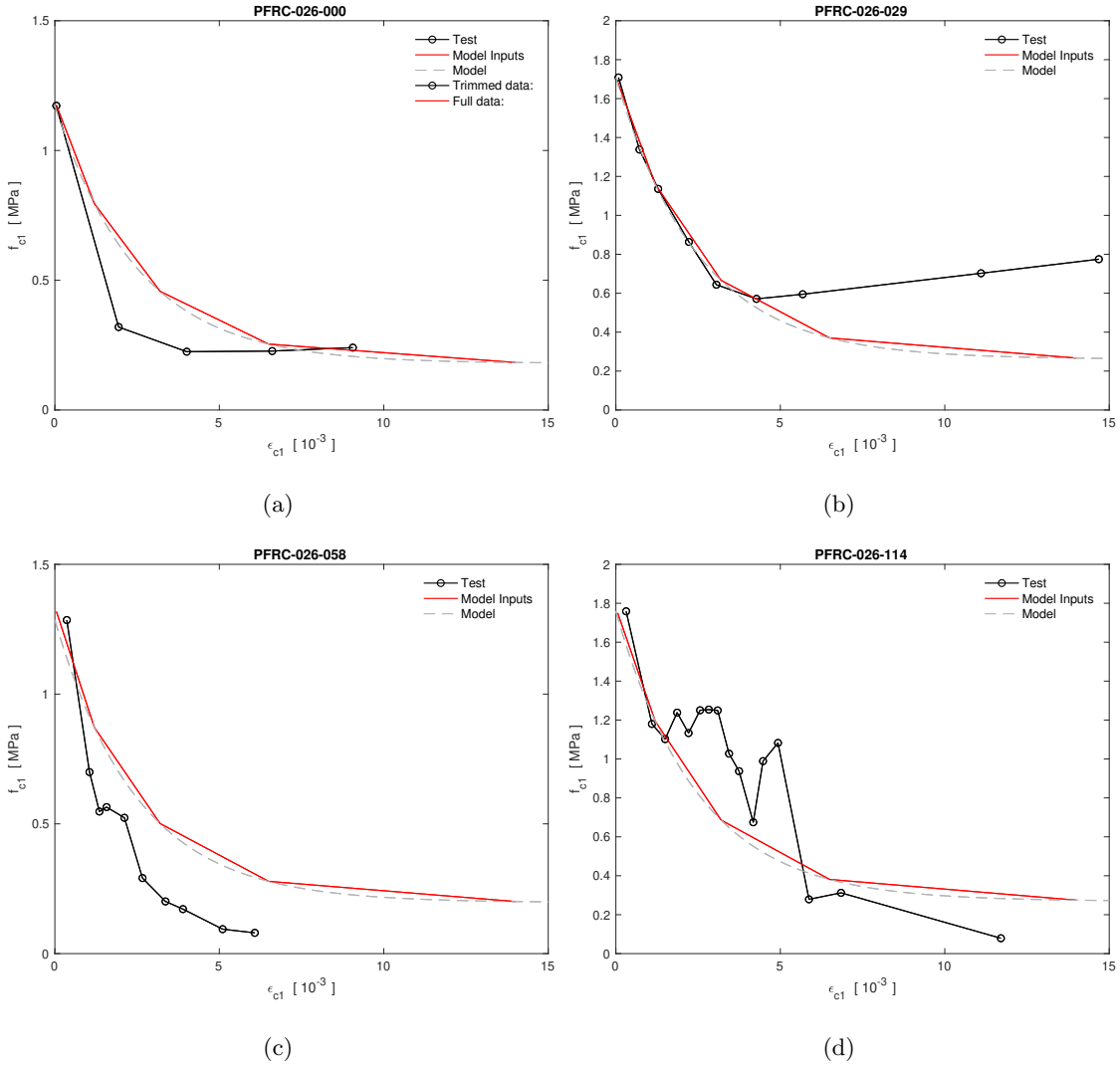

Figure A.2: Discretization of the tension softening model for inputs to the FormWorks model by Table A.6 (a) PFRC-026-000 (b) PFRC-026-029 (c) PFRC-026-058 (d) PFRC-026-114

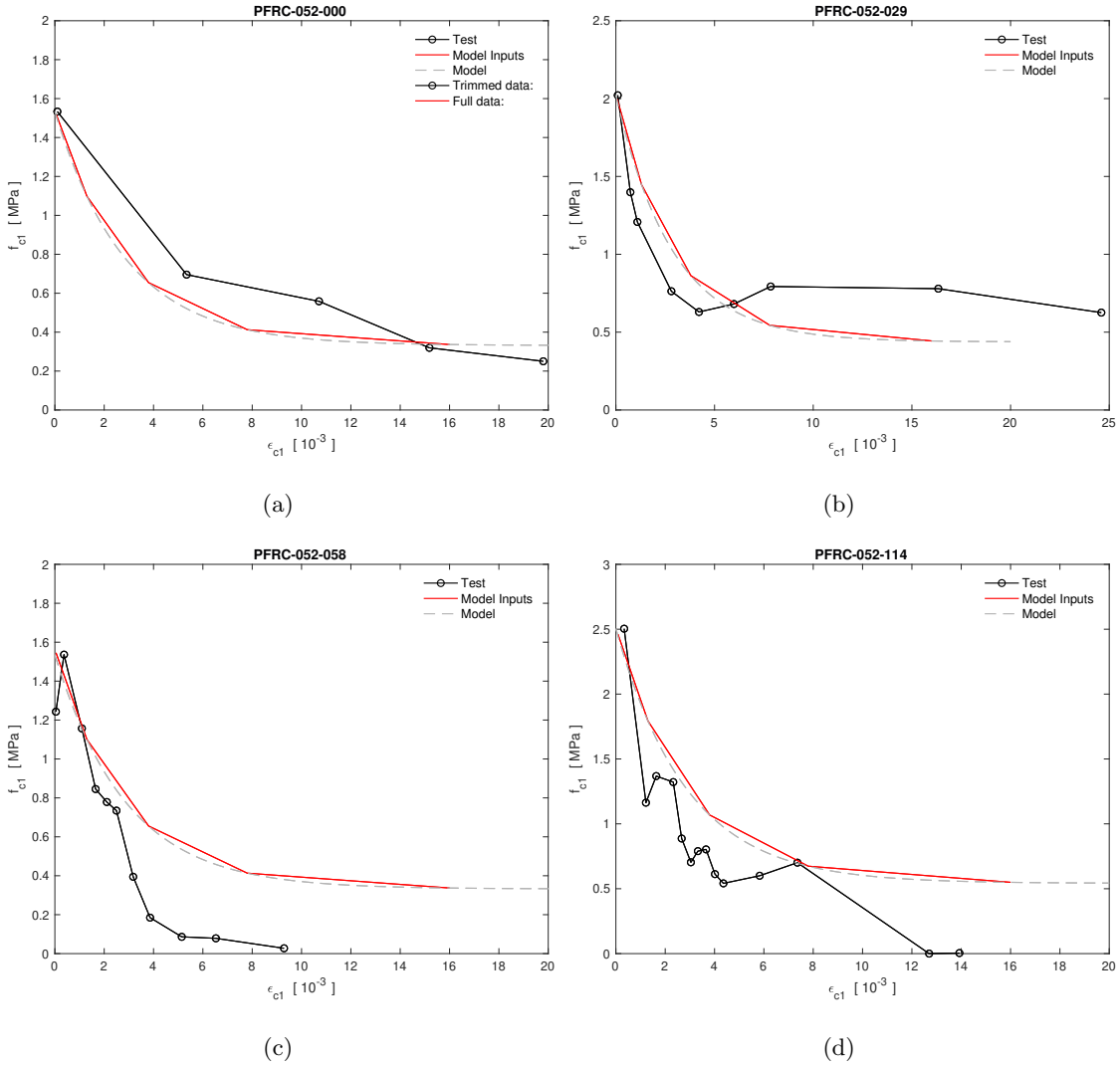

Figure A.3: Discretization of the tension softening model for inputs to the FormWorks model by Table A.6 (a) PFRC-052-000 (b) PFRC-052-029 (c) PFRC-052-058 (d) PFRC-052-114

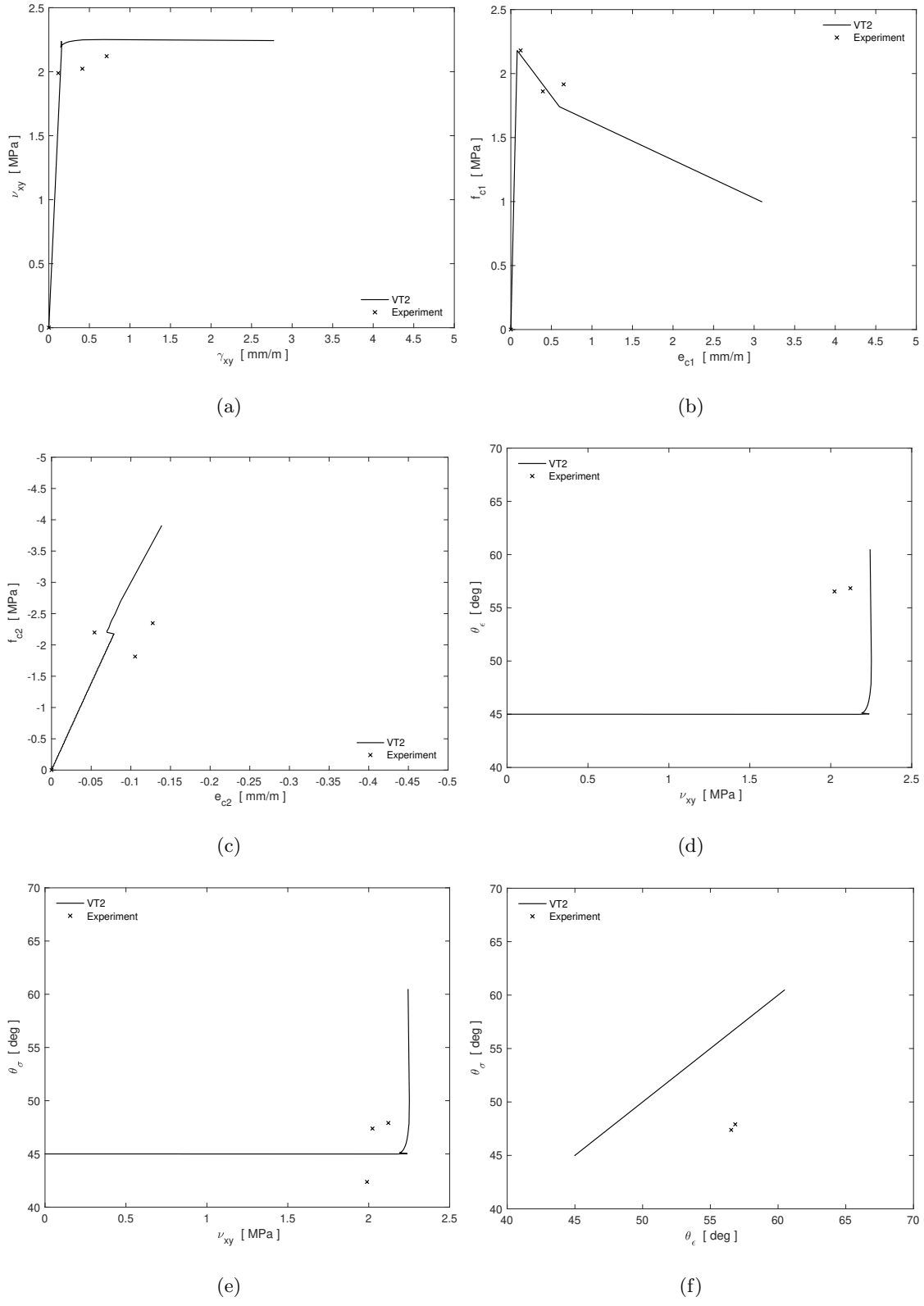

Figure A.4: Experimental response versus VT2 predicted response for PFRC-000-000 (a) $v_{xy} - \gamma_{xy}$ (b) $f_{c1} - \epsilon_{c1}$, (c) $f_{c2} - \epsilon_{c2}$ (d) $\theta_\sigma - v_{xy}$ (e) $\theta_\epsilon - v_{xy}$ (f) $\theta_\sigma - \theta_\epsilon$

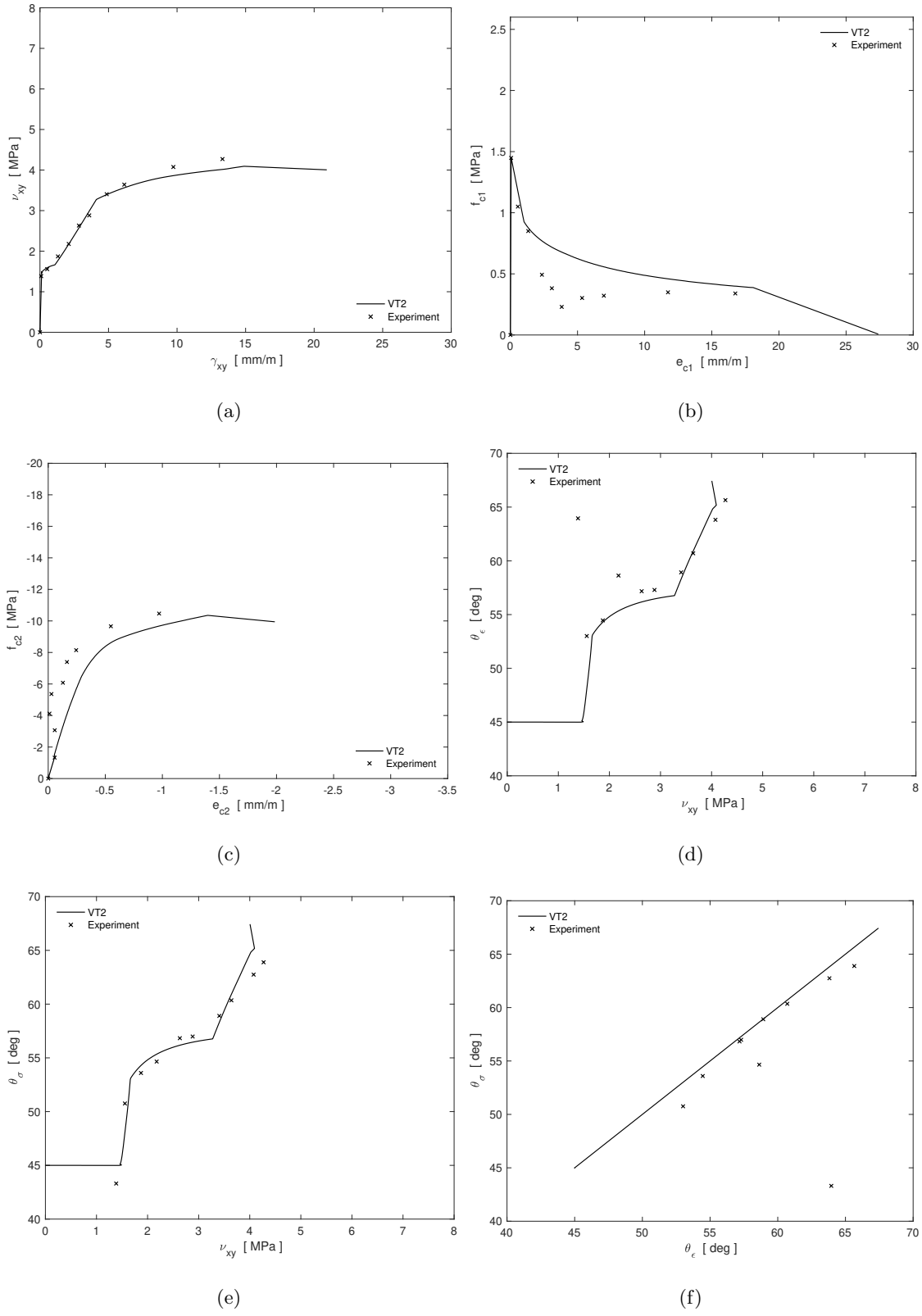

Figure A.5: Experimental response versus VT2 predicted response for PFRC-000-029 (a) $v_{xy} - \gamma_{xy}$ (b) $f_{c1} - \epsilon_{c1}$, (c) $f_{c2} - \epsilon_{c2}$ (d) $\theta_\sigma - v_{xy}$ (e) $\theta_\epsilon - v_{xy}$ (f) $\theta_\sigma - \theta_\epsilon$

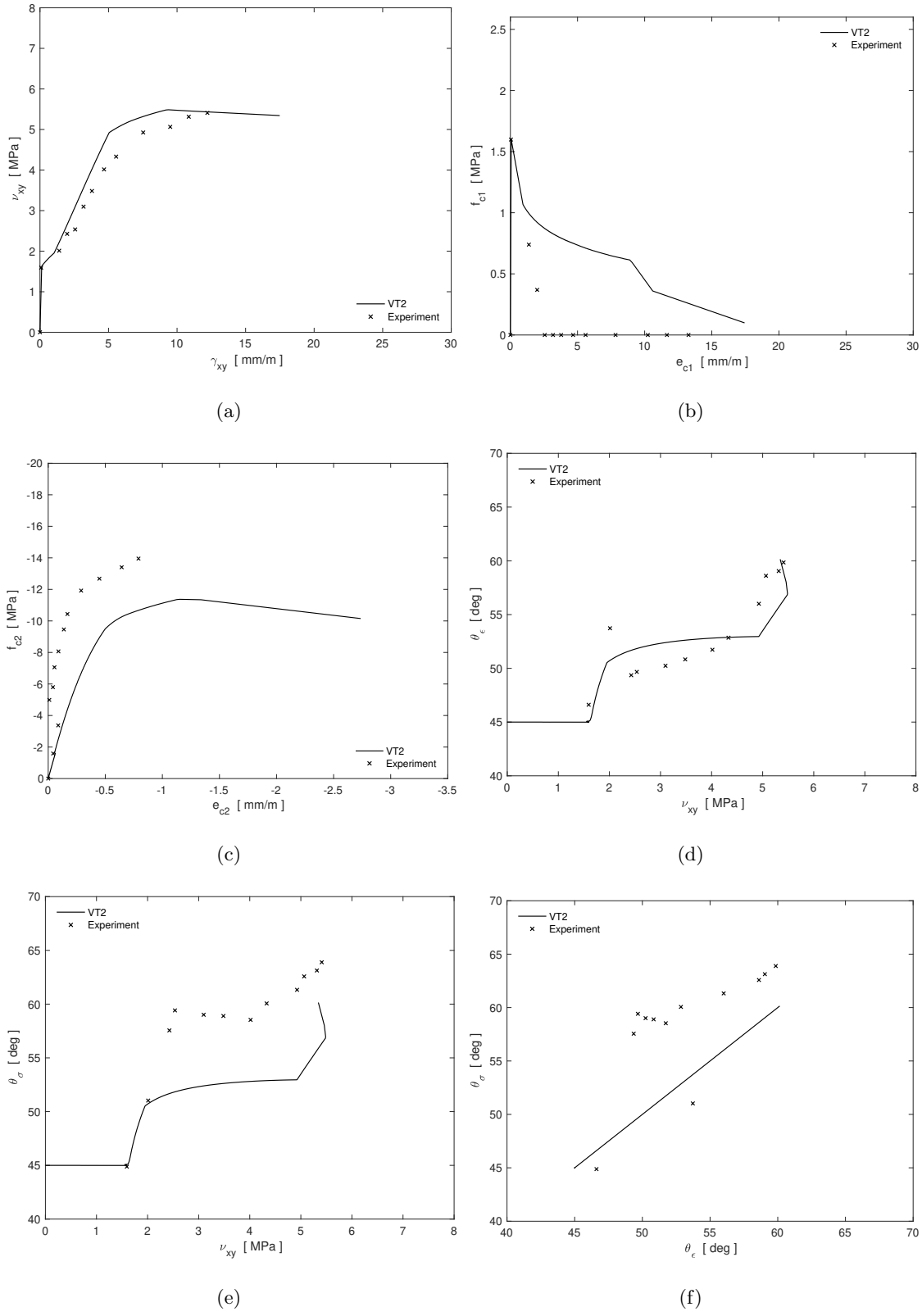

Figure A.6: Experimental response versus VT2 predicted response for PFRC-000-058 (a) $v_{xy} - \gamma_{xy}$ (b) $f_{c1} - \epsilon_{c1}$, (c) $f_{c2} - \epsilon_{c2}$ (d) $\theta_\sigma - v_{xy}$ (e) $\theta_\epsilon - v_{xy}$ (f) $\theta_\sigma - \theta_\epsilon$

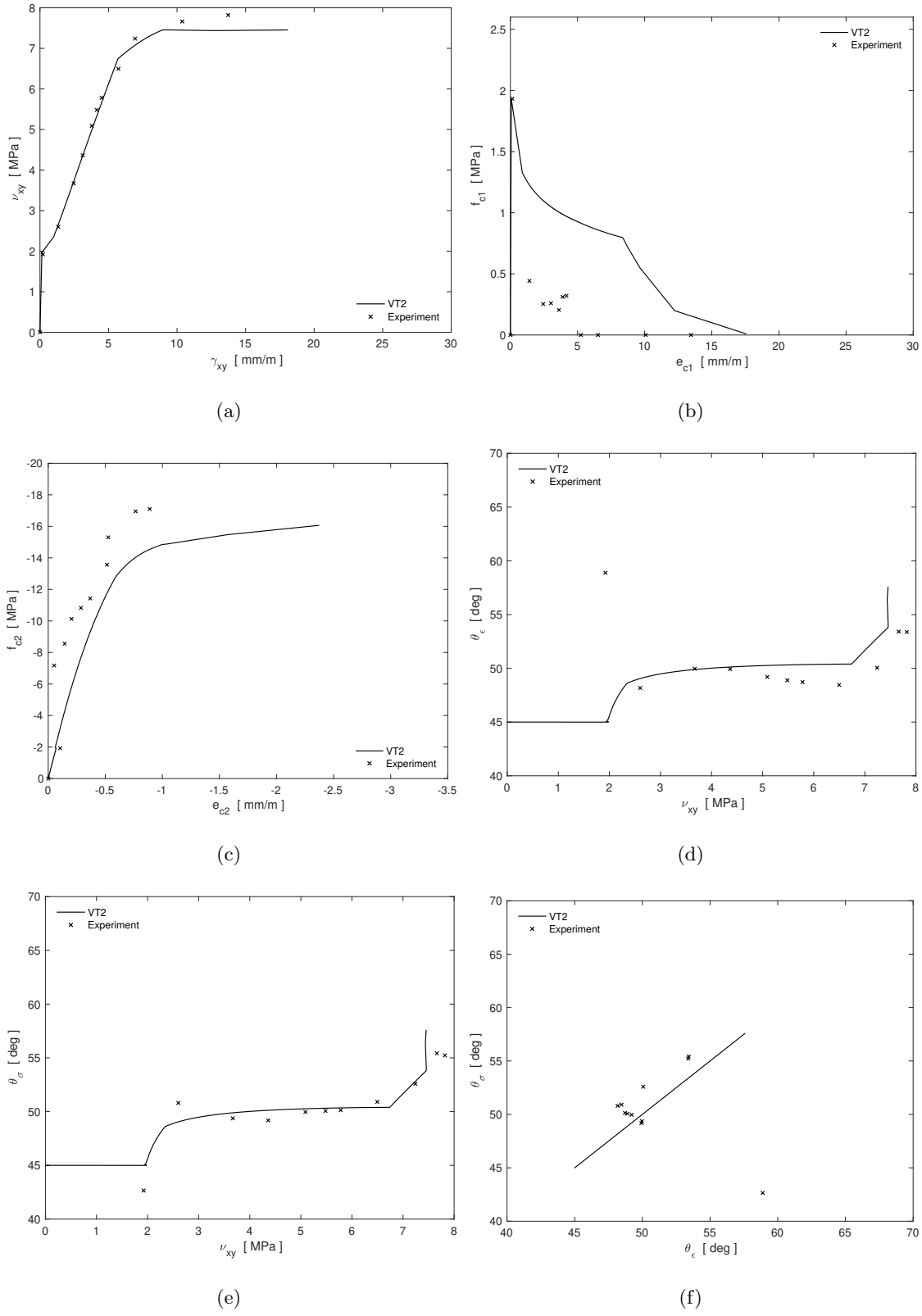

Figure A.7: Experimental response versus VT2 predicted response for PFRC-000-114 (a) $v_{xy} - \gamma_{xy}$ (b) $f_{c1} - \epsilon_{c1}$, (c) $f_{c2} - \epsilon_{c2}$ (d) $\theta_\sigma - v_{xy}$ (e) $\theta_\epsilon - v_{xy}$ (f) $\theta_\sigma - \theta_\epsilon$

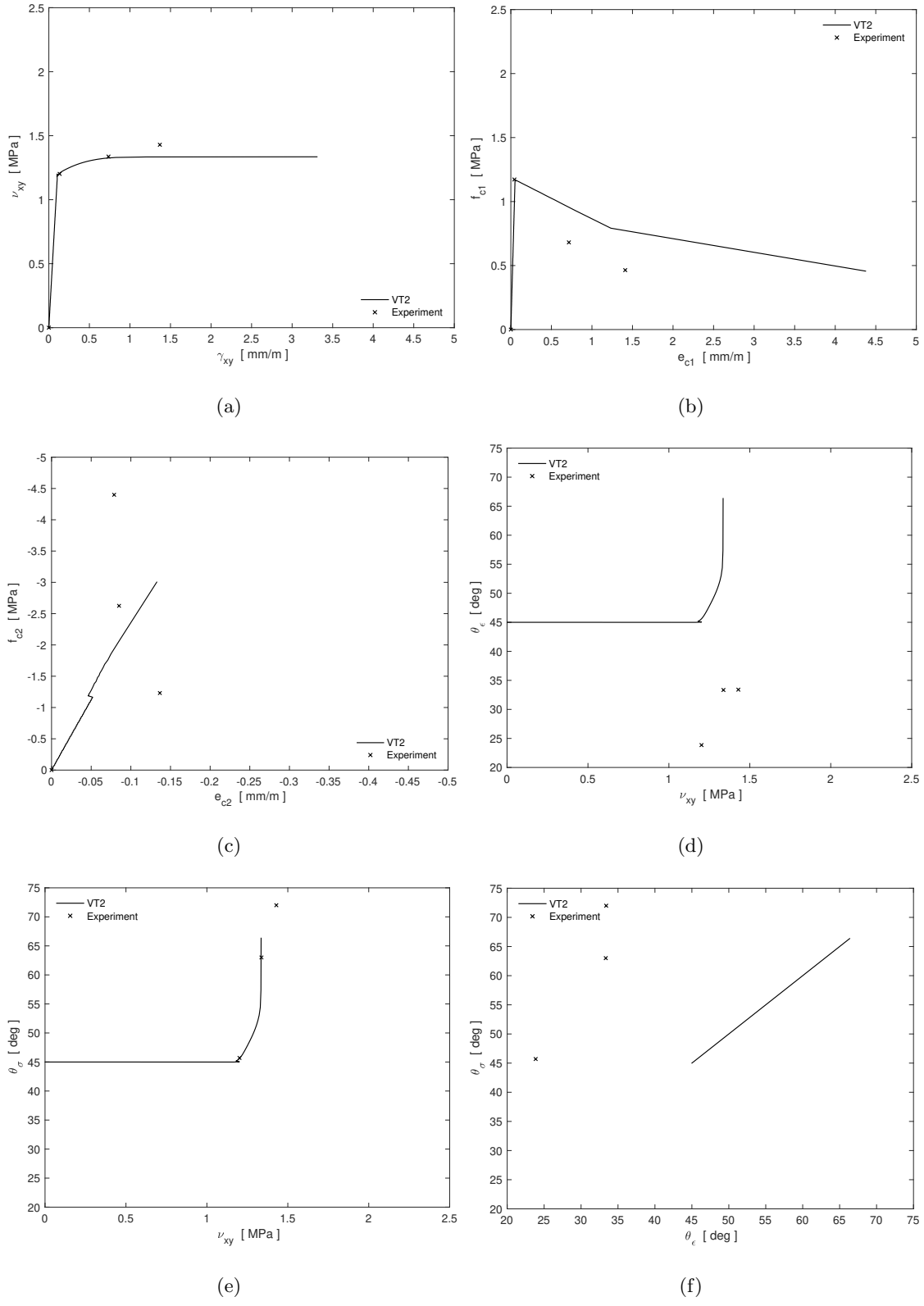

Figure A.8: Experimental response versus VT2 predicted response for PFRC-026-000 (a) $v_{xy} - \gamma_{xy}$ (b) $f_{c1} - \epsilon_{c1}$, (c) $f_{c2} - \epsilon_{c2}$ (d) $\theta_\sigma - v_{xy}$ (e) $\theta_\epsilon - v_{xy}$ (f) $\theta_\sigma - \theta_\epsilon$

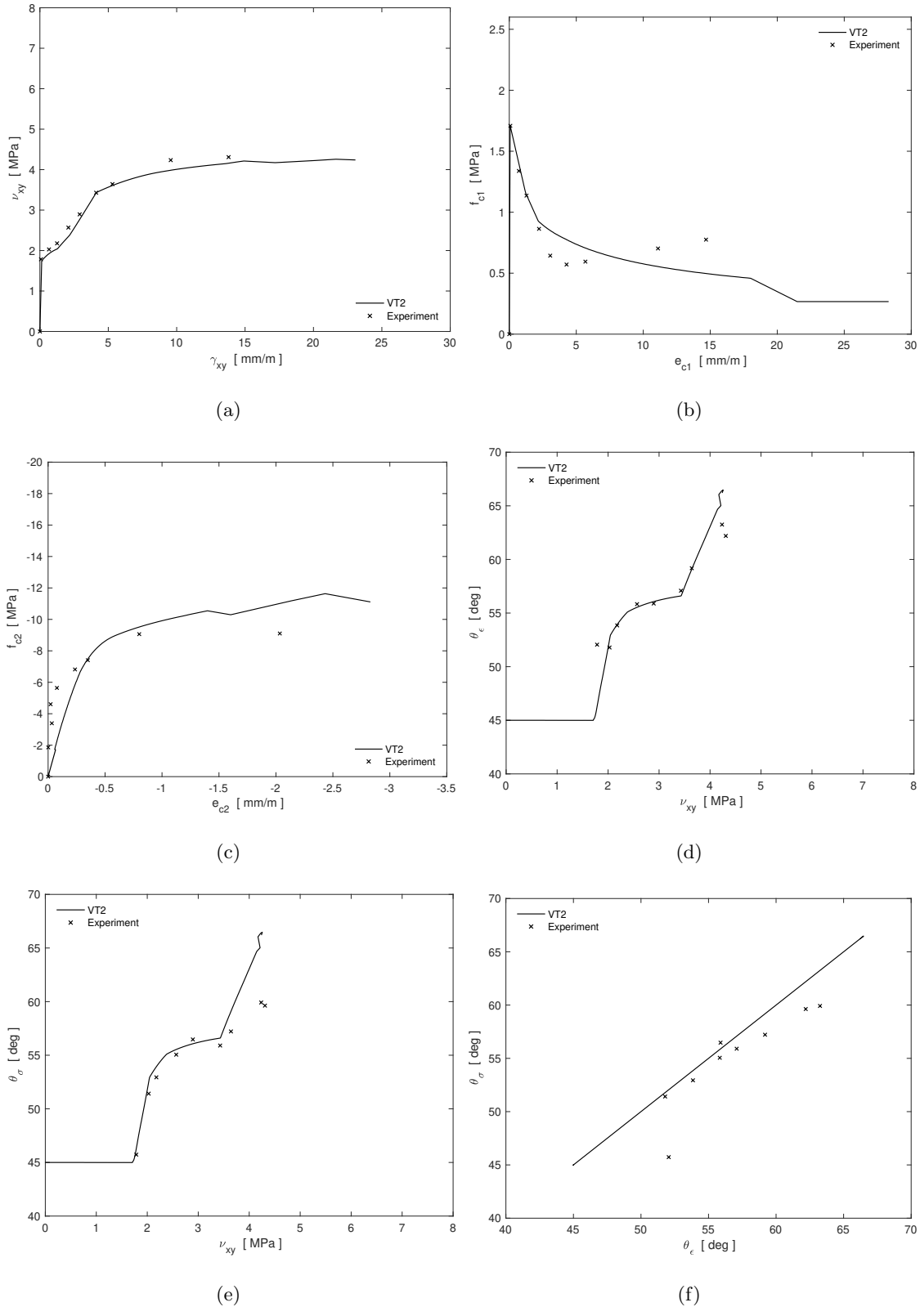

Figure A.9: Experimental response versus VT2 predicted response for PFRC-026-029 (a) $v_{xy} - \gamma_{xy}$ (b) $f_{c1} - \epsilon_{c1}$, (c) $f_{c2} - \epsilon_{c2}$ (d) $\theta_\sigma - v_{xy}$ (e) $\theta_\epsilon - v_{xy}$ (f) $\theta_\sigma - \theta_\epsilon$

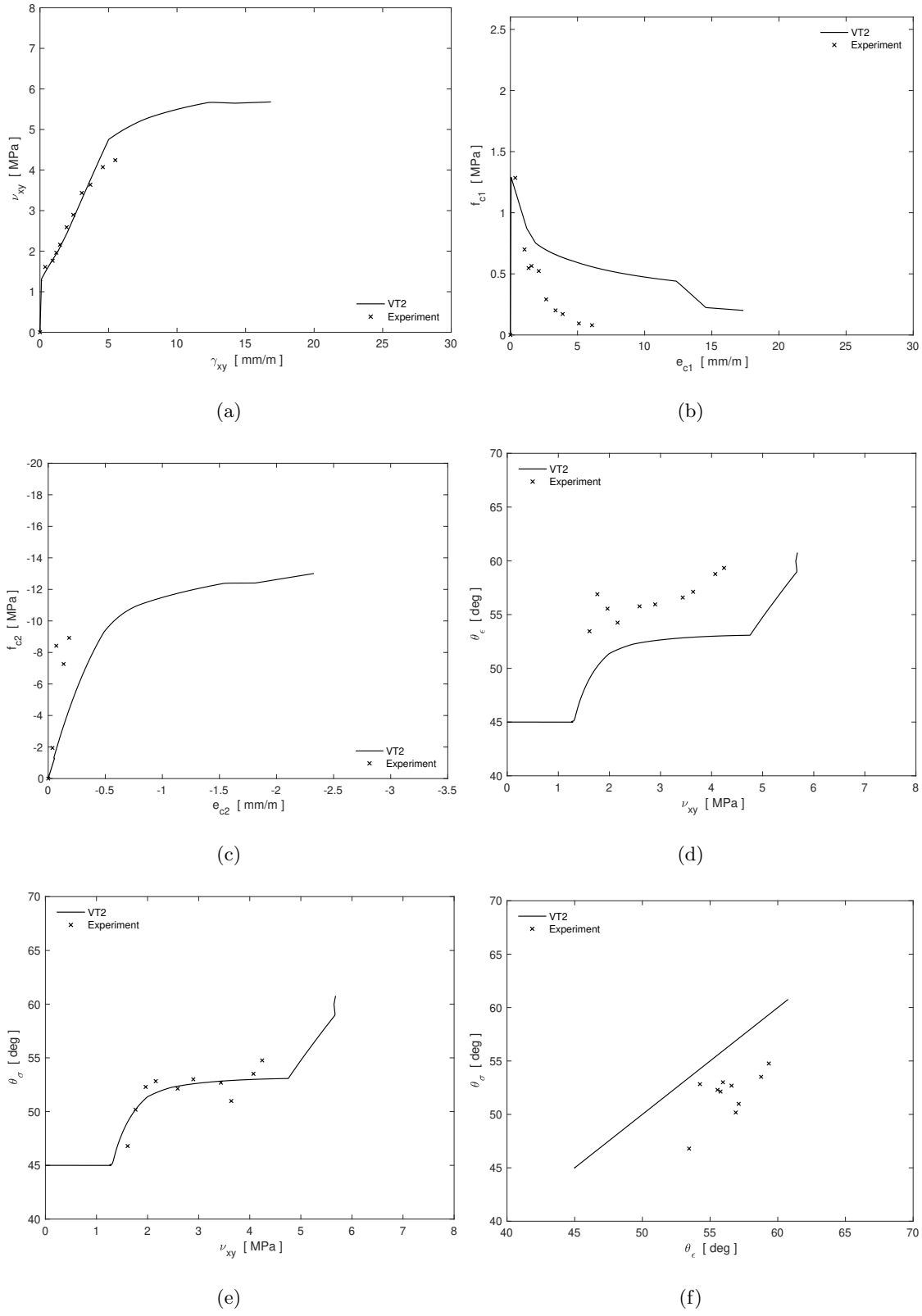

Figure A.10: Experimental response versus VT2 predicted response for PFRC-026-058 (a) $v_{xy} - \gamma_{xy}$ (b) $f_{c1} - \epsilon_{c1}$, (c) $f_{c2} - \epsilon_{c2}$ (d) $\theta_\sigma - v_{xy}$ (e) $\theta_\epsilon - v_{xy}$ (f) $\theta_\sigma - \theta_\epsilon$

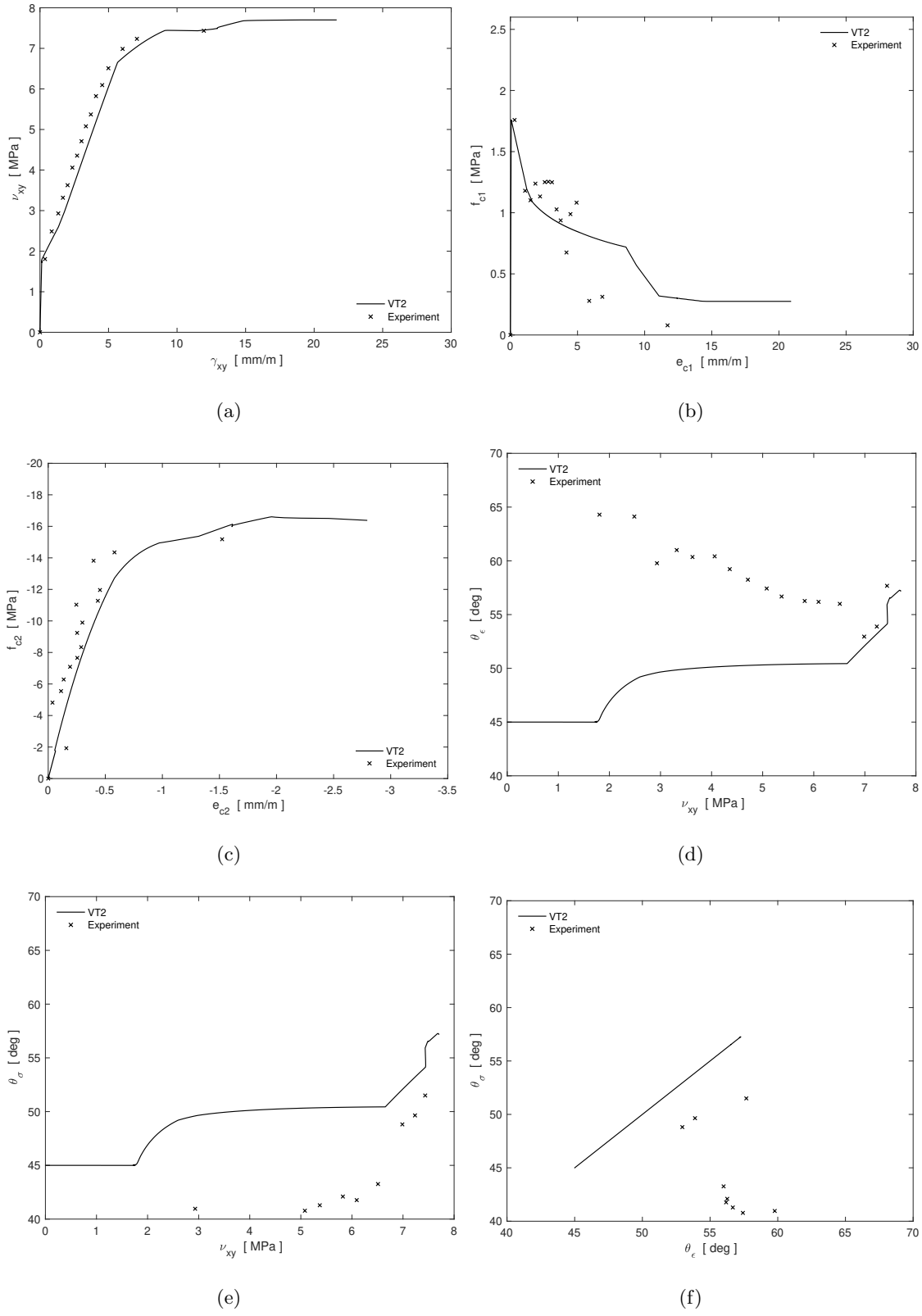

Figure A.11: Experimental response versus VT2 predicted response for PFRC-026-114 (a) $v_{xy} - \gamma_{xy}$ (b) $f_{c1} - \epsilon_{c1}$, (c) $f_{c2} - \epsilon_{c2}$ (d) $\theta_\sigma - v_{xy}$ (e) $\theta_\epsilon - v_{xy}$ (f) $\theta_\sigma - \theta_\epsilon$

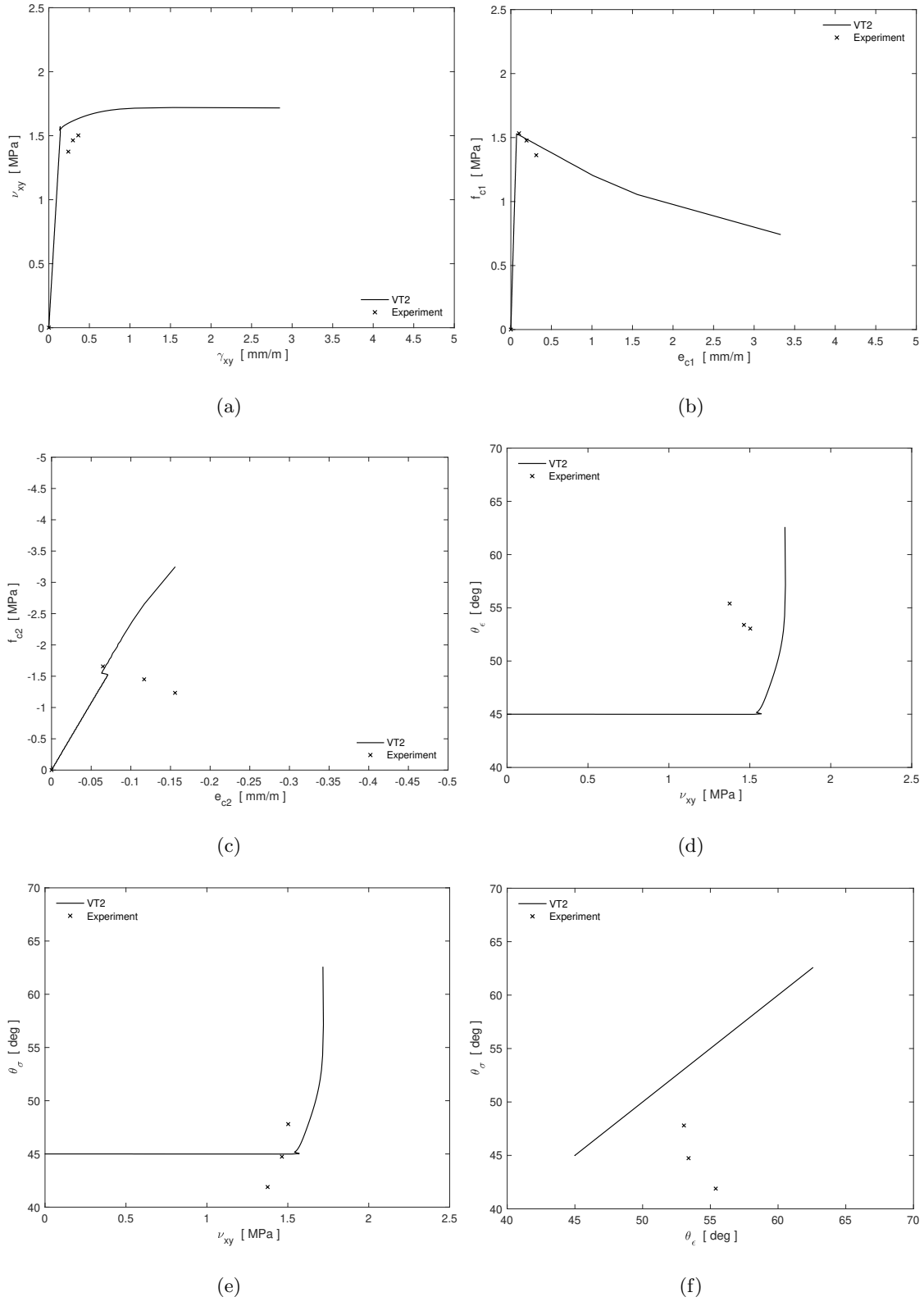

Figure A.12: Experimental response versus VT2 predicted response for PFRC-052-000 (a) $v_{xy} - \gamma_{xy}$ (b) $f_{c1} - \epsilon_{c1}$, (c) $f_{c2} - \epsilon_{c2}$ (d) $\theta_\sigma - v_{xy}$ (e) $\theta_\epsilon - v_{xy}$ (f) $\theta_\sigma - \theta_\epsilon$

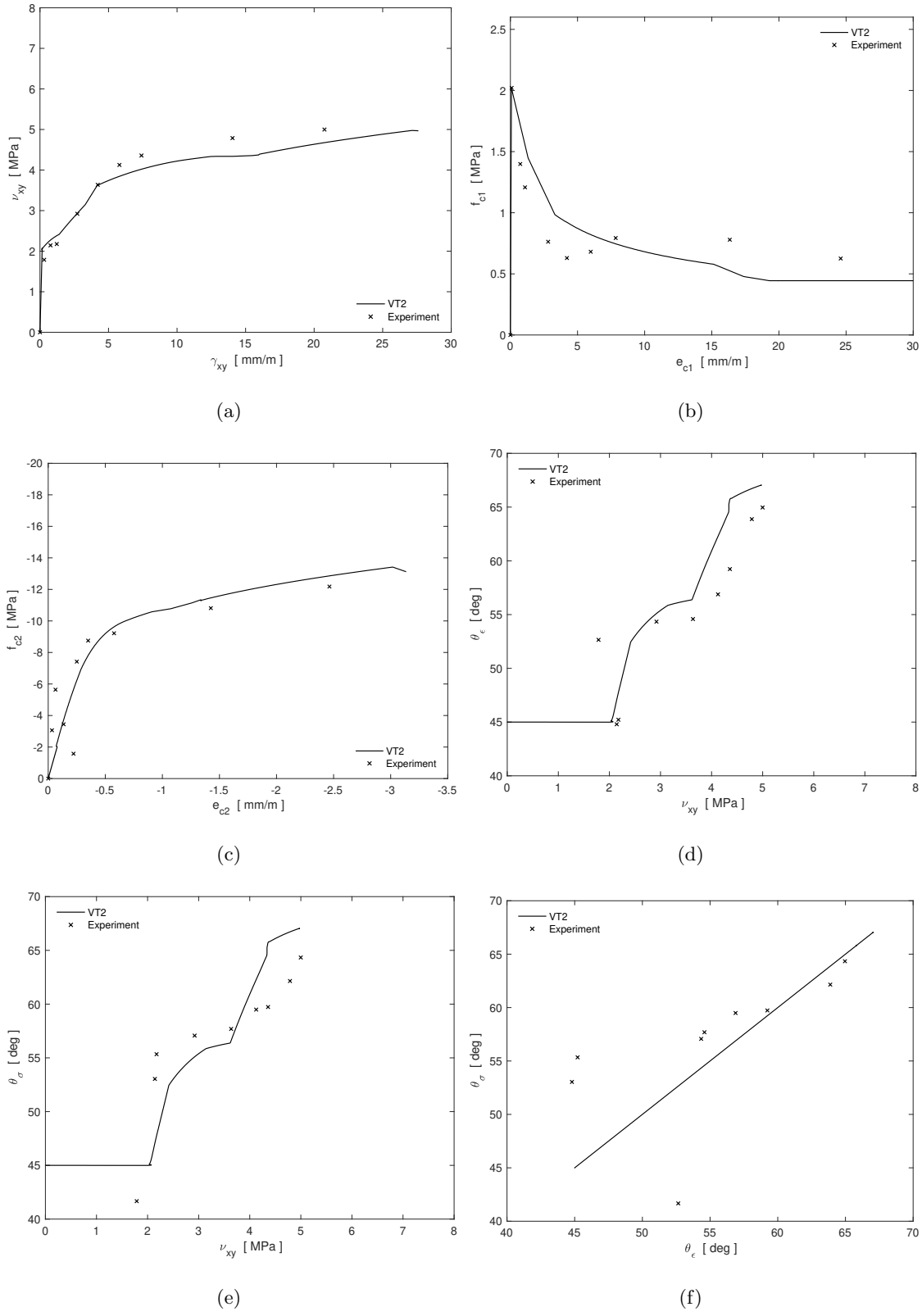

Figure A.13: Experimental response versus VT2 predicted response for PFRC-052-029 (a) $v_{xy} - \gamma_{xy}$ (b) $f_{c1} - \epsilon_{c1}$, (c) $f_{c2} - \epsilon_{c2}$ (d) $\theta_\sigma - v_{xy}$ (e) $\theta_\epsilon - v_{xy}$ (f) $\theta_\sigma - \theta_\epsilon$

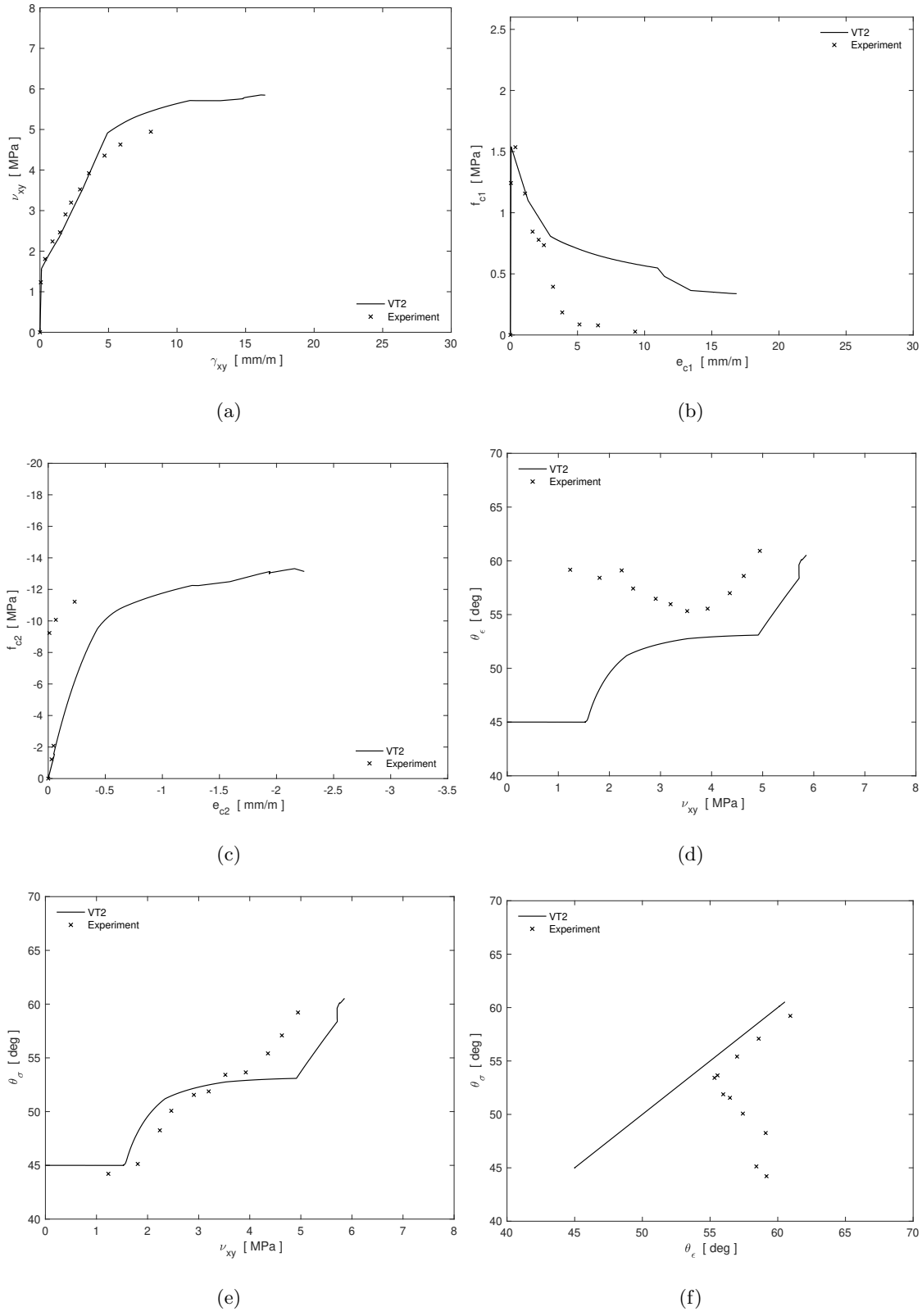

Figure A.14: Experimental response versus VT2 predicted response for PFRC-052-058 (a) $v_{xy} - \gamma_{xy}$ (b) $f_{c1} - \epsilon_{c1}$, (c) $f_{c2} - \epsilon_{c2}$ (d) $\theta_\sigma - v_{xy}$ (e) $\theta_\epsilon - v_{xy}$ (f) $\theta_\sigma - \theta_\epsilon$

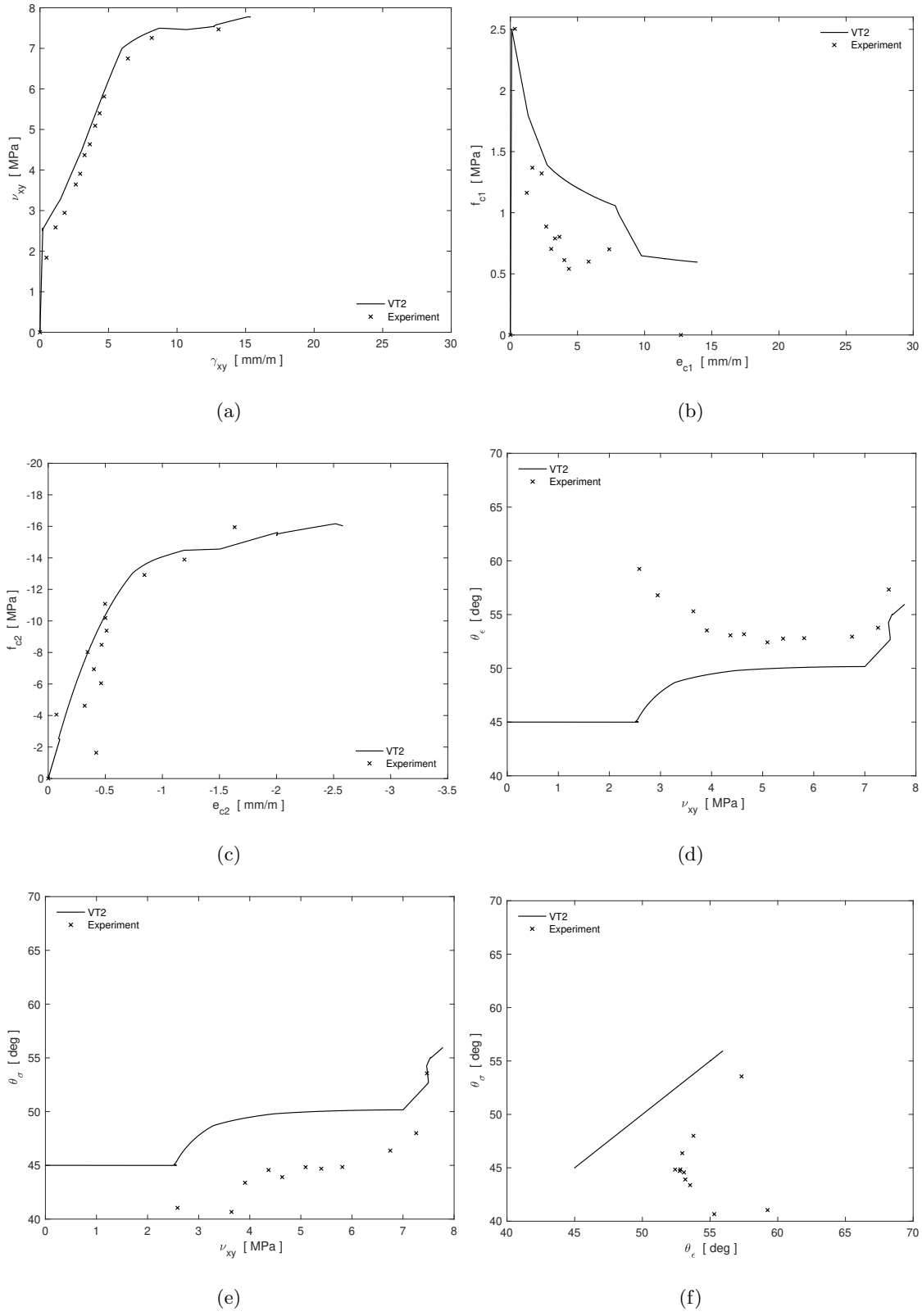

Figure A.15: Experimental response versus VT2 predicted response for PFRC-052-114 (a) $v_{xy} - \gamma_{xy}$ (b) $f_{c1} - \epsilon_{c1}$, (c) $f_{c2} - \epsilon_{c2}$ (d) $\theta_\sigma - v_{xy}$ (e) $\theta_\epsilon - v_{xy}$ (f) $\theta_\sigma - \theta_\epsilon$

Appendix B

VALIDATION MODELING RESULTS

B.1 Extrapolation Modeling

Table B.1: Tension softening inputs ($f'_t = f^{max}_{c1}$) for C1C, DC-P1, DC-P3 and DC-P5, by the proposed model (4.14)

C1C		DC-P1		DC-P3		DC-P5	
ϵ_{c1} [mm/m]	f_{c1} [MPa]	ϵ_{c1} [mm/m]	f_{c1} [MPa]	ϵ_{c1} [mm/m]	f_{c1} [MPa]	ϵ_{c1} [mm/m]	f_{c1} [MPa]
1.2	1.647	1.2	1.642	2.5	2.017	2.5	2.380
3.7	0.535	3.7	0.533	7.0	1.796	7.0	2.119
8.0	0.077	8.0	0.077	14.5	1.521	14.5	1.795
15.0	0.003	15.0	0.003	25.0	1.275	25.0	1.504

Table B.2: Tension softening inputs (VT2 default value used for f'_t) for C1C, DC-P1, DC-P3 and DC-P5, for the proposed model in Equation (4.14)

C1C		DC-P1		DC-P3		DC-P5	
ϵ_{c1} [mm/m]	f_{c1} [MPa]	ϵ_{c1} [mm/m]	f_{c1} [MPa]	ϵ_{c1} [mm/m]	f_{c1} [MPa]	ϵ_{c1} [mm/m]	f_{c1} [MPa]
1.2	1.559	1.2	1.628	2.5	2.195	2.5	2.267
3.7	0.506	3.7	0.529	7.0	1.954	7.0	2.018
8.0	0.073	8.0	0.076	14.5	1.655	14.5	1.710
15.0	0.003	15.0	0.003	25.0	1.387	25.0	1.433

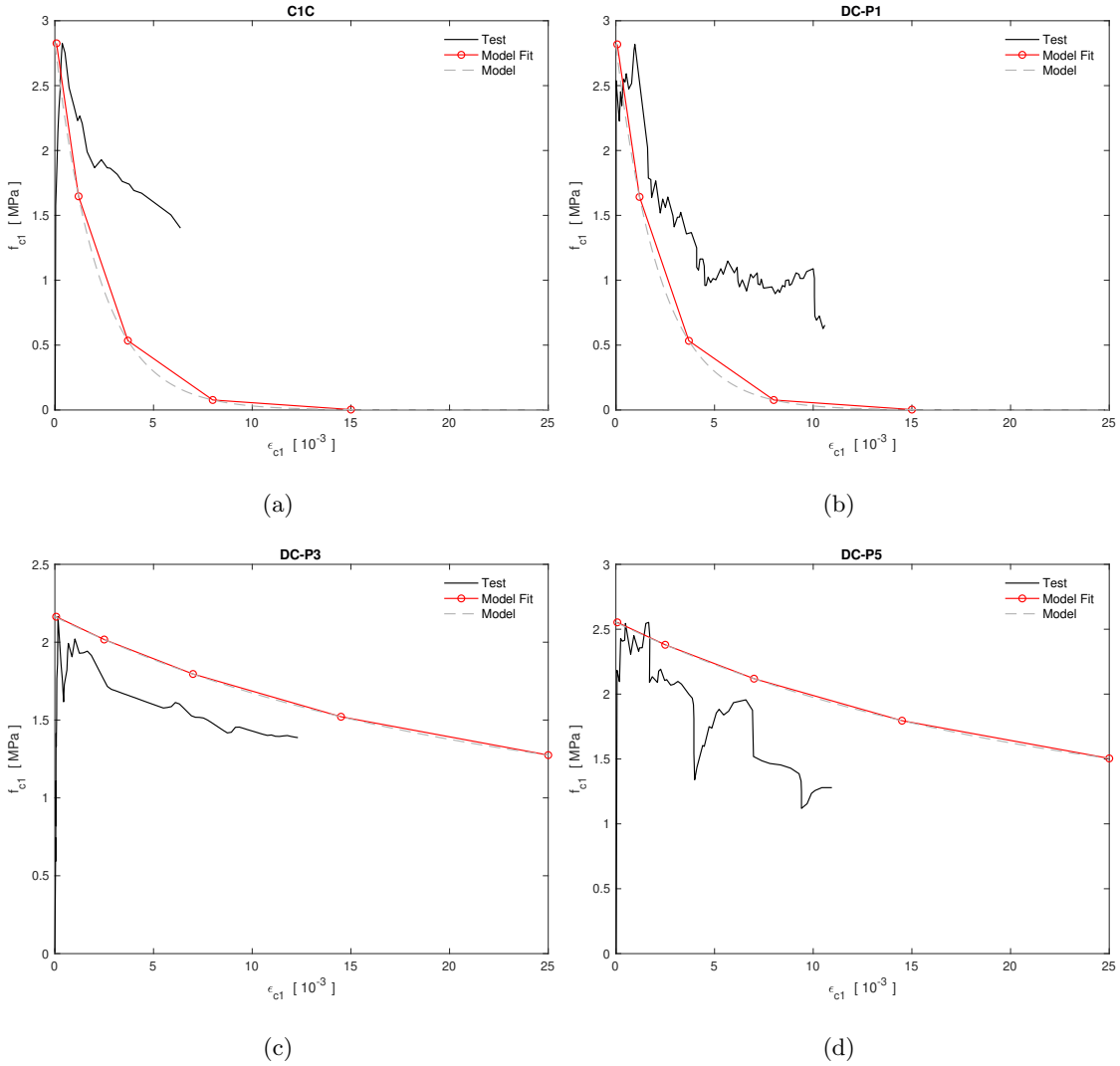

Figure B.1: Tension softening model inputs by Tables B.1 and B.2 versus experimental panel response (a) C1C (b) DC-P1 (c) DC-P3 (d) DC-P5

B.2 Material Beam Modeling

The modeling approach outlined in Chapter 4.3.6 was validated for the PFRC beams tested by Gaston (2023). The predicted response is compared to the experimental response in Figures B.2 and B.3.

It is important to note that the support displacement for beam specimens with $V_f = 0\%$ were not tracked during, unlike for beams with $V_f > 0\%$. Therefore, the modeling curves were not directly comparable to the experimental curves and are thus not showed herein.

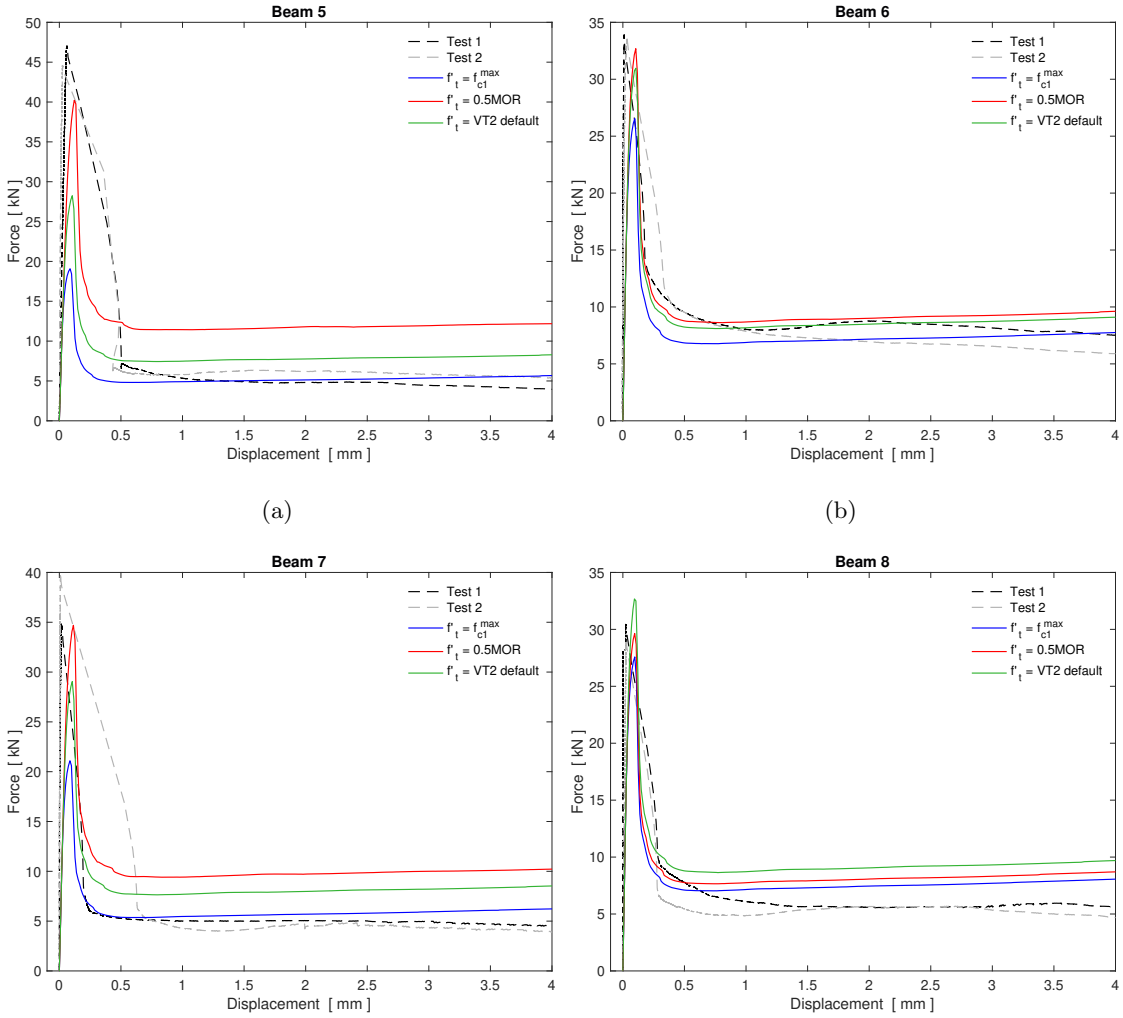

Figure B.2: Modeling of PFRC beams with $V_f = 0.26\%$ tested by Gaston (2023) companion to panel specimens (a) PFRC-026-000 (b) PFRC-026-029 (c) PFRC-026-058 (d) PFRC-026-114

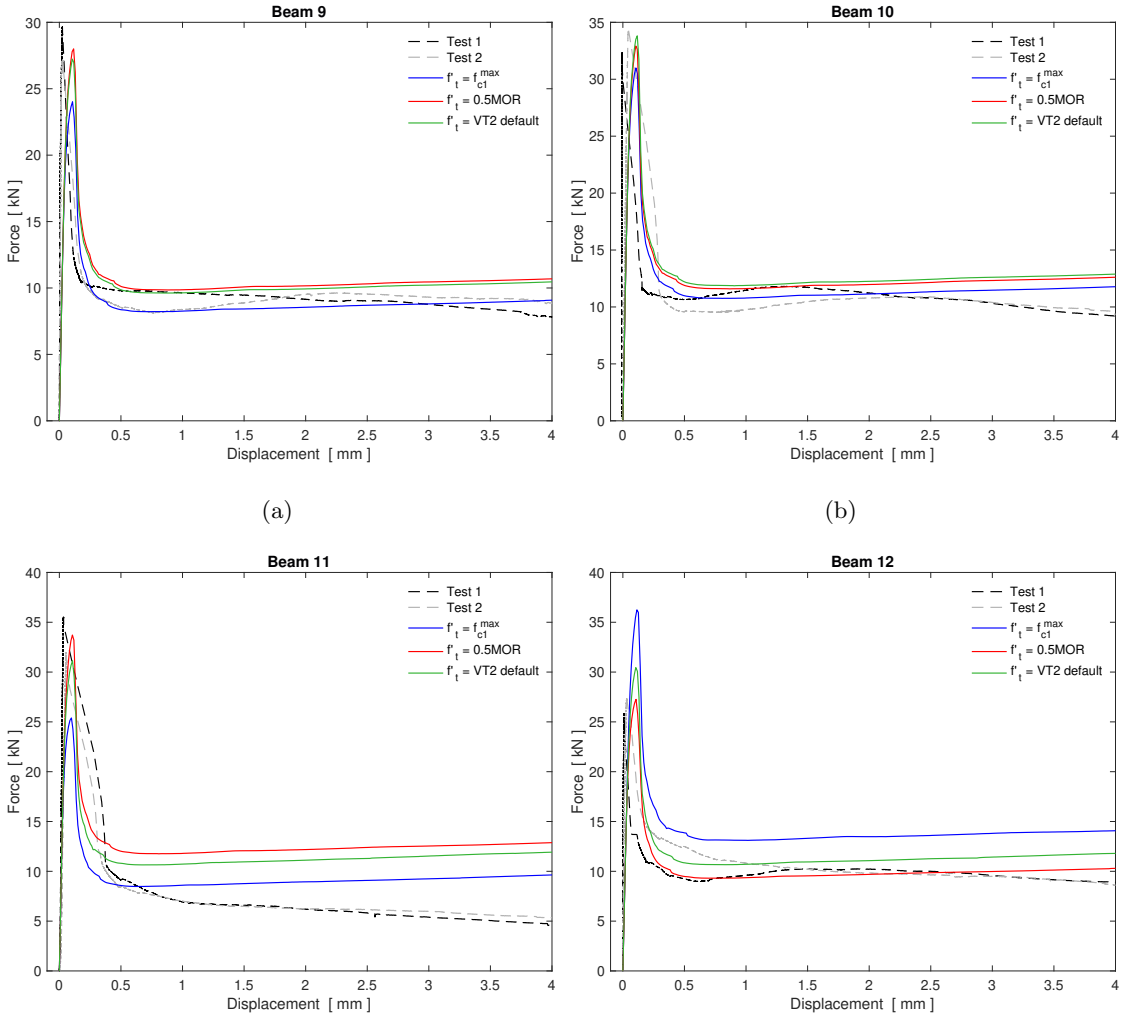

Figure B.3: Modeling of PFRC beams with $V_f = 0.26\%$ tested by Gaston (2023) companion to panel specimens (a) PFRC-052-000 (b) PFRC-052-029 (c) PFRC-052-058 (d) PFRC-052-114

Appendix C

PARAMETRIC STUDY MODELING RESULTS

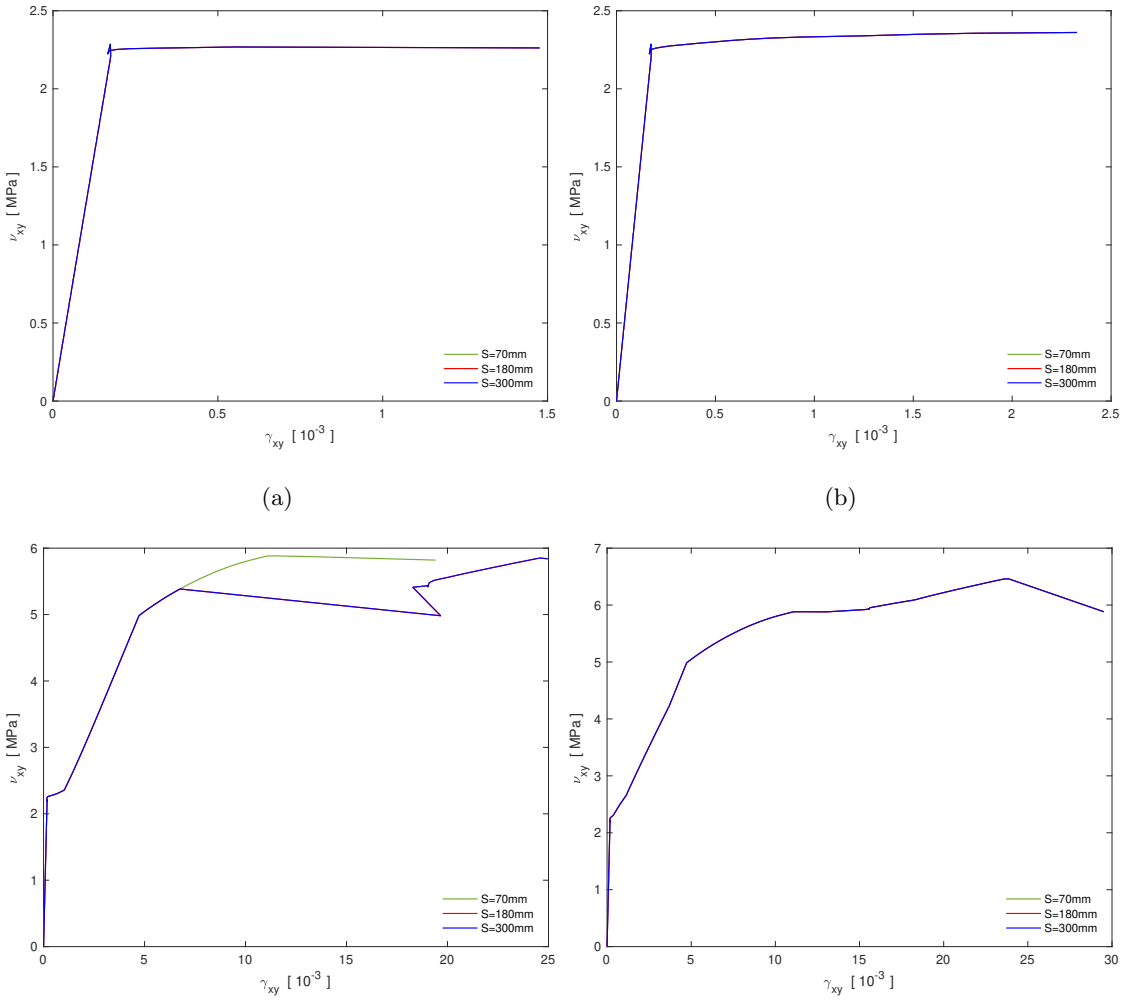

Figure C.1: Effects of specified crack spacing on the shear stress-strain response ($f'_c = 45\,MPa$) (a) $\rho_y = 0\%$, $V_f = 0\%$ (b) $\rho_y = 0\%$, $V_f = 0.5\%$ (c) $\rho_y = 0.5\%$, $V_f = 0\%$ (d) $\rho_y = 0.5\%$, $V_f = 0.5\%$

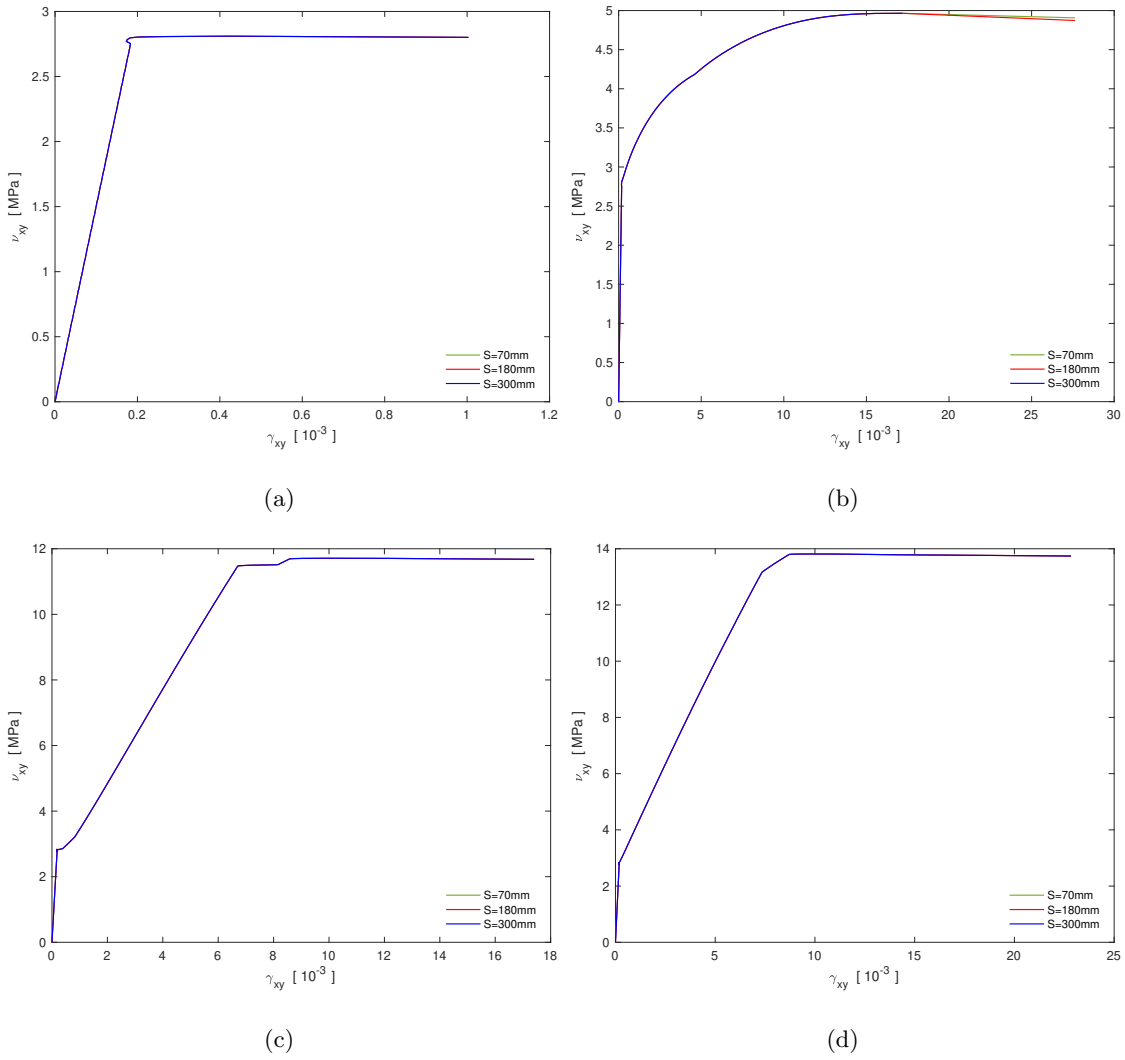

Figure C.2: Effects of specified crack spacing on the shear stress-strain response ($f'_c = 70\,MPa$) (a) $\rho_y = 0\%$, $V_f = 0\%$ (b) $\rho_y = 0\%$, $V_f = 2.0\%$ (c) $\rho_y = 2.0\%$, $V_f = 0\%$ (d) $\rho_y = 2.0\%$, $V_f = 2.0\%$

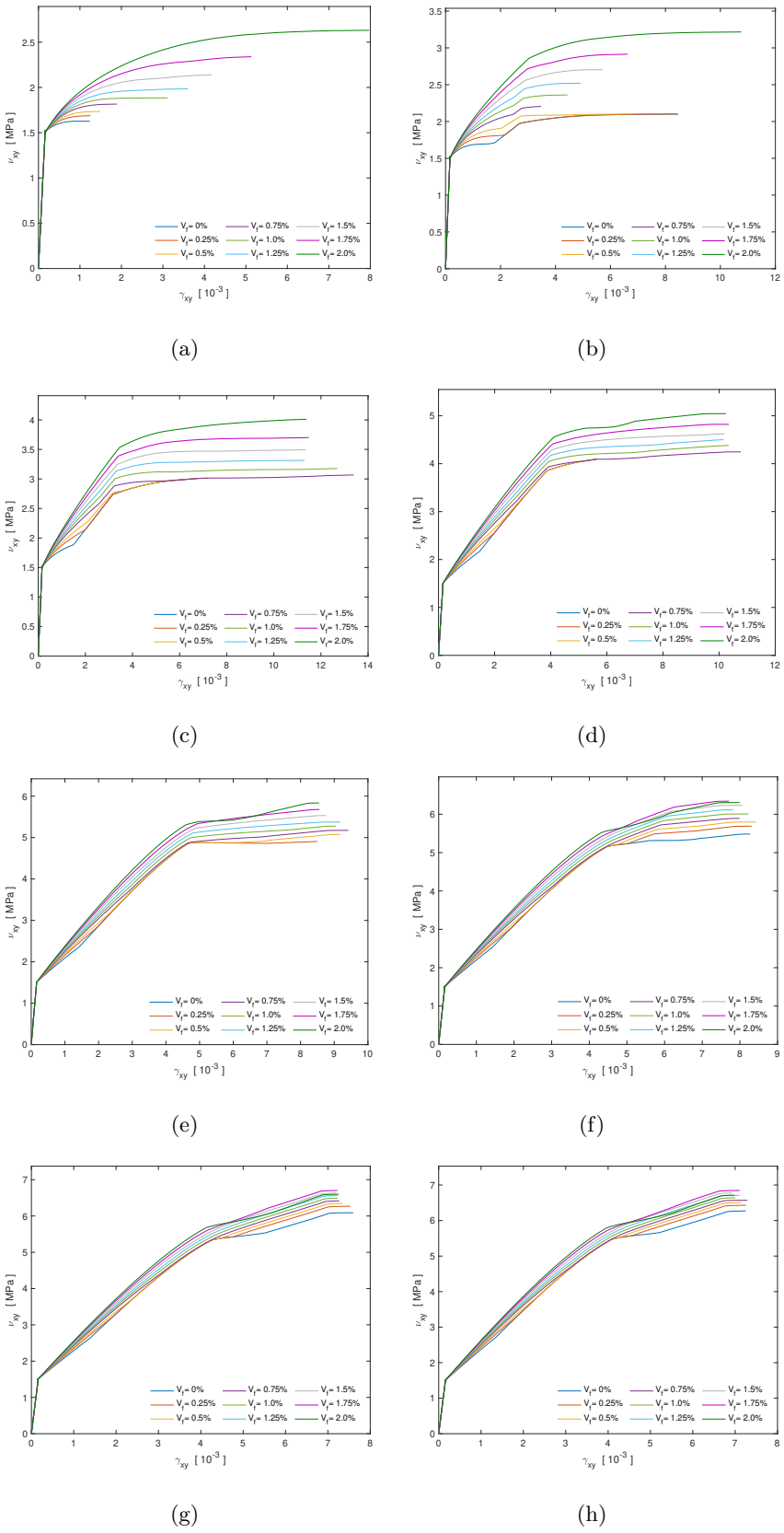

Figure C.3: Parametric study ($f'_c = 20\,MPa$) (a) $\rho_y = 0\%$ (b) $\rho_y = 0.1\%$ (c) $\rho_y = 0.25\%$ (d) $\rho_y = 0.5\%$ (e) $\rho_y = 0.75\%$ (f) $\rho_y = 1.0\%$ (g) $\rho_y = 1.25\%$ (h) $\rho_y = 1.5\%$

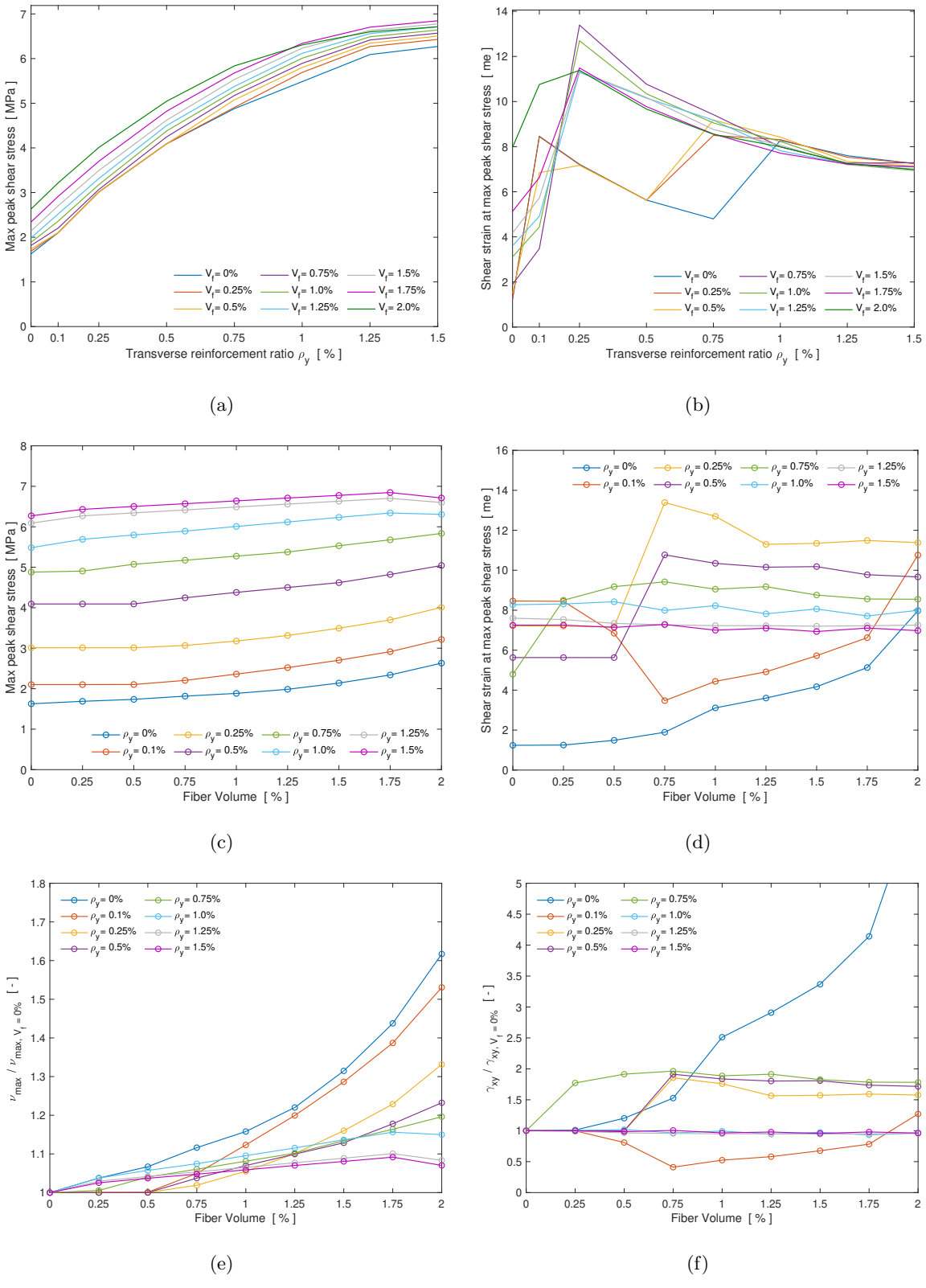

Figure C.4: Analysis of parametric study for $f'_c = 20\,MPa$

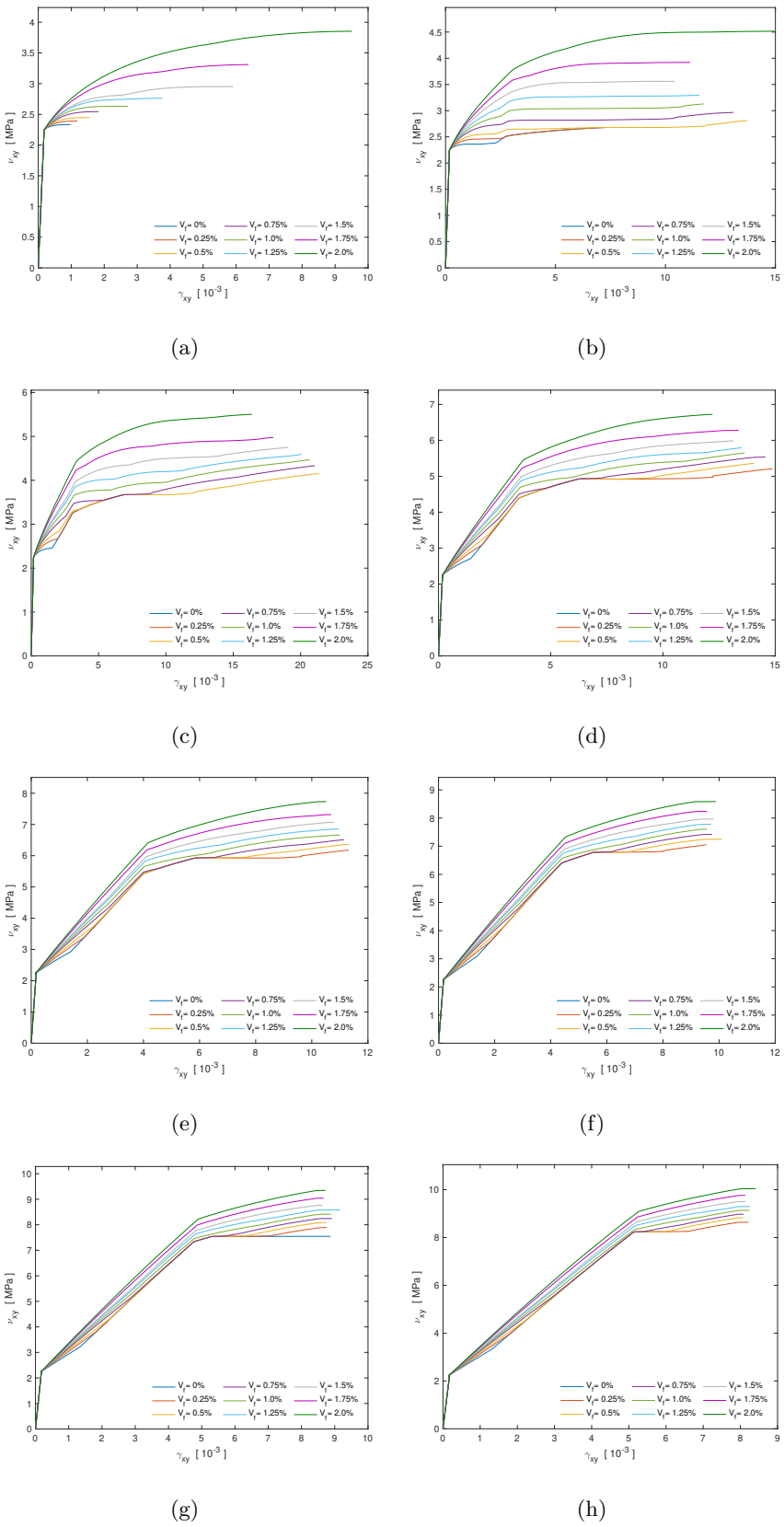

Figure C.5: Parametric study ($f'_c = 45\,MPa$) (a) $\rho_y = 0\%$ (b) $\rho_y = 0.1\%$ (c) $\rho_y = 0.25\%$ (d) $\rho_y = 0.5\%$ (e) $\rho_y = 0.75\%$ (f) $\rho_y = 1.0\%$ (g) $\rho_y = 1.25\%$ (h) $\rho_y = 1.5\%$

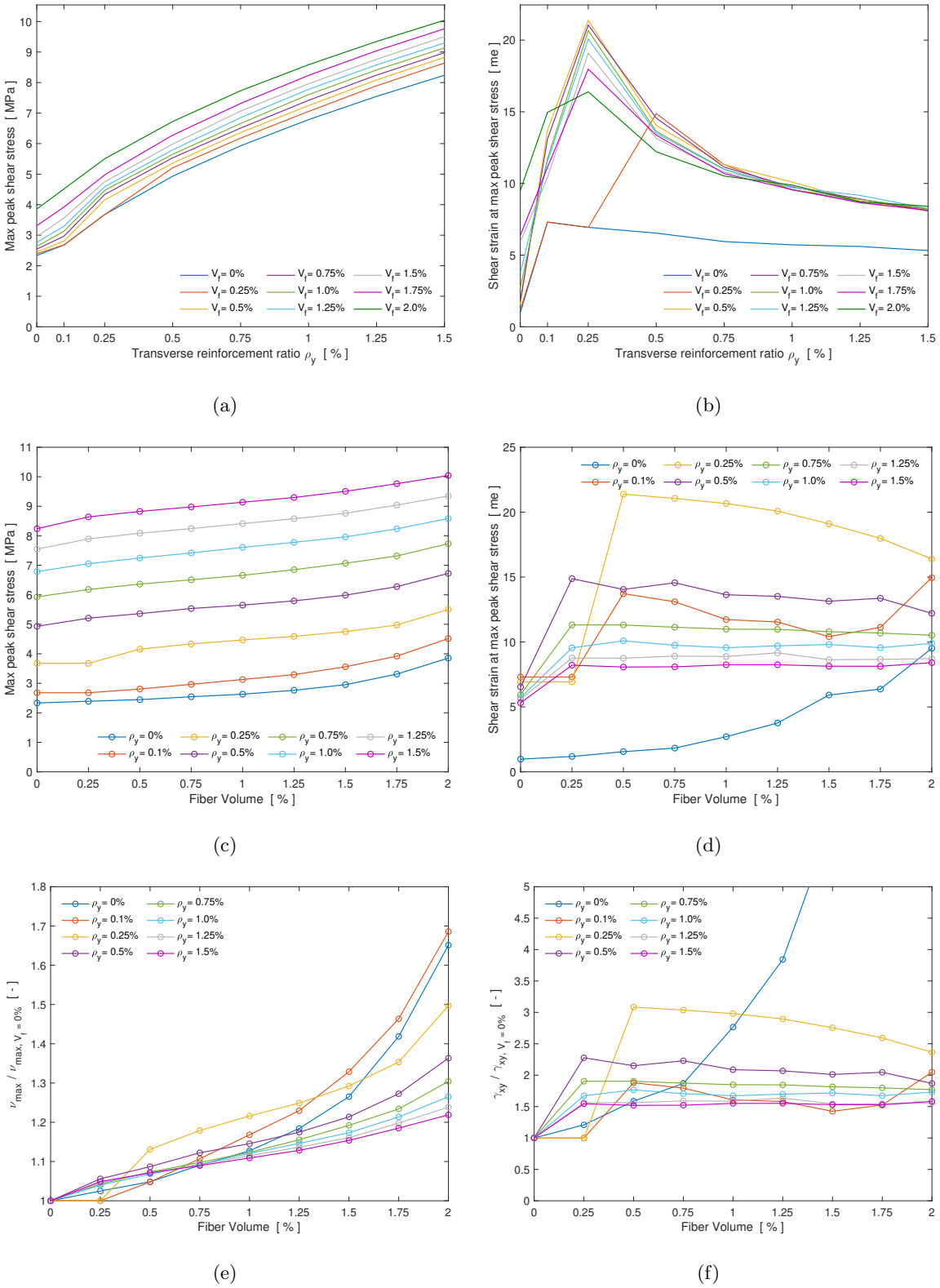

Figure C.6: Analysis of parametric study for $f'_c = 45\,MPa$

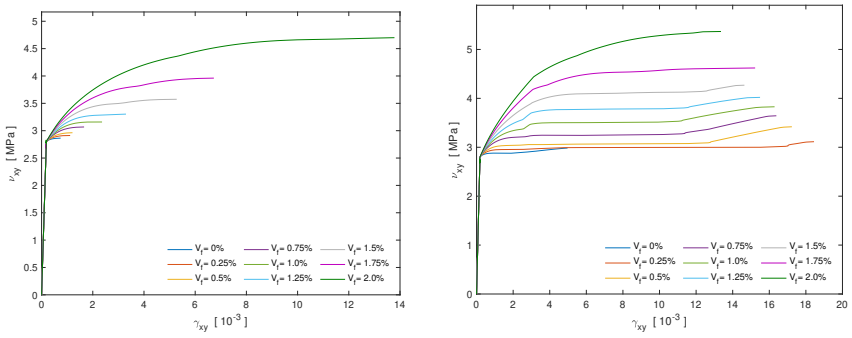

(a)

(b)

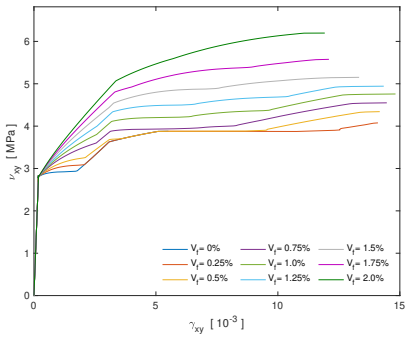

(c)

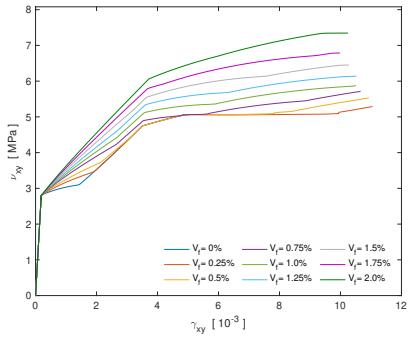

(d)

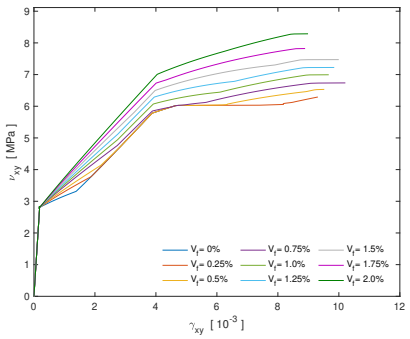

(e)

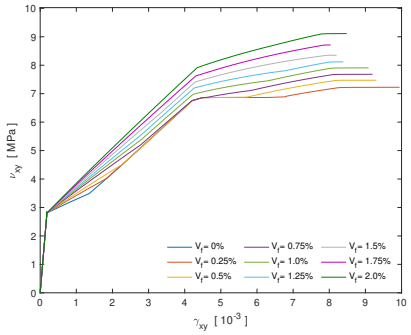

(f)

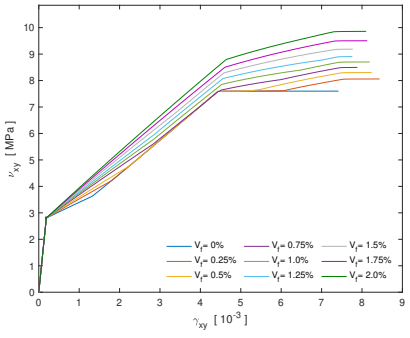

(g)

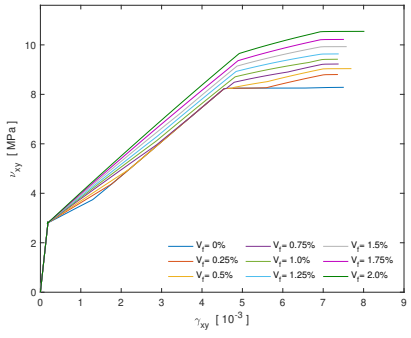

(h)

Figure C.7: Parametric study ($f'_c = 70\,MPa$) (a) $\rho_y = 0\%$ (b) $\rho_y = 0.1\%$ (c) $\rho_y = 0.25\%$ (d) $\rho_y = 0.5\%$ (e) $\rho_y = 0.75\%$ (f) $\rho_y = 1.0\%$ (g) $\rho_y = 1.25\%$ (h) $\rho_y = 1.5\%$

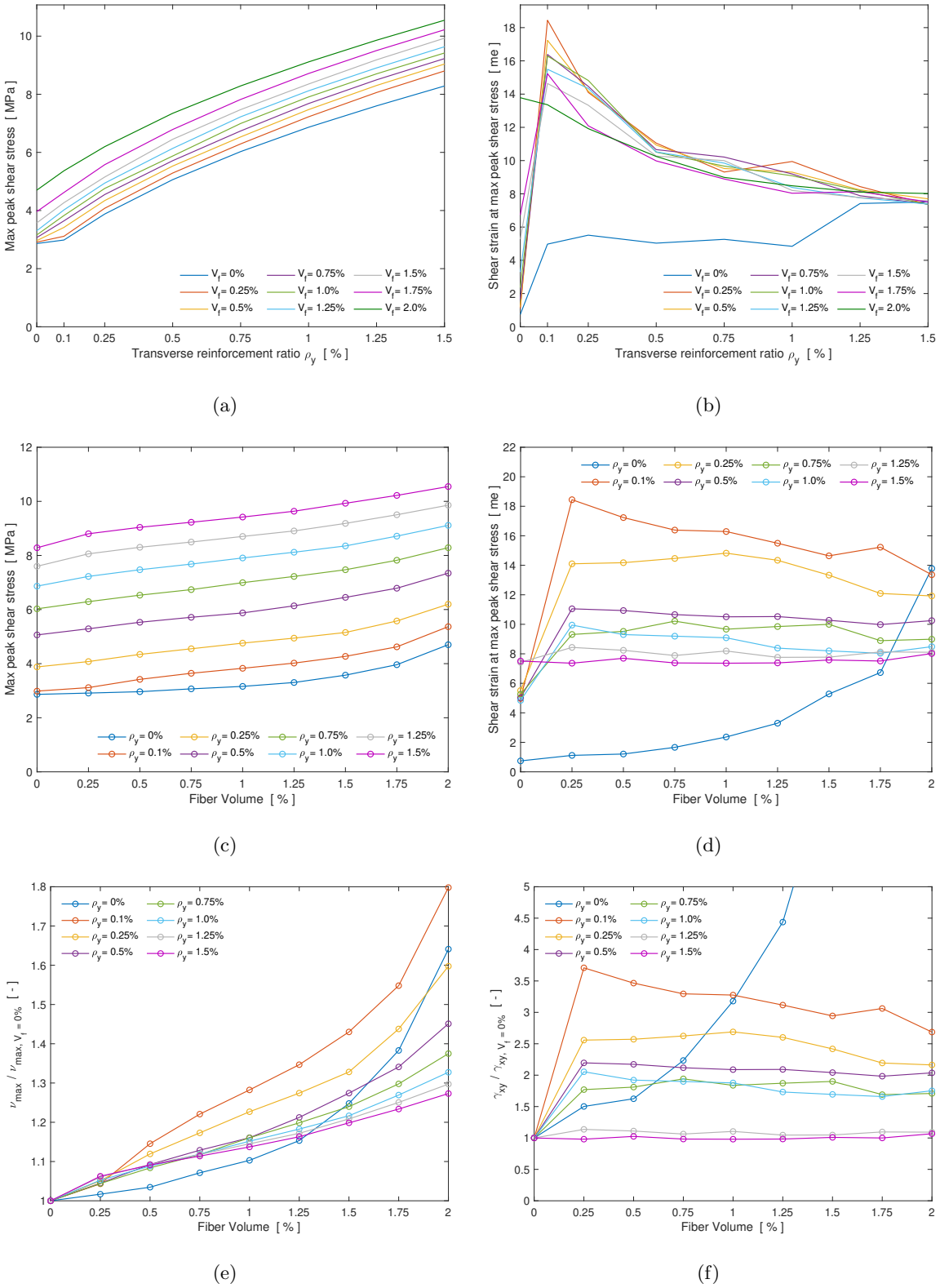

Figure C.8: Analysis of parametric study for $f'_c = 70\,MPa$

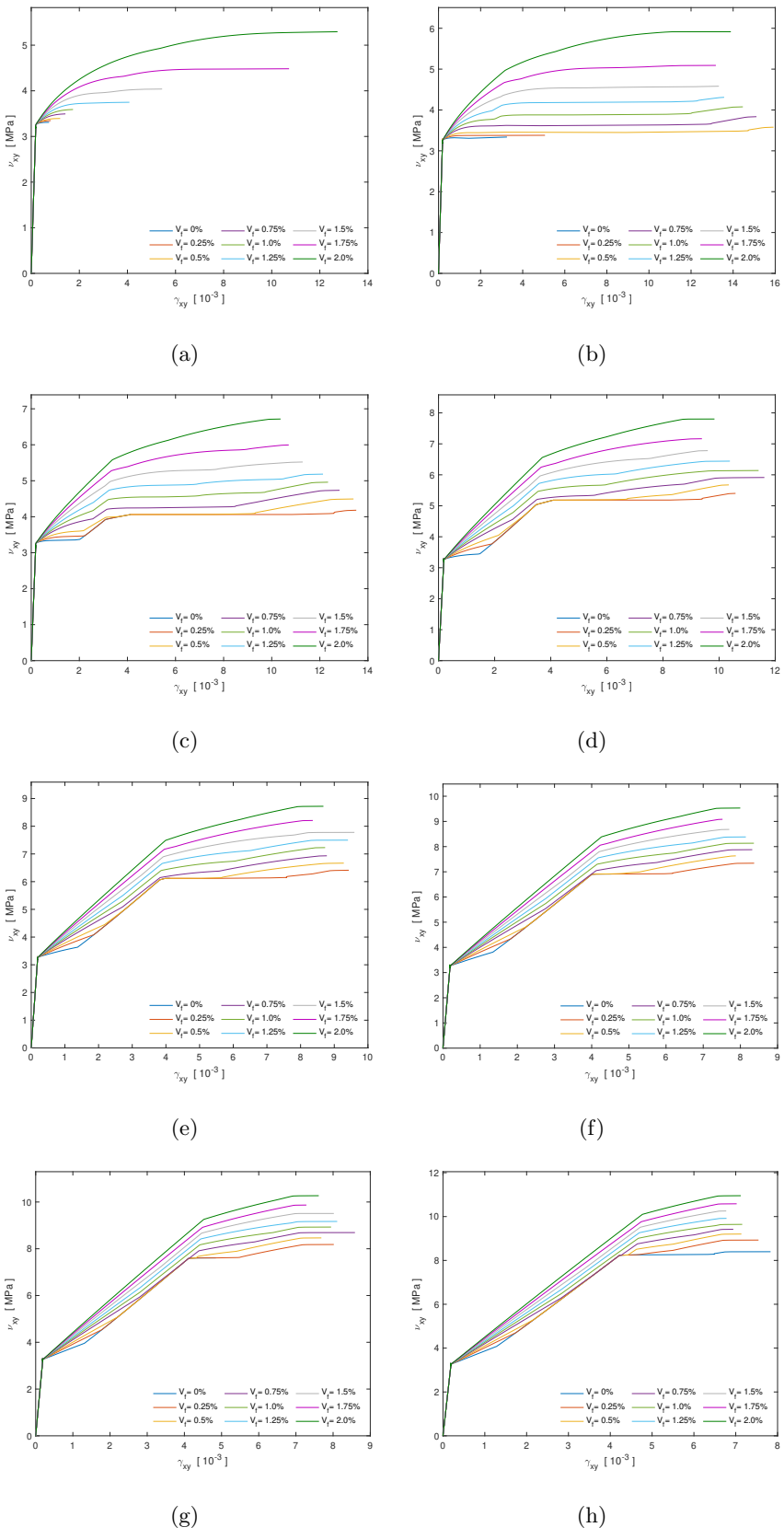

Figure C.9: Parametric study ($f'_c = 95\,MPa$) (a) $\rho_y = 0\%$ (b) $\rho_y = 0.1\%$ (c) $\rho_y = 0.25\%$ (d) $\rho_y = 0.5\%$ (e) $\rho_y = 0.75\%$ (f) $\rho_y = 1.0\%$ (g) $\rho_y = 1.25\%$ (h) $\rho_y = 1.5\%$

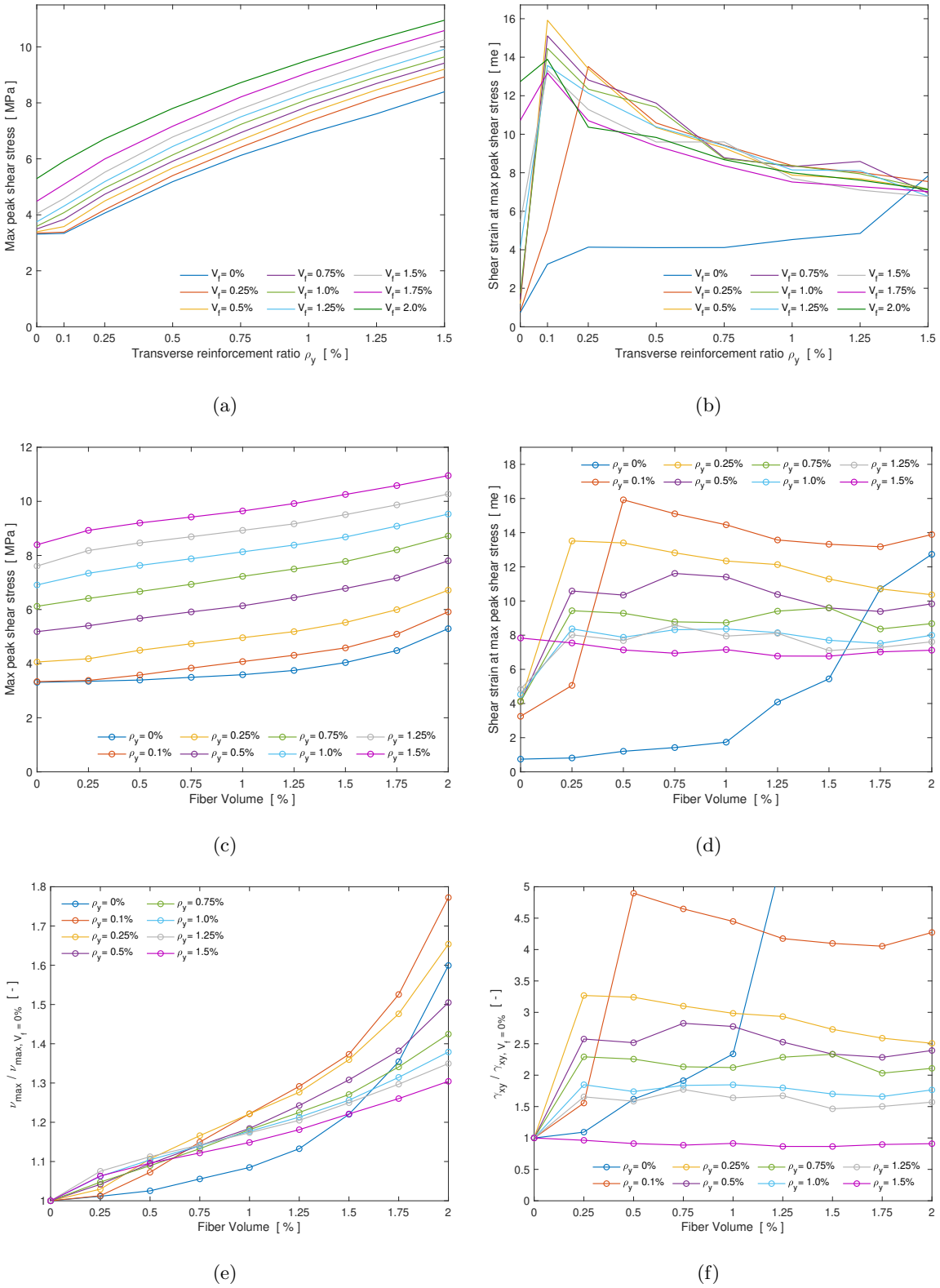

Figure C.10: Analysis of parametric study for $f'_c = 95\,MPa$

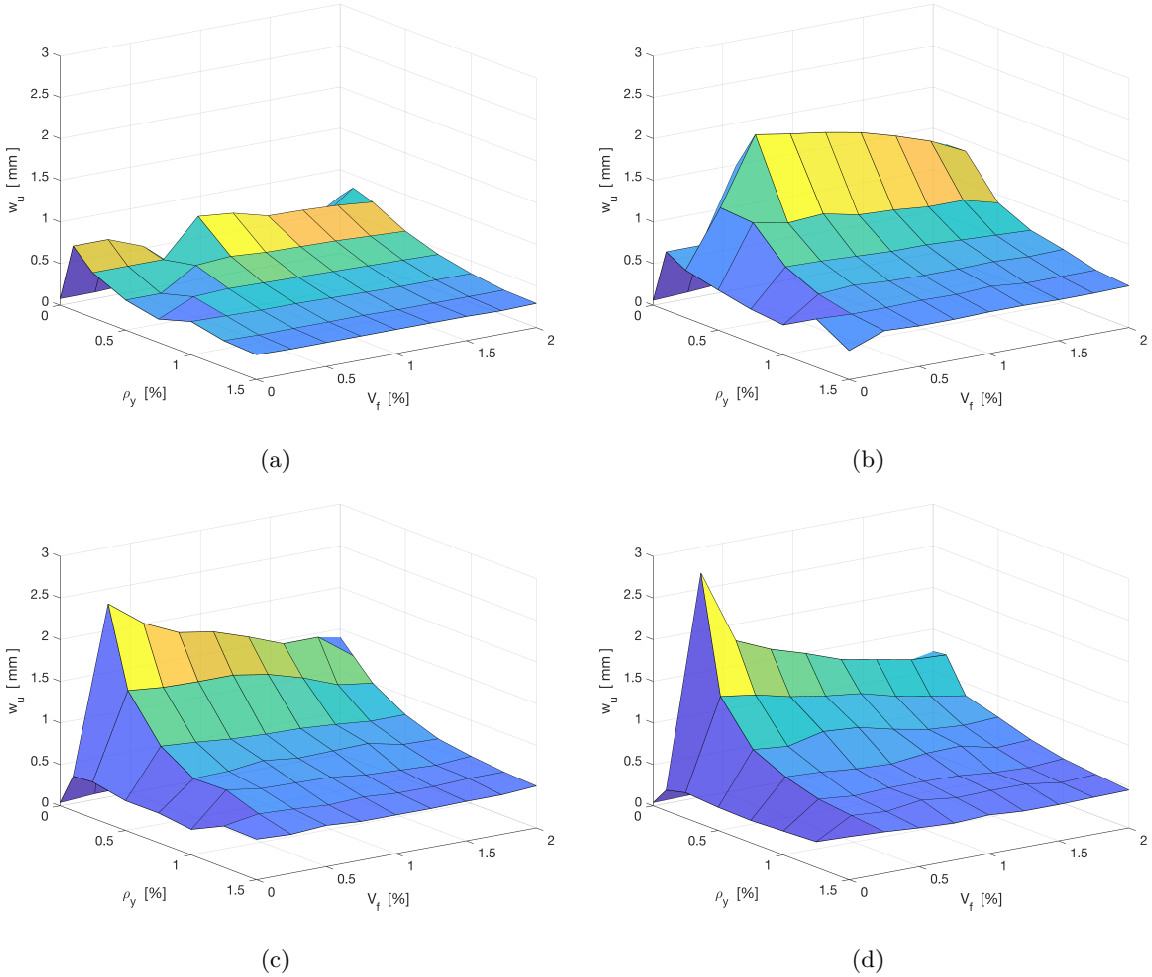

Figure C.11: Ultimate crack width of the parametric panels (a) $f'_c = 20\,MPa$ (b) $f'_c = 45\,MPa$ (c) $f'_c = 70\,MPa$ (d) $f'_c = 95\,MPa$

Appendix D

EMPIRICAL CALCULATIONS RESULTS

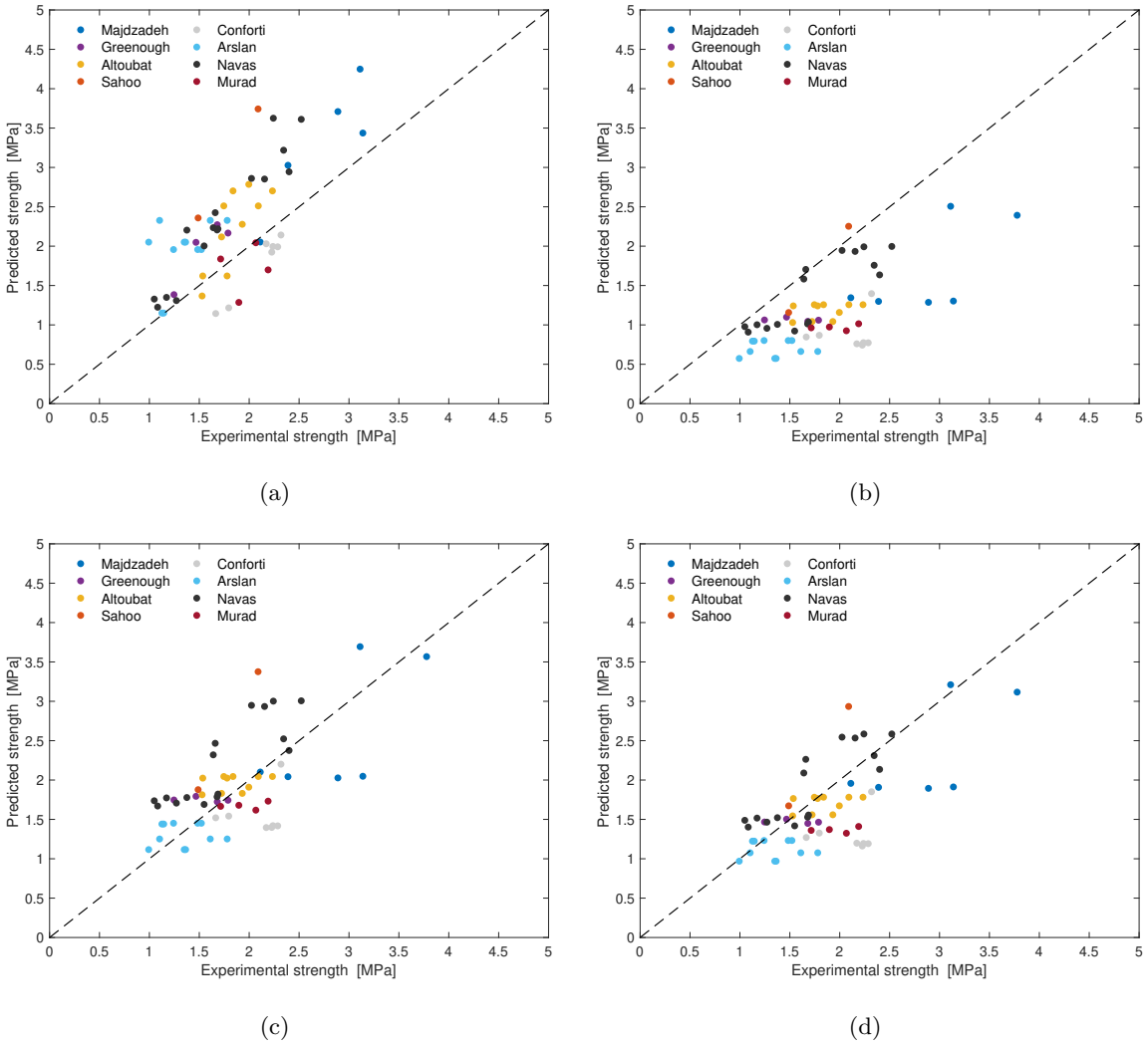

Figure D.1: Design code predictions versus experimental shear strength (a) fib Model Code (2010) (b) ACI 318 (2019) (c) AASHTO (2012) (d) CSA A23.3 (2019)

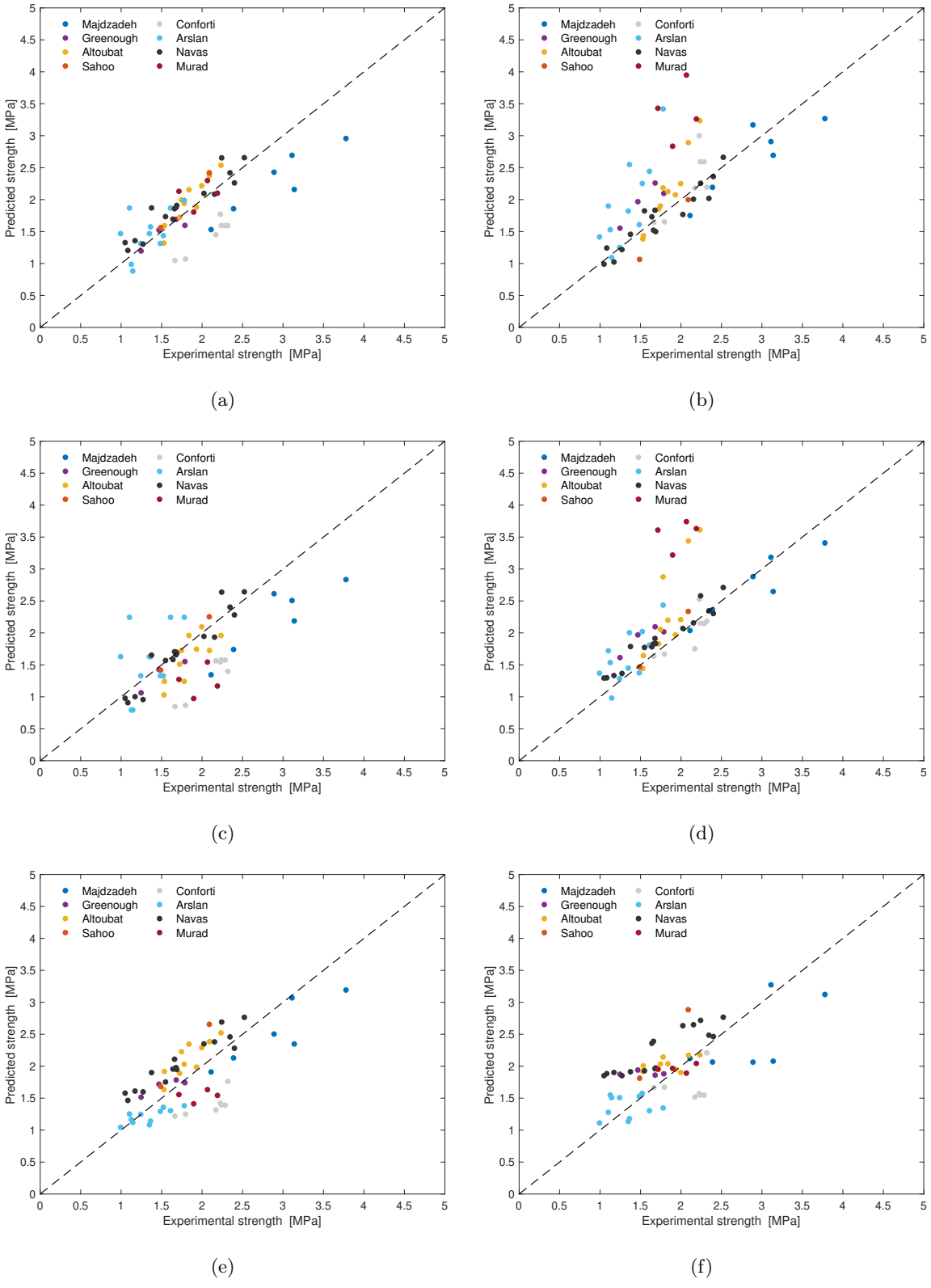

Figure D.2: Predicted strength by empirical equations versus experimental strength (a) Narayanan and Darwish (1987) (b) Ashour et al. (1992) (c) Swamy et al. (1993) (d) Arslan et al. (2017) (e) Ababneh et al. (2017)

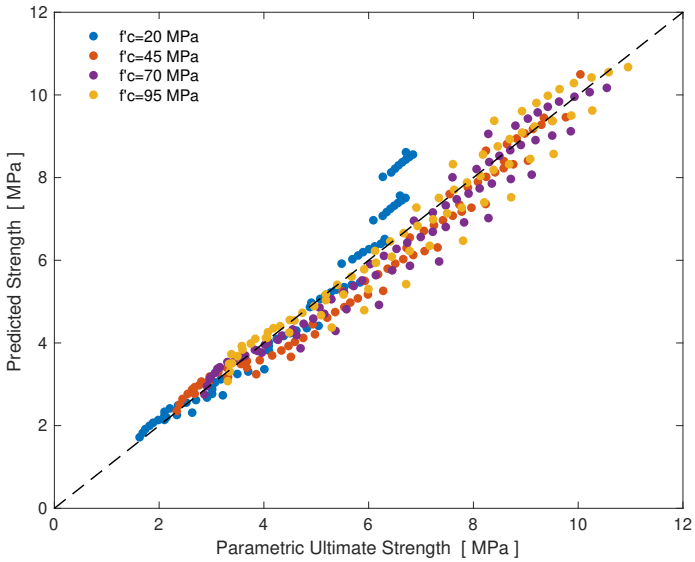

Figure D.3: Predicted strength by Equation (2.11) by Arslan et al. (2017) ($PSR = 0.5$) versus numerical strength

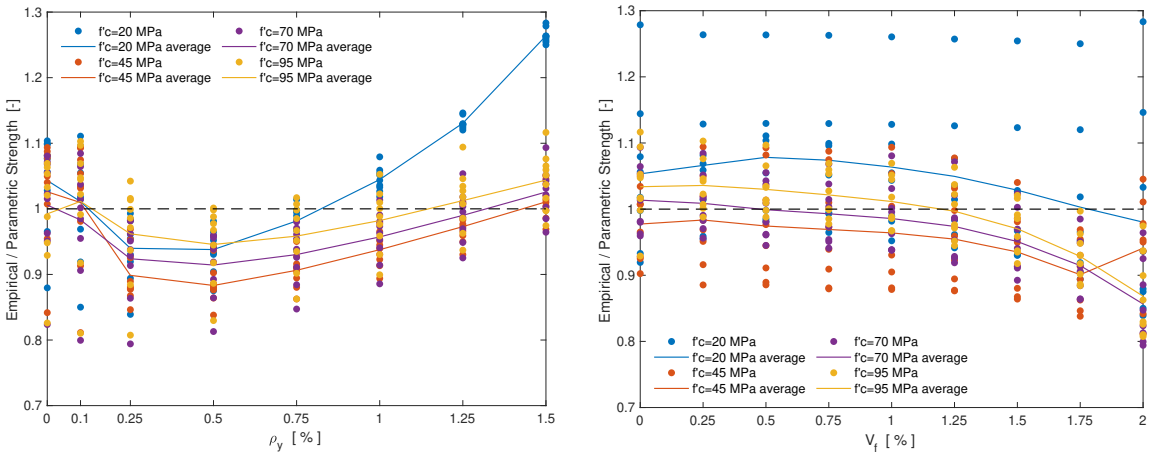

(a) (b)

Figure D.4: Predicted-to-numerical strength by Equation (2.11) by Arslan et al. (2017) ($PSR = 0.5$) versus (a) Transverse reinforcement ratio (b) Fiber volume